A systems approach to analyze the robustness of infrastructure networks to complex spatial hazards

Francesco Castellani

School of Engineering

Newcastle University

Thesis submitted for the degree of Doctor of Philosophy

October 2019

Table of Contents

Abstract

Infrastructure networks such as water supply systems, power networks, railway networks, and road networks provide essential services that underpin modern society's health, wealth, security, and wellbeing. However, infrastructures are susceptible to damage and disruption caused by extreme weather events such as floods and windstorms. For instance, in 2007, extensive disruption was caused by floods affecting a number of electricity substations in the United Kingdom, resulting in an estimated damage of GBP£3.18bn (US$4bn). In 2017, Hurricane Harvey hit the Southern United States, causing an approximated US$125bn (GBP£99.35bn) in damage due to the resulting floods and high winds. The magnitude of these impacts is at risk of being compounded by the effects of Climate Change, which is projected to increase the frequency of extreme weather events. As a result, it is anticipated that an estimated US$3.7tn (GBP£2.9tn) in investment will be required, per year, to meet the expected need between 2019 and 2035.

A key reason for the susceptibility of infrastructure networks to extreme weather events is the wide area that needs to be covered to provide essential services. For example, in the United Kingdom alone there are over 800,000 km of overhead electricity cables, suggesting that the footprint of infrastructure networks can be as extended as that of an entire Country. These networks possess different spatial structures and attributes, as a result of their evolution over long timeframes, and respond to damage and disruption in different and complex ways.

Existing approaches to understanding the impact of hazards on infrastructure networks typically either (i) use computationally expensive models, which are unable to support the investigation of enough events and scenarios to draw general insights, or (ii) use low complexity representations of hazards, with little or no consideration of their spatial properties. Consequently, this has limited the understanding of the relationship between spatial hazards, the spatial form and connectivity of infrastructure networks, and infrastructure reliability.

This thesis investigates these aspects through a systemic modelling approach, applied to a synthetic and a real case study, to evaluate the response of infrastructure networks to spatially complex hazards against a series of robustness metrics.

In the first case study, non-deterministic spatial hazards are generated by a fractal method which allows to control their spatial variability, resulting in spatial configurations that very closely resemble natural phenomena such as floods or windstorms. These hazards are then superimposed on a range of synthetic network layouts, which have spatial structures consistent

with real infrastructure networks reported in the literature. Failure of network components is initially determined as a function of hazard intensity, and cascading failure of further components is also investigated. The performance of different infrastructure configurations is captured by an array of metrics which cover different aspects of robustness, ranging from the proneness to partitioning to the ability to process flows in the face of disruptions.

Whereas analyses to date have largely adopted low complexity representations of hazards, this thesis shows that consideration of a high complexity representation which includes hazard spatial variability can reduce the robustness of the infrastructure network by nearly 40%. A "small-world" network, in which each node is within a limited number of steps from any other node, is shown to be the most robust of all the modelled networks to the different structures of spatial hazard.

The second case study uses real data to assess the robustness of a power supply network operating in the Hull region in the United Kingdom, which is split in high and low voltage lines. The spatial hazard is represented by a high-resolution wind gust model and tested under current and future climate scenarios. The analysis reveals how the high and low voltage lines interact with each other in the event of faults, which lines would benefit the most from increased robustness, and which are most exposed to cascading failures. The second case study also reveals the importance of the spatial footprint of the hazard relative to the location of the infrastructure, and how particular hazard patterns can affect low voltage lines that are more often located in exposed areas at the edge of the network. The impact of Climate Change on windstorms is highly uncertain, although it could further reduce network robustness due to more severe events.

Overall the two case studies provide important insights for infrastructure designers, asset managers, the academic sector, and practitioners in general. In fact, in the first case study, this thesis defines important design principles, such as the adoption of a small-world network layout, that can integrate the traditional design drivers of demand, efficiency, and cost. In the second case study, this thesis lays out a methodology that can help identify assets requiring increased robustness and protection against cascading failures, resulting in more effective prioritized infrastructure investments and adaptation plans.

Acknowledgements

This has been one long, exciting journey. There were ups and downs, uncertainties, rewards, headaches, and some discoveries. I also had support and guidance, but always as a side ingredient to a much more important recipe: the opportunity to roam freely and experiment. However, I cannot claim this thesis to be entirely mine, as the work and presence of others have to be acknowledged. I would like to thank Professor Richard Dawson and Professor Chris Kilsby for giving me this opportunity in the first place, and for their constant and invaluable support. Every single meeting was a chance for me to grow, and I vividly hope that the many headaches I had while going back home were a sign of an improving critical thinker. If this is the case, I hope to have experienced more headaches than those I am sure to have caused. Other people at Newcastle University have played a crucial role in these years, beginning with Dr. Caspar Hewett, to whom I am indebted for teaching me how important it is to have guts. I would also like to thank my friend Dr. Xiaodong Ming for showing me how important it is to value cultural diversity. My gratitude also goes to Dr. Maria Pregnolato, Dr. Elizabeth Lewis, Dr. David Pritchard, Dr. Robert Bertsch, Dr. Fergus McClean, Dr. Stephen Blenkinsop, and to my friend Dr. Motasem Darwish for our unbounded and culturally rich conversations about life. I would also like to thank Prof. Hiroki Sayama at SUNY Binghamton and Dr. Nicolas Kirchner-Bossi at EPFL Lausanne for their in-depth guidance. Immense gratitude is also due to the late Zia Annina, who spent countless hours teaching me Mathematics for free whilst leading by ethical and moral example. I am very sorry she is not here to see what her efforts have led to. I am also grateful to Prof. Giuseppe Mendicino at University of Calabria for inspiring me and nurturing my curiosity as an engineering student.

I am, and always will be, indebted to my family for providing their unconditional love and support. They have constantly been there for me through the many ups and downs and the countless Skype calls of these years. As much as I would like them to, I hope that they will not read past this page, as here is everything they need to know: I made it.

The last thanks on this page, but the first and most important in my heart, go to my partner, companion, friend, and rock, *Carmela*. Thank you for accompanying me every step of the way, for encouraging me ever since I made the decision to accept this challenge, for supporting me, for listening to my rants, and for being there when I had something to cheer for. All of this would have not been possible without you, so it is only fair if I say: *we* made it.

List of publications

The work contained in this PhD thesis is linked to the following publications:

Castellani, F., Kilsby, C. and Dawson, R. (2019) 'Response of a range of synthetic infrastructure networks to synthetic spatial hazards', in preparation.

Castellani, F., Kirchner-Bossi, N., Ford, A., Kilsby, C., Wilkinson, S., Kendon, E., Fowler, H. and Dawson, R. (2017) 'Analysis of Electricity Network Risks from Daily Maxima Wind Gusts using a high-resolution Climate Model', proceedings of the 2017 International Symposium for Next Generation Infrastructures, pp. 73-79. Institution of Civil Engineers, London. Available at: http://isngi.org/wp-content/uploads/2017/10/ISNGI-Conference-Proceedings-v2.pdf.

Glossary of terms

1st order failures

Failures directly caused by the impact of an external agent on the infrastructure, such as a climatic hazard.

2nd order failures

Failures not directly caused by an external agent, but by the result of a domino effect within the infrastructure.

Brownian surface

Synthetic fractal surface generated by implementing the fractional Brownian motion in a three-dimensional spatial domain. The datum of the surface is a regular x, y plane or grid. Given two points $p_1 = (x_1, y_1)$ and $p_2 = (x_2, y_2)$ on this grid, the difference in elevation $z_2 - z_1$ is correlated with the distance between $p_1$and p_2 depending on the value of the Hurst exponent H.

Bulk Supply Point

Electricity substation where the voltage is stepped down from 132kV to 33-66kV.

Cascading failures

Non-linear domino effect where failures that occur in one specific layer of a multilayer network propagate, by virtue of interlayer connections, to other layers, potentially resulting in complete shutdowns. Cascading failures are one of the mechanisms dominated by 2nd order failures, which cause an initial perturbation to evolve into a disproportionate phenomenon.

Civil engineering infrastructures

Networked systems composed of physical elements that are designed and built according to civil engineering principles. These systems are aimed at satisfying primary needs of societies, including the delivery of services, such as utility or telecommunication networks, or the flow of passengers and freight, such as transportation networks.

Climatic loading

Load being applied to a physical element or an infrastructure network as a result of the presence of a climate phenomenon acting as an external agent. Examples of climatic loading include the wind speed, the depth of flooding waters, the rainfall intensity, or the voltage potential of a lightning bolt.

Complex network

Multilayer network where a node in a given layer is not only connected with nodes in the same layer but also with nodes in other layers.

Component or tier component

Segments of the 132kV and 33-66kV tiers or electricity networks. In the context of this thesis, the former are also known as *feeders*, whilst the latter are known as *circuits*. Feeders are located hierarchically above circuits and

connect National Grid Substations with Bulk Supply Points. Circuits connect Bulk Supply Points with Primary Substations.

Control climate

Output of the control runs of a Climate Model used as initial conditions. Often compared to the output of Future climate runs to investigate projected changes.

Critical Footprint

Portions of the footprint where the climatic loading exceeds the failure threshold of the network.

Critical Infrastructures

Synonym of Civil Engineering Infrastructures, although the emphasis is more on the importance of these systems rather than technical aspects. Critical Infrastructures, often termed Critical National Infrastructures, include all utility networks, telecommunication networks, and transport networks.

Degree

Number of connections or edges featured by a node in a given network. It is denoted by the symbol k. Often mentioned is the average degree of a network, $< k >$, which represents the average number of connections or edges found in nodes.

Deterministic spatial hazard

Any footprint schematized by adopting a deterministic shape such as circles, rectangles, ellipses, squares, and so forth.

Digital twin

Digital representation of an infrastructure, the processes that it enables, and the assets it is composed of. More than a simple digital drawing, it is a complex object with attributes that can be used to represent the infrastructure behavior in a modelling environment.

Directed network

Network in which the edges connecting the nodes are directional.

Distribution network

In the United Kingdom, this represents the segment of the electricity network with a voltage lower than 275kV.

Distribution Network Operator

Private company in charge of operating, managing, and maintaining the assets of the distribution network in a specific region of the United Kingdom.

Edge

Link or connection that is attached to two nodes which act as endpoints.

Exposure

Extent to which an infrastructure is subjected to a given risk.

Failure

Complete loss of one or more nodes composing a network as a result of either external or internal factors. A 1st order failure corresponds to the failures of nodes that are directly impacted by the exceedance of their failure threshold, whilst a 2nd order failure is the result of a domino effect, and it cannot occur without at least one 1st order failure.

Failure model

Modelling tool that explains and governs the 1st and 2nd order failures of the nodes in a network.

Failure threshold

Upper bound of the load to which the nodes in a network are subjected. In a given node, the exceedance of the failure threshold results in a 1st order failure.

Fault

Failure that occurs in electricity networks.

Footprint

Shape of the surface area hit by a given natural hazard. In the case of wildfires, for instance, this corresponds to the burnt area.

Footprint hotspot

Sector of the footprint where the climatic loading reaches its maximum value.

Fractional Brownian motion

Continuous-time Gaussian stochastic process that features a covariance function governed by the Hurst exponent H. In the x, t plane, the fractional Brownian motion generates random paths composed of increments that can be completely uncorrelated, positively correlated, or negatively correlated, depending on the value of the Hurst exponent H. The fractional Brownian motion is a generalized mathematical representation of the Brownian motion.

Fractal dimension

Dimensionless statistical index that provides an indication of the space-filling capacity of an object in a given space. Such index is denoted as D. In a 2D space, the object with the highest space-filling capacity is a bi-dimensional object, for which $D = 2$. The same reasoning applies to lower and higher dimensions.

Fractal spatial hazard

Any footprint schematized according to a fractal recipe such as the fractional Brownian motion.

Fragility curve

Probabilistic model that associates the probability of failure of a given physical element to the value of an external loading used as input.

Future climate

Output of the runs of a Climate Model used as projected conditions, often used in conjunction with the output of the Control climate. The Future climate is driven by parameters that refer to future, hypothesized conditions.

Hub

Node with a high number of connections or edges.

Hurst exponent

Parameter that describes the level of correlation between two successive increments in the fractional Brownian motion. In the case of a Brownian surface, the Hurst exponent drives the degree of spatial autocorrelation found in the spatial distribution of surface elevations.

Interdependent network

Alternative definition for complex or multilayer network.

Line

Alternative name for tier. In the context of this thesis, the lines are the 132kV and 33-66kV networks.

Load and Loading map

The load is the severity of a natural hazard. A Loading Map is the equivalent of a Brownian surface, where the elevations of the latter are interpreted as the severity of a natural hazard.

Localized attack

Spatial failure pattern that affects all the nodes in a network that falls within the boundary of a circle with a given radius. All such nodes constitute 1^{st} order failures.

Main hub

Hub with the highest number of connections or edges in a network.

National Grid Substation

Electricity substation where the voltage is stepped down from 275-400kV to 132kV.

Network model

Equivalent of topology, it represents the spatial and geometrical properties, together with the relationships between nodes, found in a network.

Node

Also known as vertex, it is an abstract object acting as the primary element of a network. Two nodes are connected by an edge, and all nodes connected to a node j are its neighbors and compose the connected component of j.

Primary substation

Electricity substation where the voltage is stepped down from 33-66kV to 11-20kV.

Random attack

Failure pattern where 1st order failures occur randomly in a network.

Resilience

Ability of a network or infrastructure to recover from the disruptions caused by natural hazards.

Risk

Extent of the probable damage that a network or infrastructure is subjected to given the exposure to a natural hazard.

Robustness

Ability of a network or infrastructure to continue operating in the face of the disruptions caused by natural hazards.

Scale-free

In network theory, this corresponds to networks which degree distributions follow a power law. In terms of spatial properties, this corresponds to the presence of repetitive patterns that can be identified regardless of the scale at which a given object is being observed.

Self-contained system

A network or infrastructure that is considered to be operating in absence of interactions with out-of-system elements. Opposite of the system-of-systems perspective.

Shortest path

Path connecting two nodes in a network such that the sum of the weights associated with the edges included in the path is minimized. If the weights are all unitary or absent, the shortest path corresponds to the sequence of the shortest edges between the two nodes.

Small-world

Topological structure in which two nodes, whilst being not connected, are only a few hops away from each other.

Spatial autocorrelation

Extent of the correlation shown by the values associated with two adjacent points on a surface. These may include elevation or other spatial phenomena. If the values are positively correlated, the two points are clustered; if not, they are dispersed.

Spatial hazard

Hazard that, as opposed to occurring in pointwise locations on a surface, is spatially-distributed and features a certain degree of spatial autocorrelation.

Spatial robustness

Capacity of a network or infrastructure to limit the number of 2nd order failures.

System of systems

Systemic definition of an interdependent or multilayer infrastructure, where each layer or system relies on the others to function correctly. In the context of this thesis, the system is the two-tier electricity network, whereas the systems are the 132kV and 33-66kV networks.

Targeted attack

Failure pattern where the 1st order failures intentionally hit hubs or other significant nodes in the network or infrastructure. In the context of this thesis, the failure of edges is not modelled.

Tier

Alternative name for the systems composing the system of systems. In the context of this thesis, the two tiers are the 132kV and the 33-66kV networks.

Topology

In the context of this thesis, this term represents the structure of the network, also indicating the different spatial arrangements in which the nodes and edges are distributed in the network.

Undirected network

Network in which the edges connecting the nodes are bi-directional.

Vulnerability

Alternative definition for exposure.

Wind gust

According to the World Meteorological Organization, the wind gust is the maximum value, measured over an observing cycle, of the 3-second running average wind speed. It is measured in meters per second.

List of acronyms

BA	Barabási-Albert Scale-Free Network
CF	Critical Footprint
CPM1.5	Convection-Permitting Regional Climate Model with 1.5 km grid
DNO	Distribution Network Operator
ER	Erdős–Rényi Random Network
fBm	fractional Brownian motion
FI	Fragmentation Index
Ft	Failure threshold
LN	Lattice Network
NaFIRS	National Fault and Interruption Reporting Scheme
SN	Number of Surviving Nodes
SR	Spatial Robustness
SSm	Spectral Simulation method
UKV	Convection-Permitting Regional Climate Model with 1.5 km grid
WS	Watts-Strogatz Small-World Network

Chapter 1. Introduction

1.1 Overview

There is widespread recognition of the importance that civil engineering infrastructures, often referred to as critical national infrastructures, have in our modern society. The networked systems that compose these infrastructures, such as transportation networks, water supply networks, electricity networks, and many others (Hall et al., 2017), have been recognized as the backbone of modern lifestyle (Pant et al., 2016), providers of essential services (Thacker et al., 2017a), and vital components of modern society (Boin and McConnell, 2007).

As with any highly industrialized Country, the United Kingdom relies heavily on its infrastructures, although this is often better indicated by uptake and usage rather than the scale of investment. In the case of the energy sector, for instance, access to electricity has been available to 100% of the population for decades (Angelou et al., 2013), whereas investments amounted to approximately 0.0034% of the GDP for energy-related projects (National Infrastructure Commission, 2016). Another important aspect is the contribution of infrastructure to the overall economic output, with electricity alone contributing 2.3% of the GDP to the United Kingdom economic output in 2016 (National Statistics, 2017).

The heavy reliance on infrastructure to support quality of life and the economy, coupled with limited investment compounds the effect of disruptions caused by extreme weather events and natural hazards. The severe windstorm that hit England and France in October 1987 battered the local infrastructure with wind gusts exceeding 180 km/h, causing casualties and widespread damage (Browning, 2003). Another example is the exceptionally wet summer of 2007, during which floods affected numerous electricity substations, resulting in £138m of damage and a power outage that affected more than 170,000 households over a period of five days (Chatterton et al., 2010). More recently, Storm Desmond produced sustained rainfall over the North West of England in December 2015, causing power outage for over 60,000 customers. This prevented a significant fraction of the customer base from accessing electricity and curtailed the availability of telecommunication, transportation, and healthcare services.

These events reveal the vulnerability of our basic services to extreme weather events and natural hazards, with the ultimate impact often exceeding their geographical boundaries or footprint. This also highlights the need to understand how infrastructures behave under the external loading resulting from natural hazards, as well as the need to investigate whether the design and operation of infrastructures can be improved to increase infrastructure robustness.

1.2 Spatial complexity of hazard and infrastructure systems

A very important characteristic of water supply, electricity, rail or other infrastructure networks is their spatial domain. This is the geography over which they span, connecting the generation of a resource (water, electricity, data etc.) and the customer base (Dunn et al., 2016a). Depending on the domain size and location, natural hazards of varying type and severity may target the spatial domains where infrastructures operate, loading the system and causing disruptions that can either be direct (e.g., outright failures) or indirect (e.g., due to domino effect). Although multiple factors are at play, the size of the spatial domain of an infrastructure varies with the size and importance of its customer base (Thacker et al., 2018; Flyvbjerg et al. 2008), which likely puts systems at risk of more severe consequences. The risk to infrastructure from natural hazards and climate change has also been recognized by Governments and industry alike (Cabinet Office, 2011; ETI, 2018).

Historically, events driven by natural hazards have often taken their toll on civil engineering infrastructures. In recent years, two of the major events are Hurricane Katrina, which in August 2005 damaged 44 bridges in and around the city of New Orleans costing 1 billion USD to repair (Padgett et al., 2008), and the Christchurch Earthquake in the Canterbury Region of New Zealand, which in February 2011 damaged around 16% of the cables composing the urban electricity network and resulted in 629 million customer minutes lost (Massie and Watson, 2011). These events, although associated with different levels of damage, had one aspect in common: their footprint was characterized by spatial contiguity, affecting regions as vast as 4 US states (e.g., in the order of 600,000 km2) in the case of Hurricane Katrina, or as minute as the Lune Catchment in North West England (e.g., in the order of 1,000 km2) in the case of Storm Desmond. As such, events of this nature may be defined as natural spatial hazards – encompassing, among others, wildfires, floods, earthquakes, ice storms, and high winds – as opposed to natural hazards which footprint is more limited in space – such as lightning, sinkholes, and so forth.

Natural hazards such as precipitation, drought, or windstorms are themselves spatially complex because of the physical processes that drive them. However, assessing the impacts of disruption from a hazard is made more complex because of the distances that infrastructure networks span and the complex flows between locations of demand and locations of supply. For example, the city of Los Angeles receives part of its water supply from the Los Angeles Aqueduct, which originates 375 km away. Large communities will therefore be impacted by disruptions occurring hundreds of kilometers away from their homes.

Moreover, there is significant heterogeneity in the structure of both the natural hazard and infrastructure networks. Across a hazard footprint there are usually substantial variations in intensity of event, whilst the density of civil engineering infrastructures varies considerably, being especially concentrated in urban areas. This is of importance, as infrastructures are at greater risk of common-cause disruption, e.g. disruption resulting from a common triggering event, due to co-location (Thacker et al., 2017a).

1.3 Failure and robustness of complex infrastructure systems

Another key aspect of infrastructures is their connectivity or dependence (Thacker et al., 2017b; Fu et al., 2014), which is the result of a complex evolutionary process (Dunn et al., 2016a) shaped by factors such as changing demand, technologies, and costs (Fu et al., 2016).

In the context of infrastructures exposed to natural spatial hazards, both co-location and interdependence have an important role in the occurrence of cascading failures. This is the propagation of failures within, or between, infrastructure systems (Hall et al., 2015; Fu et al., 2014), as shown by the domino effect that brought down the critical infrastructure caused by Storm Desmond in the city of Carlisle, United Kingdom (Ferranti et al., 2017). The presence of dependencies between different infrastructure types has led to them being increasingly considered as integrated systems-of-systems (Hall et al., 2015; Pearson et al., 2018).

The robustness of the network, often described as the ability to maintain the levels of service despite the disruptions, is therefore not only driven by internal infrastructure components within the control of a particular sector, but also by the vulnerability to impacts in other sectors beyond their control. One such example is the 2003 Italian Blackout: in September 2003, the shutdown of a power plant resulted in the interruption of electrical supply to the telecommunication system, which in turn led to the disruption of the SCADA system controlling the electricity network, which ultimately led to additional electrical faults in the network (Rahnamay-Naeini et al., 2016). This has inspired a number of studies, including those that aim at characterizing the robustness of civil engineering infrastructures to natural hazards by adopting a systemic perspective (Thacker et al., 2017b).

1.4 Research gaps and research questions

Infrastructures that are robust to natural spatial hazards will provide a more reliable provision of services. However, few studies cover the relationship between the spatial structure of natural hazards and the spatial structure of infrastructure networks (Rachunok and Nateghi, 2019; Hickford et al., 2018). In addition, the methods currently available in the literature largely ignore the fact that infrastructure networks are holistic systems and that different system layouts produce different responses in terms of robustness (Kröger, 2019; Marzo et al., 2019). To address these research gaps, this thesis introduces four contributions:

1) It adopts a systems framework to analyse the impacts of spatial hazards on infrastructure networks;
2) It develops a synthetic case study where the combination of a wide range of configurations of spatial hazards and spatial infrastructure networks is assessed;
3) It uses an array of different robustness metrics to characterize the response of infrastructure networks;
4) It applies a systems approach to a realistic case study.

These contributions differ from the methods available in the literature in that they describe the infrastructure networks first from a high-level perspective, and then from a more detailed systems perspective. In the synthetic case study, the research question is centered around describing the robustness of infrastructure networks holistically, pinpointing the differences in robustness between systems with different spatial layouts. Then, in the real case study, the emphasis is on systems thinking, with the purpose of understanding how the different subsystems composing a real-world infrastructure interact with each other under the influence of spatial hazards.

Adequate representation of the spatial properties of hazards is crucial to reduce the likelihood of spatial biases affecting the assessment of infrastructure robustness. Existing approaches fall into two approaches. The first approach simplifies the behavior of the system, and usually does not account for spatial variability or uses simple shapes (e.g. a circle) to represent a hazard footprint. The second approach uses physically-based models, such as an inundation model, to simulate the hazard.

In the synthetic case study, this thesis first develops and demonstrates a fractal spatial hazard generator to create patterns which represent the spatial variability of different hazards by tuning model parameters, thereby allowing to generate a breadth of different spatial

structures. The robustness of different infrastructure network structures to different spatial hazards is subsequently determined. The framework is then applied to a real case study using a high-resolution wind gust model to evaluate the response of an electricity infrastructure network to windstorms under current and future climates.

1.5 Scope of work, aims and objectives

The scope of work of this thesis is to study the behavior of infrastructures exposed to spatial hazards by adopting a systems approach. This thesis intends to accomplish this by investigating both synthetic and realistic infrastructures, infrastructures considered as standalone systems and infrastructures considered as systems-of-systems, and synthetic and realistic spatial hazards. This thesis also demonstrates the importance of adopting spatial hazards that cannot be described by a deterministic model.

The delimitations of this study include the analysis of selected, planar network models that are commonly used in the literature (see paragraphs 4.4 and 5.3), a specific stochastic model to reproduce spatial hazards (see paragraph 4.2), and a specific output of a climate model used as realistic spatial hazard (see paragraph 5.2). This thesis focuses on quantifying the robustness of infrastructures in terms of failures happening in the immediate aftermath of the manifestation of spatial hazards, and it is not concerned with modelling their temporal evolution. In the paragraphs mentioned above, reasons are provided as to why other network models, metrics, and climate outputs are not used.

More in detail, this aim of this work is to characterize the robustness of different infrastructure network structures to natural hazards of different spatial structure, and to quantify the robustness of these structures using adequate metrics. The ultimate goal is to provide researchers, asset managers, designers, and infrastructure investors with strategies to identify the vulnerability of their infrastructures to spatial hazards.

To achieve the aims discussed before, the following objectives will be accomplished:

1. Reviewing the existing methods for modelling spatial hazards and proposing a new approach;
2. Comparing the spatial properties of non-deterministic and real-world spatial natural hazards;

3. Analyzing the interaction between different types of spatial hazards and different types of synthetic infrastructures;
4. Assessing infrastructure resilience by applying a range of topology-based metrics on various synthetic infrastructure models;
5. Assessing the interaction between a real-world natural hazard and a real-world infrastructure;
6. Highlighting the most critical segments of the infrastructure based on their exposure to the hazard and their potential to trigger cascading failures;
7. Distilling key recommendations for engineers, policy makers and other stakeholders to inform the design and operation of infrastructure systems.

1.6 Structure of this thesis

This thesis is organized into several chapters addressing two case studies. The first one is an investigation of the robustness of synthetic infrastructure network models exposed to natural spatial hazards represented by fractal surfaces, whereas the second one analyzes the robustness of a real-world infrastructure subjected to a real-world natural hazard. Following this introduction, Chapter 2 presents a detailed and exhaustive examination of the body of literature addressing the many interdisciplinary topics revolving around civil engineering infrastructures, robustness, and natural hazards. Chapter 3 offers a high-level description of the common modelling framework that is applied to two case studies. Chapter 4 and Chapter 5 describe how the framework is applied to the synthetic case study and real case study respectively. Chapter 6 and Chapter 7 report results and discuss the implications of the results for the synthetic and real case study, respectively. Finally, Chapter 8 highlights the major findings of the work and draws together insights from both case studies to provide recommendations to policy makers and set out priorities for future research on this topic.

Chapter 2. Literature review

2.1 Introduction

2.1.1 The complex nature of civil engineering infrastructures

Civil engineering infrastructures are one of the pillars of modern societies. Highways, railway networks, water supply systems, electricity networks, gas networks and telecommunication systems are only a few of the many systems that support progress and civilization. Over the last decades, infrastructures have evolved from being the response to primary needs such as drinking water, reliable energy and transportation, to entities with multiple levels of complexity. As recognized by Dunović et al. (2014), it is possible to identify four different layers of complexity: *i*) organizational and economical complexity (Baccarini, 1996); *ii*) structural complexity (Williams, 2002); *iii*) technical, directional, and temporal complexity (Remington and Pollack, 2007); *iv*) factual and interactional complexity (Geraldi, 2008). However, additional factors alter this landscape, rendering infrastructures not only difficult to design, but also extremely complicated to manage. According to Setola et al. (2016), the increasing population, the widespread use of information technology, the migration waves towards cities that increase urbanization, and the decreased governmental control due to infrastructure privatization are the major factors affecting the benefits provided by civil engineering infrastructures. In addition, climate change (Schweikert et al., 2014) and terrorism (Apostolakis and Lemon, 2005) are certainly capable of playing a crucial role. It is notable that the structural and design aspect is only a marginal contributor to the overall complexity, stressing the idea that infrastructures continue to exist after the decommissioning of their construction sites. A non-exhaustive list of dimensions relevant to managing infrastructure systems from a holistic perspective includes:

- *Risk and resilience;*
- *Procurement and infrastructure performance;*
- *Asset management;*
- *Safety and sustainability;*
- *Technology;*
- *Policy and regulation.*

The area of *risk and resilience* is concerned with determining the level of risk to which infrastructures are subjected, and their level of resilience or capacity to regain functionality once damaged. Studies around this subject, usually termed *impact studies*, include exposure to the risk of natural hazards (Wilkinson et al., 2012; Pregnolato et al., 2016), risk of man-made attacks (Little, 2003; Chopra et al., 2016) or financial risks (Grimsey and Lewis, 2002). The most recurrent objective of this area is to provide infrastructure operators with indications regarding the weakest components of their networks, in such a way that a tailored *strategic investment* or *adaptation plan* can be put in place (Walsh et al., 2013; Sayers et al., 2015).

The dimension of *procurement and infrastructure performance* focuses on the processes regulating how infrastructures are provided and how well they meet user demand and expectations. The aspects of investigation for procurement include the economic capacity of infrastructure agencies to participate in investment programs (Kajewski, 2016) and the reliability of contracting programs that involve Public-Private Partnerships (Regan et al., 2015). Performance aspects concern, amongst others, the behavior of infrastructures under extreme loading, such as severe earthquakes (Palermo et al., 2017), and the hindrance due to the scarcity of resources such as water (Fontanazza et al., 2007) or crude oil (Gross et al., 2012), and how this affects revenue projections, availability of goods, and service failings.

Asset management, at the interface between research and industry, is an area driven by the recent emergence of Building Information Modelling (BIM), a framework for the generation and analysis of digital representations (*digital twins*) of the physical components of infrastructures. Applications of BIM can be found in the energy sector for detecting faults in buildings (Dong et al., 2014) and in the monitoring and maintenance of subways (Marzouk and Aty, 2012). These studies highlight the importance of the BIM framework for checking the status of infrastructure assets and for driving investment strategies.

The *safety and sustainability* dimension addresses the safety aspects surrounding the construction and operation of infrastructures, as well as their sustainability and environmental impact. Relevant studies focus, for instance, on monitoring aging bridges and other structures (Frangopol and Tsompanakis, 2014), and on the environmental performance of infrastructures operating at the urban level (Zavrl and Zeren, 2010).

The *technology* dimension focuses on how solutions coming from research and development can improve the efficiency of construction and services. Among recent developments, the *Internet of Things* framework (IoT) was used to improve the performance of urban infrastructures by monitoring the services provided with an integrated network of sensors (Sánchez et al., 2013). This leads to the concept of *Smart Cities*, an urban environment where

infrastructures are smart as they adapt intelligently to changes in demand, the surrounding environment, and the interaction with other infrastructures to improve their performance (Royal Academy of Engineering, 2012).

Finally, the area of *policy and regulations* is concerned with delineating a set of administrative solutions that enhance the role of infrastructures. Studies in this field focus on the governance of infrastructures with respect to themes such as market liberalization (Bošković and Bugarinović, 2015), the management of excess infrastructures (Albalate et al., 2015), and development and sustainability plans (Willets et al., 2010). By evaluating the robustness of civil engineering infrastructures to spatial hazards (Figure 2.1) and their systemic behavior and performance, this thesis aims at providing innovative contributions mainly to the dimension of risk and resilience.

Figure 2.1. Electricity substation being flooded in Gloucestershire, United Kingdom, on 23 July 2007. Floods are one of the most common natural spatial hazards to which infrastructures are subjected. REUTERS/Stephen Hird.

2.1.2 Risk, resilience, and robustness of infrastructures

2.1.2.1 Definition of risk, resilience, and robustness

The concept of *risk* has long been associated with civil engineering. As highlighted by Flint (1981), it falls into two categories: the one that applies to the physical elements, and the one that concerns the overall system. From the physical point of view, *risk* is associated with the idea of being exposed to collapse due to lack of structural integrity, such as the failure of a beam or viaduct pillar (e.g., the Hintze Ribeiro disaster in Portugal in 2001). From the perspective of a system, *risk* is associated with the inability to provide the intended service due to failures that reduce the systemic performance, as in the case of widespread blackouts (e.g., the Northeast blackout in United States and Canada in 2003) or transport disruptions due to floods (e.g., Storm Desmond in the United Kingdom in 2015). Given the variety of environments in which infrastructures operate and their complexity, it is realistic to assume that infrastructures are exposed to both physical and systemic risk. These may involve risks from: *i*) *cyber-attacks*, which may result in power outages (e.g., the 2015 incident in Western Ukraine that left 230,000 people without power for 6 hours); *ii*) *intentional* or *malicious attacks*, which may cause partial or total disruption due to damages occurring in targeted, high-profile locations (e.g., the London Underground); *iii*) *random attacks*, which involve damages occurring in a casual location; and *iv*) *spatial attacks*, resulting in the simultaneous failure of multiple infrastructure assets that are geographically proximal to each other due to *common cause failure* (Setola and Theocharidou, 2016), which is the typical failure mode featured by natural hazards.

Faber and Stewart (2003) define risk (*R*) as a function of the probability (*P*) of an event and its consequence (*C*). The model output aligns with the concept of expected losses adopted by the insurance industry (equation 2.1):

$$R = P * C \qquad (2.1)$$

The identification of risks is carried out by means of a risk analysis, during which the potential sources of risk, termed *hazards*, are identified (Faber and Stewart, 2003). The probability associated with risk is determined by identifying a *limit state function* that shapes the probability domain. Dawson and Hall (2006) state that a system composed of *n* variables $x := (x_1, \dots, x_n)$ which belong to $\chi \subseteq \mathbb{R}^n$ can be used to represent an object, in this case an infrastructure and its components. Defined the limit state function $g(x)$ as the separation between the region of failure $F = \{x: g(x) \leq 0\}$ and the region of uneventfulness $U = \{x: g(x) > 0\}$, with $F \cup U = \chi$, the *probability of failure* p_P is given by equation 2.2:

$$p_P = p(g(x) \leq 0) = \int_{\chi} I(g(x) \leq 0)\, \rho(x)\, dx \qquad (2.2)$$

where I represents the indicator function and $\rho(x)$ is the joint probability density function referring to the system variables. The *consequence* of an event is a function of the type of event and the accuracy and complexity of the loss model used to describe the impact. One of the most notable high-complexity models is the Florida Public Hurricane Loss Model (FPHLM), which was developed by Pinelli et al. (2009) to characterize the damage to properties exposed to the risk of Hurricanes. The FPHLM couples a wind model with a storm surge component and an actuarial module to estimate the cost associated with insured lost property. Less complex loss models include those with non-monetary purposes, such as the fragility curves that characterize the robustness of electricity networks by estimating the number of faults (Dunn et al., 2018).

The concept of *resilience* finds application in many different fields and has multiple definitions. In the context of civil engineering, resilience is generally defined as the ability of an infrastructure to recover rapidly from disruptions (Blockley and Godfrey, 2017). Additional definitions describe it as the capacity of learning to bounce back (Wildavsky, 1991), or as the ability to withstand loadings of environmental nature (Horne and Orr, 1998). The latter demonstrates that the idea of resilience for civil engineering infrastructures is tightly coupled with that of an external agent threatening the system. Although infrastructures are also exposed to malicious attacks (Apostolakis and Lemon, 2005), the external agents considered in this thesis are natural hazards only, in line with Wilkinson et al. (2012) and Pregnolato et al. (2016). As pointed out by Bruneau et al. (2003), the idea of resilience is best explained with reference to a system that is hit by an external agent, has its performance diminished by the ensuing disruption, and then recovers (Figure 2.2). Often the concept of resilience is associated with that of the *speed of recovery*, and as such the latter becomes a metric used to indirectly quantify resilience. This approach has been implemented by studies addressing the resilience of water supply networks (Herrera, 2016; Zhao et al., 2017) and railway networks (Bhatia et al., 2015). Modelling recovery requires sound and realistic tools that can deliver reliable results, and it also entails acquiring infrastructure-specific data that can be used to describe the infrastructure behavior. Without these, there is a risk that the recovery is not modelled properly.

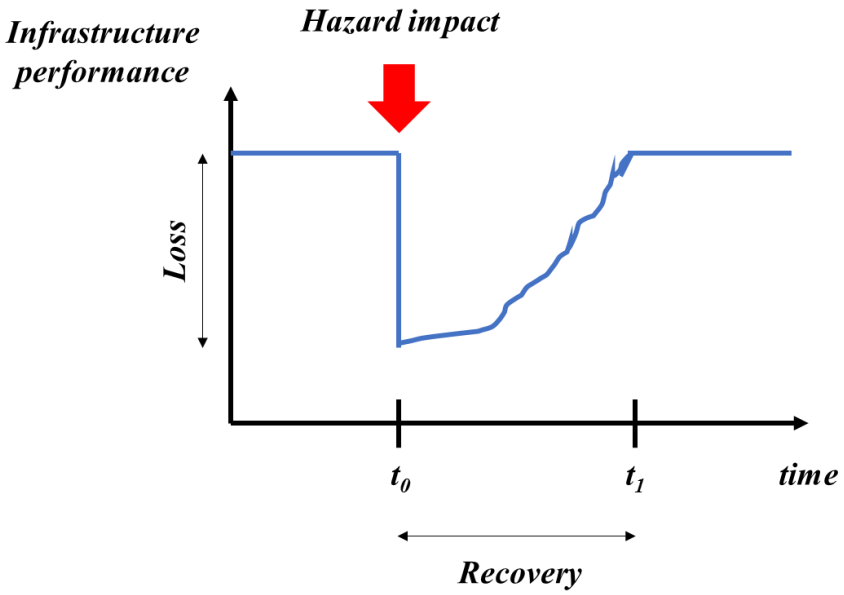

Figure 2.2. Conceptual scheme of the resilience of a system adapted from Bruneau et al. (2003) (e.g., the *impact-recovery cycle*). The speed of recovery is often used as a measure of resilience: the lower $t_1 - t_0$, the more resilient the system. The area under the curve was defined by Bruneau as a measure of Resilience.

Another important concept is that of *robustness*. Blockley and Godfrey (2017) define a robust system as a system that is not vulnerable to loadings or attacks such as natural hazards or man-made sabotage. Moreover, robust systems limit disruptions that are disproportionate with respect to the root cause by absorbing or withstanding them (WEF, 2013). Notable robustness studies have addressed the vulnerability of the United States electricity network (Wang and Rong, 2011), that of urban water infrastructures (Mikovits et al., 2017), and also the available strategies to improve robustness (Khoury et al., 2014). The concepts of resilience and robustness are often used interchangeably, and their definitions seem to have fuzzy boundaries. However, authors such as Bruneau et al. (2003), the World Economic Forum (2013), and Blockley and Godfrey (2017) concur in identifying robustness as being a necessary, although not sufficient, condition for resilience.

2.1.2.2 Infrastructures as complex systems

The need of integrating systemic points of view in civil engineering arises from the inherent complexity of engineering undertakings, which is often a function of the scale of a project. Such complexity is even more noticeable in infrastructure design and construction, where it is important that the different parts composing the infrastructure operate in a coordinated manner. Not only does systemic mean "*building or creating a whole from parts*" (Langford, 2013), but it also represents a necessary approach because infrastructures are systems "*consisting of interacting components arranged in a hierarchical and decomposable structure*" (Brady and Davies, 2014). In addition, the range of services delivered by infrastructures may be spread across the different components, as is the case with the generation, transmission, and distribution segments of the electricity network. For these reasons, the shift from "project" to "system" (Whyte, 2016) is an invaluable opportunity to reframe many of the problems that affect infrastructures and the analytical methods used to address them.

This shift entails looking at the system in terms of an ensemble of parts that are required to function organically by means of *interdependencies*, much as it happens for interdependent networks (Fu et al., 2014; Havlin et al., 2015; Radicchi, 2015). Interdependency seems to be an inherent property of civil engineering infrastructures – regardless of whether it was created on purpose or was simply the result of convenient choices – and has in fact been the subject of numerous studies (Peerenboom, 2001; Leavitt and Kiefer, 2006; Wang, 2011). Not only is its presence a catalyst for the transition from traditional engineering to a systemic approach, but it is an implicit definition of the latter, where the individual components of an infrastructure are designed to not just deliver, but to operate in co-ordination with other components as well. One example of such functional paradigm can be found in water supply systems, where the co-ordination between the intake, transportation, and delivery components plays a crucial role in ensuring that the service is reliable and meets high quality standards.

2.1.3 Systemic approaches to understanding risk, robustness, and resilience

2.1.3.1 Systems of systems and hierarchies

The response of civil engineering infrastructures to hazards has been extensively investigated in literature by adopting a system-of-systems perspective. This allows to model the impact of disruptions taking into account the multiple interactions that infrastructures typically feature (Peerenboom et al., 2001; Rinaldi et al., 2001), as opposed to analyzing the impact on each system in isolation and then aggregating the outcome. Further to this, as pointed out by Eusgeld et al. (2011) and Mostafavi (2017), infrastructures are an ensemble of physical elements that are interconnected and related to each other, which functions could not be performed in absence of any of them. As such, infrastructures may be seen as systems in which *the whole is greater than the sum of the parts*. This approach requires doing away with considering infrastructure elements as if they were standalone, disconnected entities, and as such it represents the opposite of performing *in-silo* analysis. Further to this, the extreme vulnerability that civil engineering infrastructures have repeatedly shown when hit by extreme weather or natural disasters indicate that another set of interactions should be taken into consideration, e.g. the interactions with the *geographical domain* embedding them. Consequently, it may be possible to call *systemic* any approach to evaluating risk, resilience, and robustness that models the presence of interactions within the same infrastructure, or between infrastructures, and between infrastructures and the geographical domain where they operate.

The first studies investigating infrastructure interactions were aimed at identifying the relationships between different systems, in an attempt to depict the intricacy that the built environment has come to represent over time. The renowned studies by Peerenboom et al. (2001) and Rinaldi et al. (2001) highlighted the presence of multiple relationships between infrastructure systems (Figure 2.3), and defined *dependencies* as a one-directional connection between two infrastructures and *inter-dependencies* as a two-directional connection, where the status of one infrastructure influences that of another and is in turn affected by it.

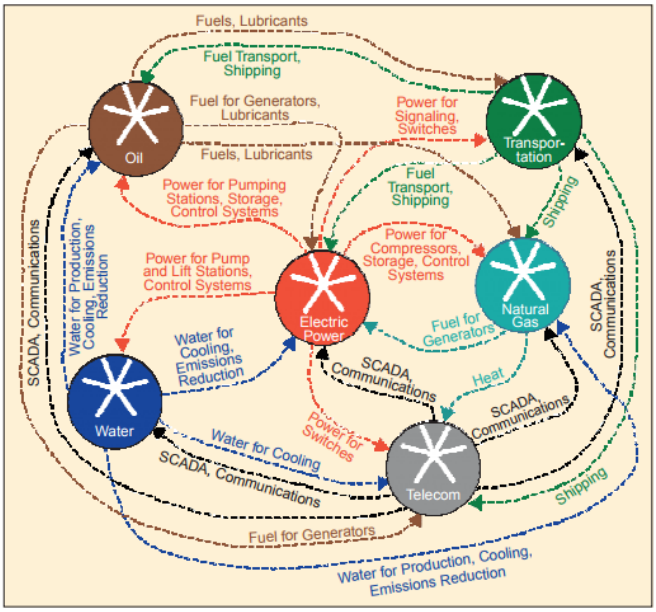

Figure 2.3. Visualization of the inter-dependencies between infrastructure systems that provide six of the most important services. Adapted from Rinaldi et al. (2001).

The concept of *intra-dependencies* has been proposed by Buxton and Pringle (2014) as a two-way connection that occurs within the same infrastructure system. The process of identifying the intra-dependencies occurring in a system relies heavily on the unequivocal identification of the set of components or elements that compose the infrastructure itself. One example of a set is the lines with different voltage that compose the electricity transmission and distribution network (Figure 2.4). As a result of this functional partition, the overall behavior of the infrastructure is dictated by the *emergent behavior*, which puts infrastructures perfectly in line with the concept of complex systems (Amin, 2000).

The existing body of literature addressing this subject is rather extensive, although the number of studies directly investigating how the different infrastructure elements interact with each other in a failure scenario appears to be limited. Pitilakis et al. (2016) adopted the concept of intra-dependencies to study the effect of earthquakes, soil liquefaction, and ground deformations on the transportation network of the city of Thessaloniki, in Greece. The study revealed that the loss of connectivity of the transportation network is significantly increased when the interaction with collapsed buildings is considered. Panzieri and Setola (2008) modelled the mutual dependency of infrastructures to explore the effects of man-made attacks, and adopted a linearized Markov chain to estimate the overall level of inoperability faced by a complex energy-transportation-urban system. Soltan et al. (2017) adopted a system-of-systems approach to study how cascading failures propagate in an electricity network subjected to individual failures.

As highlighted by Brady and Davies (2014), analyzing an infrastructure by means of the systemic approach implies acknowledging the existence of hierarchies. The range of infrastructures that feature well-defined hierarchical models is vast (Svendsen and Wolthusen, 2007; Bagler, 2008; Robson, 2016), and encompasses, among others, electricity networks, water supply systems, gas networks, and transport networks (Yerra and Levinson, 2005). In impact studies where private stakeholders provide confidential asset information and geocoded files, hierarchies are easily recognized and modelled, reducing the hierarchical uncertainty to a bare minimum. However, there are instances where detailed information and datasets are not available, and as such the identification of hierarchies may rely on pattern recognition or clustering techniques applied to networks (Sanchez-Silva and Gómez, 2013).

The point of view of Brady and Davies about implementing a systemic analysis by acknowledging the existence of hierarchies is confirmed by topological considerations. In fact, it can be argued that it is the presence of functional hierarchies, or *dependencies*, that gives an infrastructure the status of a system of systems. The case of electricity networks is rather exemplificative (Figure 2.4), although the same applies to road networks (Lämmer et al., 2006) and water supply networks (Diao et al., 2014), for instance. In these examples, there is a neat separation between the different co-operating systems, the discriminating factor being either their *capacity* (voltage for electricity networks, flow rate for water supply networks) or their pre-assigned *importance* (classification for road networks).

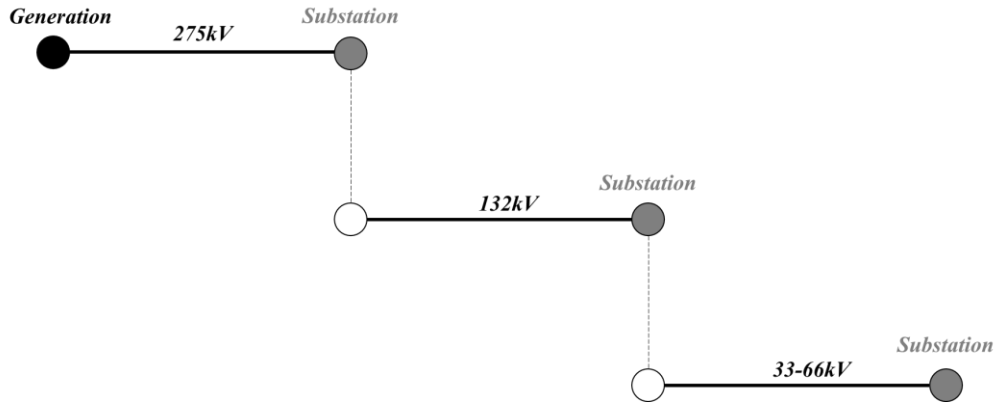

Figure 2.4. Schematized version of the typical hierarchy of electricity networks. The voltage is progressively stepped down to meet user demand. Segments at higher voltage can be seen as more important as they feed one or more segments with lower voltage.

2.1.3.2 Two possible systemic approaches

The idea that infrastructures often follow a hierarchical structure is reinforced by Robson (2016), Bogler (2009), and Yerra and Levinson (2005), who highlighted the fact that several *levels* may exist within the same system, which are often identifiable based on *capacity* (e.g., traffic flow or rank for transportation, flow for water supply systems, voltage for power networks, and so forth). These levels correspond to the different stratifications which can be identified as part of the same self-contained system. This is the case, for example, of the electricity network, a system composed of transmission and distribution lines operating at different voltages and on different spatial domains. Based on this reasoning, two different approaches may be identified:

1. A macro-systemic approach, with or without partitions;
2. A micro-systemic approach.

The first approach involves analyzing an infrastructure at the macro-system level by performing a macro-scale analysis. This considers the system as a whole, and it may be performed with or without partitions. In the context of this thesis, partitions can be considered as self-contained sub-systems composing the larger infrastructure. When partitions are not modelled, and the infrastructure is considered as a whole, indications regarding the behavior of a system from a holistic perspective may be obtained, whereas the presence of partitions may be driven by the need to understand, at a finer scale, how the response to disturbances of a specific infrastructure component such as a specific voltage line influences the behavior of intra-dependent lines. The presence of partitions may entail looking at inter-dependencies and/or intra-dependencies. Overall, a macro-system level study allows to analyze risk, robustness, and resilience in terms of the overall impact of system-wide disruptions, leaving the analysis of localized behavior and impacts to smaller-scale studies. Although the macro-system level appears to be the scale of choice for investment strategies, governance, regulation (Roelich et al., 2015), and digital transformation (ICE, 2017), robustness studies performed at this level have targeted the London Underground system (D'Lima and Medda, 2015; Chopra et al., 2016), the airline traffic network (Wilkinson et al., 2012), and the electricity network (Panteli et al., 2017). Many of the lessons learned from these studies point toward implementing adaptation strategies and changes that span the entire length of existing systems. This is non-trivial and requires accurate retrofitting, as shown by O'Donnell et al. (2014) for concrete tunnels and Pregnolato et al. (2016) for the road network and the built environment.

The second approach is, by contrast, a highly refined, computationally expensive, and as such difficult to implement procedure, where detailed information such as structural and behavioral characteristics are needed to model the response of each element composing the infrastructure system (Proske et al., 2018). For instance, to evaluate the response of the power network to high winds using a microsystemic approach would involve analyzing the behavior of every single pylon, which would in turn require models that are flexible enough to accommodate for variables such as materials, age, dimensions, altitude, presence of natural or physical shields and height, all of which may vary greatly even in a small region.

2.1.3.3 Modelling the relationships between infrastructures

Within the context of civil engineering infrastructures exposed to natural hazards, the concepts of risk, resilience, robustness, together with the systemic approaches used to understanding them, highlight the important role of the relationship between systems operating in the same geographical domain. As it emerges from the previous paragraphs, modelling these relationships is, essentially, what distinguishes a systemic approach from an in-silo approach. Setola and Theocharidou (2016) offer a thorough overview of how the relationships between infrastructures may be analyzed, understood, and modelled. According to the authors, *dependency* is a unidirectional relationship where variations in the state of one infrastructure affect the state of other, dependent infrastructures. Examples of this may include outages in the power network that affect the ability of a water supply system to increase the pressure in water mains or of a wastewater plant to operate (Dawson et al., 2018). Contrarily, *interdependency* is a bidirectional relationship where disturbances in the first infrastructure not only affect the dependent infrastructures, but ultimately backfire, as the first infrastructure is itself dependent on the affected ones. The latter appears to be a rather complex situation, where the intricate texture of dependencies exposes the multi-infrastructure system to *cascading failures* (Buldyrev et al., 2010; Lu et al, 2018) (see paragraph 2.2.4.3). Setola and Theocharidou (2016) and Dawson (2015) categorize interdependencies as being of physical, cyber, geographical, logical, and social nature. Although all of them play a key role in ensuring a healthy infrastructure system, within the context of this thesis the *geographical interdependency* is of primary importance, as it is the mechanisms that enables *common mode failures* to occur.

Setola and Theocharidou also categorize the different modelling approaches to dependency and interdependency (Figure 2.5). These include: *i*) *holistic approaches*, which deploy simplified models aimed at providing qualitative information, and which tend to model

infrastructures as single entities by adopting a certain degree of abstraction and large-scale, coarse information; *ii*) *network-based* or *topology-based* or *structure-based approaches*, where graphs from network theory are adopted to model the infrastructure as an ensemble of identical entities in which relationships are represented by connections, and where the emphasis on topological or functional aspects allow to capture the structural properties and to work with discrete working states (e.g., active or failed); and *iii*) *simulation-based approaches*, where more complex models are used in an attempt to unravel dependency or interdependency as they emerge from the collective behavior of the parts composing the infrastructure. Figure 2.5 shows where the three different approaches are positioned with respect to each other and the three key aspects of application domain, implementation effort, and access to information. Based on the problem at hand, the requirements, and the constraints posed on the three key aspects, the choice of the preferred approach is driven by the need to make an optimized decision. If a network-based approach is selected, then a decision should be made regarding the adoption of a structural or purely topological model, or a functional, topological- and flow-based model.

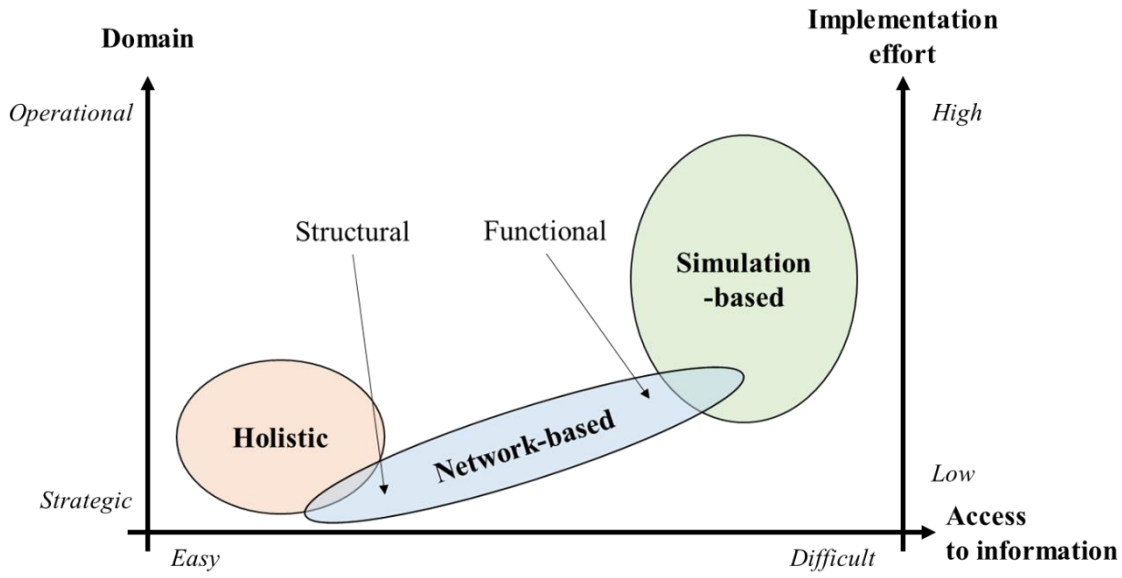

Figure 2.5. Qualitative chart showing the positions of the modelling approaches with respect to each other and the three key aspects of application domain, implementation effort, and access to information. Adapted from Setola and Theocharidou (2016).

2.1.4 Formulation of the research problem

The research problem addressed by this thesis is tightly coupled with the concepts of risk, resilience, robustness, and systemicity presented in the previous paragraphs. In generic terms, *this thesis aims at adopting systemic approaches to evaluate the robustness of civil engineering infrastructures, as well as the risks, to the spatial attacks induced by natural hazards*. This research problem comes with a degree of complexity that requires a multi-stage approach in order to derive the necessary information, or building blocks, on top of which the workflow of this thesis is built. Whilst detailed information on these building blocks or stages is provided in paragraph 2.2, some important, generic aspects have to be taken into consideration before zooming in on the technicalities of the problem itself.

As discussed in paragraph 2.1.3.3, given the level of complexity that civil engineering infrastructures feature (Dunović et al., 2014), the need to adopt systemic approaches is justified by the necessity to take into consideration the mutual relationships between infrastructure components and their contribution to the overall response to disturbances. This thesis is concerned with adopting a macro-scale analysis performed at different hierarchical levels and on different infrastructure systems, the aim being to compare the outcomes and then draw meaningful conclusions based on them. Another crucial element is the timing of the robustness evaluation. With respect to the impact-recovery cycle proposed by Bruneau et al. (2003), this thesis focuses on the immediate aftermath of the hazard impact (Figure 2.2), so as to gauge the *immediate response* of infrastructures. This is done in order to avoid the numerous uncertainties affecting the recovery phase. In line with Dunn et al. (2018), the losses caused by natural hazards are not interpreted in monetary terms, but rather in topological terms.

The final, important aspect to consider is that the problem of evaluating the robustness of infrastructures to natural spatial hazards is addressed from two different perspectives: the first involves analyzing the response of abstract infrastructure models exposed to abstract hazards, whilst the second revolves around analyzing real-world assets exposed to real-world natural hazards. This two-sided approach is implemented in order to gain insights on how future infrastructures may be designed given the presence of natural hazards (first perspective), and on how existing infrastructures may be reconfigured to better cope with them (second perspective). Insights of this nature may be of relevance to infrastructure practitioners and the wider field of asset management, as the latter are the intended audience of this research problem.

2.1.5 Original contributions of this thesis

In the context defined by the previous paragraphs, this thesis aims at providing the following novel contributions:

- Generate an array of realistic, synthetic spatial hazards by using a computationally inexpensive methodology which enables ease of reproducibility and reduced runtimes;
- Compare the impact on a range of infrastructure topological models of the realistic, synthetic spatial hazards to that of the most common model used in the literature;
- Develop a range of topology-based metrics and compare the performances of the topological models to highlight differences and similarities and gain insights on the most robust topology against all hazards;
- Evaluate the impact of a very high-resolution climatic hazard, obtained from a state-of-the-art Regional Climate Model, on a real-world, multi-level infrastructure;
- Highlight the sections of the infrastructure that are mostly affected by failures that could benefit the most from a strategic investment plan.

2.2 Six stages to understanding the risk, resilience, and robustness of infrastructures

The task of evaluating the response of an infrastructure system exposed to an external threatening agent such as natural hazards is rather complex and requires multiple levels of information. An extensive literature review allowed to identify six stages that constitute one approach to understanding the risk, resilience, and robustness of infrastructures (see paragraph 2.2.7). These stages are listed in the following sections and represent the end-to-end working pipeline used throughout this thesis.

2.2.1 Stage 1: spatial hazards

2.2.1.1 Background: characteristics of spatial hazards

Natural hazards are the paramount personification of spatial hazards, being capable of affecting areas as large as geographic regions (Gill and Malamud, 2014). Their spatial structure is one of the most visible effects, e.g. the extent and shape of a flooded area (Figure 2.1) or those of a burnt area. Upon evaluating the impact on infrastructures, estimating the extent of the area affected by a natural hazard adds valuable information on the overall description of the event. This area is often referred to as *footprint* (Guha-Sapir et al., 2011). The spatial component of wildfires, windstorms, floods, ice storms and other hazards is driven by multiple factors, among which are: *i*) the magnitude of the event; *ii*) the topography and the physical constraints it poses; *iii*) the built environment; *iv*) the latitude and longitude of the location; *v*) possible boundary conditions. Providing a characteristic footprint size for each natural hazard is non-trivial, given the variation in the driving factors; however, size ranges are available in literature (Gill and Malamud, 2014).

Despite the fact that different natural hazards occur at different spatial scales (Gill and Malamud, 2014) and with different degrees of severity, their behavior with respect to infrastructures seems to be, in general, the same. Regardless of the physical process that governs them, natural hazards act as an external agent attacking physical elements with the aggravating factor of being *spatially-distributed*, featuring spatial contiguity across their domain. As such, their impact may be spread over large areas, resulting in significant disruption. The Fort McMurray wildfire in Canada, Storm Desmond in North West England, Hurricane Harvey in Texas, and the 2014 Tehran Dust Storm stand out among the most recent events. When infrastructures are modelled as networks (Peerenboom et al., 2001; Rinaldi et al., 2001) and the

disruption is interpreted as an attack to their nodes, culminating in events such as the failure of flooded electricity substations, natural hazards assume the significance of *spatially-distributed attacks*. The spatial structure of natural hazards can be described by using hazard maps or hazard fields, which not only depict the spatial extent of the hazard but also how the severity or magnitude is distributed across the domain.

The pattern followed by spatial hazards is significantly different from the well-known attack models used in *network theory* to investigate the *robustness* of networks. These models include *random attacks* (Albert et al., 2000; Albert and Barabási, 2002) and *targeted attacks* (Tanizawa et al., 2005; Estrada, 2006). In these, either a node or group of nodes is removed from the network and the overall impact on the system is eventually determined based on the underlying network topology. Therefore, these models may be categorized as *node-driven* since the propagation of failures depends on the location of the node and its importance. Examples of *targeted attacks* include those events defined as *man-made* or *malicious*, which are intended to create disruption in one crucial location, such as the sabotage of electricity substations, generation plants, or water pumping stations. Examples of *random attacks* may involve events targeting less important nodes.

On the other hand, *localized attacks* (Berezin et al., 2015; Shao et al., 2015) were introduced to model the occurrence of spatially-distributed events as circles, including natural hazards. Being spatially-distributed attacks, the localized attacks do not focus on single nodes; rather, they target groups of nodes, and their effect is influenced by the size and intensity of the event. These attacks also take into consideration the spatial extent of the area in which the networks are embedded. Accordingly, spatially-distributed attacks may be categorized as *spatially-driven*, as their impact on the network is influenced by their spatial variability across the entire domain.

2.2.1.2 Interactions between infrastructures and spatial hazards

Infrastructures operate on spatial domains of different size. For instance, sewer systems, fiber networks, and road networks operate at the level of urban environments (micro and local extent); water supply networks and gas networks operate at the district and regional level (local and regional extent); highway networks operate at the regional or interregional level (regional and global extent). Railway networks, electricity networks, and telecommunication networks operate at all scales. These examples highlight that civil engineering infrastructures virtually occupy all spatial scales, and as such they are exposed to a wide range of natural spatial hazards. On the one hand, infrastructures thrive due to the positives of their domain, such as size, location, and customer base; on the other, they suffer from the negatives, such as exposure to hazards. As pointed out by Gill and Malamud (2014), it is possible to categorize natural hazards based on their spatial scale. Table 2.1 shows the infrastructures that are mostly impacted.

Table 2.1. Spatial scale of a selection of natural hazards and impacted infrastructures as per Gill and Malamud (2014). The extent of the exposed infrastructure may exceed the scale of the hazard.

Natural spatial hazard	Spatial scale (km^2)	Spatial extent	Examples of exposed infrastructures	References
Landslides and sinkholes	$[10^{-2}, 10^{2}]$	Micro, Local	Roads, railways, gas network, water supply network, telecommunication network	Terranova et al. (2016); Gibson et al. (2005)
Local floods	$[10^{0}, 10^{2}]$	Local	Roads, railways	Pregnolato et al. (2017)
Wildfires	$[10^{-2}, 10^{4}]$	Micro, Local, Regional	Roads, railways, telecommunication network, electricity network	Ward (2013); Cova et al. (2011)
High winds, hurricanes, tornadoes	$[10^{3}, 10^{5}]$	Regional	Railways, electricity network, telecommunication network	Panteli et al. (2017); Dunn et al. (2018)
Major floods and extreme precipitations	$[10^{4}, 10^{5}]$	Regional	Roads, railways, electricity network	Hong et al. (2015); Eleutério et al. (2013)
Earthquakes	$[10^{0}, 10^{5}]$	Micro, Local, Regional	All the above (potentially)	Koks et al. (2019)
Volcanic eruptions, ashes, dust clouds	$[10^{0}, 10^{8}]$	Micro, Local, Regional, Global	All the above (potentially)	Batista e Silva et al. (2019)

The interaction between infrastructures and spatial natural hazards is a very well investigated area of research. Studies carried out without the direct involvement of stakeholders have addressed the impact of volcanic ashes on airline traffic (Wilkinson et al., 2012), the damage caused by wildfires to the energy infrastructure (Sathaye et al., 2011), the effect of floods on the road network (Pregnolato et al., 2016), and the impact of extreme weather on the electricity network (Panteli et al., 2017). However, the involvement of private stakeholders and government institutions, which find this field crucially important, is also notable. This is the case for the quantification of damage caused by floods to the Austrian railway network (Kellermann et al., 2015), the analysis of flood risk policies throughout England (Begg et al., 2015), and the definition of appropriate fragility curves for the electricity network exposed to high winds (Dunn et al., 2018). In this respect, this thesis constitutes a mixed approach, as it addresses the problem of natural hazards interacting with infrastructures both from a research-only perspective and a stakeholder perspective.

2.2.1.3 Review of the existing approaches to modelling spatial hazards

A thorough analysis of the relevant literature has identified four different approaches to modelling spatial hazards:

- The *deterministic approach*;
- The *geometric approach*;
- The *probabilistic approach*;
- The *computation-based approach*.

The *deterministic approach* is the most recurrent in the literature, and it relies on the use of regular shapes to describe the spatial extent and presence of natural hazard footprints. This approach is computationally inexpensive and also attractive, as it assumes that there is either a rule or an equation describing the shape used as footprint. As such, the elements of an infrastructure that are immediately affected by the footprint can be easily predicted, as they are located inside the footprint itself. On the one hand, this approach allows the emphasis to be put on how the network responds and other modelling aspects, but on the other hand it does not take into account the spatial variability that natural hazard footprints typically feature. The shapes used in literature are mainly circles (Figure 2.4) (Berezin et al., 2015; Gao et al., 2015; Shao et al., 2015; Hu et al., 2016; Neumayer and Modiano, 2016; Ouyang, 2016; Dunn and Wilkinson, 2017), although squares (Li et al., 2016), ellipses (Little, 2003; Saito, 2015), and

other deterministic structures have been implemented, such as lines (Neumayer et al., 2011; Long et al. 2014).

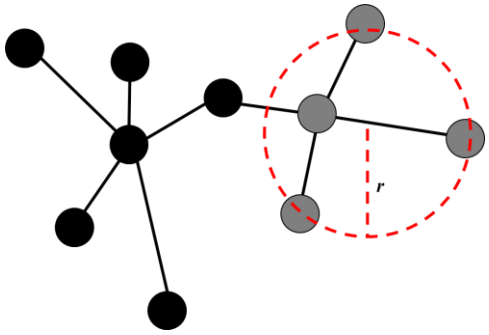

Figure 2.4. The dashed red line represents the most recurrent incarnation of deterministic shapes, the circle. Every node (or infrastructure component) falling within or intersected by the shape with radius *r* fails (grey). The center of the circle may correspond with a random node (Berezin et al., 2015), or with a different location.

The *geometric approach* is similar in nature to the deterministic approach in that they also fail to consider the spatial variability of natural hazard footprints. The difference between the geometric and the deterministic approach is in the type of shapes used. The choice in this case is to adopt geometric shapes that are non-deterministic, such as irregular polygons. This solution is both computationally inexpensive and attractive but has the downside of having to rely on a dataset that divides the footprint into polygons or regions. One relevant example is found in Wilkinson et al. (2012), where the footprint is split into irregular polygons based on the data on closed airspaces following the 2011 Eyjafjallajökull eruption in Iceland (Figure 2.5).

Figure 2.5. The irregular polygons describing the closed airspaces on 18 April 2011, following the eruption of the Eyjafjallajökull volcano in Iceland (adapted from Wilkinson et al., 2012).

The *probabilistic approach* relies on the implementation of probability surfaces to describe the footprint of natural hazards. Their adoption is not necessarily computationally expensive, but it may require extensive analysis of large datasets to produce the contours and confidence intervals that characterize the surface. This approach is extensively used in the prediction of the strength of tropical cyclone winds, where cone-shaped probability surfaces are forecast (Figure 2.6) (Aberson, 2001), and was also used by other authors addressing the response of generic (Sterbenz et al., 2011) and specific networks (Agarwal et al., 2010; Agarwal et al., 2013) to physical and geographical failures. The disadvantages of probability surfaces are that they do not take into account the spatial variability of natural hazard footprints, and their requiring extensive datasets might prevent their use in a wider context.

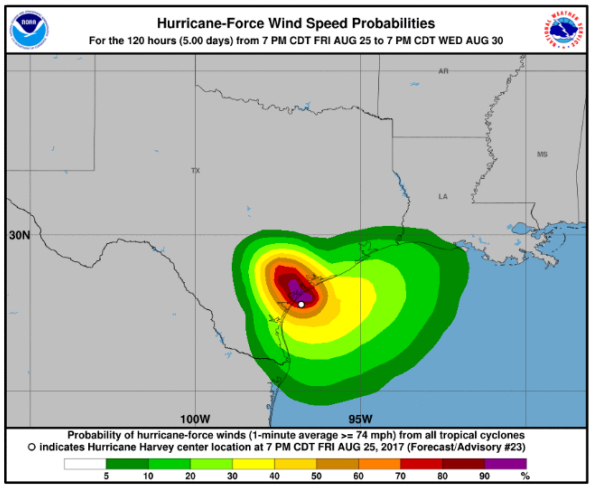

Figure 2.6. The probability surface of hurricane-force wind speed for Hurricane Harvey. The white dot is the eye of the hurricane, while the colored contours show the probability of wind speed exceeding 74 miles per hour (120 km/h) (National Hurricane Center, 2017).

Finally, the *computation-based approach* allows to produce hazard maps or hazard fields using dedicated software packages. The main advantages are software optimization, reliance on high-resolution equations to model physical processes (FLO-2D Software, 2009; Glenis et al., 2013) or cellular automata (Guidolin et al., 2016), and availability of output time series. These packages might also have the advantage of being open-source (Guidolin et al., 2016), supporting cloud computing (Glenis et al., 2013), and being valid commercial solutions (FLO-2D Software, 2009). Among the main disadvantages are the requirement of accurate input datasets about topography and the built environment, runtime, and license or Cloud access costs. Moreover, although these packages have been used to model the impact on infrastructures (Pregnolato et al., 2016), their use appears to be limited to the analysis of floods (Figure 2.7).

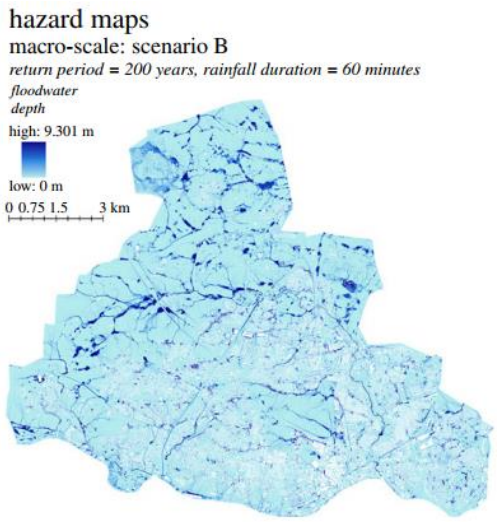

Figure 2.7. Hazard map of floods for Newcastle upon Tyne (United Kingdom). The field shows floodwater depths as a result of rainfall with a return period of 200 years (adapted from Pregnolato et al., 2016).

2.2.1.4 Advantages and disadvantages of the existing recipes for spatial hazards

The existing approaches to reproducing spatial hazards are characterized by a number of advantageous aspects, although they are not bereft of disadvantages either. To assess these, five different aspects, identified in the literature, have been used:

1. Ease of implementation;
2. Input information required;
3. Computational effort;
4. Realism or ability to capture spatial variability;
5. Specificity.

Figure 2.8 aims to offer a qualitative classification of the existing recipes for spatial hazards based on the above aspects. This is offered based on the ability of the methodologies discussed in paragraph 2.2.1.3 to reproduce realistic natural hazard footprints.

The *deterministic approaches* (DA) are the easiest to implement, owing to the simplicity of the hazard shapes or footprint that they adopt (e.g., circles, squares, ellipses, etc.). Consequently, they require limited input information, which may only include the center location and the extent of the footprint, whilst the computational effort of reproducing a deterministic shape is negligible. On the negative side, it can be argued that these shapes do not capture any degree of the spatial variability typical of natural hazards, and they are also highly non-specific, as they have come to represent a plethora of different situations ranging from

generic events (Berezin et al., 2015; Gao et al., 2015; Shao et al., 2015) to failures of the telecommunication infrastructure (Neumayer et al., 2011; Long et al. 2014).

The *geometric approaches* (GA) may feature a slightly more demanding implementation compared to DA, in that these are very similar to deterministic shapes, but they may require extensive information. Once the polygons typically featured in GA have been defined, the computational effort to reproduce them is likely to be low, whereas the level of realism may be limited by the accuracy with which the polygons themselves have been defined. On the contrary, the level of specificity is tightly coupled with the type of information required (Wilkinson et al., 2012).

The *probabilistic approach* (PA) may still be easy to implement and may come with limited computational effort, but these positives are offset by the large amount of data required to produce a meaningful and reliable footprint, as is the case with the probability surface of hurricane-force winds (National Hurricane Center, 2017; Figure 2.6). The level of realism may be higher than DA and GA, although this is highly dependent on the accuracy of input information. As with GA, PA is typically tightly coupled to the phenomenon it is trying to map.

Finally, the *computation-based approach* (CBA) may be classified as the hardest to implement, due to the effort required in creating the appropriate model for the appropriate phenomenon. In order to produce accurate results, these models usually necessitate detailed information and lengthy run times, which may justify the adoption of cloud computing (Glenis et al., 2013). Given their extensive deployment in reproducing past events or simulating future scenarios, the level of realism offered by CBA is typically higher than other approaches, although it is bound by its hazard-specificity.

Of the five aspects depicted in Figure 2.8, it may be argued that the most valuable and desirable is the ability to produce footprints that capture the typical spatial variability featured by the footprint of natural hazards. In fact, this is so crucial that the risk of producing inaccurate footprints, for instance while trying to map flood risks for the insurance industry or with urban planning purposes, may very well cripple all the resources and efforts put into generating them. As such, the most desirable combination of the five aspects presented in Figure 2.8 consists of a maximized level of realism as primary constituent, followed by minimized ease of implementation, input information required, and computational effort. It may be argued that the importance of specificity is really dictated by the intended outcome, and that the higher the specificity, the less generalized conclusions can be drawn regarding the impact of the footprint.

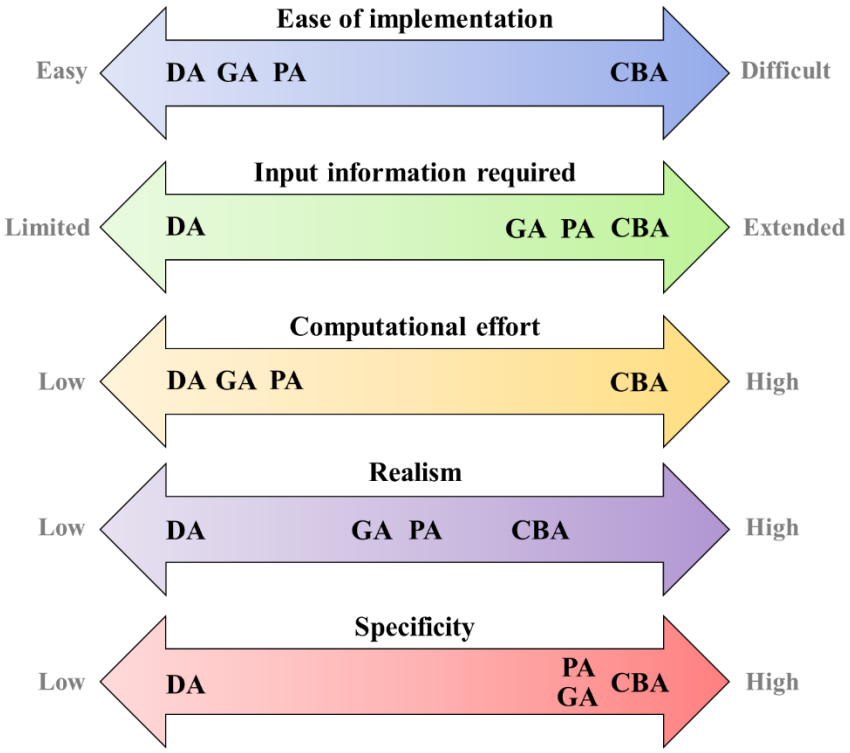

Figure 2.8. Qualitative and non-exhaustive categorization of the four existing approaches to producing spatial hazards based on the ability to reproduce the footprint of natural spatial hazards.

2.2.1.5 The need for more accurate hazard footprints

When considering natural spatial hazards, a crucial element of a reliable infrastructure robustness analysis is the availability of hazard footprints. In the literature, these footprints originate from multiple sources, based on the hazard and the infrastructure considered by the study. A list of sources includes: *i*) inventory or susceptibility analysis, as it is the case for landslides (Malamud et al., 2004; Postance et al., 2017); *ii*) datasets officially released by international bodies, as with airspace closures (Wilkinson et al., 2012); *iii*) forecasting, as in the case of tropical depressions (Aberson, 2001); *iv*) the identification of probability surfaces, as with geographical failures hitting fiber-optic networks (Agarwal et al., 2010; Agarwal et al., 2013); and *v*) the adoption of deterministic shapes, as in the case of failures targeting air traffic networks (Dunn and Wilkinson, 2016). There is a likelihood that these approaches exhibit limitations due to the availability of data, the accuracy of forecasting models, the rate with which new forecasts are issued to replace old projections, and the inability of modelling spatial variation typical of deterministic shapes.

A considerable amount of attention has been recently building up around Regional Climate Models, given their role in modelling extreme events such as heavy rainfall or severe wind storms (Nikulin et al., 2011). This type of event certainly falls within the category of natural hazards given the extensive damage that they cause to infrastructures (Pregnolato et al., 2017; Panteli et al., 2017). Regional models offer a significant improvement in terms of spatial resolution over global models. However, the spatial resolution of extensively used Regional Climate Models, such as the UK Met Office North Atlantic and European model (Davies et al., 2005) with its 12-km resolution, did not allow for proper convective modelling, resulting in the limited feasibility of impact studies. In recent years, the UK Met Office has developed a high-resolution Regional Climate Model known as UKV (Lean et al., 2008) that explicitly resolves convection, making the study of small-scale, convective events possible (Kendon et al., 2014).

2.2.2 Stage 2: hierarchies and dependencies

2.2.2.1 Background: intra-dependencies, inter-dependencies, and systems

The concepts of intra-dependency and inter-dependency permeate the literature focused on robustness and resilience. A concise definition of these two notions is given by Buxton and Pringle (2014), according to whom *intra-dependencies* are dependencies occurring between components of the same system, whereas *inter-dependencies* are dependencies involving components of different, although related, networks. One example of intra-dependencies involves the segments of the electricity transmission and distribution network (feeders and circuits), whereas inter-dependencies describe the feedback loop that, for instance, governs the interactions between the electricity and the telecommunication network (Rosato et al., 2008).

The complexity behind civil engineering infrastructures, as first highlighted by Peerenboom et al. (2001) and Rinaldi et al. (2001), is well documented. As such, it is realistic to consider failures resulting from spatial hazards not in terms of independent events, but as chains of events (Rahnamay-Naeini and Hayat, 2016). In fact, failures occurring in one infrastructures ripple through other systems that are coupled or interdependent (Svendsen and Wolthusen, 2007; Wang et al., 2011; Fu et al., 2014). Examples of these nature include the coupling of the electricity network and the water distribution network, or the interdependency between the electricity network and the railway network. The unwelcomed result is that failures manifest themselves not just in different geographic locations, but also in different systems. Therefore, the impact of spatial hazards in real-world infrastructures can have deeper, tentacular

consequences that span systems of systems (Eusgeld et al., 2011). However, the same is true for self-contained systems in which components are partitioned based on their role – the *intra-dependencies* - such as the intake, treatment, and distribution components of the water supply network. In this case, hierarchies are still present, although within the same system, and are known as intra-dependencies. This confirms that a more detailed level of analysis may be achieved by adopting the systemic approaches discussed in previous sections, under the assumption that infrastructures are not only seen as self-contained systems or systems with dependencies, but as systems of systems. The emergent behaviour is that individual components from different infrastructures interact with each other, with dependencies playing an active role in determining the overall response.

2.2.2.2 Advantages and disadvantages of the existing approaches

The accuracy with which intra-dependency and inter-dependency are modelled is crucial to understanding how an infrastructure system copes with the impact of natural hazards. In fact, over-simplifications, errors, or failure to understand the underlying relationships may significantly alter the reliability of the outcome. However, trade-offs between representativity and computational costs (and, rather frequently, the availability of detailed information) are often sought-after in an attempt to build a close-ended and manageable problem. The approaches that can be found in the literature seem to be mostly concerned with the study of power networks. These sources seem to follow the schematic provided by Figure 2.5, and include:

- *Holistic approaches;*
- *Purely topological approaches;*
- *Functional approaches;*
- *Simulation-based approaches*.

Holistic approaches look at the overall behaviour of the infrastructure system, where the aggregated behaviour of one infrastructure is responsible for the aggregated behaviour of another, regardless of the detailed performance of the individual components. One example of this approach might be the study performed by Buldyrev et al. (2010) on the Italian Blackout

occurred in 2003, where it was highlighted that the aggregated behaviour of the power network – a fault caused by three flashovers – caused the failure of the telecommunication system.

Purely topological approaches analyse the interactions between different infrastructures, as well as components of the same infrastructures, by adopting abstract models borrowed from network theory. The latter are helpful when trying to evaluate, in absence of a visible structure, the implications of the failures that occur in one or multiple systems. These approaches often follow the *contagion phenomenon*, where an element *j* downstream of, and directly connected to, an element *i* fails conditional to the latter failing. This entails that the performance of the individual components is evaluated. Examples of this nature include the study performed by Korkali et al. (2017), where an increase in infrastructure interdependency was tested against the risk of cascading failures in power networks.

Whilst still considering the underlying topological relationships, functional approaches incorporate some elements of flow modelling. As an example of this methodology, in order to quantify the robustness of the power network to single-line failures, Soltan et al. (2017) devised a study in which the effect of power outages occurring on one specific power line impacted on the other lines. The re-routing of electrical flows was implemented to observe where in the network the next faults would occur based on both topological and flow-related aspects.

Lastly, simulation-based approaches are meant to reproduce the actual rules and operational constraints adopted by that real-world infrastructures. One such example is the study conducted by Petrenj and Trucco (2014), in which the transportation system of the city of Milan is modelled to understand the impacts of large meteorological events and determine the disruption response of the system. Another example is the study performed by Esposito et al. (2015) on the seismic risk to which the gas supply network is exposed, in which the contribution of the individual components is evaluated.

By critically analyzing the four classes of methodologies, it emerges that holistic approaches are tempting due to the ease of implementation; this, however, comes at the expense of accuracy in the results, and its reliability is heavily influenced by the assumptions made to simplify complex systems. Topological approaches allow to explicit relationships that are often hidden under the operational aspects of infrastructures, and they represent a convenient solution when topological information regarding connections or hierarchies is available. The advantage is in the fact that, as highlighted by Hines et al. (2010), the results might be misleading if based on topology only. Leveraging on this shortcoming, the functional approaches may offer the best of both worlds, as they incorporate elements of flow-modelling. However, their advantages may be rapidly offset by the computational costs associated with the analysis of a complex system

that is large in size, which entails high computational costs and limited opportunities to experiment with multiple scenarios or settings. Finally, simulation-based approaches may be classed as the most accurate methodology due to their detailed outcomes; however, their potential may be severely restricted by the fact that the detailed information that they require may not be available, or by the lack of a well-defined scope. In conclusion, the choice of one approach instead of another might be dictated by a multitude of factors, among which the degree of accuracy of the available information and the computational costs are often decisive.

2.2.3 Stage 3: use of models from network theory and real-world infrastructures

2.2.3.1 Background: network models representing infrastructures

When analyzed from a systemic perspective, civil engineering infrastructures can be modelled as networked systems, as first done by Peerenboom et al. (2001) and Rinaldi et al. (2001), and later by Latora and Marchiori (2005), Lewis (2006), and Gao et al. (2014). A great deal of research has focused on the use of network theory and models for reproducing the behavior and performance of technological systems (Fu et al., 2014). Relevant examples can be found in recent studies investigating electricity transmission networks (Panteli et al., 2015; Ren et al., 2016; Panteli et al., 2017; Fu et al., 2017; Castellani et al., 2017), but also generic infrastructure systems (Dunn et al., 2013), coupled energy, water, and wastewater systems (Holden et al., 2013), air traffic networks (Dunn et al., 2016), and transportation and pipeline networks (Inanloo et al., 2016). The general idea is that it is possible to create an abstract representation of a real-world infrastructure by borrowing the concept of *graph* from *network theory*. The graph is an object composed of n_i *nodes* which can be seen as entities performing actions, and v_i *edges* which connect the nodes and as such transport the interactions between them. The parallelism between a graph and a networked infrastructure arises when the physical elements of an infrastructure, such as transmission towers, bridge piers, and road junctions, are schematized as nodes. Similarly, the cables between two towers, the decks between two piers, and the road segments between two junctions are all modelled as edges.

The importance of a node in a network can be inferred from the number of edges going through it, although this is not the only criterion in use. The edges could either be *directed* (from node *i* to node *j*) or *undirected* (from node *i* to node *j* and then back again) (Figure 2.8). The number of edges identifies the degree of a node, *k* (Newman, 2003); therefore, the concepts of degree and number of connections or edges of a node are interchangeable. The average degree,

<*k*>, is often used to characterize the network as a whole. In the case of a directed network, the degree must specify the number of edges going in and out of a node using the in-degree (k_{in}) and out-degree (k_{out}) notations. An undirected network may be used to represent a generic infrastructure or a transport network; a directed network may be appropriate for hierarchical systems such as water supply networks and power grids.

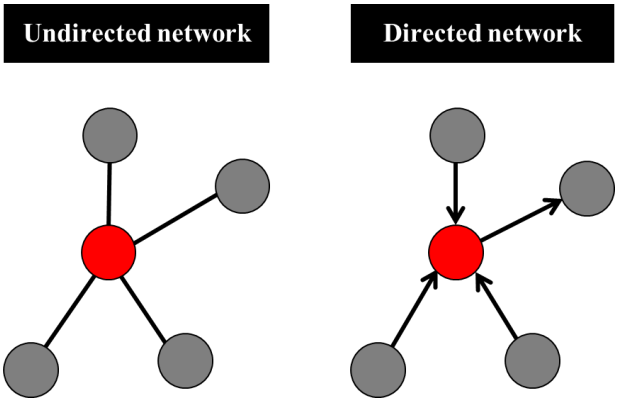

Figure 2.8. In the undirected network, the red node has a degree k=4, whereas the whole network has an average degree <k>=8/5=1.6; the edges can be gone through in both directions. In the directed network, the red node has an in-degree k_{in}=3 and an out-degree k_{out}=1, whereas the network has an average in-degree $<k_{in}>$=4/5=0.8 and an average out-degree $<k_{out}>$=4/5=0.8. In the directed case, the edges can only be gone through in the assigned direction.

2.2.3.2 Advantages and disadvantages of the graphs used in the literature

As soon as the rendition of civil engineering infrastructures as graphs became a staple in impact studies, it also became clear that these models were very advantageous, as they could explicitly reveal the relationships underpinning their complex functions (Rosato et al., 2008; Fu et al., 2014; Chopra et al., 2016). It can be argued that these relationships were hardly clear if not observed through the lenses of an abstract, yet ground based, topological model.

However, it has been suggested by certain authors that the exclusive use of a topology-based model may provide results that are unrealistic if looked at through the lenses of dynamism (Hines et al., 2010). This aspect seems to align very well with the diagram provided in Figure 2.5, according to which the use of a topology-based approach only may be perceived as unorthodox when the goal is to derive operational insights. Another important aspect which may enhance the value of graphs in impact studies is the presence of a realistic geographic representation of the modelled infrastructure (Edmondson et al., 2018). In fact, it is possible to speculate that a non-realistic representation of node locations may lead to an altered model of the infrastructure, which in turn may result in unreliable outcomes. One way of decreasing the

likelihood of inaccuracies, especially in impact studies based on real-world assets, is to make sure that the graph adopted is a direct rendition of the infrastructure itself rather than a completely abstract model.

2.2.4 Stage 4: mechanisms of failure propagation

2.2.4.1 Background: percolation and failure propagation

The failure of a node n_i in a network is likely to ripple throughout the system as a function of how many nodes are directly connected to node n_i. This means that the higher the number of nodes connected to a failed node, the higher the likelihood of additional failures, especially if the neighbors were only connected to the failed node. This concept describes how the failure of a node *percolates* through a network, and it constitutes the focus of *percolation theory*, a subject studied in condensed matter and statistical physics (Stauffer and Aharony, 1991), as well as network theory (Callaway et al., 2000; Albert and Barabási, 2002). The same problem has been investigated in infrastructure systems modelled as complex, interdependent networks (Fu et al., 2014; Radicchi, 2015; Gao et al., 2015; Havlin et al., 2015).

In the context of either single or interdependent networks, percolation emerges as a result of two distinct failure processes (Robson, 2016):

- *1st order failures*, which describe the failure of nodes directly affected by an external agent or event. In the context of this research, the external agent is any natural hazard. All failures occurring within the footprint of such hazard are referred to as *1st order failures*;
- *2nd order failures*, which describe the failure of nodes not directly affected by the external agent. All failures occurring outside the footprint of the natural hazard are referred to as *2nd order failures*. The exposure to this failure mechanism is maximized in nodes that find themselves closer to the boundary of the footprint (Figure 2.9).

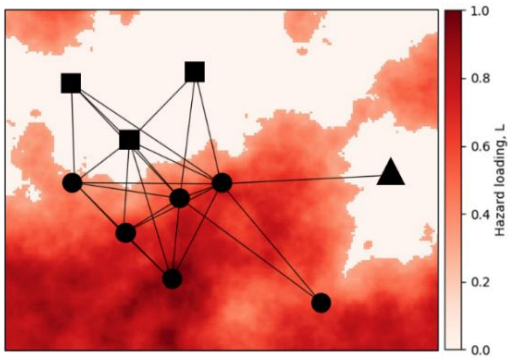

Figure 2.9. Visualization of 1st and 2nd order failures in a network subjected to a hazard footprint. The circular nodes are located inside the footprint, and as such they constitute 1st order failures. The triangle is outside the footprint, but since it is connected to a node that is inside the footprint (1st order failure), it is a 2nd order failure. The square-shaped nodes survive the hazard.

2.2.4.2 Simulating infrastructure failures

Accurately defining the process that leads to infrastructure failure is not only key to understanding the emergent behavior of the system, but also a potential weakness, as the adopted models need to be an appropriate fit for the analyzed infrastructure. In general terms, the failure of an infrastructure component is often described as the result of excessive *external loading*. Classical engineering studies have investigated this aspect with reference to embankments exposed to flooding and seepage (Polemio and Lollino, 2011) or railway bridge components subjected to severe ground acceleration (Kang et al., 2017). From a perspective purely based on performance, the fragility curves developed by van der Meer et al. (2009) for flooding and those defined for Earthquake Engineering by Grossi and Kunreuther (2005), for instance, describe the failure probability of single elements. However, given that infrastructures have evolved over time to resemble distributed systems (Whyte, 2016; Thacker et al., 2017) that are also complex and adaptive (Ouyang, 2014), there is the need to switch to failure models that incorporate interactions between components and interdependency. The literature on the subject presents four main approaches that incorporate systemic aspects:

- *Selective failure models*;
- *Hierarchy-based failure models*;
- *System dynamics failure models*;
- *Agent-based failure models*.

Selective failure models are the most represented in literature. They require the transformation of the physical infrastructure into an abstract graph object, which is then used

to identify nodes by means of specific criteria. One relevant example is the study of the vulnerability of interdependent infrastructures carried out by Wang et al. (2012), where random and degree-based selection methods were used to identify crucial nodes and remove them from the network. Robson et al. (2014) used similar approaches in analyzing the resilience of infrastructure networks, which were complemented by a betweenness-based criterion to identify crucial nodes to remove. Finally, Dunn and Wilkinson (2017) used a spatial footprint as selection criterion, so that all the nodes of the airline traffic network that fell within the boundary of a circle were removed from the system.

Hierarchy-based failure models study the propagation of failures through the infrastructure by considering the hierarchy with which they operate. Fares and Zayad (2010) used a hierarchical model to identify the sections of a water distribution system to which the highest failure risk is attributable. Soltan et al. (2017) analyzed the phenomenon of cascading failures in the electricity network by identifying subgraphs of the US Western Interconnection grid, in addition to considering the entire system.

System dynamics failure models take advantage of an appropriate set of equations describing the flow of goods or services through a perturbed infrastructure. Hines et al. (2010) highlighted the importance of using the linear approximation of power flow equations as an accurate descriptor of failures. Soltan et al. (2017) followed the same approach to find that overloads and consequent failures may occur in locations that are not proximal to the area where the triggering failure originated.

Agent-based failure models reinterpret infrastructure components in terms of individual agents that can take different statuses based on a number of pre-set rules that describe their behavior (Barton et al., 2000). Based on the consequence and type of the external loading, these statuses may include, among others, *active, failed*, or *reduced functionality* instances that are dictated by the failures themselves and the interactions between agents. In the context of infrastructure failures, such interactions may include intra- and inter-dependencies (Figure 2.3). The objective is to identify any behavior that emerges from the collective set of failures and interactions. Applications of this methodology are limited, and this is likely to be due to the extensive knowledge required in order to properly define agent statuses and interaction rules. Authors that used agent-based models in their studies include Dudenhoeffer et al. (2007), who illustrated how modelling infrastructure elements as agents can be beneficial in understanding the emergent behavior of a complex, interdependent infrastructure exposed to flooding, and Kundur et al. (2011), who modelled the impact of cyber-attacks on the smart grid by modelling the grid components as agents.

2.2.4.3 Cascading failures

The concept of *cascading failures* originates from the study of interconnected networks in network theory. The idea is that in an interconnected network composed of several networks, failures occurring in one network could spread to other networks via nodes that act as gateways to other networks. Interconnected networks are defined by the presence of these nodes, and as such were found extremely vulnerable to cascading failures (Buldyrev et al., 2010).

Ensuing studies quickly turned their attention to infrastructure networks, prompted by events such as the 2003 Italian Blackout (Rosato et al., 2008; Buldyrev et al., 2010), where disruptions attributed to power stations resulted in failures in the telecommunication network, which in turn decreased the controllability of other parts of the electricity network itself. Due to the fundamental importance of a reliable electricity supply, the occurrence of cascading failures is a risk to which electricity networks are particularly exposed. Studies have addressed it by deriving failure models and mechanisms that incorporate the idea of *redistribution of flows* (Crucitti et al., 2004; Soltan et al., 2017; Guo et al., 2017).

This idea stems from that of a dynamic system where failures along a transmission line force the electric flow to adjust to a new configuration, modifying the load to which other lines are exposed (Crucitti et al., 2004). A similar approach is followed by Dueñas-Osorio and Vemuru (2009), who looked at the overloads generated in power systems by cascading failures triggered by natural hazards. Another proposed approach is to adopt purely topological metrics to evaluate the response of the electricity network. However, Hines et al. (2010) showed that this approach does not return reliable results compared to the implementation of flow redistribution.

The status of cascading failures as a source of risk for infrastructures is well established and it applies to all systems, including cities (Dawson, 2007), and both intra-dependent and inter-dependent infrastructures (Korkali et al., 2017). Derrible (2017) highlighted the fact that the tendency of building more complex and congested cities may facilitate the occurrence of chains of failures bouncing from one network to another. As a result, studies have been carried out investigating the possible solutions, two of which were reported to be: *i*) from a topological perspective, increasing the level of interdependency (Korkali et al., 2017); and *ii*) from a risk-vulnerability perspective, hardening the most important nodes (Fu et al., 2014).

2.2.4.4 Advantages and disadvantages of the existing approaches to failure models

The problem of defining advantages and disadvantages of the different mechanisms of failure propagation is similar to the definition of advantages and disadvantages of the graphs and metrics adopted to represent the infrastructure system (see paragraph 2.2.3.2). Essentially, this discussion comes down to defining the exact purpose of the study, the nature of the infrastructure studied, and the need to strike a balance between computational costs and accuracy. These three aspects are key driving factors in the choice of the most appropriate failure model.

From a generic perspective, it is possible to argue that *selective failure models*, as well as *hierarchy-based failure models*, may offer limited computational requirements, as the first one is most often directly assigned the fraction of failed nodes as input, whereas the second relies on the specification of hierarchy rules, which do not have to be inferred or learned from the infrastructure model, but are assigned as input. It is possible to speculate that the *selective failure models* and the *hierarchy-based failure models* may come with increased computational requirements as a function of the size of the network to which they are applied. The *system dynamics* and *agent-based models*, on the other hand, require the definition of the dynamic models and the rules underpinning the behavior of the different agents, respectively. Depending on the complexity of the problem at hand, the models and rules may become demanding, leading to computational costs that do not only scale with the size of the systems to be studied, but also with their complexity. Whatever the failure model adopted, studying cascading failures contributes to increasing the complexity and computational costs of the analysis.

2.2.5 Stage 5: quantification of fragility

2.2.5.1 Background: fragility functions to describe infrastructure performance

The multiple definitions of infrastructure robustness existing in literature are in good agreement on a basic principle: a robust system is one that is capable of withstanding perturbations, maintaining a residual functionality. Even specific definitions, such as that for the railway infrastructure - the ability to resist specified disturbances so at least some functionality can be maintained (Norrbin et al., 2016) - mirror the generic ones given by McDaniels et al. (2008), Madni and Jackson (2009), and Bocchini et al. (2014). The concept of

robustness is made even more important by its being one of the four constituents of resilience, according to Bruneau et al. (2003).

Previous research has adopted *fragility curves* to characterize and quantify robustness. Originating in the field of Earthquake Engineering, a fragility curve is a probabilistic catastrophic (CAT) model (Grossi and Kunreuther, 2005) used to predict the degree of probable damage to a physical element such as a pillar or a building given an external load that increases gradually (Karim and Yamazaki, 2003). When the load is severe, the probability of damage may be very high, suggesting a conceptual parallelism with cumulative distribution functions. The notion of fragility curves finds application in Flood Risk Management (Sultana and Chen, 2009), Catastrophe Risk Modelling for electricity networks (Dunn et al., 2018), and Seismic Risk Assessment of nuclear plants (Kaplan et al., 1983). This statistical model relies on the fact that two physical elements of the same nature may respond differently to the same external load as a result of varying marginal factors. For instance, two electricity towers of the same size and structure may respond differently to the same wind gust due to different terrains, which may result in one of them being shielded. This makes it difficult to identify a threshold past which the element is certainly failed, hence the need for a probabilistic approach.

The procedure for generating an accurate fragility curve is by no means straightforward: the process can be data-intensive, as it demands sample sizes that cover sufficiently large spatio-temporal windows, and it is reliant on the ability to track down the hazard loading that caused a specific failure. The advantage of working with fragility curves is that they are both hazard-specific and infrastructure-specific: in fact, they constitute a detailed model for predicting the response of the relevant infrastructure assets to the relevant hazard in areas where data are not available, or where the infrastructure has yet to be created.

On the other hand, they are disadvantageous because they may be affected by wide confidence intervals, and their high specificity makes them unsuitable for applications that are outside their scope. This thesis adopts the approach of fragility curves despite their shortcomings, as they represent a research field where developments are occurring at a fast pace, resulting in improved accuracy and reliability.

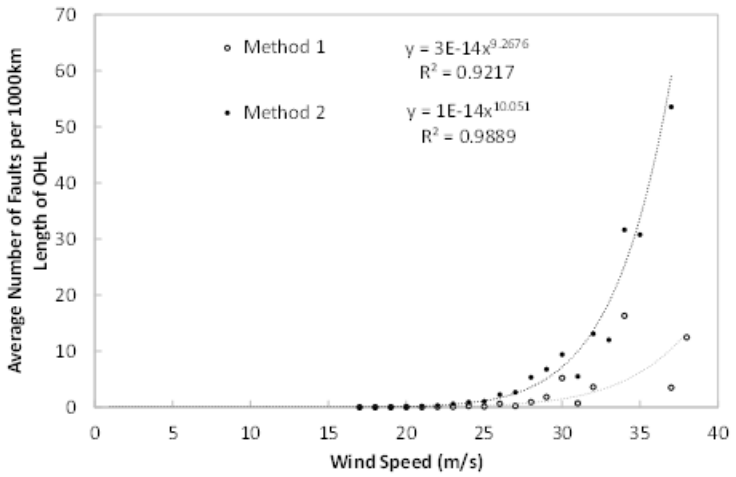

Figure 2.10. Fragility curve proposing correlation models involving wind speed and the number of faults occurring every 1000 km of overhead transmission and distribution lines (Dunn et al., 2018).

2.2.5.2 Advantages and disadvantages of the current approaches to fragility

The adoption of fragility curves to quantify the impact of natural hazards is more and more frequent, and for a wide variety of hazards. The main advantage in the use of fragility curves is their ability to provide a model that describes how the impact varies with the load. In certain situations (Karim and Yamazaki, 2003; Grossi and Kunreuther, 2005), the accuracy with which the relationship load-damage or load-impact is described is rather high. This has the consequential advantage of enabling a more informed design phase, which can build on past experiences and the amount of data collected. Another important advantage comes from the first applications of fragility models, in situations where the load-damage relationship for a specific hazard is uncharted territory. For instance, applications such as those enabled by the work of Dunn et al. (2018) greatly enhance the understanding of how high winds impact on overhead electricity lines.

However, three major advantages have to be taken into account. The first one is that fragility curves are hazard-specific, and as such models developed for one particular situation are unsuitable to describe other phenomena. The second aspect is the dependency on high quality data, which are needed to produce a meaningful model. The quality of data is also highly influenced by the spatial variation of the particular natural hazard that is being studied, as well as the sampling distance used to collect the measurements. For instance, ground acceleration varies in space, but it is measured with sensors that can be placed virtually anywhere on the studied domain. This results in a ground acceleration map that can be rather detailed. In the case of high winds, however, this level of accuracy is not easily achievable. For instance, the

best, up-to-date model used by Dunn et al. (2018) to compute the load-damage relationship relies on data sampled with spacings between 1-2.5 km. The third and final disadvantage revolves around the regional properties of the targeted natural hazard. In fact, fragility curves aimed at describing the load-impact relationship of high winds or lightning, for instance, have to take into account the fact that the weather patterns may change significantly with both the latitude and longitude. This results in the limited applicability of a specific model. As such, if the domain of the problem at hand is extended, it may be convenient to divide it into smaller domains, such that the changes in weather patterns are limited within the same sub-domain.

2.2.6 Stage 6: use of systemic indicators

2.2.6.1 Background: systemic indicators of performance

The idea of measuring the performance of an infrastructure, a system, or a network exposed to certain risks is not new to the literature on civil engineering infrastructures. However, the accuracy, appropriateness, and peculiarities of each study are relative to the problem at hand. It is also the case that, given the complexity of these problems, a set of metrics is used instead of single indicators. The majority of metrics are based on graph theory, as a result of the common practice of creating an abstract model of the infrastructure by using graphs. With reference to the metrics used in impact studies, the vast majority of studies seem to generally gather around two main categories: *i*) *structural metrics*, and *ii*) *functional metrics*.

The first category includes metrics that gauge, among others, the number of nodes or edges in a network, the degree distribution (Guimerà and Amaral, 2004), the geographical length of edges, the edge length distribution (Fu et al., 2016), and the presence of *planarity*, e.g. when edges do not cross each other (Gastner and Newman, 2006a), or the centrality measures (Brandes, 2008).

The category of *functional metrics* includes, among others, path lengths (Watts and Strogatz, 1998), network efficiency (Latora and Marchiori, 2001), the analysis of travelling times in urban road networks (Leclercq, 2007; Pregnolato et al., 2017), and the plethora of algorithms used to determine the flow of commodities across infrastructures, one example of which are power flow equations (Soltan et al., 2017).

A more specific characterization of the metrics adopted reveal that four main aspects are investigated in the literature:

- *Structural aspects*, involving measures of topological nature but also fragility characteristics such as the frequency of disruptions;
- *Fragmentation aspects*, with the aim of investigating the tendency of infrastructures to break up into multiple partitions as a result of failures;
- *Flow-related aspects*, with the purpose of assessing the ability of the infrastructure to meet the demand despite the failures;
- *Domino effect aspects*, focusing on how infrastructures cope with failures that occur further away from the hazard area, such as cascading failures.

The *structural aspects* are studied using metrics that are topology-based, with the aim of characterizing infrastructures based on concepts from graph theory. In their analysis of the robustness of the London Underground, Chopra et al. (2016) used the average short path length and the clustering coefficient to derive the topological properties of the system. Kong et al. (2013) adopted a bespoke version of centrality measures with the aim of determining the most central nodes of electricity networks, based on the resistance between two nodes as opposed to the topological configuration. Derrible and Kennedy (2010) characterized the robustness of transportation networks by studying their *assortativity* – which is the tendency of a network to exhibit connections between nodes of similar degree – showing that a high degree of robustness is the consequence of reciprocal connections between high-degree nodes.

Analyzing the *fragmentation aspects* is studying the problem of unintended *islanding*. Panteli et al. (2016) proposed islanding as a defense strategy used by energy systems against extreme weather. This technique is based on an intentional partition of the network into self-sufficient islands with the aim of limiting the spreading of failures. However, in the context of robustness to natural spatial hazards, it has to be noted that a network can be partitioned by failures. This concept was introduced by Hawick (2012), who showed how the failure and removal of electricity substations from the UK National Grid could create islands. The same problem was analyzed by Chopra et al. (2016), who proposed a coefficient that estimates the size of the isolated components that could result from the failure or removal of an edge. With reference to water supply systems, Hawick (2011) adopted the betweenness centrality measure to identify the pipe which failure is most likely to produce fragmentation.

A considerable amount of attention has been drawn by the *flow-related aspects*, as infrastructures are explicitly designed and built to deliver a service, be it the flow of freight, passengers, or utilities. Chopra et al. (2016) used the concept of efficiency from Latora and Marchiori (2001) to determine how well the London Underground meets passenger demand

when subjected to node failures modelled as station removals. Pregnolato et al. (2016) adopted the betweenness centrality metric to locate the urban sections where traffic flow was most impacted by pluvial flooding. Poljanšek et al. (2012) focused their attention on a connectivity-based metric used to quantify the reduced serviceability of the European gas and electricity network subjected to the seismic risk. Finally, Cavalieri et al. (2017) proposed a metric for assessing the serviceability performance of water distribution networks based on the ratio between the demanded flow and the delivered flow.

The *domino effect aspects* are mostly addressed by the literature on cascading failures. The basic concept is that hazards pose a risk for infrastructures that may exceed the severity of the hazard itself, with additional failures, often termed *2nd order failures*, occurring further away from the event hotspot (Little, 2003; Robson, 2016). The literature that *de facto* addresses cascading failures caused by natural hazards is not extensive, with studies being predominantly concerned with operational incidents. However, Dueñas-Osorio and Vemuru (2009) proposed a metric that quantifies the 2nd order failures occurring in electricity networks as a result of both natural and man-made hazards. Shuang et al. (2017) investigated the failure propagation in water supply networks affected by valve-triggered cascading failures, which in turn could be caused by landslides or soil erosion.

2.2.6.2 Advantages and disadvantages of the existing indicators

The discussion around advantages and disadvantages of the metrics adopted does not appear straightforward, and it is rendered complex by the number of driving factors that play a key role in the selection of a specific metric. First of all, the choice of a metric is likely to be driven by the type of infrastructure analyzed, as certain metrics may be better suited than others to describe the characteristics of certain systems.

Another driving aspect is the nature of the impact study itself, which may lead to the adoption of multiple metrics to compute the same parameter. This may be the case, for instance, for travelling times in urban road networks, which may be computed using a bespoke curve (Pregnolato et al., 2017) or more classic algorithms (Leclercq, 2007), allowing room for comparisons.

From a generic perspective, one trivial aspect is that structural metrics and functional metrics do not seem interchangeable, implying that they do not offer reliable results if inadequately applied. From a procedural point of view, it is possible to argue that the adoption of one set of metrics rather than the other, or of a combination, may be influenced by the need

to balance computational costs with accuracy. The adoption of *functional metrics* seems to always imply an increased computational cost given the complexity that, at times, is being modelled. This is offset by the more accurate representation of the dynamical functions of the infrastructure. On the other hand, whilst *structural metrics* may be alluring given their limited computational requirements, their partial accuracy may hinder their effectiveness.

2.2.7 Justification for adopting the six stages

The six stages mentioned in this Chapter were derived from recommendations provided by authors addressing the impact of spatial hazards on infrastructure from different points of view. These recommendations were integrated and used as building blocks of an end-to-end pipeline that allows addressing this research problem in a rather comprehensive way.

The emphasis placed by Stage 1 on the generation of realistic spatial hazards with different degrees of severity reflects the recommendations of Dunn et al. (2013), on the nature and magnitude of disruptive events, and Pradhan (2018), on the importance of reproducing accurate spatial phenomena.

The importance of accurately capturing hierarchies and dependencies while modelling infrastructures addressed in Stage 2 is also highlighted by Dunn and Holmes (2019), who emphasized the use of graph models where connections between sources and the source-sink dependency model are explicit, and by Qin and Faber (2019), who underlined the importance of considering hierarchical levels.

Stage 3 focuses on the use of a range of models from both real-world infrastructures and network theory. This approach mirrors the recommendations made by Gastner and Newman (2006a; 2006b) on using models from network theory, by Panteli et al. (2017) on studying electricity networks, and by Dawson et al. (2018), who stressed the importance of adopting systemic views.

The rationale behind stage 4, which introduces failure mechanisms, is in the work by Hines et al. (2010), where the importance of an appropriate failure mechanism is highlighted, and in that of Korkali et al. (2017), where coupled infrastructures are examined.

Stage 5 is concerned with quantifying the fragility of infrastructures when exposed to spatial hazards. This draws inspiration from D'Amato Avanzi et al. (2013), who emphasized the importance of quantifying infrastructure fragility, Dunn et al. (2018), who adapted the

concept of fragility curves to electricity networks, and Sarker and Lester (2019), who extended the concept of fragility quantification to all critical infrastructures.

Finally, stage 6 examines the need for systemic indicators when assessing the impact of spatial hazards on infrastructures. This follows the recommendations provided by Ghosn et al. (2016) on the importance of using systemic metrics during the design and assessment phase of infrastructure fragility, and those provided by Dawson et al. (2018) on the need to adopt systems approaches at a national level.

Chapter 3. Research Design Framework

This chapter provides a general description of the research design framework and its rationale. This framework is partially based on the work of Dunn et al. (2013), who defined an operational framework for assessing the impact of disruptions using network theory. As this thesis is composed of two separate case studies, this chapter introduces a generic modelling framework that applies to both, given the commonalities detailed in paragraph 3.1.2. In addition, this chapter provides an overview of the main advancements proposed by this thesis, and details regarding the datasets used.

3.1 Two separate case studies under the same framework

3.1.1 Overview of the two case studies

As briefly mentioned in the Introduction chapter, this thesis is composed of two separate case studies:

1. ***Case Study 1: Response of synthetic infrastructure networks to synthetic, although realistic, spatial hazards***

   This case study addressed the problem of the robustness to natural spatial hazards by introducing the use of fractal models to reproduce realistic spatial footprints. The aim was to study the response of infrastructure network models to spatial hazards with variable degrees of spatial correlation, and to identify behavioral insights that can be incorporated in the design phase of infrastructures. This case study looked at infrastructures from a macro-systemic perspective without dependencies, hence at an aggregate level. However, at variance from a typical *in-silo* approach, the emphasis was placed on infrastructure models that interact with the domain in which they are embedded, and the natural spatial hazards;
2. ***Case Study 2: Impacts of windstorms on electrical distribution infrastructure networks***. By adopting a spatial dataset of unprecedented accuracy, this case study developed a hierarchy-based network model to determine the most vulnerable components of the infrastructure and the risk of cascading failures to which the network is exposed when subjected high winds. The aim of this case study was to

derive behavioral insights that can be integrated in the infrastructure operational phase. This case study adopted a macro-systemic approach with dependencies, hence moving further away from an *in-silo* approach. In fact, the interaction with natural spatial hazards was evaluated by taking into account the robustness of each individual component, focusing on identifying the components that performed systematically worse than others, rather than providing an aggregate description of robustness.

3.1.2 General similarities between the two case studies

The first case study has the characteristics of a theoretical study, given the extensive use of synthetic models and hazards, whilst the second one represents a more realistic situation, as it adopts both a real-world hazard dataset and infrastructure. Although the two case studies differ in terms of aim and technicalities, they share substantial similarities in terms of workflow and overall computational structure. These similarities can be summarized as follows:

- Both case studies addressed the response of infrastructure networks to spatial hazards;
- Both case studies adopted a Monte Carlo-inspired approach to quantify the impact of spatial input datasets on infrastructures;
- Both case studies modelled infrastructure systems by creating equivalent graph objects and taking advantage of network theory;
- Both case studies estimated the impact of spatial hazards by defining metrics appropriate to the nature of their aim.

A common modelling framework was used in the two case studies. This is a computational, Monte Carlo-inspired, workflow that takes advantage of repeated simulations. This workflow is composed of several consequential blocks (Figure 3.1):

1. First block: *spatial hazard input*;
2. Second block: *infrastructure network modelling*;
3. Third block: *failure modelling*;
4. Fourth block: *robustness metrics*.

Each block is illustrated in a dedicated section of the next chapters, and details are given on their rationale, procedures and implementation.

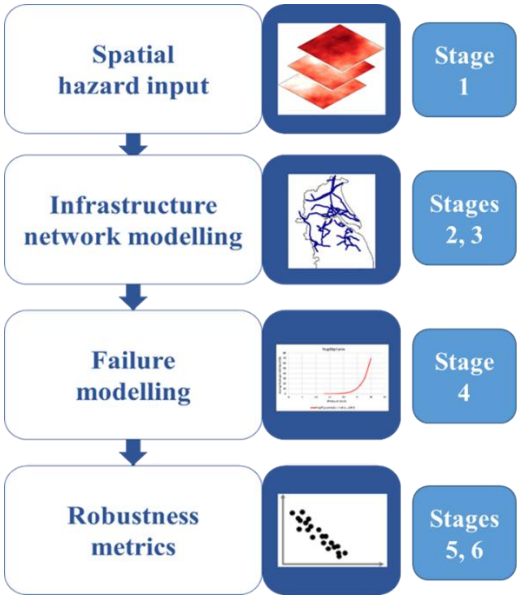

Figure 3.1. Visualization of the four main blocks that compose the shared computational workflow of the two case studies of this thesis. The different stages discussed in Chapter 2 are also mapped against the four blocks.

3.1.3 A common approach inspired by network theory

This thesis was developed by adopting concepts and models from *network theory* which apply to both case studies. The rationale for this choice is the recurrent adoption in the literature of the *graph*, or network, as an abstract model for representing infrastructure systems (Peerenboom et al., 2001; Rinaldi et al., 2001; Latora and Marchiori, 2005; Lewis, 2006; Gao et al., 2014; Fu et al., 2014; Panteli et al., 2017). A graph $G = (v, e)$ can be classed as a mathematical diagram composed of N_v vertices v, also known as *nodes*, which represent individual entities, and N_e connections e, also known as *edges*, which represent relationships between the nodes. The number of edges linking node v_i to any other node is defined as the degree k of node v_i; computing the average value of k allows to determine the average degree of the graph or network, $<k>$.

Depending on the relationships existing within G, either $N_v \neq N_e$ or $N_v = N_e$, which influences the structure or *topological layout* of the graph. Throughout this thesis, it was assumed that the edges could be either *directed* or *undirected* based on the problem at hand. In the first case study, a set of *undirected graphs* was implemented, where any edge can connect node v_i to node v_j in a bi-directional fashion, entailing that $e_{ij} = e_{ji}$. This was done based on the assumption that the generic network models implemented were not the representation of

real infrastructures, thus implying that specifying the direction of flow was not necessary. In the second case study, a simplified version of a *directed graph* was implemented, where every edge is associated with an indication of the direction it follows, entailing that $e_{ij} \neq e_{ji}$, since the two might have different characteristics or might be mutually exclusive. The simplified version implemented in the second case study stemmed from the direction of flow followed by electricity, hence from lines with higher voltage to lines with lower voltage, hence from the set of nodes representing the former to that representing the latter.

3.1.4 A common definition of hazard loading

In addition to the network theory-based approach discussed in the previous paragraph, this thesis also relied on another crucial element, which is the superimposition of a hazard field on the infrastructure. A hazard field $H(x, y)$ can be defined as a three-dimensional field in which the field H represents the distribution of the severity of the hazard associated with the spatial coordinates (x, y). The intensity of the hazard is defined, throughout this thesis, as the hazard loading $L = H(x, y)$, which is a rational number corresponding to the intensity of a natural hazard.

Depending on the hazard, admissible values of L may only be positive ($L \in \mathbb{Q}^+$), as is the case with peak ground accelerations, or may cover the entire spectrum of $\mathbb{Q}$, as is the case with temperatures ($L \in \mathbb{Q}_0$). In addition to that, the variation of L across its domain is very much dependent on the physical phenomena driving the hazard itself.

As pointed out by Gill and Malamud (2014), an additional factor driving such variation is the typical scale at which certain natural hazards occur, ranging from tens of square kilometers (e.g., floods) to hundreds of millions of square kilometers (e.g., the fallout of volcanic ashes). In this thesis, two different $H(x, y)$ fields were considered: in the first case study, a square $H(x, y)$ field was produced by using a fractal process, where the hazard loading $L \in \mathbb{Q}_0^+$ was non-dimensional; in the second case study, a rectangular $H(x, y)$ field was obtained from the output of a high-resolution climate model, where the hazard loading $L \in \mathbb{Q}_0^+$ represented the daily maximum wind speed of a certain location.

3.1.5 An open source approach to robustness modelling

This thesis provides an example of how open-source programming languages can be used to produce code that models the robustness of infrastructures exposed to spatial hazards.

The computational workflow of Figure 3.1 was implemented in *Python* (van Rossum, 1995), a high-level, general purpose open source programming language with an extensive library of dedicated packages.

The scripts developed for this thesis follow the procedural programming paradigm (Stevenson, 2013), and was implemented in Python 2.7 via *Python Jupyter*, a web-based, virtual computational notebook (Kluyver et al., 2016). The *spatial hazard input* block was structured in such a way that the functionalities of Python's *Numpy*, *Scipy* and *NetCDF4* packages could be fully exploited, allowing to import netcdf files and to perform data analysis, queries, and slicing operations. The *infrastructure network modelling* block took advantage of the flexibility and functionalities of the *NetworkX* package (Hagberg et al., 2008), which allows to create and analyze graphs based on theoretical network models or real-world asset datasets. The *failure modelling* block was implemented by means of basic language constructs such as control flow statements for iterative procedures and assignment statements for storage, without the use of any particular package. Finally, the *robustness metrics* block relied on the data analysis functionalities made available by the Numpy and Scipy packages, and the visualization functions available through the *Matplotlib* package (Hunter, 2007). The use of an open-source programming language was advantageous in many respects, including the possibility to make the code reproducible and available to the research community, and the absence of license costs charged for the use of proprietary software.

The reader is advised to refer to the Appendix section in this thesis, where the Python scripts are made available for education and reproducibility purposes. This section includes the scripts used for Case Study 1, which are entirely open-source. Confidentiality agreements prevent the public release of the scripts used for Case Study 2, for which implementation guidelines are provided.

3.1.6 Datasets used in this thesis

A collection of datasets originating from different sources has been used in this thesis. Following the structure given in section 2.2, these datasets were used at different stages of the research. Table 3.1 shows important details of the datasets used, covering aspects such as: *i*) the relevant case study; *ii*) the relevant stage; *iii*) source; *iv*) spatio-temporal scale; *v*) quality checks; *vi*) selection criterion.

Table 3.1. Details of the datasets used in this thesis.

Dataset	Case Study	Stage	Source	Spatio-temporal scale	Quality checks	Selection criterion
Synthetic spatial hazards	1	1	Own work	Spatial scale: 10x10 cells Temporal scale: static	Absence of periodicity; Absence of symmetry	Only valid in absence of periodicity and symmetry
Infrastructure network models	1	3	Own work	Spatial scale: 10x10 cells Temporal scale: static	Absence of disconnected nodes	Only valid in absence of disconnected nodes
Topology-based metrics	1	6	Literature	Spatial scale: 10x10 cells Temporal scale: static	Absence of negative values	Only valid if not negative
Wind gust	2	1	UK MetOffice	Spatial scale: circa 120x120 km^2 Temporal scale: daily	Absence of negative values; use of land-sea mask	Only valid if not negative and relative to study area
Electricity network	2	2	Northern Powergrid	Spatial scale: circa 120x120 km^2 Temporal scale: static	Absence of topological errors (overshooting, undershooting, gaps, etc.)	Only valid in absence of topological errors, which were fixed during pre-processing
Impact indicators	2	6	Own work	Spatial scale: circa 120x120 km^2 Temporal scale: daily	Absence of negative values	Only valid if not negative

3.2 Main contributions and rationale behind this thesis

3.2.1 Overview

With reference to the six stages described in Chapter 2, this thesis aims at providing three novel contributions. The first is concerned with spatial hazards, the second with network-based systemic approaches, and the third with performance metrics highlighting structural and topological weaknesses in the fabric of the infrastructure. These contributions target four of the six stages mentioned in Chapter 2, except for Stage 4 and Stage 5:

- **Stage 1:**
  Implementing a new method for generating realistic spatial hazards to enhance the results of natural hazard-related impact studies. This allowed to derive important design principles that can better inform the choice of one specific network model during the design phase of an infrastructure, so as to include the robustness to spatial hazards in the list of design requirements. This innovation was applied to both case studies;
- **Stage 2 and Stage 3:**
  In Case Study 1, the infrastructure was considered to be a self-contained system that could interact with its surroundings, hence moving away from the concept of *in-silo* infrastructures. This allowed to create a framework where an aggregate measure of the robustness to spatial hazards could be defined, leading to hazard-proof design considerations (Stage 3). In Case Study 2, partitioning the infrastructure into meaningful operational components and evaluating the role of intra-dependencies in a situation where the infrastructure is subjected to a specific natural hazard (Stage 2). This allowed to identify the most vulnerable components to be targeted by a strategic investment plan, so as to enable the infrastructure to become an adaptive system by changing its spatial structure;
- **Stage 6:**
  Highlight the performance of the infrastructure at the aggregate level when subjected to spatial hazards to understand the behavior of a specific infrastructure layout, and highlight the performance of the single, primary components by breaking down the response of the infrastructure to disturbances in the form of spatial hazards. These approaches allowed, in the first case, to identify an implicit weakness of a given layout, and in the second case to analyze

the single components to pick up criticalities that cannot be picked up at an aggregate level. This innovation was applied to both case studies.

3.2.2 Stage 1: new methods for spatial hazards

In the first case study, this thesis proposed an alternative, innovative, and open-source approach to producing spatially-distributed hazards, which was based on the use of *fractals*. Such method overcame the inability to model spatial variability featured by deterministic, geometric, and probabilistic approaches, and it also allowed to sensibly reduce runtimes. In addition, this method allowed to put the emphasis not just on specific hazards, as computation-based approaches tend to do, but on generic spatial hazards as well. In the context of this thesis, opting to model generic rather than specific spatial hazards allowed to establish important and generalizable principles that can be applied to the design of all infrastructures.

The adoption of a fractal model with the purpose of describing the spatial characteristics of natural properties and disasters is not infrequent in literature. Fractals have been used to uncover potentially unnoticed patterns in natural hazards such as floods, wildfires, and earthquakes (Cello and Malamud, 2006; Llasat, 2007). Fractals have also been studied for investigating the complexity of spatial domains hit by natural disasters (Scheidegger, 1997), for assessing the damage resulting from natural disasters (Myint et al., 2008), and for describing terrain properties (Comegna et al., 2013). Fractal theory has also played an important role in characterizing the frequency-area statistics of a number of natural disasters (Malamud and Turcotte, 2006). Finally, in a work by Smith (2009), a fractal model was used to create synthetic rainfall maps to reproduce the spatial textures associated with rain and cloud fields, based on a work by Callaghan and Vilar (2007).

This thesis adopted a fractal model known in literature as *fractional Brownian motion* (fBm), being inspired by the observed Brownian motion (Brown, 1828), and it is used to generate synthetic hazard fields. For specific values in its input parameters, fBm is said to produce fields that very closely resemble those resulting from natural phenomena, and as such they were called *fractal forgeries* (Voss, 1985). The mathematical foundation of fBm is found in the fractal theory proposed by Mandelbrot and Van Ness (1968) and expanded by Voss (1985) and Saupe (1988). These authors have paved the way for the implementation of a procedure that produces fractal surfaces known as *Brownian surfaces*. Given a finite grid of discrete integer values $G = \{x: x \subseteq \mathbb{Z},\ y: y \subseteq \mathbb{Z}\}$ that serves as spatial domain, the Brownian

surface is a three-dimensional object that associates an elevation $Z = f(x, y)$ to each point in the grid by means of a fractal elevation function (Russ, 1994).

The need for an enhanced recipe for spatial hazards was also addressed in the second case study, although with less emphasis. In the second case study, this thesis took advantage of the high-resolution UKV Regional Climate Model, to analyze the impact of daily maxima wind gusts on the electricity infrastructure, using an input dataset with a spatial resolution of 1.5 km. From the point of view of natural spatial hazards, this represents an innovative approach, as the availability of datasets with such spatial precision is likely to be, at the time of this writing, unprecedented. The latter also represents part of the rationale behind the use of wind gusts. The other reason is the remarkable frequency of damage reported by Distribution Network Operators that are attributable to sustained winds. According to the NaFIRS database, the official source of information on electricity faults (Dunn et al., 2018), in Yorkshire and Lincolnshire nearly 42% of natural hazard-related damages recorded between 2004 and March 2017 were attributed to wind.

3.2.3 Stage 2 and Stage 3: topological approaches with and without dependencies

Targeting Stage 3, the first case study investigated the aggregated impact of synthetic spatial hazards on synthetic infrastructure network models. This case study adopted a macro-systemic perspective that was based on the fact that monitoring the aggregated performance is crucial given that localized events may still affect the overall behavior of the system (Albert et al., 2004). The rationale behind the macro-systemic approach was to pursue a methodology that could reveal whether a specific network structure or topology was more or less robust to spatial hazards as a whole. This unprecedented objective was achieved, based the example provided by Gastner and Newman (2006a; 2006b), by adopting a range of network models, in such a way as to compare the different structures or layouts. The ultimate goal was to determine if the different topologies, which are based on theoretical models but at the same time are also representative of real-world examples (Guimerà et al., 2005; Kalapala et al., 2006; Carvalho et al., 2009), contained structural aspects that made them inherently more or less robust to the failures caused by spatial hazards.

Targeting Stage 2, the second case study analyzed the impact of a real-world, high-definition dataset of wind gusts on an electricity infrastructure by exploiting a macro-systemic approach that includes an intra-dependency model. Such case study was devised to identify the primary components of the infrastructure that were most often affected by disruptions over a

given timeframe. This case study was structured by taking advantage of a state-of-the-art Regional Climate Model that enables fine-scale climatic determinations (Kendon et al., 2012; Chan et al., 2014), which very high-resolution output was, for the first time, adopted in an impact study. The objective was to inform asset management practitioners seeking strategic investment plans of the presence of segments or components of the infrastructure that, based on topological considerations, were significantly less robust to disruptions than others.

3.2.4 Stage 6: implementation of a set of bespoke performance metrics

In the first case study, this thesis adopted a network theory-based perspective with regards to the structural, fragmentation, flow-related, and domino-effect aspects driving the use of performance indicators. With reference to the structural aspects, a basic count of the number of failures was implemented, in order to quantify the impact of natural spatial hazards by determining the fraction of nodes that were not disrupted. The fragmentation aspect was dealt with by counting the number of connected components in which the infrastructure network was partitioned as a result of failures. The flow-related aspects were investigated by adopting a variation of the betweenness centrality metric used by Pregnolato et al. (2016), comparing the unperturbed to the perturbed situation. Finally, the domino-effect aspects were addressed by implementing the enumeration of 2nd order failures as defined by Little (2003) and Robson (2016) and illustrated in paragraph 2.2.4.1. The rationale behind the use of this combination of metrics, which is unprecedented in the literature, is attempting to capture the main functional aspects shaping the complex operations of networked infrastructures.

In the second case study, the emphasis was placed on applying a state-of-the-art fragility model to each component or line of an existing electricity infrastructure (Soltan et al., 2017) rather than to the whole system. The innovative approach consisted in the fact that performance metrics addressing the expected number of faults produced in a given line by the wind gusts, the frequency of caused cascading failures, as well as the risk associated with them were also provided at the component level rather than at the macro-systemic level. This was done as the objective was to break down the response to characterize the robustness of the individual components. This was driven by the assumption that any strategic investment plan is budgeted, and there are not enough funds to address the lack of robustness of the entire system. Particularly innovative was the definition of the risk of cascading failures propagating from each component, which is likely to have never been attempted with a wind gust dataset of the same resolution as the one adopted in this thesis.

Chapter 4. Case Study 1: Methodology

4.1 Rationale for adopting a macro-systemic approach

In agreement with studies performed on the London Underground system (D'Lima and Medda, 2015; Chopra et al., 2016), the airline traffic network (Wilkinson et al., 2012), and the electricity network (Panteli et al., 2017), this thesis focused on how infrastructures respond to spatial hazards as a unique system, without considering the presence of sub-systems. Accordingly, in Case Study 1 the impact of spatial hazards was analyzed at the macro-system level. Here, the infrastructure was considered as a self-contained system without partitions, its behavior coinciding with a system-wide response that does not include the interaction of its sub-systems. However, at variance from the in-silo approach, the modelled behavior includes the interaction with spatial hazards, which played the role of an external agent. Contrarily to the concept of *emergent behavior*, where the cumulative outcome of a process is the result of the contributions of each sub-system and their interactions, the macro-systemic approach adopted in this thesis allowed to look at the response of the infrastructure as it if was captured from an elevated view (Figure 4.1). This approach was implemented with the purpose of determining if a certain system design – e.g., a topological model describing the layout of generic infrastructure systems – is more or less robust to spatial hazards. The task of specifying how many sub-systems are present, how they behave individually, and what is their emergent behavior was intentionally avoided, being implemented in Case Study 2.

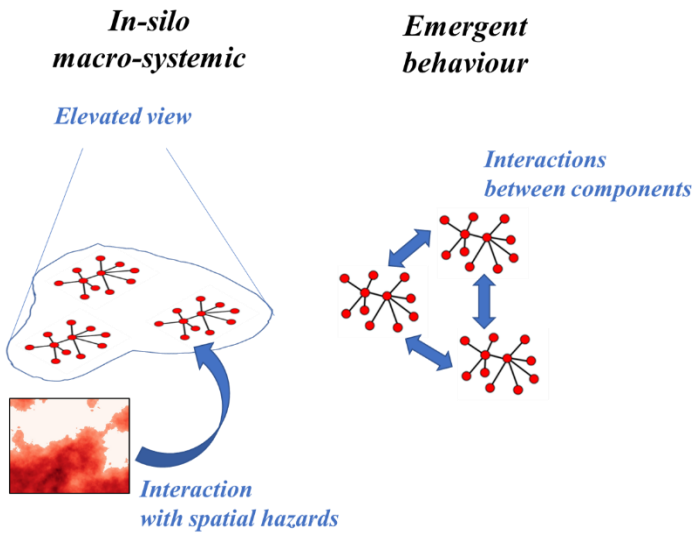

Figure 4.1. Difference between the macro-systemic approach implemented in this thesis and the concept of emergent behavior.

4.2 Stage 1: fractal spatial hazards

4.2.1 Rationale for adopting fractal spatial models

In this work, the fractional Brownian motion (fBm) was used as a generator of fractal surfaces. The elevation of these surfaces represents the severity of natural hazards. The fBm is a stochastic, isotropic process that creates a 3D surface with elevations spanning the range $\in[0,1]$. The *x* and *y* axes control the size and resolution of the domain, and the *z* axis represents the elevation of the surface (Figure 4.2). The elevation was used as a proxy for the intensity of generic natural hazards, so that peaks are associated with highs and valleys with lows.

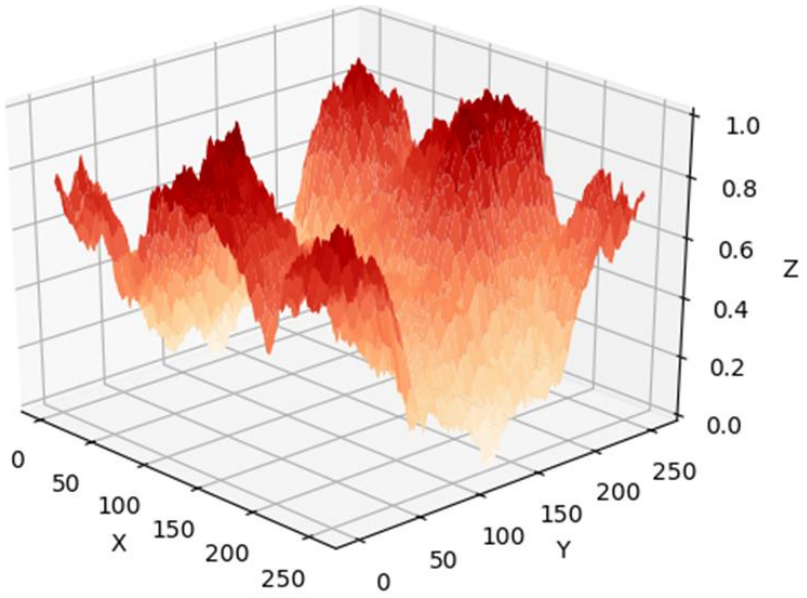

Figure 4.2. Visualization of a three-dimensional fractal Brownian surface over a grid composed of 256x256 cells. Darker shades indicate higher values of the elevation function Z, which fluctuates between 0 and 1. The same surface can be visualized using a two-dimensional, eye-view plot.

The adoption of the fBm as a spatial hazard generator, as opposed to the use of the approaches frequently found in literature, is convenient for multiple reasons:

- It features a single parameter, the Hurst exponent *H* (Hurst, 1951), which controls the degree of spatial correlation in the surface; by varying it, a wide range of spatial variability can be reproduced;
- For specific values of the Hurst exponent, the fBm model is reported in literature (Voss, 1985; Saupe, 1988) as the best fractal approach for reproducing the occurrence of natural phenomena;

- Pseudo-code scripts are largely available, so that a language-specific implementation of the fBm process for automation purposes is possible (Smith, 2009), generally requiring limited computational demand and programming effort;
- Contrarily to non-fractal approaches, the fBm process exhibits statistical self-similarity (Mandelbrot, 1967), implying that each smaller portion of the fractal surface is a reduced-scale version of the larger object;
- The *z* values of the surfaces are non-specific and can therefore represent generic natural hazards.

4.2.2 Mathematical description of the fractional Brownian motion

The fractional Brownian motion (fBm) is a Gaussian random process which operates over a continuous-time interval $[0, T]$ (Mandelbrot and Van Ness, 1968). Defined t as the time and ω as the set of all possible values of the process, the function $B(t, \omega)$ represents the ordinary Brownian motion (Lévy, 1953), which describes the path followed by a particle in the space ω at time t. This function features independent Gaussian increments, in such a way that it is possible to determine that $B(t_2, \omega) - B(t_1, \omega)$ is characterized by zero mean and variance $|t_2 - t_1|$, and that $B(t_2, \omega) - B(t_1, \omega)$ is independent of $B(t_4, \omega) - B(t_3, \omega)$, provided that the time intervals $|t_2 - t_1|$ and $|t_4 - t_3|$ are not overlapped. Defined $0 < H < 1$ as the Hurst exponent (Hurst, 1951) and b_0 as a real number, $B_H(t, \omega)$ is the fractional Brownian motion having parameter H and starting value b_0. Being s another variable for measuring time, with $s \neq t$, $B_H(t, \omega)$ can be defined as:

$$B_H(0, \omega) = b_0 \tag{4.1}$$

$$B_H(t, \omega) - B_H(0, \omega) = \frac{1}{\Gamma(H + 1/2)} \left\{ \int_{-\infty}^{0} \left[(t - s)^{H - 1/2} - (-s)^{H - 1/2} \right] dB(s, \omega) + \int_{0}^{t} (t - s)^{H - 1/2} dB(s, \omega) \right\} \tag{4.2}$$

Equation 4.2 represents the moving average of $dB(t, \omega)$, where the increments of $B(t, \omega)$ are weighted by the kernel $(t - s)^{H - 1/2}$ (Mandelbrot and Van Ness, 1968). Based on

the values of *H*, equation 4.2 generates three different families of functions, which can be used to produce numerical series. These functions are distinguished based on the value of $H \in [0, 1]$:

- When $0 < H < 0.5$, the increments of $B_H(t, \omega)$ show negative correlation;
- When $H = 0.5$, the random process $B_H(t, \omega)$ corresponds to the ordinary Brownian motion $B(t, \omega)$, where the increments show no correlation;
- When $H > 0.5$, there is positive correlation between the increments.

4.2.3 Spatial properties of fBm and significance of the Hurst exponent

As first outlined by Mandelbrot (1967) and later supported by Borrough (1981) and Baas (2002), the fBm process is characterized by statistical self-similarity. This implies that as the fractal object is magnified, the shapes and the statistical properties that are featured at a given scale are highly similar to those observed at other scales. One effective example of such property is visible in the Sierpińksi triangle or gasket, shown in Figure 4.3.

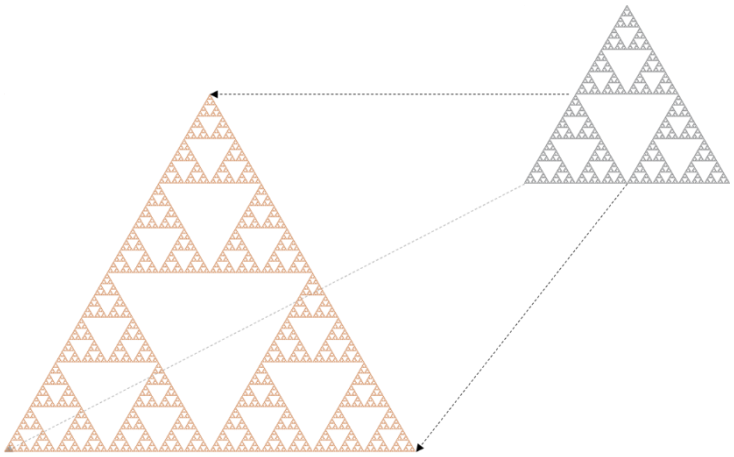

Figure 4.3. Visual representation of the notion of statistical self-similarity in the Sierpińksi triangle or gasket.

The concept of statistical self-similarity is tied to that of spatial autocorrelation by means of the fractal dimension D (Klinkenberg, 1992; Klinkenberg, 2004). This parameter is a measure of how efficiently a given geometrical shape fills the space in which it is embedded. In the case of regular geometric elements such as lines, squares, or cubes, D corresponds to the dimension of the Euclidean space they occupy, and it is an integer number ($1D$, $2D$, $3D$). In the case of fractals, as the word itself suggests, this dimension is not an integer number, but rather a fractional number. According to Klinkenberg (1992; 2004), given a three-dimensional space, high values of D, such as 2.8, designate highly irregular geometric objects. On the contrary,

low values of D, such as 2.2, designate more regular objects. Consequently, to determine the irregularity of an object, the fractal dimension D must always be compared with the integer part of D. It is also reported by Klinkenberg (1992; 2004) that, in a $3D$ Euclidean space, for instance, the self-similarity of an object with $D = 2.1$ features high positive spatial correlation. On the other hand, if the object has $D = 2.9$, its self-similarity comes with a high negative spatial correlation. If the object has a fractal dimension of 2.5, it shows no spatial correlation. This property applies to every dimension of the Euclidean space. This property also justifies the choice of a fractal model over the use of pseudo-random generators, as spatial correlation does not appear to be an intrinsic property of the latter.

The fractal dimension D is also tied to the Hurst exponent H. As reported by Voss (1985), there is a linear relationship between D and H, and thus, the Hurst exponent can be estimated from the fractal dimension of a particular process:

$$D = 3 - H \text{ (in a three-dimensional space)}$$
$$D = 2 - H \text{ (in a bi-dimensional space)} \tag{4.3}$$

The Hurst exponent plays a multi-faceted role in the outcome produced by the fBm process:

- As it is the only parameter to be accounted for, the Hurst exponent governs the fBm model making it simple to manage, flexible, and computationally inexpensive;
- It describes the degree of autocorrelation featured by the output of equation 4.2, and as such, it carries information regarding the long-term memory of the elevations generated by equation 4.2;
- As a consequence of the above, H also characterizes the level of ruggedness or roughness shown by the motion of the output series.

As previously mentioned, the output of the fBm model is a numerical series. This series can be plotted on a bi-dimensional graph to highlight the effect played by changing values of H. As depicted in Figure 4.6, the series produced by fBm visually resemble the motion of a particle on a surface or through a medium. The lines describing such motion also represent a path with a specific degree of roughness that changes with the value of H. The paths shown in Figure 4.4 refer to a discrete integration of equation 4.2 performed in a unidimensional space in which time is represented by the x-axis.

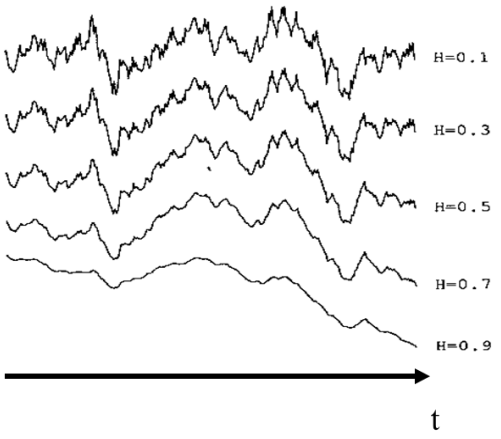

Figure 4.4. Visual representation of the numerical paths produced by the fBm model and of their change in roughness (adapted from Voss, 1985). For H=0.1, the path is highly irregular, with peaks being followed by significantly lower values. This sequence is essentially unaltered by higher values of H, although the peaks become gradually smoother as H increases. For H=0.7, the path almost completely loses its sharpness. For H=0.9, the peaks are so flattened out that the resulting path hardly resembles that with H=0.1. Not only does this chart illustrate the effect of changing values of H on the degree of ruggedness, but it also allows to visualize how H determines the level of correlation between two consecutive values in each series.

When the pointwise integration of equation 4.2 is performed on a bi-dimensional xy-plane, the paths shown in Figure 4.4 are transformed into a surface, which is then known as Brownian surface. In the xy-plane, given two points with coordinates (x_1, y_1) and (x_2, y_2), it is possible to compute their elevation by applying equation 4.2 following Saupe (1988) and Stein (2002). As with the unidimensional case, the roughness of a surface is dictated by the value of H, as shown in Figure 4.5. The Brownian surfaces are referred to as *forgeries* by Voss (1985), since when assigned a proper color bar, they constitute a fictional landscape which resembles a true-life terrain.

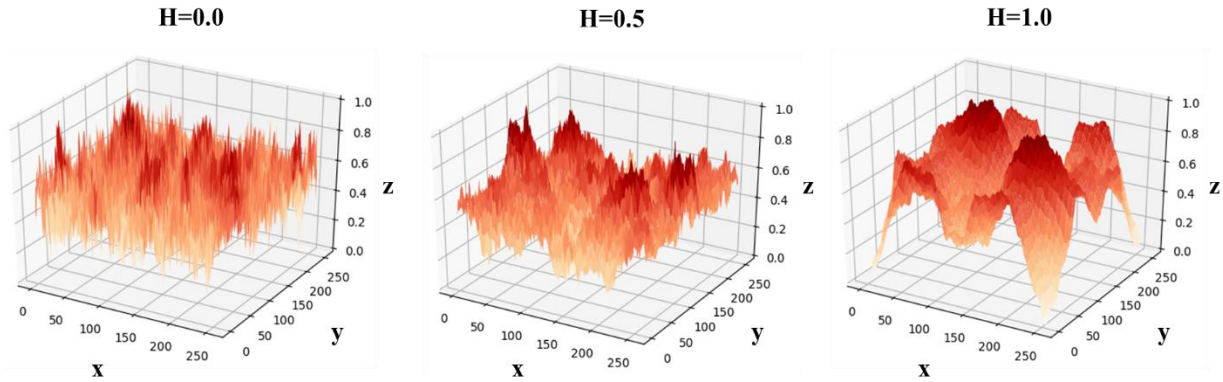

Figure 4.5. Three fractal surfaces obtained with the fBm process following the examples in Kroese and Botev (2013). The image to the left was generated with H=0.0 (D=3.0) and produces a very rough surface. The central image was produced with H=0.5 (D=2.5), and features uncorrelated changes in z. As such, this image is excessively rough to resemble a true-life landscape. The third image was created with H=1.0 (D=2.0) and features a smoother surface. These images were generated with an approximate method. As such, inevitable numerical inaccuracies prevent the image with H=0.0 from being truly 3D, and that with H=1.0 from being truly 2D.

4.2.4 The Spectral Simulation method for recreating Brownian surfaces

The generation of a Brownian surface revolves around implementing a numerical procedure in which equation 4.2 is solved by an automated procedure. According to Dieker (2002), there are numerous approaches available in literature, and it is possible to distinguish between exact methods and approximate methods. Among such methods, it is worth mentioning:

- Exact methods:
  - The Hosking method (Hosking, 1984);
  - The Davies and Harte method (Davies and Harte, 1989);
  - The Cholesky decomposition method (Asmussen, 1999);
  - The Stein method (Stein, 2002);
- Approximate methods:
  - The Random Midpoint Displacement method (Fournier et al., 1982);
  - The Spectral Simulation method (Priestley, 1981; Saupe, 1988);
  - The Wavelet method (Abry et al., 1995);
  - The Aggregating Packet Processes method (Willinger et al., 1997).

To avoid the computational effort associated with exact methods, this research focused on approximate methods, and specifically on deploying the Spectral Simulation method for generating the Brownian surfaces. This procedure was first introduced by Priestley (1981), and its pseudo-code version was provided by Saupe (1988). As pointed out by Dieker (2003), the

Spectral Simulation method (SSm) is widely used in literature and yields a reliable approximation of the fBm process in the spectral or frequency domain. In addition, it is characterized by algorithmic efficiency, requiring limited time and computational resources. While the fBm process is by construction non-stationary, the pseudo-code of the SSm implementation provided by Saupe (1988) produces stationary outcomes (Dieker, 2003). This property is extremely relevant to the generation of synthetic hazards. In fact, the Brownian surfaces are intended to represent the stationary outcome of the manifestation of a natural hazard, implying that after the event has occurred, its severity is time-invariant. The objective of the Spectral Simulation method is to analyze the fBm process, which by construction operates in the time domain, in the spectral or frequency domain (Dieker, 2003). Therefore, this method defines the spectral density function associated with the fBm process, and then adopts the inverse Fast Fourier Transform for reconstructing the spectral signal, as opposed to directly solving its equation.

Given an xy-plane and defined u and v as the variables describing how the frequency changes, respectively, along the x and y directions, the spectral density S is given by:

$$S(u,v) = \frac{1}{(u^2+v^2)^{H+1}} \tag{4.4}$$

According to Saupe (1988), the corresponding bi-dimensional inverse Fast Fourier Transform of equation 4.4, in the discrete form, is given by:

$$X(x,y) = \sum_{k=0}^{N-1} \sum_{l=0}^{N-1} a_{kl} e^{2\pi i(kx+ly)} \tag{4.5}$$

In this equation, N is the resolution of the algorithm, corresponding to the size of the array in which the $X(x,y)$ results are stored, while k and l index the steps in the x and y directions, respectively. The term a_{kl} refers to the Fourier or frequency coefficients used to reconstruct the spectral density signal. As a consequence of equation 4.4, these coefficients are expressed as follows:

$$E(|a_{kl}|^2) \propto \frac{1}{(k^2+l^2)^{H+1}} \tag{4.6}$$

4.2.5 Automated implementation of the Spectral Simulation method

The function described in equation 4.5 was implemented in Python, in order to take advantage of the high flexibility offered by this programming language (Van Rossum, 1995). The choice of Python over other programming languages is also justified by the fact that Python requires less lines of code than alternative options such as C++ or Java (McConnell, 2004). As outlined by Voss (1988), Weisstein (2008), and Smith (2009), higher computational feasibility is achieved when the spatial domain of equation 4.5 is a square grid. In addition, the same authors suggest that the size of grid must be an exact power of two. Accordingly, this research adopted a grid resolution of:

$$N = 2^8 = 256 \tag{4.7}$$

As such, the spatial domain of equation 4.5 is composed of $NxN = 65536$ cells. As evidenced by Saupe (1988), the surfaces resulting from the fBm process in the frequency domain are more and more detailed as the number of Fourier coefficients increases. Specifically, the most accurate and definite surfaces are obtained when the number of coefficients matches the resolution of the spatial domain. Consequently, the number of Fourier coefficients initially used in this thesis was 256. The Brownian surface was obtained by means of two nested Python scripts. The inner script implements the automated computation of equation 4.5 and the Fast Fourier Transform, whereas the outer script calls the previous one to generate the surface with the appropriate parameters (Figure 4.6).

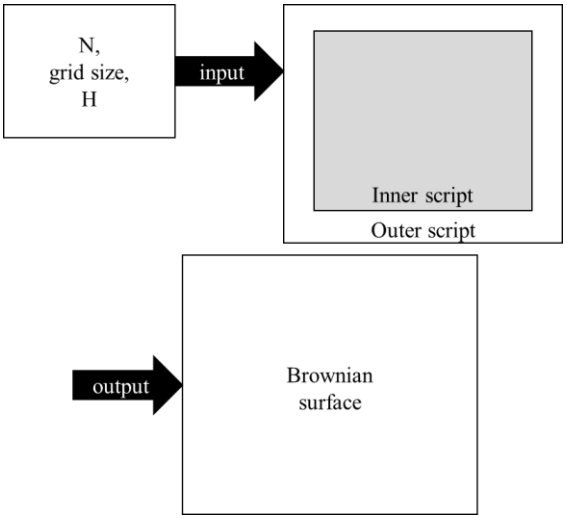

Figure 4.6. The two nested Python scripts and the input values used to generate the Brownian surfaces.

In addition to the mentioned inputs, the outer script also specified the initial standard deviation of the fractal values, which was selected to be $\sigma = 1$ in order to preserve the alignment with Saupe (1988). The outcome of this procedure is visible in Figure 4.9, where one Brownian surface is depicted as a bi-dimensional map. As shown by the color bar, completely white shades suggest absence of hazard loading ($L = 0.0$), while dark red cells denote maximum hazard loading ($L = 1.0$). The shades of red in between these two extremes symbolize values higher than 0.0 and lower than 1.0.

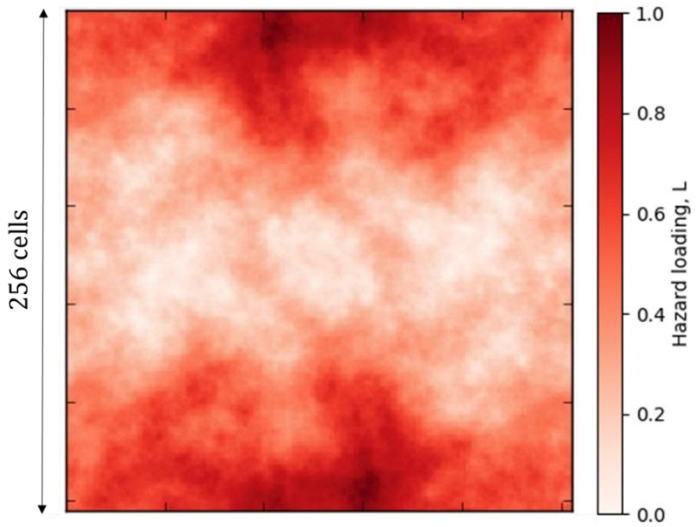

Figure 4.7. This image represents the eye-view of a Brownian surface similar to that described in Figure 4.2. It was obtained with $H = 0.8$ and a resolution of $N = 256$ cells.

The raw output produced by the randomized fractal nature of the surface depicted in Figure 4.7 followed a normal distribution with $\mu = 0$ and $\sigma \approx 1/N$, where N is the resolution (Smith, 2009). The application of equation 4.5 to the outcome of equation 4.2 converted the fractal values from the time domain to the frequency domain by applying the Fast Fourier Transform. This resulted in the fractal values being rescaled to a range $\in$[0.0, 1.0] (Walker, 1991). One discernible feature of the fractals obtained with the numerical recipe provided by Saupe (1988) is periodicity (Smith, 2009). This implies repeated shape patterns that can be easily recognized by the human eye. The presence of such periodicity is a direct consequence of the use of the Fast Fourier Transform. The periodicity is visible in Figure 4.8, where an axis of symmetry overlaps the $y = x$ line.

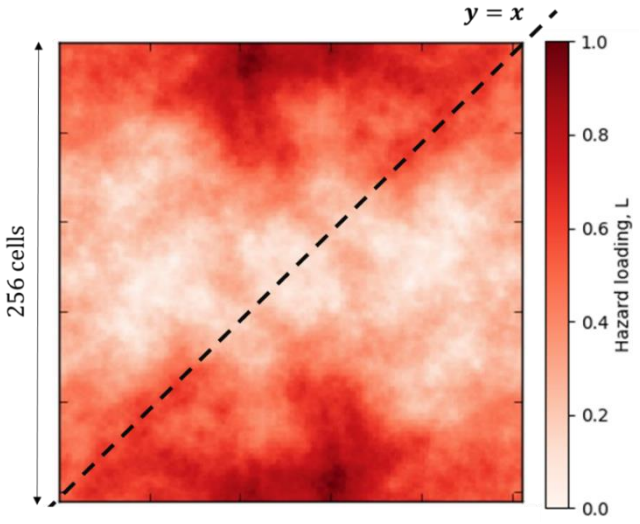

Figure 4.8. Visualization of the periodicity associated with Brownian surfaces. The axis of symmetry is represented by the dashed black line, which also happens to be the $y = x$ line. The repetitiveness of shape patterns is an intrinsic property of the Fast Fourier Transform, which is applied to equation 4.2. This image was produced with H=0.8.

The repetitiveness of certain patterns is not a desired element of this research, because natural hazards are geographically distributed according to a whole host of different drivers. As illustrated by El Morjani et al. (2007), the combination of these drivers hardly results in the repetition of any specific geometric shape. Therefore, periodicity is an undesirable property. The outer script was designed to avoid such property by slicing each fractal into a smaller domain. As highlighted by Smith (2009), the size of this new domain should be half that of the original; however, computational aspects may influence the choice of the final size, especially if the fractals are used as input to demanding downstream analysis. The smaller domain was sliced from the original fractal in such a way as to not intersect the axis of symmetry, thus avoiding repeated patterns, and the fractal boundary, to minimize boundary effects.

In mathematical terms, the Brownian surfaces returned by the Spectral Simulation method are second order stationary random processes, and as such they are also isotropic (Saupe, 1988). This means that the occurrence of peaks and valleys is equally likely anywhere within the domain (Smith, 2009). Focusing on a smaller region, therefore, does not impede capturing the degree of spatial variability offered by the fractal. When the Brownian surfaces are used as spatial hazard generators, the fraction of cells which elevation exceeds a cut-off is a crucial areal descriptor, which corresponds to the spatial extent of the hazard represented by the surface. For the purpose of this research, such extent is defined as the *Critical Footprint* (CF) as it denotes the fraction of footprint that is most likely to cause disruption in an underlying

network. The Critical Footprint is expressed in percentage, and it is sensitive to both the fractal spatial pattern and the cut-off value.

4.2.6 Role of the Hurst exponent in influencing the spatial variability of fractal hazards

The Hurst exponent, denoted by *H*, is the only parameter controlling the fractional Brownian motion, its admissible values ranging from 0.0 to 1.0 (Mandelbrot, 1968). It is a measure of long-term memory originating from the analysis of hydrological time series, and it is also related to their autocorrelations (Hurst, 1951). In the context of fractal geometry, it assumes a spatial significance given its relationship with the fractal dimension *D* (equation 3.3).

From a spatial perspective, the Hurst exponent is a proxy for the spatial correlation of the elevation of two adjacent points on a surface: the range $H < 0.5$ yields a gradual increase in negative correlation as it approaches 0; the value $H = 0.5$ represents uncorrelated elevations; the range $H > 0.5$ is associated with a gradual increase in positive correlation as it approaches 1 (Saupe, 1988).

By changing *H*, it is therefore possible to obtain surfaces with varying degrees of ruggedness, from very rough surfaces, generated with low values of *H*, to very smooth surfaces, generated with high values of *H*. The array $H = [0.6, 0.7, 0.8, 0.9, 1.0]$ was used in this research. It is centered around $H = 0.8$ as it is reported to be the most reliable value for representing natural phenomena (Voss, 1985; Saupe, 1988). More peculiar spatial configurations were reproduced by including relatively extreme values such as $H = 0.6$ and $H = 1.0$. Figure 4.9 illustrates the change in ruggedness induced by the array of *H* values.

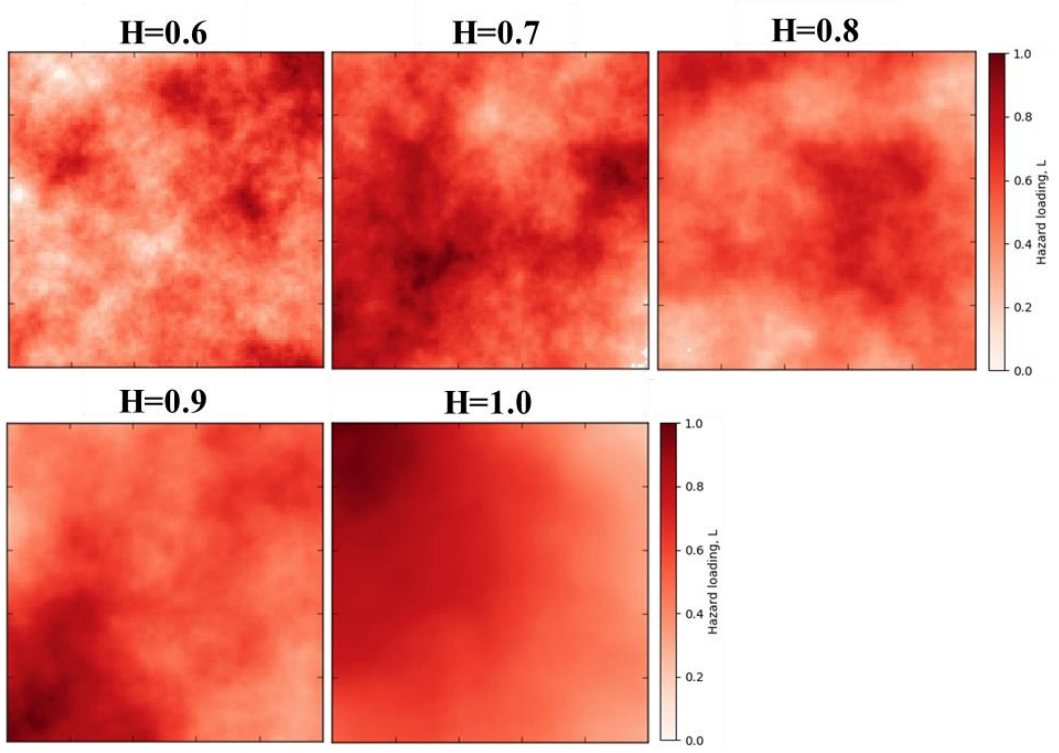

Figure 4.9. Representation of the change in ruggedness in the Brownian surfaces. As H gradually increases, the spatial fragmentation associated with H=0.6 is progressively smoothed out, and more homogeneous surfaces begin to appear. This implies that the loading hotspots (dark red shades) change their behavior as H increases: for lower values of the Hurst exponent, the loading hotspots are scattered across the 2D surface; as H approaches 1, the hotspots gather in one specific region of the 2D surface (the upper left corner in the realization with H=1.0).

4.2.7 Advantages and disadvantages of the fractal approach

In terms of disadvantages and limitations, this fractal approach features a notable degree of randomness due to its isotropy (Saupe, 1988), which can result in unrealistic spatial patterns if compared to real natural hazards. Also, the range of elevation values does not exceed the interval $[0, 1]$, requiring appropriate data transformation in order to accurately describe specific natural hazards. Despite the negative aspects, the reduced computational demand, the possibility to include the surface generation inside a streamlined Monte Carlo simulation flow, and, particularly, the ability to produce surfaces with varying degrees of spatial correlation are the driving factors behind their adoption in this thesis.

4.2.8 Comparing fractal spatial hazards to deterministic spatial hazards

4.2.8.1 Generation of circular-shaped hazards as the most common deterministic example

A substantial body of literature has recently grown up around the topic of *localized attacks* (Berezin et al., 2015; Shao et al., 2015; Yuan et al., 2015) as an alternative to the well-established and extensively studied *random attacks* (Albert et al., 2000; Albert and Barabási, 2002) and *targeted* or *informed attacks* (Tanizawa et al., 2005; Estrada, 2006) to describe how networks fail. Among all deterministic approaches, the idea behind the localized attacks is by far the most commonly used by the literature on spatial hazards. As explained by Berezin et al. (2015), the localized attack randomly selects a node in the network to act as the center of a circle. Then, using a failure radius $r > 0$, the boundary of the circle is drawn, producing a region of failure. All nodes intersected by or inscribed within this region are assumed as failed, creating discontinuity regions or holes within the texture of the affected network (Figure 4.10).

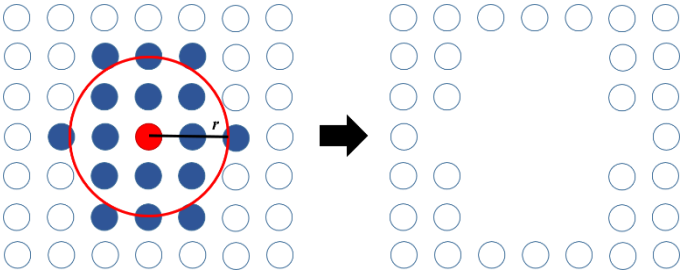

Figure 4.10. Illustration of a *localized attack*. The red node in the left panel is randomly selected to be the center of a circle superimposed to the network texture. In this case, the network is represented by a square lattice in which edges are not shown. Then, a failure radius $r > 0$ is selected to define the size of the circle. All nodes within or crossed by the red circle are assumed as failed. The extent to which the network is affected is dictated by the failure radius and the underlying topology or layout.

To compare the impact of fractal spatial hazards to that of the most prominent of all deterministic approaches, the *localized attacks* were implemented. This was done with a Python script that rasterizes and fills a circle on a mesh grid combining the *Bresenham's Midpoint Circle Generation Algorithm* (Bresenham, 1977) with the *Flood-Fill Algorithm* (Pavlidis, 1979), producing a circle. This script receives as input the size of two nested mesh grids, the radius (an integer number sampled from a discrete uniform distribution, so that all sizes are equally probable to be drawn), and the (x_c, y_c) coordinates for the center of the circle (two integer numbers sampled out of a discrete uniform distribution) (Figure 4.11). The use of two nested mesh grids allows for the truncated circles to be generated. The output is an image of the inner grid with either whole or truncated circles. (Figure 4.11).

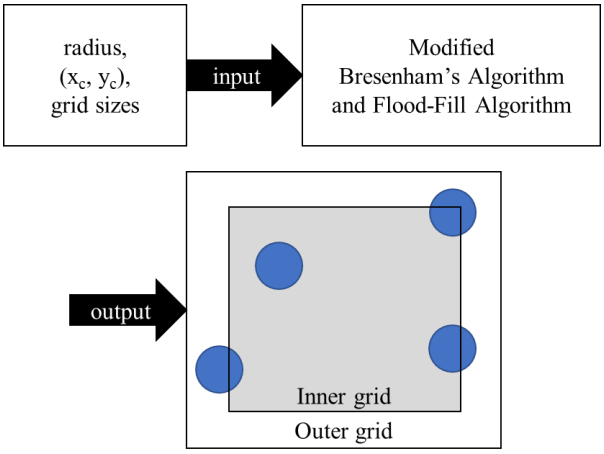

Figure 4.11. Structure of the algorithm producing the localized attacks. The coordinates of the center range from 0 to $Outer\ grid_{size} - radius$ to ensure that the circles entirely fall within the boundaries of the outer grid.

The circles are drawn in two steps. In the first step, the circle is drawn on the grid based on the coordinates of the center and the radius. In the second step, all the cells within the circle are filled. To accomplish the first task, the Bresenham's Midpoint Circle Algorithm takes advantage of the symmetry of a circle, dividing it into 8 octants of 45 degrees each. The goal is to identify a path of adjacent cells or pixels in the lattice so that the equation $x^2 + y^2 = r^2$ is satisfied, resulting in a *rasterized* circle (Figure 4.12). Each cell or pixel is added to the path if $x_{pixel}^2 + y_{pixel}^2 \leq r^2$, provided $x_{pixel}^2 + y_{pixel}^2$ is a maximized sum of integer numbers. The Bresenham's Midpoint Circle Algorithm can be briefly described with the following steps:

- Using integer numbers only, the coordinates of the center and the radius are assigned;
- The algorithm considered the center of the circle as the new origin, shifting the grid origin from its original location to the center of the circle;
- At the beginning, only the first octant is considered, and a curve starting at point $(r, 0)$ is drawn. The drawing proceeds counterclockwise until the angle of 45 degrees is reached;
- While drawing the arc, the algorithm uses a decision variable to determine whether a pixel should be added to the path or not. Given two vertically aligned pixels crossed by the circle, the algorithm decides which pixel is added to the path based on the sum of distances between the centers of the pixels and the arc. The upper pixel is considered only when the sum is ≤0; otherwise, the lower pixel is added to the path;
- The algorithm takes advantage of the four axes of symmetry featured in the circle, so that the coordinates of the pixels in other octants can be referred to the coordinates of

the pixels in the first octant. This results in the circular path being drawn simultaneously across all 8 octants (Figure 4.12);

- The script uses the Bresenham's Midpoint Circle Algorithm to assign 1 to each pixel composing the path.

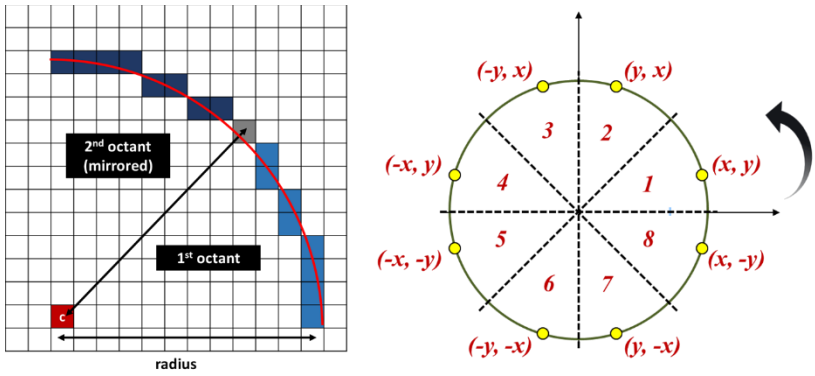

Figure 4.12. On the left, the rasterization of a circle carried out by the Bresenham's Midpoint Circle Algorithm. The algorithm uses the radius to highlight the pixels composing the path across the first octant. The algorithm also uses a decision parameter to determine, for each couple of vertically aligned pixels, which one to include based on the value of the parameter. The lower pixel was added only when the decision parameter was higher than 0; otherwise, when the parameter was ≤0, the upper pixel was added to the path. In the first octant, the algorithm starts drawing a vertical segment since it always takes a step upwards, increasing the y coordinate. The right panel depicts the position of each octant in the circle and the symmetry equations used by the algorithm to refer the coordinates of the pixels in other octants to those in the first octant. This resulted in a simultaneous drawing of the circle across all 8 octants.

The second task consisted of filling the rasterized circle, in such a way that each pixel falling within the circle could be assigned 1. This task was carried out using a simplified version of the *Flood-Fill Algorithm* (Pavlidis, 1979). Each pixel satisfying the equation $x_{pixel}^2 + y_{pixel}^2 < r^2$ and falling within the boundaries of the visualized lattice was assigned 1. Thus, each pixel inside and on the circle was attributed 1, whereas those outside the circle were given 0. The circles generated as such act as generators of spatial hazards. By matching the size of the inner grid to that of the fractal grid, it is possible to compare the two outcomes. The circles may remind of specific realizations of Poisson point processes or clustered point processes, in the likes of the Neyman-Scott Rectangular Pulse (Cowpertwait, 1991; Cowpertwait, 1995; Fowler et al., 2000; Fowler et al., 2004; Burton et al., 2008). The main visual difference is that only one circle is created for each event. At variance from fractals, which can be scattered across the grid, the circles consist of one single, aggregated, and spatially continuous object. As with fractals, the circles feature a hazard loading ranging from 0.0 to 1.0, although no value between 0.0 and 1.0 is present (Figure 4.13).

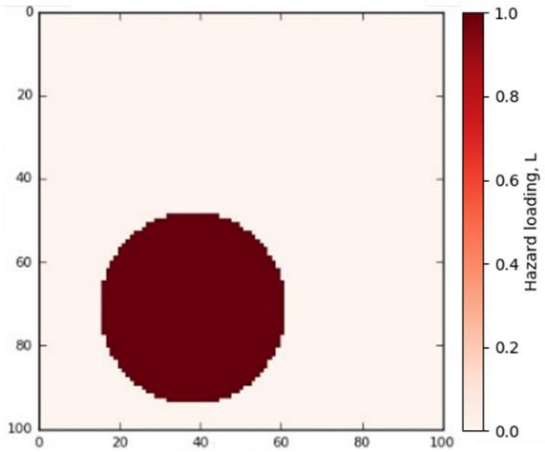

Figure 4.13. One realization of the localized attacks on a 100x100 mesh grid. The circle is entirely located in the inner grid and occupies 16.49% of the cells. As such, the corresponding Critical Footprint is 16.49%.

4.2.8.2 Geometrical difference between circular-shaped and fractal spatial hazards

Given the recurrence of the circle as the most common deterministic shape used in literature to represent natural spatial hazards, this research focused on highlighting the *geometrical difference* between circular-shaped and fBm-generated fractal spatial hazards. In this context, the *geometrical difference* refers to the fact that circles have a characteristic 1D geometric descriptor, namely the diameter, whereas fractals are known for not having a characteristic 1D geometric quantity (e.g., the diameter or an axis). As such, fractals are typically described by the fractal dimension D, which is a fractional measure of how well the pattern fills the space in which it is embedded (Mandelbrot, 1967). Therefore, circles and fractals do not share any geometric dimensions that can be directly compared. This problem was addressed by resorting to the image processing techniques implemented in Python by the *Scikit* package (van der Walt et al., 2014). These techniques were used to generate an ellipse with the same *2nd central moments* as the fractal or the circle, according to the following steps (Figure 4.14a):

1. Generate one circle and one fractal shape with the same area, $A_{disk} = A_{fractal} = A$;
2. Compute the 2nd central moments for both the circle and the fractal;
3. Generate the ellipses with the same moments as those computed, so that each shape has its corresponding ellipse;
4. Compute and compare the lengths of the major axes of the two ellipses, l_{disk} and $l_{fractal}$.

The use of equivalent ellipses was implemented to allow to make a meaningful geometric comparison between the circle and the fBm-generated shape, provided the two original shapes had the same area. The comparison was carried out based on two sets of 10,000 realizations performed over a mesh grid of 50x50 cells, using $H = 0.6$ as a spatial parameter for the fractal shape and the range $\in[3, 50]$ for the radius of the circle. This specific value was selected in order to highlight the differences between the two families of shapes in the worst-case scenario. To favor reproducibility, Figure 4.14b uses a generic object to show the procedure followed to obtain the ellipses and major axes mentioned in Figure 4.14a.

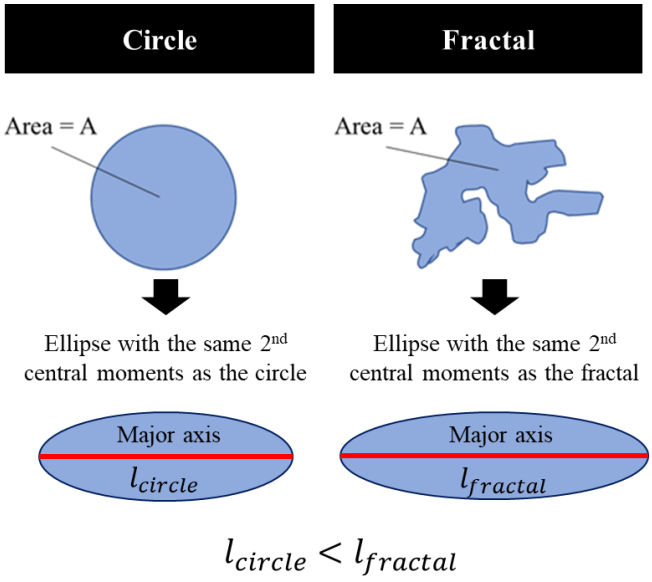

Figure 4.14a. The major axes of the ellipses with the same 2nd central moments as a circle and fractal. The circle and the fractal have the same area (Critical Footprint), however they produce different major axes due to the spatial distribution of the points that compose their surfaces. The major axis of the fractal is longer due to its points being more scattered compared to the circle.

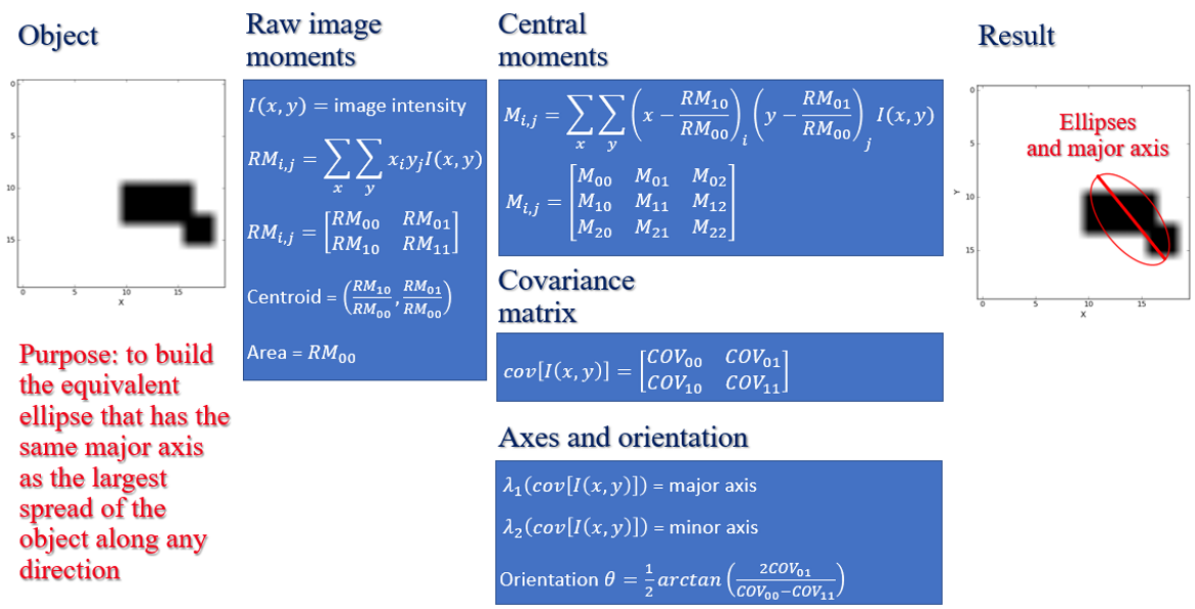

Figure 4.14b. Procedure to obtain the ellipse built on the same 2nd central moments as an object (shown here in black) of a generic shape, as well as the corresponding major axis with its orientation in a 2D plane. These were the steps followed to obtain the two major axes mentioned in Figure 4.14a.

4.3 Stage 2: hierarchies and dependencies

As discussed in paragraph 3.2.3, Case Study 1 was developed to study the response of synthetic infrastructure models to synthetic spatial hazards at the aggregate level. This entails that the perspective adopted did not take into account any hierarchies or dependencies, and the overall robustness to the spatial hazards was determined based on the assumption that the network responded as a self-contained system.

4.4 Stage 3: infrastructure network models

4.4.1 Synthetic models of infrastructure networks

Following Gastner and Newman (2006a; 2006b), four of the most common topologies were implemented as *undirected graphs* or *networks* and used as synthetic infrastructure models. These networks were generated using the dedicated Python package *NetworkX* (Hagberg et al., 2008). Although no reference to specific real-world infrastructures was made, these four models were included to establish a link with the most recurrent topologies found in real-world infrastructures. The implemented topologies include:

1. The Lattice Network (LN);
2. The Scale-Free Network (BA);
3. The Small-World Network (WS);
4. The Random Network (ER).

The Lattice Network (LN) features a highly regular topology with evenly spaced nodes, and it was adopted given its recurrence in grid-iron street layouts and water supply systems (Musa et al., 2009). It resembles a grid with a constant edge length across the entire network, and it is also referred to as the Manhattan Lattice (Beamond et al., 2003) given its resemblance to the street layout of the New York City borough. The Scale-Free Network (BA) is extensively found in real-world infrastructures such as the railway network (Gastner and Newman, 2006b), the airline network (Guimerà et al., 2005), the gas network (Carvalho et al., 2009), as well as the road network (Kalapala et al., 2006). This model features a small number of highly connected nodes known as *hubs*, whereas most of its nodes only have a few connections. The model also features long-range edges. In the context of this research, only the Barabási–Albert

(BA) variation of the Scale-Free Network is adopted, where the topological structure arises from the *growth* and *preferential attachment* algorithm (Albert and Barabási, 2002). The Small-World Network (WS) was adopted based on the WS model proposed by Watts and Strogatz (Watts and Strogatz, 1998), where the path connecting any two nodes in the network is composed of just a few edges or hops. As such, the hubs emerging in this topology have significantly less connections than those emerging in the BA model. Variations of the WS model, largely contaminated by the BA model, can be found in the airline network (Guimerà et al., 2005; Barthélemy, 2011), particularly for airlines operating the point-to-point transport model. Water supply networks follow a closely related scheme when their degree distribution follows the Poisson distribution (Giustolisi et al., 2017). The Random Network (ER) was implemented following the Erdős–Rényi model (Erdős and Rényi, 1959). In ER, an edge connecting two nodes has a certain probability of existing, which is completely independent of the probability associated with other edges. The randomness behind the occurrence of a specific edge puts this model in a different category than the others, due to the apparent lack of a topological criterion and its theoretical nature. This is likely to be the reason why ER models are only used for comparison in infrastructure studies (e.g., Cotilla-Sanchez et al., 2011). Therefore, this research adopted the ER model only for purposes of comparison.

The list of network models used does not include: *i*) hierarchical networks and *ii*) exponential networks. Hierarchical networks are not included in Case Study 1 as the objective was to determine the overall behavior of networks considered without partitions, whereas hierarchical networks do feature partitions. However, hierarchical networks were used in Case Study 2. Exponential networks (Jing-Zhou and Yi-Fa, 2005) were not included in Case Study 1 as they are generated with a variation of the growth and preferential attachment algorithm that also generates BA networks. Also, the small network size would have prevented to see meaningful differences in behavior between exponential and BA networks.

Given that the *NetworkX* functions used to generate the synthetic models rely on a random seed, and that a change in seed produces a change in the spatial distribution of edges (Figure 4.15), an ensemble of realizations was generated using the same seeds for all models. This enabled to extend the results to the entire family of networks. For each synthetic model, 300 different realizations were generated, except for the LN model, where edges are fixed in space. Given the use of resource-intensive metrics, the size of the ensemble was designed to preserve the balance between computational costs and the generalization of results.

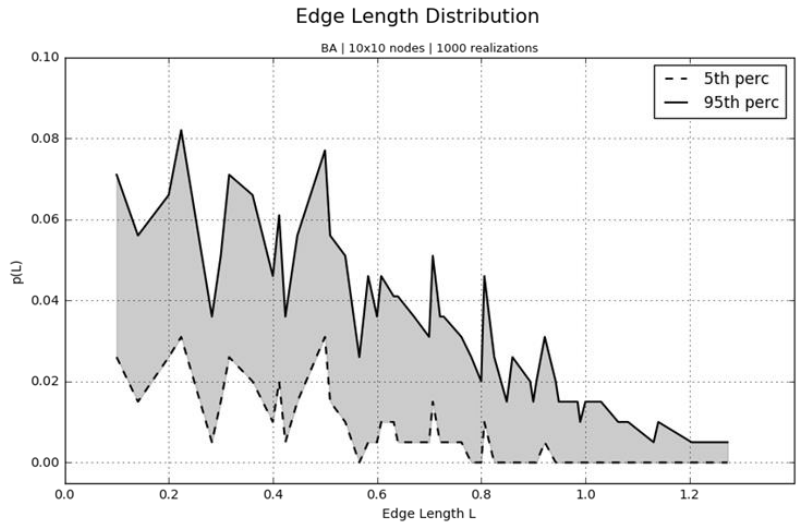

Figure 4.15. Changes in the distribution of edge length in a small-sized BA model using an ensemble of 1,000 realizations. The 5th and 95th percentile boundaries are visible. The length L is normalized with respect to the size of the regular grid hosting the network.

Following Abundo et al. (2014), the synthetic models were generated using a regular grid of 10 by 10 cells, each hosting one individual node. The size of such grid, which dictated the network size, was identified as a compromise between computational costs and accuracy, although improved results might be obtained using larger grids. However, the major constraint to adopting larger grids was the computational cost associated with the CFI metric (see paragraph 4.7.1). The Barabási-Albert algorithm used to generate the BA model, when applied to the 10 by 10 grid, generated networks in which the hubs were always located in the top-left corner of the grid. This is a natural consequence of the growth and preferential attachment processes applied to a grid. To ensure that the BA networks were all comparable to each other, hub locations were not allowed to vary, creating a consistent topological structure. Details regarding the growth and preferential attachment processes can be found in Albert and Barabási (2002).

The total number of nodes for each realization, 100, implies that the networks were always small-sized, and this is a computational advantage. Parameters such as the probability of rewiring for the ER model, the number of initial links for the BA model, and the number of nearest neighbors for the WS model were selected in such a way as to keep the number of edges comparable between the four ensembles of synthetic networks. Figure 4.16 shows single realizations of the four ensembles, whereas Table 4.1 specifies their details. The change in seed in the BA, WS and ER models entails that the spatial distribution of edges was different for each realization.

As shown in Table 4.1, the edge-to-node ratio of the network models varies between 1.8 (LN) and 2.0 (ER). This was driven by the LN model and it was kept as close to 1.8 as possible, the variation being dictated by the topological differences between LN and the other ensembles.

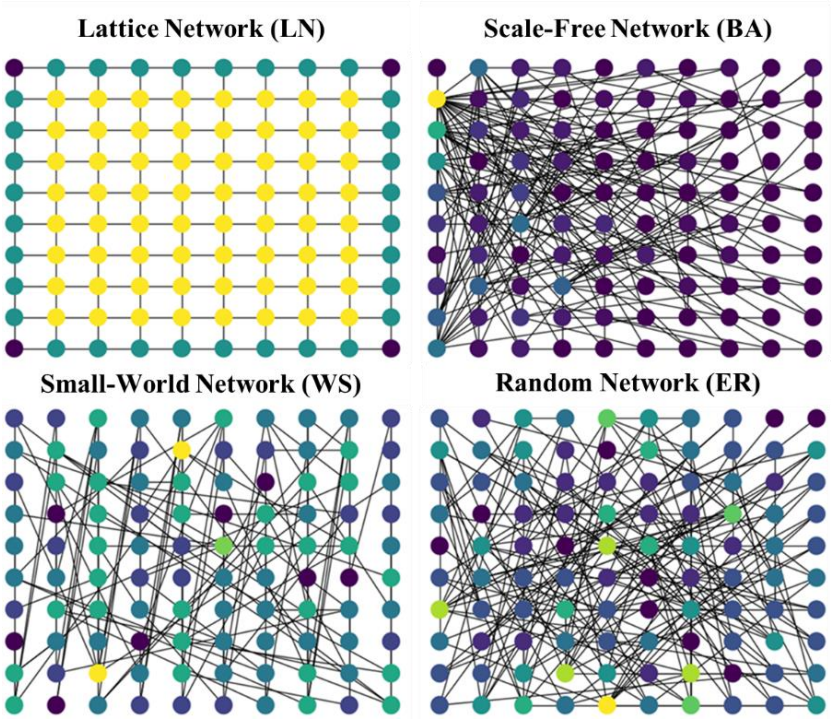

Figure 4.16. Single realizations of the four synthetic network models. The brighter colors indicate a higher degree relatively to each model. In the LN model, the highest degree is always 4. In the other models, it may vary based on the seed used. The BA models always feature hubs with the highest degree, followed by the ER and WS models. The presence of edges shows the underlying topological structure.

Table 4.1. Topological characteristics of the four ensembles of synthetic networks.

	Network model	Nodes	Edges	Edge-to-node ratio	Average degree <k>	Realizations
1	Lattice Network (LN)	100	180	1.80	3.60	1
2	Scale-Free Network (BA)	100	196	1.96	3.92	300
3	Small-World Network (WS)	100	198	1.98	3.96	300
4	Random Network (ER)	100	200	2.00	4.00	300

4.5 Stage 4: propagation of failures

4.5.1 Mechanisms of failure

The mechanisms of 1st and 2nd order failures were implemented using a basic model loosely based on *agent-based models*, following Niazi and Hussain (2009). Agent-based models are computational models revolving around the idea of autonomous entities. These, known as *agents*, collectively define, through their actions and interactions, the status of the system they are part of. Upon analyzing the impact of fractal spatial hazards, the nodes of a network were considered as agents that can take only two statuses, *active* or *failed*, based on whether they had withstood the hazard loading or not. Since the interaction between nodes is dictated by how the edges are distributed across the network, a higher number of edges going in and out of a node signals a higher volume of interactions. This offers the node the natural role of an *agent* capable of influencing the performance of other nodes as a function of how many nodes it is connected to. Agent-based models typically feature a higher number of statuses than the version described here, and find applications in smart grids (Ferreira et al., 2015), air traffic network (Darabi and Mansouri, 2015), and local energy networks (De Durana et al., 2015). Mathematically, the basic agent-based model adopted is a variation of the general definition of resilience of natural and man-made complex systems given in literature (Barzel and Barabási, 2013; Barzel et al., 2015; Gao et al., 2016):

$$\frac{dx_i}{dt} = F(x_i) * \sum_{j=1}^{N} A_{ij} G(x_i, x_j) \tag{4.8}$$

In equation 4.8, the $\frac{dx_i}{dt}$ term refers to the change in status of node i, which can be either *active* or *failed*. The term $F(x_i)$ is the self-dynamics (Gao et al., 2016) of each node, which in this context describes the impact of the fractal spatial hazards on the node itself. The terms under summation, the adjacency matrix A_{ij} and the law governing interactions $G(x_i, x_j)$, jointly define the exchanges occurring between connected neighbors. The summation itself indicates that such exchanges are only taken into account if they involve the connected neighbors of node i. Equation 4.8 was applied in two steps: first, the outcome of $F(x_i)$ was computed for each node; then, when the outcome was *failed*, the computation was stopped and the next node in the network was analyzed; on the contrary, when the outcome was *active*, the summation term

was also processed. To simplify computations, two assumptions were made before applying the agent-based failure model:

1. A one-to-one relationship linked the network nodes to the cells in the hazard fields (Figure 4.17). This was made possible by the non-specificity of the fractal spatial hazards and the network models described in paragraph 4.4.1;
2. The *Failure threshold (Ft)* values previously described were used one at a time and consistently across the entire network.

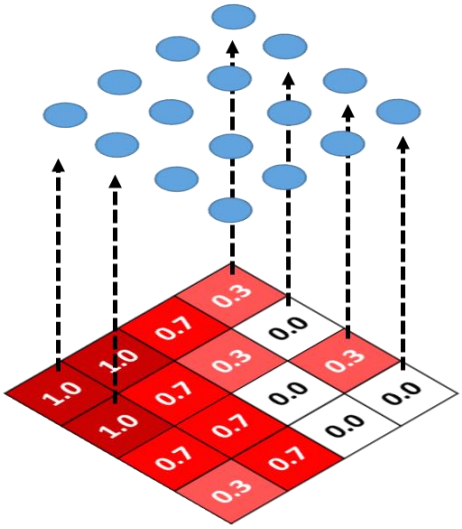

Figure 4.17. Schematic of the 1-to-1 pairing between the cells of the fractal hazard and the nodes in the network. This arrangement follows the idea that each node is hosted by a corresponding cell. As a result, each node only takes as input the hazard loading displayed in the relevant cell.

In order to detect the two failure mechanisms described in paragraph 2.2.4.1, the agent-based model was implemented in two steps (Figure 4.18):

1. The first step detected 1st order failures. The input to each node was compared to the failure threshold in effect: when $hazard\ loading \leq Ft$, the node was considered as *active*; when $hazard\ loading > Ft$, the node was considered as *failed*, and was removed from the network. This step evaluated how the *action* of the hazard loading impacts on the *agents*, and implemented the term $F(x_i)$ of equation (4.8);
2. The second step detected 2nd order failures. The status of all nodes connected to any active node (the *connected subgraph*) was checked, inheriting the output of the first step. The aim was to determine whether an active node was still connected to other active nodes or was the only active one in its original connected subgraph. In the latter

case, the node would be considered as isolated. Any node connected to at least one other active node was left untouched. Any isolated node, although active, was removed from the network under the assumption that isolated nodes cannot interact with other nodes, and as such they act as if they had failed. This step is a rendition of the summation term in equation 4.8 and quantifies how the *interaction* between one node (the agent) and its dependencies influences the performance of the connected subgraph.

Any node retaining an active status after the second step was not subjected to further modelling. As such, the transition from step one to step two is associated with a possible decrease in the number of active nodes. Consequently, the first step can be considered as unstable, whereas the second step is stable, given that no further failures were allowed to occur. The only situation in which the first step is stable is when the hazard loading is severe enough to result in the failure of all nodes. Using networks with different topological arrangements, the two failure mechanisms may have different impacts on the final number of active nodes. According to network theory, in fact, it is the network topology that dictates how and with what probability the nodes are connected, and how extended the edges are (Estrada and Knight, 2015).

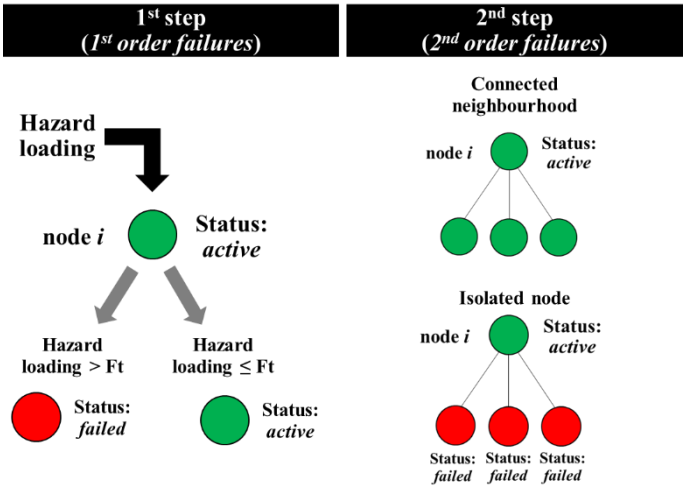

Figure 4.18. The adopted failure model. In the 1st step, the nodes withstand the hazard loading only if the failure threshold exceeds it. In the 2nd step, every connected neighborhood is searched for active nodes. If only one active node is found, it is considered as failed due to isolation.

This failure model did not take into account aspects such as the recovery of nodes. This is because any information on the recovery process is likely to be highly infrastructure-specific, and the infrastructure models adopted in this section were generic. As a result, the response of the models to the fractal spatial hazards are to be seen in the context of the immediate aftermath of the realization of a hazard.

4.6 Stage 5: fragility and propagation of failures

4.6.1 Fragility curves

In order to define how the failures caused by the impact of the fractal spatial hazards percolated to other nodes, a simplified set of fragility curves was adopted, where the failure of a node was not determined based on a probabilistic approach applied to the hazard loading. Instead, the failure was only triggered by the exceedance of a specific threshold called the *Failure threshold (Ft)*. The nodes subjected to a loading greater than *Ft* were considered failed with a probability of 100%, thus resulting in a binary fragility curve (Figure 4.19). Each threshold was used as a proxy for indicating the capability of a node to withstand a fraction of the maximum hazard loading. This simplified approach was adopted to decrease the computational demand, and to match the non-specificity of the fractal spatial hazards and infrastructure models discussed in paragraph 4.4.1. In fact, an accurate analysis of specific infrastructure models requires the adoption of relevant and hazard-specific fragility curves. To take uncertainty into account, multiple thresholds were implemented, covering the range $Ft = [0.1, 0.3, 0.5, 0.7, 0.9]$. These values indicate that a node can progressively withstand 10% of the maximum loading, then 30%, and so forth, up to 90% of the maximum loading. For instance, Ft=0.3 is representative of a weak network, whereas Ft=0.7 describes a strong network.

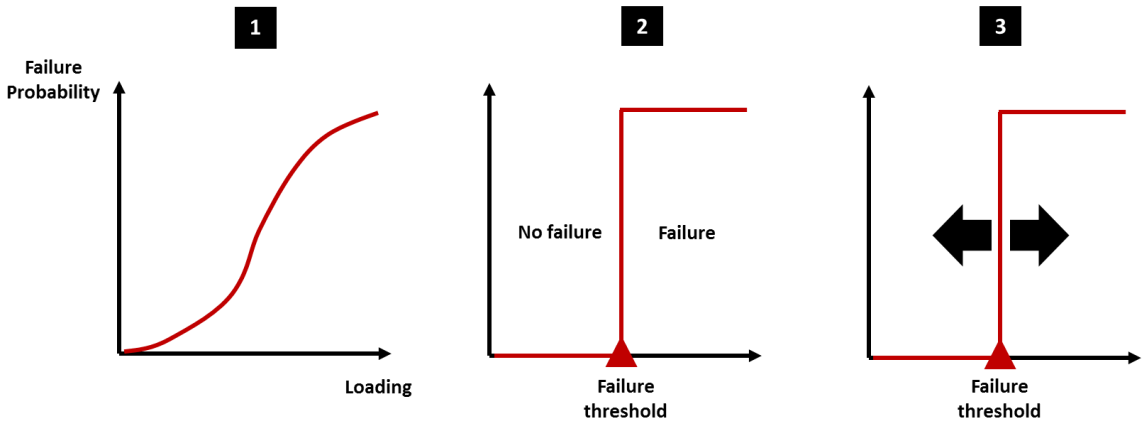

Figure 4.19. Curve 1 represents the typical probabilistic approach of a fragility curve. Curve 2 represents the binary fragility curve. The failure of an element in a system is controlled by the value of the failure threshold: if this value is exceeded, the element is then considered failed with a probability of 100%. If the loading is less than the failure threshold, the element is considered active with a probability of 100%. Curve 3 represents the flexibility given by the adoption of a range of failure thresholds as opposed to a single value.

4.7 Stage 6: systemic indicators

4.7.1 Robustness metrics

To thoroughly capture and describe the effects of the fractal spatial hazards on the synthetic networks described in paragraph 4.1.1, a range of different robustness metrics was used. The reason for adopting multiple indicators is in the need for understanding the behavior of networks from multiple points of view. Adopting only a single metric would have likely offered an incomplete understanding of the dynamics involved. Drawing from the vast amount of network metrics available in literature (Zhu et al., 2011), four measures were implemented. These were either directly based on existing parameters or were adapted to match the purposes of this research. The metrics include:

1. *Number of Surviving Nodes (SN)*;
2. *Spatial Robustness (SR);*
3. *Fragmentation Index (FI);*
4. *Cross-Flow Index (CFI).*

Given a network with N_A nodes in the unperturbed state, the *number of Surviving Nodes (SN)* refers to the number of nodes still active after the perturbed state, which corresponds to the second step of the failure model discussed in paragraph 4.5.1. The SN value is given by:

$$SN = N_A - N'_A = N_A - \sum_{i=1}^{N_A} A'_i \tag{4.9}$$

where N'_A is the total number of nodes failed due to the hazard loading, and A'_i represents the individual failed node. The SN value varies based on the failure threshold in use, the severity of the hazard loading, and the associated spatial pattern (Figure 4.20).

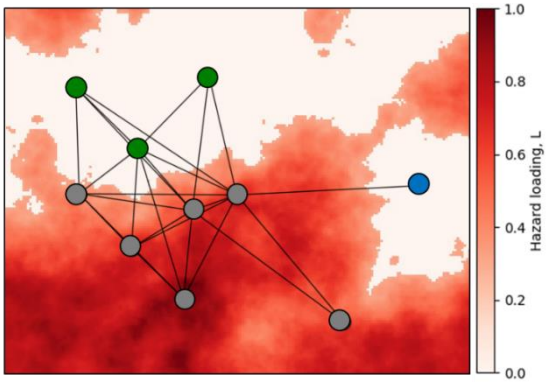

Figure 4.20. Hazard loading obtained with Ft=0.3 and H=0.8. The grey nodes have failed due to 1st order failures, whereas the blue node has failed due to 2nd order failures. As such, the depicted network has SN=3, the three green nodes, with a Critical Footprint of 67.7%. The light shades were obtained by applying an Ft=0.3 cut-off.

Plotting the SN value on the y-axis and the Critical Footprint of each fractal spatial hazard on the x-axis offers insights on the structural robustness of the network, as well as on the difference in responses between the synthetic network models. Simply counting the number of surviving nodes constitutes a quantitative measure of robustness of the network to the hazard loading. This can be seen as a survey conducted after a disrupting event to ascertain the number of elements of an infrastructure that are still functional. It can be argued that, in the face of a disruption that has a spatial component, networks that are able to preserve their nodes are also likely to recover faster, relying on a fraction of functioning assets (McDaniels et al., 2008).

The second metric adopted is the *Spatial Robustness (SR)*, which idea originates from the possibility that different topologies may have a different impact on how far from the footprint the failures occur. As such, the definition of Spatial Robustness is the ability of the network to minimize the failures occurring outside the footprint of the hazard, which happen to correspond to the 2nd order failures (Figure 4.20). This concept has already been investigated by Little (2003) and Robson (2016), although not in conjunction with a more realistic, fractal hazard generator. The adopted formulation of the Spatial Robustness (SR) is:

$$SR = \sum_{i=1}^{Failed_{2nd\ order}} node_{i,failed} \tag{4.10}$$

where the summation adds up all the nodes that failed as a result of the 2nd order failure mechanism, and $node_{i,failed}$ represents each node failed because of that mechanism. The spreading of failures outside the hazard footprint has a potentially fatal impact on the network, in that it can end up disrupting nodes that are not in the proximity of the footprint. A low SR value indicates that the network topology opposes the spreading of failures, and as such, the lack of

robustness of the network receives little to no contribution from the structural configuration. On the other hand, a high SR value implies that the response of the network to the hazard cannot be quantified by just surveying the number of surviving nodes.

In fact, in addition to the fraction of nodes affected by 1st order failures, a further fraction of nodes fails simply because of the unfortunate structural configuration. This means that the effects of the perturbation are compounded by the topology. Another important aspect that helps to understand spatial robustness is the Euclidean distance between 2nd order failures and the edge of the footprint. As an example, the blue node in Figure 4.20 is a 2nd order failure occurring at a certain distance from the boundary of the fractal hazard. Defined as *propagation buffer* (p_b) the distance between the edge of the footprint and the location of the farthest 2nd order failure (Figure 4.21 and equation 4.11), it can be argued that spatially robust topologies are able to constrain the value of such distance, keeping 2nd order failures closer to the footprint.

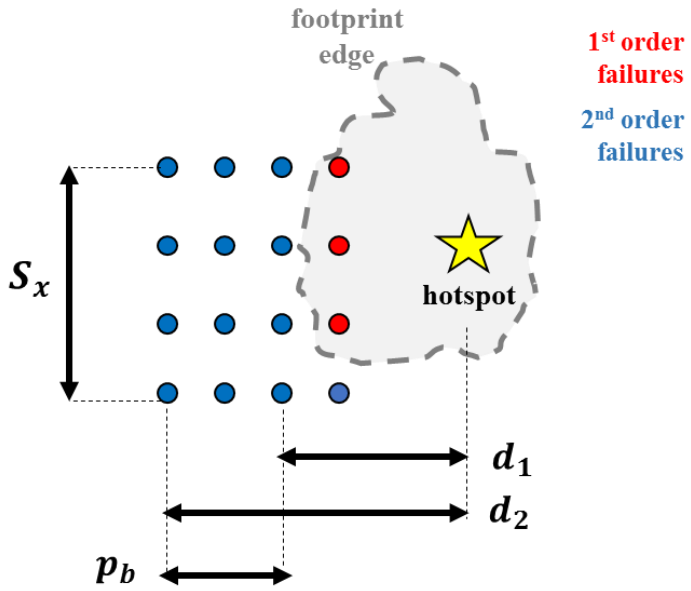

Figure 4.21. Schematization of the propagation buffer p_b given a footprint causing 3 first order failures and 13 second order failures. The hotspot is where the highest values of the footprint are located.

The *propagation buffer* was measured in all four models of synthetic networks by computing the Euclidean distance between the closest and the farthest 2nd order failure from the footprint edge. The terms in Figure 4.21 are defined according to equations 4.11, 4.12, and 4.13:

$$p_b = d_2 - d_1 \tag{4.11}$$

$$d_1 = \frac{1}{S_x}\sqrt{(x_{2c} - x_h)^2 + (y_{2c} - y_h)^2} \tag{4.12}$$

$$d_2 = \frac{1}{S_x}\sqrt{\left(x_{2f} - x_h\right)^2 + \left(y_{2f} - y_h\right)^2} \tag{4.13}$$

where S_x represents the size of the mesh grid (for the purpose of this work, $S_x = 10$), $(x_{h,}y_h)$ the coordinates of the hazard hotspot, and $(x_{2c,}y_{2c})$ and $(x_{2f,}y_{2f})$ the coordinates of the closest and farthest 2nd order failures measured from the hotspot. High values of p_b identify deeper propagation of failures into the network topology, meaning that the impact of the hazard is not only *local* (1st order failures), reaching a more extended domain. The values of p_b, d_1, and d_2 are computed for each network realizations and hazard surfaces to obtain a value representative of each configuration.

The third metric used draws inspiration from the concept of *fragmentation*: as a result of the failures caused by a specific hazard loading, the texture of a network *A* may be modified to the point that it is partitioned into clusters of active nodes, or subgraphs, separated by gaps (Figure 4.22). The largest of these clusters is known in literature as the *giant component*. The resulting clusters are referred to as *connected components*. By counting the number of components or partitions, the *Fragmentation Index (FI)* provided insights on the proneness of each synthetic network model to being fragmented:

$$FI = \sum_{i=1}^{N_{comp}} comp_i(A) \tag{4.14}$$

where the N_{comp} term refers to the total number of partitions appearing in the perturbed network A, whereas $comp_i$ is the individual connected component. The FI value is influenced by the topology in use, the adopted failure threshold, and the severity, spatial extent and spatial pattern of the hazard loading. By plotting the FI value on the y-axis and the Critical Footprint on the x-axis, the effects of progressively larger fractal hazards on the integrity of the synthetic network models were highlighted. From the point of view of infrastructures, the proneness to fragmentation can be interpreted either positively or negatively. In the case of heavily centralized infrastructures, such as high-voltage electricity distribution systems, a high FI value is negatively interpreted. These systems are in fact designed to operate under the control of a

central entity, such as a generation plant. A fragmented texture may imply that it is no longer possible to guarantee the service, since not all partitions can be accessed from the central entity. The same FI value may not have such a dramatic impact on microgrids or water distribution systems (Hines et al., 2015), as these are fragmented by design.

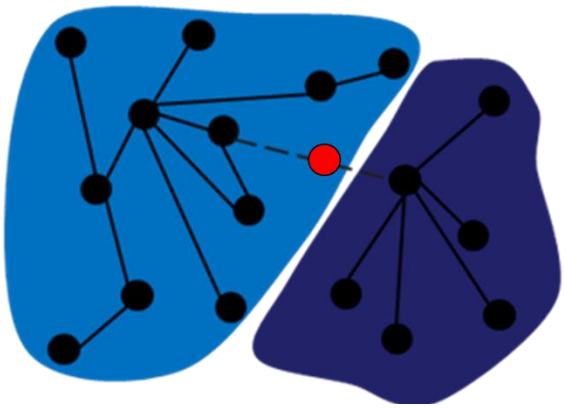

Figure 4.22. Schematization of the fragmentation of a network. The system is partitioned into two components as a result of the failure of the red node. In this case, the resulting fragmentation index is FI=2.

The fourth and last metric adopted in Case Study 1 of this thesis was the *Cross-Flow Index* (CFI). This indicator was developed to compensate for the fact that flow is not explicitly modelled in the study of the fractal spatial hazards. In fact, the network models discussed in paragraph 4.1.1 are intended to be generic, without any specific reference to the exact type of service that they deliver nor to any specific real-world infrastructure. The computation of the CFI provided a theoretical estimate of the amount of flow each node can handle based on its location in the network. Such estimate was computed in the form of a ratio between the amount of flow theoretically processed by each node in the network in presence of the hazard loading (*perturbed state*) and the equivalent quantity in absence of the hazard loading (*unperturbed state*).

This specific formulation allowed to monitor the change in the amount of flow going from the unperturbed to the perturbed state, in such a way as to quantify the reduction experienced by each node. To accomplish this task, the computation relies on a centrality measure known in literature as *Stress Centrality* (SC) (Brandes, 2008). Stress Centrality is an absolute measure of the amount of *stress* each node is subjected to when the network is operating, the term *stress* referring to the number of operations carried out by each node. In a network providing a service, such operations could include the loading and unloading of cargo or passengers at a railway station, the volume of water received by a regulation basin and then passed on to the pipe network for delivery, or the number of watts an electrical substation

processes and delivers to the power grid at any given time. For each pair of nodes (n, j), and given all the possible shortest paths between them, Stress Centrality determines how many of these paths or geodesics pass through each node v lying between node n and node j (Figure 4.23). The formulation of the Stress Centrality is defined as follows:

$$SC(v) = \sum_{n \neq v \in V} \sum_{j \neq v \in V} \sigma_{nj}(v) \tag{4.15}$$

where v represents any node located between nodes n and j, V is the set of all vertices or nodes in the network, and $\sigma_{nj}(v)$ denotes the number of shortest paths or geodesics containing vertex v. A high value of $SC(v)$ implies that node v is central to the operations performed by the network, whereas a low value indicates that node v is rather peripheral. In absence of failures (e.g., in the unperturbed state), assuming that the network is operating at full capacity and that no additional flow can be handled, the stress faced by each node also corresponds to the maximum stress admissible. In the perturbed state, given the occurrence of node failures, the number of shortest paths passing through node v is reduced, resulting in such node handling less flow than usual. The *Cross-Flow Index (CFI)* refers to the ratio between perturbed Stress Centrality and unperturbed Stress Centrality for each node:

$$CFI = \frac{1}{SN} \sum_{v} \frac{SC(v)_{perturbed}}{SC(v)_{unperturbed}} \tag{4.16}$$

where the CFI value was averaged over the number of surviving nodes SN to obtain a single indicator to gauge the overall performance of the network. The CFI values span the range $\in [0, 1]$: a null CFI implied that no flow could be handled by the network, a status typical of completely failed networks. In the case of an individual node, the absence of a shortest path passing through it entailed that the beginning and terminus of that path were failed nodes. The absence of all shortest paths previously passing through that node entailed that all beginnings and terminuses were failed nodes. Therefore, the node in question was isolated, and as per the adopted agent-based failure model, it was considered as failed.

When $CFI = 1$, the network could handle the maximum flow admissible. As well as measuring the overall performance of the network, this metric allowed to evaluate the change in Stress Centrality for each node, with lower values denoting a more conspicuous change. Additionally, the computation of CFI allowed to determine how the impact of a fractal spatial hazard influenced the theoretical amount of flow processed by the most highly connected hub

in each one of the network models in Table 4.1. This computation was performed by determining the Euclidean distance d_{hh} from the footprint hotspot to the most highly-connected hub of each network model:

$$d_{hh} = \frac{\sqrt{(x_{hub} - x_h)^2 + (y_{hub} - y_h)^2}}{S_x} \tag{4.17}$$

where $(x_{hub,}y_{hub})$ and $(x_{h,}y_h)$ are the coordinates of the most highly-connected hub and the hazard hotspot, respectively. As with equation 4.11, S_x is the size of the mesh grid.

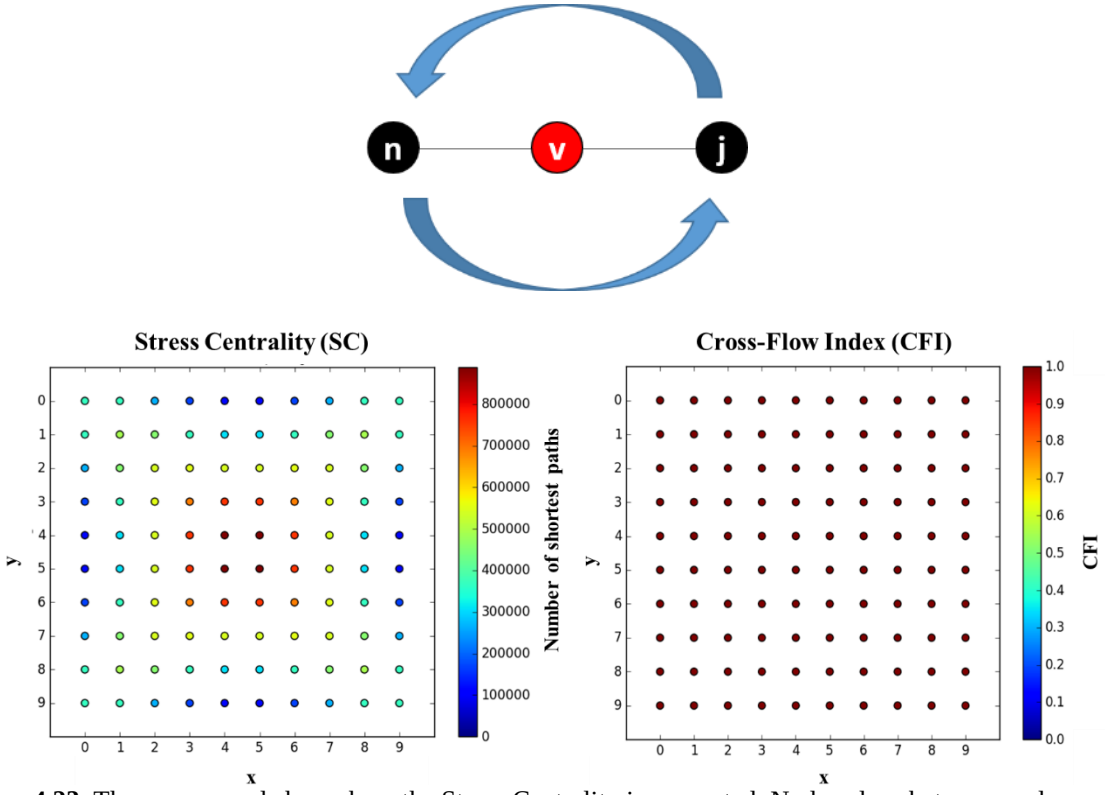

Figure 4.23. The upper panel shows how the Stress Centrality is computed. Node v lays between nodes n and j, and given the existence of two shortest paths connecting them, $SC(v) = 2$. In the lower image to the left, the distribution of Stress Centrality in a $10x10$ Lattice Network in the unperturbed state. The four nodes in dark red, being the most central, are traversed by the highest number of shortest paths (upwards of 800,000), implying that their role is pivotal in the functioning of the network. Nodes on the boundaries and away from the corners are shown to have the lowest values of Stress Centrality, as they are traversed by less shortest paths (around 100,000). The image to the lower right shows how CFI is distributed in the unperturbed situation for the same Lattice Network. This image shows the presence of a unique value (1.0) across the network: it is meant to show that each node, in the unperturbed state, handles the maximum flow allowed based on its location in the network.

In terms of computational demand, the four metrics offered different performances. Given a network A with N_A nodes and V_A edges, the computational demand of each metric was given by the *Time Complexity* of the algorithm used to compute it. The Time Complexity of an algorithm is defined in Computer Science as the amount of time required to execute the algorithm as a function of the size of the input (Sipser, 2012). In the case of the synthetic networks, the input was the number of nodes, N_A, and the number of edges, V_A.

The Time Complexity is a purely theoretical estimation. Instead of being expressed in seconds, which would be misleading because the actual time required to perform a computation varies based on the machine in use, it is expressed in terms of *Big O Notation*. This represents an estimation based on higher-order terms only. For instance, finding the maximum value in an array involves a Time Complexity of $T(n) = O(n)$, where n is the number of elements in the array that need to be analyzed. On the other hand, performing an element-to-element comparison using two arrays of n elements has a Time Complexity of $T(n) = O(n^2)$, as it involves iterating over both arrays. A useful rule of thumb to determine Time Complexity is that the exponent of n equals the number of *for loops* used by the algorithm.

As such, algorithms that run in polynomial time are among the most demanding, even more so as the exponent increases. Table 4.2 shows the Time Complexity associated with the four metrics, as well as their range of values. The Cross-Flow Index was by far the most demanding to compute, whereas the other metrics shared the same computational cost. With respect to the values taken by each metric, it should be noted that: i) $SN = N_A$ was an upper bound imposed by the number of nodes in a network; ii) $SR = N_A - 1$ was dictated by the fact that it is not possible to have any 2nd order failures without at least one 1st order failure; iii) $FI = 1$ means that in the unperturbed state the network was composed by a unique partition, whereas $FI = N_{comp}(A)$ is an upper bound that changes with the topology, as it is not possible to define *a priori* the maximum admissible number of partitions; iv) $CFI = 0$ entailed a completely failed network, whereas $CFI = 1$ implied absence of failures.

Table 4.2. Meaning, Time Complexity, and range of values of the robustness metrics adopted.

Metric	Meaning	Time Complexity	Range of values
Number of Surviving Nodes (SN)	Nodes that have survived 1st and 2nd order failures	$O(N_A)$	$0 \leq SN \leq N_A$
Spatial Robustness (SR)	Number of 2nd order failures	$O(N_A)$	$0 \leq SR \leq N_A - 1$
Fragmentation Index (FI)	Number of partitions	$O(N_A)$	$1 \leq FI \leq N_{comp}(A)$
Cross-Flow Index (CFI)	Ratio between perturbed and unperturbed Stress Centrality	$O({N_A}^3)$	$0 \leq CFI \leq 1$

4.7.2 Difference in impact between circular-shaped and fractal spatial hazards

The main visual difference between the circular-shaped and the fractal spatial hazards is that, in the first case, the hazard loading L is concentrated in a smaller and regular region, whereas in the second case it is spread out irregularly (Figure 4.24). Objective of this Case Study was also to investigate any *causal differences* existing between circular-shaped hazards, modelled according to the procedure in paragraph 4.2.8.1, and fBm-generated fractal surfaces *of the same area*. In this context, the causal difference represents the difference in impact of the two hazard shapes on an underlying infrastructure network. With reference to the robustness metrics introduced in paragraph 4.7.1, the difference in impact was evaluated by superimposing the two sets of 10,000 spatial hazards each (first the circles, and then the fractals) on a BA Scale-Free Network with $N_A = 2{,}500$ evenly spaced nodes and plotting the SN value against the binned Critical Footprint. The choice for this specific network model is in the frequency with which scale-free properties are observed in real-world infrastructure networks (Guimerà et al., 2005; Gastner and Newman, 2006b; Kalapala et al., 2006; Carvalho et al., 2009). This procedure was set up in such a way as to gauge whether two spatial hazards of the same area, but of different origin, produced the same number of failed nodes on the same network model. The objective was to ultimately test if the difference between circular-shaped and fractal spatial hazards is only visual or geometrical (Figure 4.24), or if there is also a functional component that makes fractals more detrimental than circles.

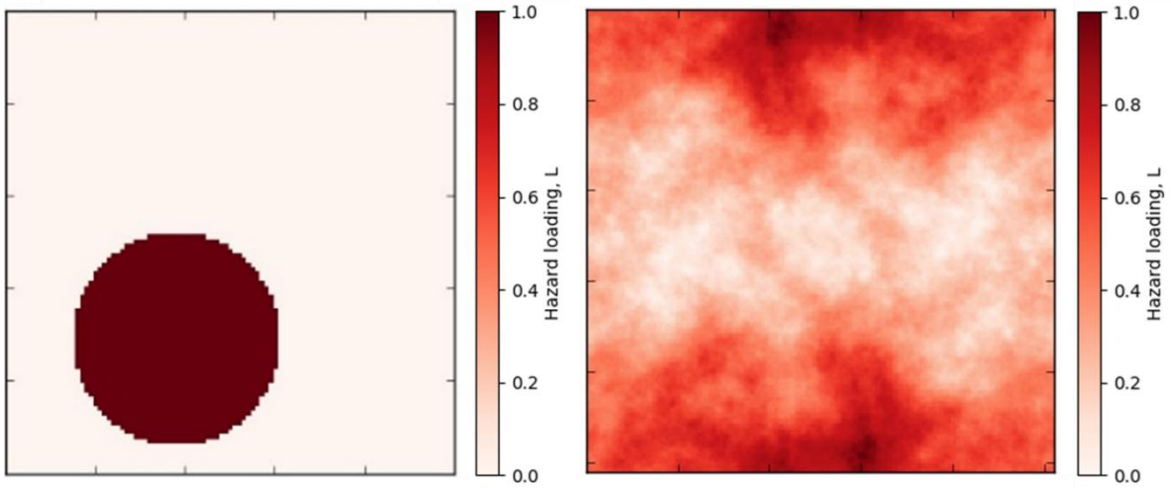

Figure 4.24. Visual comparison of a circular-shaped hazard (left) obtained with the procedure described in paragraph 3.2.5, and a fractal spatial hazard generated with the fBm model described in paragraph 3.2.4. Although the two shapes do not have the same area and are only shown for purposes of comparison, two distinct spatial patterns are observable.

4.8 Computational implications of Case Study 1

4.8.1 An automated Monte Carlo approach

From a computational point of view, the impact of fractal spatial hazards on synthetic network models was evaluated by following an automated Monte Carlo procedure implemented in Python. The computational architecture is composed of four blocks, each of which is performed by a dedicated script (Figure 4.25). The automation was implemented by running the scripts in loop, following the order in Figure 4.26.

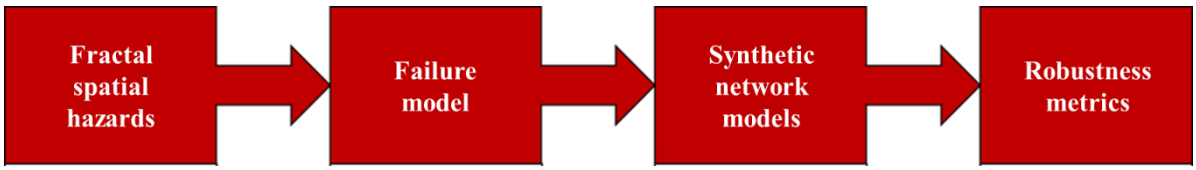

Figure 4.25. The four blocks of the Monte Carlo approach implemented in Case Study 1.

Capitalizing on the use of a range of values for both the Hurst exponent *H* and the failure threshold *Ft*, 25 combinations of values $C = (H, Ft)$ were identified. The adoption of a specific *Ft* value implied that the spatial pattern generated by the Brownian surface was modified, as visible in Figure 4.20. In fact, any grid cell where the hazard loading (or elevation) was $L \leq Ft$ was recast as $L = 0$ (Figure 4.27). This was done under the assumption that when the hazard loading did not exceed the threshold, no failures could occur. Table 4.3 shows the specific values associated with each combination $C = (H, Ft)$. The values of each robustness metric were aggregated and analyzed for each individual combination.

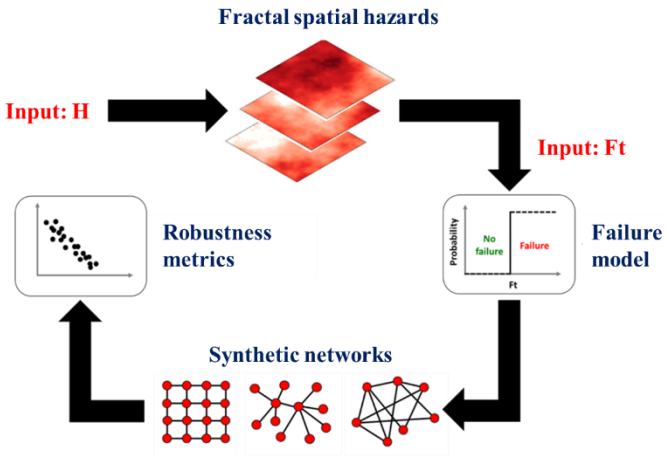

Figure 4.26. Schematic of the flow chart discussed in Figure 3.25. This process represents an open loop where the input values of the Hurst exponent (H) and the node failure threshold (Ft) govern the entire flow. The Monte Carlo approach was implemented producing large numbers of simulations, and the results were aggregated based on the combination $C = (H, Ft)$.

Table 4.3. The 25 combinations $C = (H, Ft)$ and their values in progressive order.

C	*H*	*Ft*	*C*	*H*	*Ft*	*C*	*H*	*Ft*	*C*	*H*	*Ft*	*C*	*H*	*Ft*
1	0.6	0.1	**6**	0.7	0.1	**11**	0.8	0.1	**16**	0.9	0.1	**21**	1.0	0.1
2	0.6	0.3	**7**	0.7	0.3	**12**	0.8	0.3	**17**	0.9	0.3	**22**	1.0	0.3
3	0.6	0.5	**8**	0.7	0.5	**13**	0.8	0.5	**18**	0.9	0.5	**23**	1.0	0.5
4	0.6	0.7	**9**	0.7	0.7	**14**	0.8	0.7	**19**	0.9	0.7	**24**	1.0	0.7
5	0.6	0.9	**10**	0.7	0.9	**15**	0.8	0.9	**20**	0.9	0.9	**25**	1.0	0.9

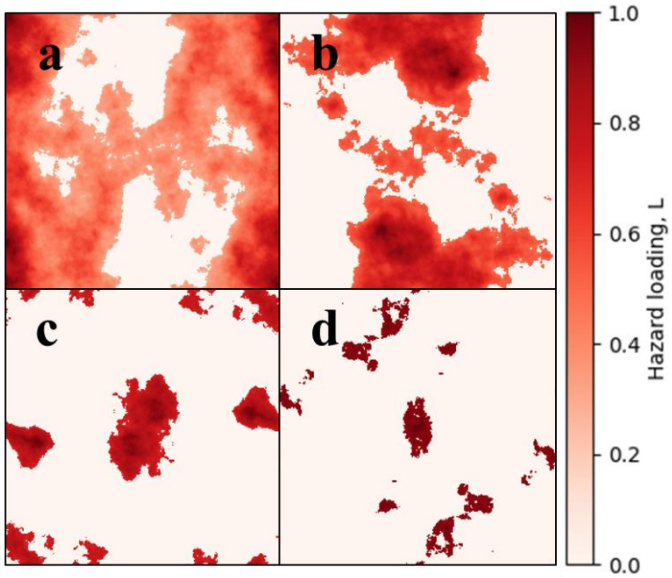

Figure 4.27. Representation of the fractal footprints after the failure threshold is applied to different fractals obtained with *H*=0.8. (a) *Ft*=0.3, (b) *Ft*=0.5, (c) *Ft*=0.7, (d) *Ft*=0.9. The increase in Ft produces an increase in the light shades, for which *L=0*.

4.8.2 Calibration of the automated Monte Carlo procedure

The flow chart in Figure 4.26 was subjected to a calibration test to determine:

- The optimal number of runs required for each combination $C = (H, Ft)$;
- The optimal number of nodes composing the synthetic network models.

The test was performed on a Lattice Network of $100x100$ nodes and consisted of executing the flowchart in Figure 4.26 using specific $C = (H, Ft)$ combinations with a number of runs between 50 and 1,500. The test was conceived to compute the frequency of complete failures (e.g., when 100% of nodes have failed, which is equivalent to $SN = 0$) associated with each number of runs. For each $C = (H, Ft)$ combination and number of runs, the frequency of complete failures was plotted, together with its 3-point Sample Moving Average (SMA) and the percent error between the two (equation 4.18). The number of runs was considered optimal only when the percent error was <5% (Figure 4.28). The formulation used for the percent error was:

$$Error_{\%} = \frac{100}{freq_{SMA}} * \sqrt{\frac{\sum(freq_{measured} - freq_{SMA})^2}{3}} \tag{4.18}$$

where $freq_{measured}$ refers to the frequency of complete failures computed for each number of runs between 50 and 1,500. The term $freq_{SMA}$ represents the 3-point SMA, which was computed every three frequencies. The numerator under the radical sign is the sum of squares, and it is divided by 3 in order to take into account the number of values needed to compute the SMA. This procedure was applied to all five combinations with $Ft = 0.1$ since higher failure thresholds would have yielded gradually lower failure frequencies, which in turn would have resulted in magnified error percentages due to the latter being an absolute measure. The calibration test returned an optimal number of runs of around 1,000 for each combination. However, to increase the statistical power of the automated Monte Carlo procedure, the number of runs for each combination was set at 2,000. As such, the impact of fractal spatial hazards on synthetic networks was evaluated using a total number of 50,000 fBm-generated surfaces for each network model.

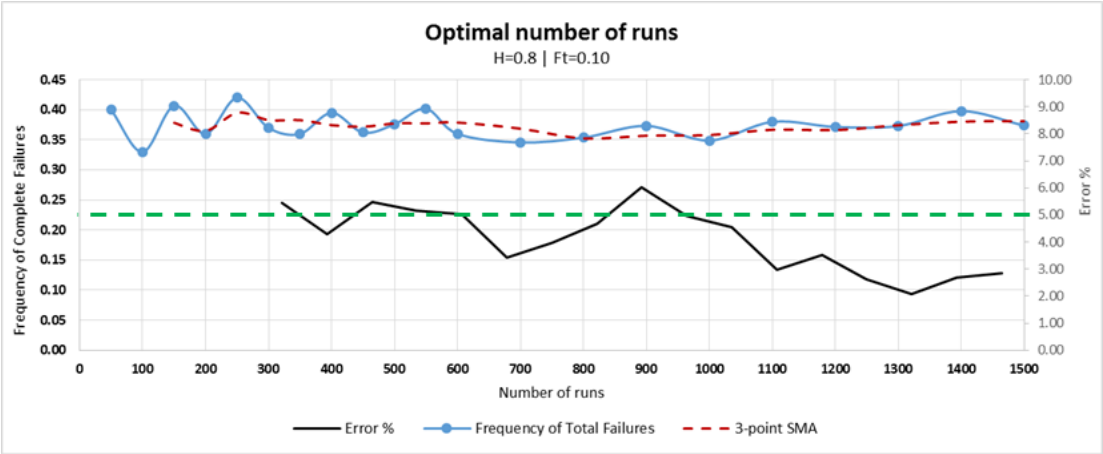

Figure 4.28. Chart showing the frequency of complete failures, its 3-point Sample Moving Average (SMA), and the percent error as defined in equation 3.17. The dashed green line represents the 5% error.

The optimal number of nodes in each synthetic network was defined based on computational considerations involving the actual number of runs performed and the Time Complexity of the four robustness metrics (Table 4.2). The limiting factor of assigning an appropriate size for the network models was the Cross-Flow Index. Its computation was performed in $O({N_A}^3)$ time, where N_A is the number of nodes in a network A. As such, any slight increase in N_A would have yielded a cubic increase in the runtime. Consequently, the optimal number of nodes was set at $N_A = 100$.

Given the requirement of the failure model to operate with a 1-to-1 relationship between the nodes and the grid cells in the fractal surface, the nodes were placed on a regular $10x10$ grid (Abundo et al., 2014). This ultimately influenced the size of the Brownian surfaces that were used to model the fractal hazards: the smaller domain mentioned in paragraph 4.2.5 was in fact assigned a dimension of $10x10$ grid cells, matching the dimension of the synthetic network models. Considerations regarding the limitations induced by this dimension are given in paragraph 4.9.

4.9 Limitations of Case Study 1

The methodology presented in Chapter 4 is characterized by three major limitations. The first limitation pertains the size of network models, as described in paragraph 4.4.1. The extent of these models is 10x10 nodes, which entails that small networks were used. As a consequence, given the 1-to-1 pairing between nodes and cells of the fractal surfaces, the Brownian surfaces were also sized accordingly. The reason for these restrictions is the resource-intensive calculation of the Cross-Flow Index metric, which requires computational resources that grow with a rate of $O(N^3)$, where N is the number of nodes in the network. To overcome this obstacle, different computational strategies may be adopted, such as parallel computing or multi-threading.

Another limitation is the fact that only node failures were modelled in Case Study 1, and not edge or link failures. This is a misrepresentation of reality, in that water supply systems and electricity networks may experience failures in pipes and cables as well, which represent edges, and not just at junctions or pylons. However, modelling the failure of edges was found to be in contrast with the 1-to-1 pairing discussed above. Nevertheless, edge failure could have been implemented by assigning a weight to each edge based on how often the corresponding start and end node were found to have failed in the simulations, which could have modified the final Cross-Flow Index values obtained.

An additional source of limitation is the fact that the failure propagation mechanism described in paragraph 4.5.1 did not consider that nodes within a network may have different failure thresholds, owing to a number of factors such as location, age, material, possible increased or decreased exposure, material fatigue, and so forth. The adoption of a unique threshold for all networks is a simplification which may be eliminated by assigning thresholds that vary with the degree of a node, in order to reflect its importance.

Although the limitations discussed in this paragraph constitute a source of uncertainty, they do not detract significantly from the final results shown in Chapter 6. Moreover, they represent details that can be improved in future iterations of this work.

Chapter 5. Case Study 2: Methodology

5.1 Rationale for adopting a system-of-systems approach

Case Study 2 of this thesis analyzed the response of a two-tier electricity network to wind gusts. As opposed to the macro-systemic approach followed in Case Study 1, the focus was placed on a real-world infrastructure system that operates by means of interactions between its internal sub-systems. Because of the ubiquitous presence of systems-of-systems in real world infrastructures (Yerra and Levinson, 2005; Svendsen and Wolthusen, 2007; Bagler, 2008; Robson, 2016), the analysis was shaped in such a way as to model these interactions and take into account the *emergent behavior* discussed in paragraph 4.1, rather than deriving how the system behaved as a whole. More specifically, the emergent behavior is here intended to represent the ensemble of top-down interactions that characterize the network operations. This approach is in line with the study on structural and dynamic complexity of infrastructures by Brady and Davies (2014), which highlighted the fact that adopting a system-of-systems perspective entails considering the *functional hierarchies* that describe infrastructure operations. With respect to the targeted electricity infrastructure, the functional hierarchies were modelled as *dependencies* (Figure 5.1), according to the top-down direction – from a higher voltage to a lower voltage – of the flow of electricity. Not only is this structural scheme found in electricity networks, but it is also shared by many other civil engineering infrastructures, including water supply systems, gas networks, and transport networks. The adoption of a system-of-systems perspective enabled to identify the response of each sub-system to the climatic hazard, also pinpointing the most vulnerable components.

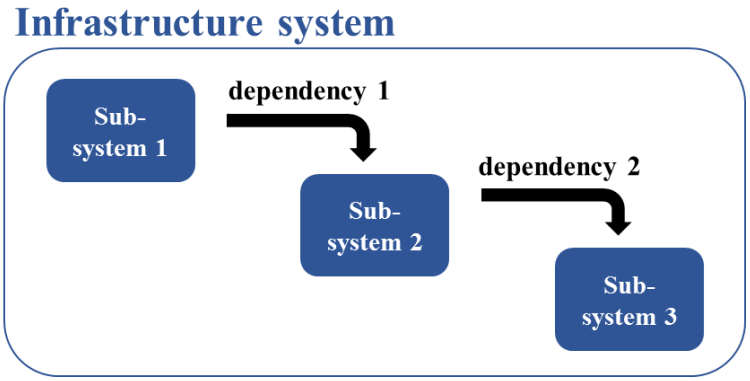

Figure 5.1. The infrastructure system depicted as a system-of-systems, where the internal interactions occur due to dependencies.

5.2 Stage 1: high winds as real-world natural spatial hazards

5.2.1 Rationale for adopting high winds

The choice of high winds as a real-world natural spatial hazard was driven by the adoption of the electricity distribution network discussed in paragraph 5.1, as the two entities exhibit a certain degree of interaction. In fact, according to the National Faults Incident Reporting Scheme (NaFIRS) database, natural hazard-related incidents with damage due to high winds are rather frequent. The NaFIRS database is a repository that every Distribution Network Operator is required to populate with statistics about recorded disruptions (OFGEM, 2017) occurred in their regions, including details about duration, suspected cause, and an estimate of the impact in terms of Customer-Minutes Loss. Given that the NaFIRS database is not available to the general public, the data used in this thesis were provided by Northern Powergrid after a confidentiality agreement was signed. In the period from January 2004 to March 2017, 42.1% of all incidents with damage recorded in Yorkshire and Lincolnshire and attributable to natural hazards were caused by "wind and gale". As visible in Figure 5.2, this percentage is remarkably higher than the share of incidents attributed to lightning (27.4%), snow (6.1%), or a combination of other natural hazards (24.4%). It can be argued that these numbers categorize Yorkshire and Lincolnshire as being particularly exposed to the risk of wind-related faults. In this area, the overhead lines carrying 132kV, 66kV, 33kV, and 11kV voltage electricity, combined, experienced a total of 941 incidents with damage in the 2004-2017 timeframe, resulting in nearly 73 faults per year affecting an average of 26,405 customers in the same temporal window.

The overhead lines are manifestly the most exposed section of the electricity network, being often unsheltered from high winds. Apart from their severity, the impact of the latter varies based on whether the lines are supported by a steel tower (for high voltage lines) or a wooden pole (for low voltage lines). In general, the disruptions are a consequence of direct effects (e.g., collapsed towers or poles, electrical arcs induced by cable oscillation, melting of equipment, shackle failures, detachments, ruptures, and cable misplacements), indirect effects (e.g., fallen trees causing cables to be severed or misplaced, debris, or windborne objects), or a combination of the two. Aspects such as elevation, shielding or exacerbation due to the local terrain, topographic exposure, seasonality, and proximity to coastal areas may exert an influence as well.

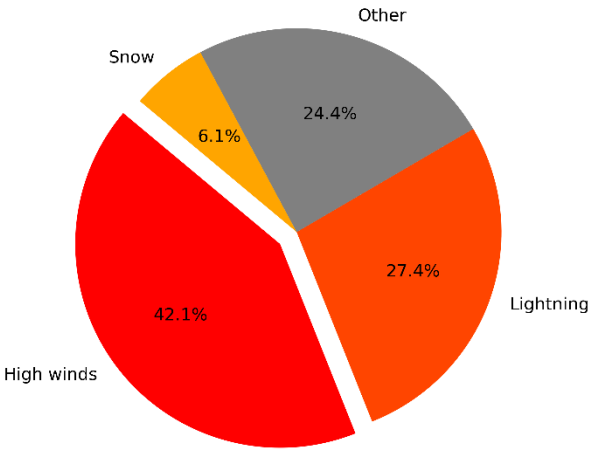

Figure 5.2. Pie chart showing the share of incidents with damage recorded in the NaFIRS database and attributed to a number of natural hazards in parts of the United Kingdom. The data refer to the area encompassing Yorkshire and Lincolnshire and the timeframe January 2004-March 2017.

5.2.2 Grids of daily maxima wind gusts

5.2.2.1 Use of a state-of-the-art, high resolution Regional Climate Model

Whilst the term *high winds* is generically intended to represent extreme wind speeds, a more precise definition is needed to categorize this spatial hazard. According to the World Meteorological Organization, a *wind gust* is defined as the highest wind speed averaged over a 3-second observation period (Harper et al., 2010; Kirchner-Bossi et al., 2019). Studies carried out on the impact of wind gusts or wind storms on infrastructures are not frequent in literature. Significant examples include the use of Regional Climate Models with a horizontal resolution of approximately 55x55km to characterize winter wind storms in Europe (Schwierz et al., 2010), or the adoption of wind gust time series obtained from a 73x55km reanalysis model to quantify the resilience of the United Kingdom National Grid (Panteli et al., 2016).

However, it is argued that spatial scales as large as these may represent a spatially coarse approach in dealing with the spatial variability of wind speeds, which was categorized as being large by Yu et al. (2015). Herrmann et al. (2011) corroborate this point of view by highlighting the fact that any increase in the spatial resolution of wind datasets comes with a more realistic interpretation of local orography. More recently, the adoption of the 12km RACMO22 Regional Climate Model by Dunn et al. (2018) to compute empirical fragility curves for the electricity network marked the transition toward the use of finer spatial resolutions in impact studies.

This Case Study, however, departs from these approaches in that it adopted new and previously unavailable high-resolution wind gust datasets derived from Kirchner-Bossi et al.

(2019). These datasets were obtained by complementing the use of a 12km model (known as RCM12) with a state-of-the-art Regional Climate Model featuring a very detailed 1.5km horizontal resolution (known as CPM1.5 or UKV). The CPM1.5 model is a convection-permitting configuration of the Met Office Unified Model (Cullen, 1993), and it is driven at its boundaries by the RCM12 model, another configuration of the Unified Model.

The transition from the 1.5km to the 12km grid is handled by an interface grid with a resolution that decreases from 1.5x1.5km to 4x1.5km on the edges and from 1.5x1.5km to 4x4km on the corners of the domain (Figure 5.3a). The eightfold increase in the horizontal resolution of CPM1.5 compared to RCM12 (Figure 5.3b) enabled finer climate simulations (Kendon et al., 2012; Chan et al., 2014), leading to an increased capacity to represent local-scale phenomena and extreme events, including wind gusts (Balog et al., 2016).

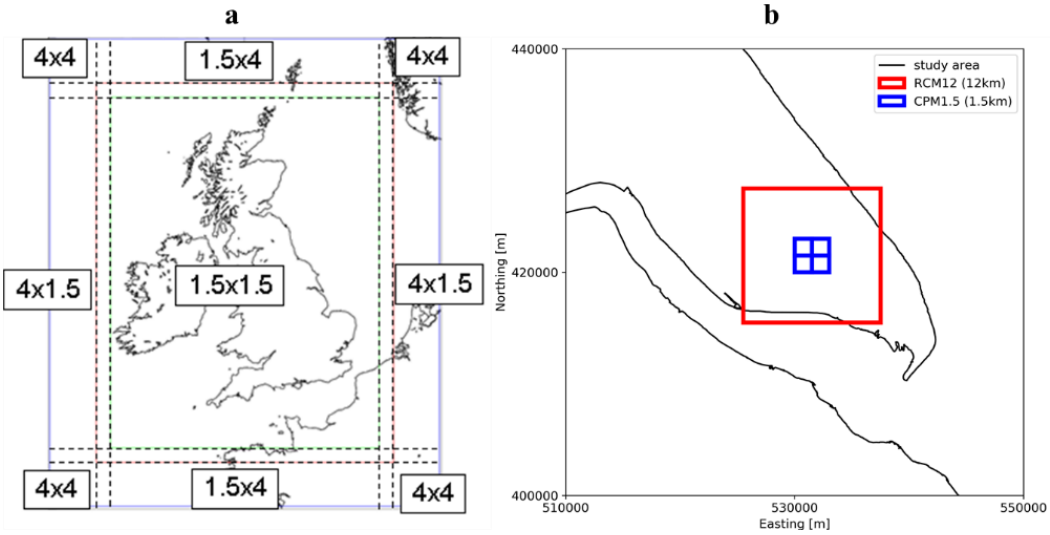

Figure 5.3. (a) Representation of the CPM1.5 1.5x1.5km grid and the interface grid on the outer frame, leading to the RCM12 12x12km grid. Image adapted from MetOffice (2012). (b) The difference in spatial resolution between the 12x12km (in red) and the 1.5x1.5km grids (in blue).

5.2.2.2 The computation of wind gust grids

The wind gust grids used in this Case Study were obtained from Kirchner-Bossi et al. (2019). By using CPM1.5 nested inside RCM12, grids of daily maxima wind gusts for England and Wales were derived. These grids were obtained for two different climate horizons: Control and Future (Table 5.1). The Control horizon is a set of simulations covering 13 years, which was obtained from the CPM1.5 control run initialized with ERA-Interim re-analysis data. These simulations refer to external forcings (e.g., concentrations of greenhouse gases, aerosols, solar input, and so forth) similar to those observed in the year 2000. The Future horizon also covers

13 years and was computed by a CPM1.5 run with RCP8.5 external forcings, thus following a high-emission scenario (Riahi et al., 2011) centered around the year 2100.

Table 5.1. Details of the wind gust climate horizons, together with suitable reference values.

Climate horizon	Scenario	Temporal length	Grid temporal resolution	Grid spatial resolution	Average gust over the study area	Maximum gust over the study area
Control	Baseline	13 years	Daily	1.5x1.5 km	11.46 m/s	49.79 m/s
Future	RCP8.5	13 years	Daily	1.5x1.5 km	11.17 m/s	52.80 m/s

The wind gust grids were obtained directly from the output of the Control and Future runs, which consisted of grids (hereafter called $g_{10,10}$) of wind speeds $s_{10,10}$ referring to a surface elevation of 10 meters and time intervals of 10 minutes. Each $w_{10,10}$ value in the $g_{10,10}$ grids was computed by adding a positive quantity q to the wind speed $s_{10,10}$ (equation 5.1), following Panofsky et al. (1977) and Beljaars (1987):

$$w_{10,10} = s_{10,10} + q \tag{5.1}$$

where the quantity q is defined as:

$$q = f\left(\sigma_{flow,h}\right) = f(z_i, L) \tag{5.2}$$

In equation 5.2, $\sigma_{flow,h}$ is the standard deviation of the horizontal flow, z_i represents the height of the boundary layer, which is the height measured from the surface to the point where the horizontal flow velocity is 99% of the free stream velocity, and L is the Monin-Obukhov length (Figure 5.4). Finally, the wind gusts values referring to a surface elevation of 10 meters and 3-second observation periods (hereafter called $w_{10,3}$) were obtained by resampling the $g_{10,10}$ grids every 3 seconds, thus creating $g_{10,3}$ grids (Figure 5.5).

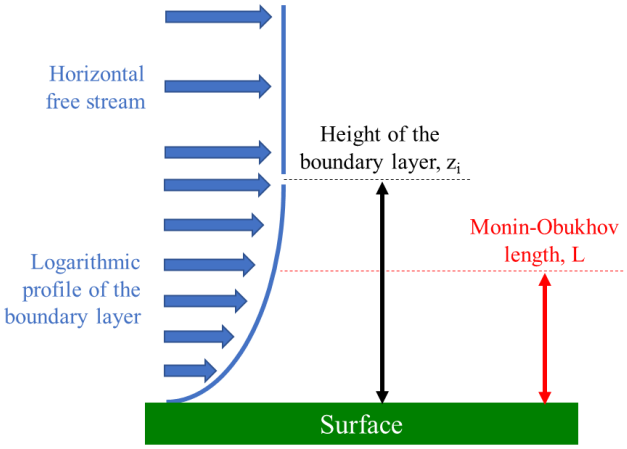

Figure 5.4. Representation of the horizontal flow, the height of the boundary layer, and the Monin-Obukhov length. The Monin-Obukhov length represents the height where turbulence is caused more by buoyancy than wind shear, whereas the logarithmic curve represents the increase in horizontal flow velocity until z_i is reached.

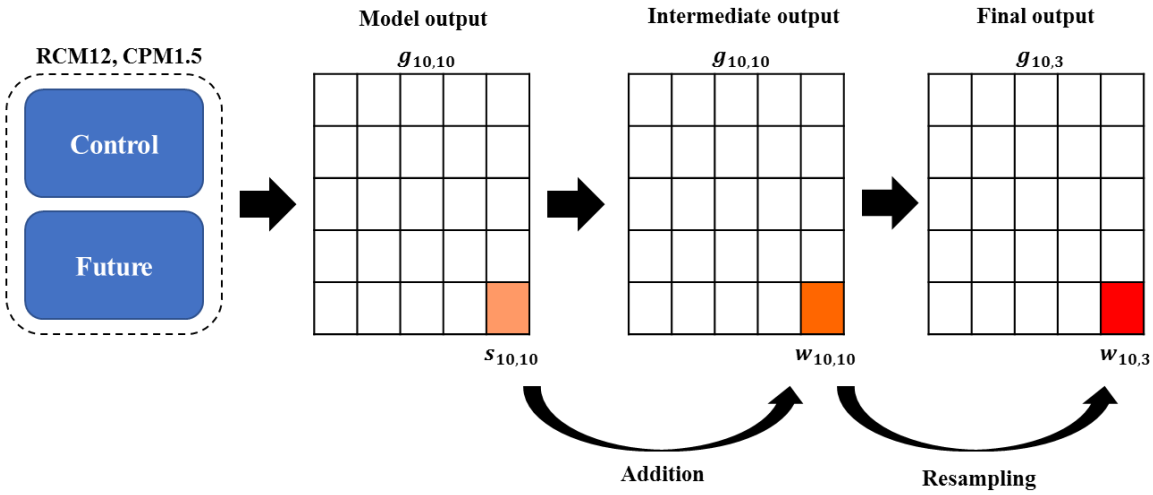

Figure 5.5. Process similar to the one that Kirchner-Bossi et al. (2019) followed to compute the wind gust grids (final output) that were used in this Case Study.

The grids obtained according to the two-step process in Figure 5.5 are composed of 74 1.5x1.5km cells along the x-axis, and 83 cells along the y-axis. The sea was masked out and it was rendered in white, as it is outside the scope of this Case Study. Figure 5.6 shows the average daily maxima wind gusts for the Control and Future horizons, as well as their difference. As a consequence of the very detailed resolution, and in agreement with Herrmann et al. (2011), the local orography appears to be well interpreted, with the most exposed areas being located in the North York Moors and along the coast. Despite the range of average wind gusts is the same for the two horizons, the difference between the two grids reveals a decrease in severity going from

the baseline to the future scenario. This matches the observations of Tobin et al. (2016), with the drop reaching almost 1 m/s along the coast.

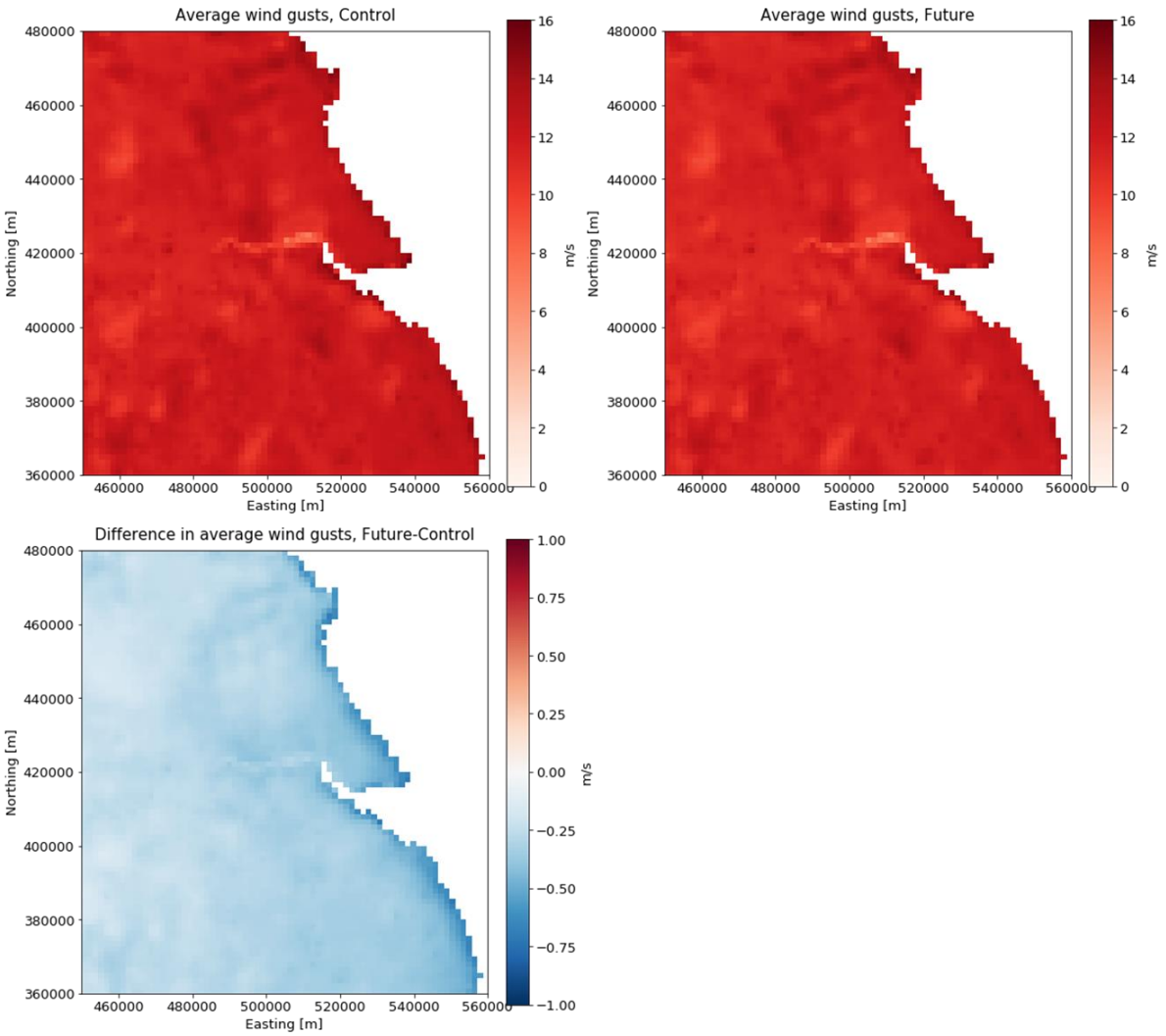

Figure 5.6. Wind gust grids for the study area showing the average daily maxima wind gust for Control and Future, as well as their difference. For reference, the North York Moors are located in a central position in the upper part of the study area.

In terms of variance, Figure 5.7 shows that daily maxima wind gusts are projected to become more uncertain under the RCP8.5 scenario in the North York Moors area. The 95th percentile grids reveal that, although the average wind gusts are projected to decrease, events relatively more severe are projected to affect the North York Moors as well the western parts of the study area, with the coast experiencing milder gusts.

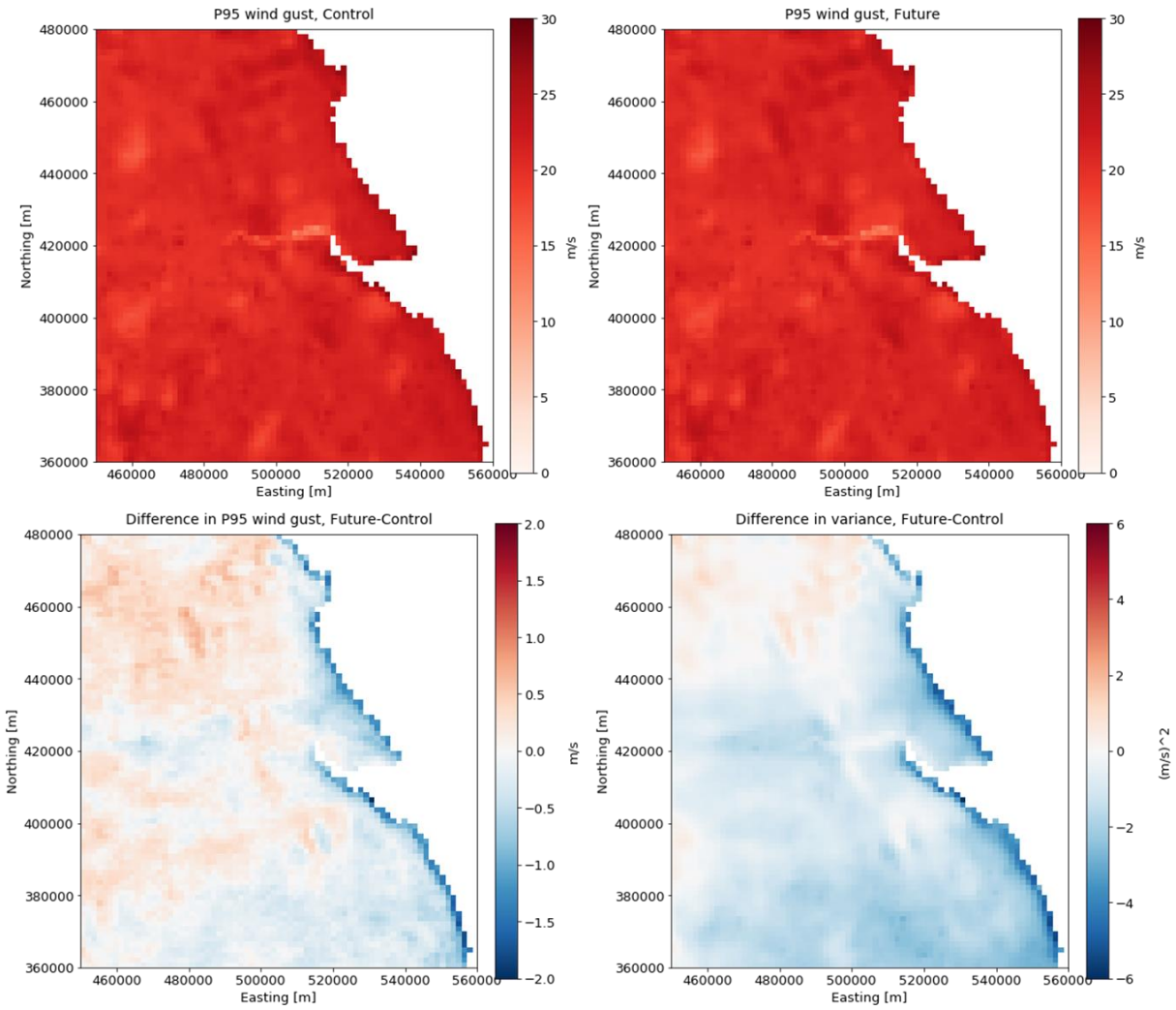

Figure 5.7. Grids showing the 95th percentile of daily maxima wind gust for the study area and the two climate horizons, the difference in percentiles, and the difference in variance.

5.2.3 Fractal properties of the wind gust grids

5.2.3.1 Fractal considerations corroborating the adoption of wind gusts

Apart from the motivations discussed in paragraph 5.1, the rationale for adopting the wind gusts as a real-world natural spatial hazard also included the need to find an appropriate spatial hazard that could be comparable, at least to a certain extent, to the fractal surfaces described in paragraph 4.4. As such, the adoption of wind gusts was pursued as several authors (Chang et al., 2012; Fortuna et al., 2014) report that the time series of wind speeds show fractal properties at different temporal scales.

For instance, the fractal or Hausdorff dimension D of the bi-dimensional time series of hourly mean wind speeds as recorded in three stations in Taiwan is $D \cong 1.6$ (Chang et al.,

2012), where $D = 2 - H$ in a bi-dimensional space (see equation 4.3). Similarly, Fortuna et al. (2014) found that the time series of hourly mean wind speeds recorded in one station in Italy exhibit $D = 1.46$. These values are a direct consequence of the wind speed fluctuation, and as outlined in paragraph 3.2.3, $D > 1.5$ means progressively high fluctuations and negative time correlation, whereas $D < 1.5$ describes milder fluctuations and positive time correlation. In terms of the Hurst exponent H (see paragraph 4.2.3), given the bi-dimensionality of the time series, $D > 1.5$ corresponds to $H < 0.5$ and thus to highly corrugated time series profiles, whereas $D < 1.5$ corresponds to $H > 0.5$, which describes smoother profiles.

These considerations apply to time series, e.g. curves with a fractal dimension $1 \leq D \leq 2$, where the lower bound represents a line and the upper bound any bi-dimensional object (Figure 5.8a), and clearly refer to the *temporal domain*. Objective of this thesis was to investigate whether the fractal properties of wind gusts also held in the *spatial domain*. In it, the surfaces described by the $g_{10,3}$ grids have an *a priori* dimension $2 \leq D \leq 3$, where the lower bound represents any flat surface with $z = 0$ and the upper bound a cube (Figure 5.8b). In the spatial domain, positive or negative correlations refer to the correlation between wind gusts in adjacent locations rather than adjacent time intervals.

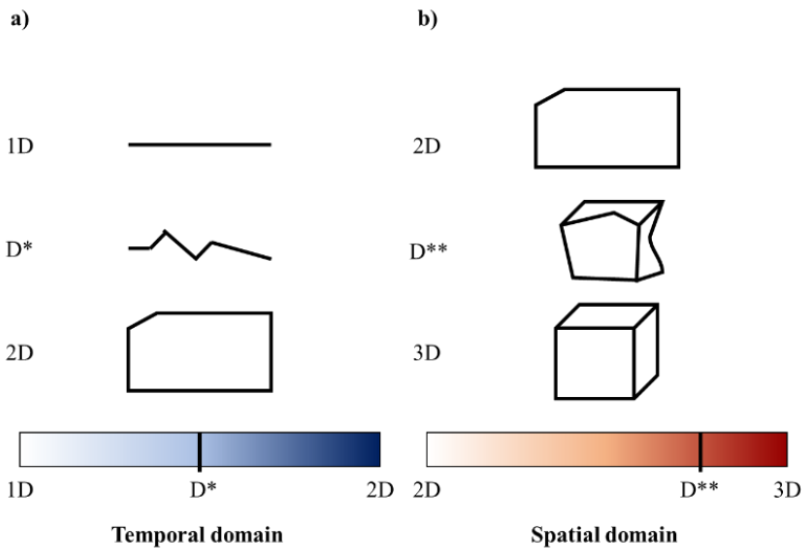

Figure 5.8. (a) In the temporal domain, any object has a fractal dimension constrained by $1 \leq D^{*} \leq 2$. (b) In the spatial domain, the fractal dimension is constrained by $2 \leq D^{**} \leq 3$.

5.2.3.2 Area-Frequency curves

The Area-Frequency curve was first introduced by Malamud et al. (2004) to count the number of landslides of different sizes occurring in a given area. This count was then transformed into the frequency with which landslides belonging to the same size range were observed. In this curve, the range of occurrences (or frequencies) is displayed along the y-axis, whereas the range of sizes is displayed along the x-axis. When generalized for an unspecified class of spatial objects, the Area-Frequency curve is defined as:

$$p(A_{obj}) = \frac{1}{N_{obj,tot}} \frac{dN_{obj,A}}{dA_{obj}} \tag{5.3}$$

In equation 5.3, A_{obj} is the specific area of an object belonging to the range of sizes, $N_{obj,tot}$ represents the total number of objects analysed, $dN_{obj,A}$ is the number of objects with $size = A_{obj}$, and dA_{obj} represents a differential increase in area. Taken together, the term $\frac{dN_{obj,A}}{dA_{obj}}$ refers to the number of objects with areas between A_{obj} and $A_{obj} + dA_{obj}$. The authors found that the distribution of landslide sizes features an exponential trend for small sizes, and then a power-law decay for medium and large sizes. This implies that, for a limited section of the size range (e.g., where the objects are medium to large in size), the area-frequency curve is scale-invariant or scale-free (Malamud et al., 2004). Such property is also found in fractals, as outlined by Mandelbrot (1967), Borrough (1981), and Baas (2002), and it is the consequence of statistical self-similarity (see paragraph 4.2.1). The ultimate implication is that, as the spatial object is progressively magnified or miniaturized, the same shape and statistical properties observed at a given scale are observable at other scales (Figure 4.3).

In this Case Study, the Area-Frequency curves as described by Malamud et al. (2004) were adopted to determine whether scale-free properties emerged from the analysis of the $g_{10,3}$ wind gust grids, and for which section of the size range. The adoption of a statistical tool developed for landslides in a study concerning wind gusts is justified by two reasons:

1. The distribution of landslide sizes has been categorized as having fractal properties (Yokoi et al., 1995);
2. As such, it was found appropriate to determine whether the $g_{10,3}$ grids exhibited fractal properties by comparing their Area-Frequency curve to those of the fBm-generated fractal spatial hazards.

The implementation of the Area-Frequency curve was preceded by a set of pre-processing operations:

1. To ensure that the $g_{10,3}$ wind gust grids were comparable to the fBm-generated fractal surfaces, it was mandatory for the two class of objects to share the same horizontal dimension (e.g., 73 cells along the x-axis and 84 cells along the y-axis). This was obtained by retrieving the dataset originally generated for Case Study 1 of this thesis, and slicing the fractal surfaces in Figure 4.7 in such a way as to match the horizontal dimension of the $g_{10,3}$ grids;
2. From the original dataset of fractal surfaces, 2,000 objects were sampled for each combination $C = (H, Ft)$, for a total dataset of 50,000 surfaces. This dataset was obtained with the same thresholds as Case Study 1, to ensure a meaningful comparison with the wind gust grids;
3. For both climate horizons, the $g_{10,3}$ wind gust grids were binarized by using appropriate wind filters w_f, following the procedure described in paragraph 4.5.1 and 4.5.2: any wind gust $w_{10,3} \leq w_f$ was set to zero, whereas any value $w_{10,3} > w_f$ was set to one (Figure 5.9). The w_f filters were determined by computing the 10%, 30%, 50%, 70%, and 90% fraction of the maximum $w_{10,3}$ in the two horizons (Table 5.2). This binarization is equivalent to raising the $z = 0$ datum of the grids to progressively higher values.

The Area-Frequency curves were computed by using a dedicated Python algorithm that implements equation 5.3, thus determining the relative frequency of the size ranges of the spatial objects emerging in the $g_{10,3}$ grids. These spatial objects are hereafter defined as *blobs* and were obtained by binarizing each grid in step 3 (Figure 5.9). The binarization was implemented for three reasons: *i*) to ensure that the fractals used in Case Study 2 were the same as those used in Case Study 1, except for the larger size; *ii*) to allow the algorithm to identify the blobs; and *iii*) to avoid the trivial and frequent case where $w_{10,3} \neq 0$ over the entire study area, which would return the area-frequency distribution of the study area itself. The comparison between the fractal surfaces and the $g_{10,3}$ grids was performed for both climate horizons, using the same dataset of fractal surfaces in both cases. The different filter values between the two horizons are due to the different maximum wind gusts obtained by Kirchner-Bossi et al. (2019).

Table 5.2. The w_f filters used in step 3 of the pre-processing phase and the corresponding failure thresholds. Each filter is associated with a maximum load or wind gust speed.

Max fractal load	Failure thresholds F_t	Max $w_{10,3}$, Control	w_f filters, Control	Max $w_{10,3}$, Future	w_f filters, Future
1.0	0.1	49.79 m/s	4.98	52.80 m/s	5.28
	0.3		14.94		15.84
	0.5		24.89		26.40
	0.7		34.85		36.96
	0.9		44.81		47.52

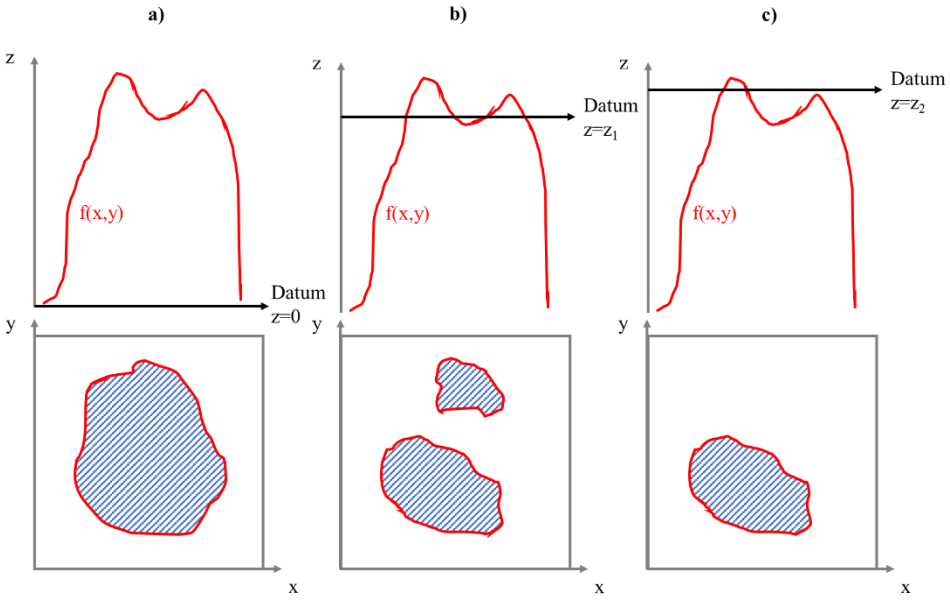

Figure 5.9. Representation of the effects of binarization. In the top row, the same function $z = f(x, y)$ is shown, with its datum progressively increased from 0 to $z_1 > 0$, and then to $z_2 > z_1 > 0$. In the bottom row, the blobs as an eye-view representation of the function z where everything inside the red lines equals 1, whereas everything outside equals 0. (a) Only one blob is visible, as the datum corresponds with $z = 0$. (b) As the datum raises and exceeds the sag, two blobs are visible. (c) When the datum reaches z_2, only the highest peak is visible as a blob.

5.2.3.3 The Box-Counting Algorithm (BCA)

The next step after verifying the emergence of scale-free phenomena in the wind gust grids was to estimate their fractal dimension D. This was accomplished by computing, in a dedicated Python script, the Minkowski–Bouligand dimension D_{MB} (Peleg et al., 1984; Soille and Rivest, 1996), which is a convenient approximation of the fractal dimension (Tijera et al.,

2012) and as such it was used as its proxy. The computation of the Minkowski–Bouligand dimension D_{MB} was performed by implementing the *Box-Counting Algorithm* (BCA), as done by many authors (e.g., Li et al., 2009), on the grounds of its simplicity, limited computational requirements, and applicability to objects with or without self-similarity (Peitgen et al., 2004).

Defined a set S in a Euclidean space R^n, the objective of BCA is to determine the number of squares (in the case of a bi-dimensional object) or boxes (for a three-dimensional object) that are necessary to cover the entire set S. The procedure is repeated by using progressively smaller squares or boxes (Figure 5.10), and at each step, the number of boxes $N(\varepsilon)$ with side length ε is recorded, until a cut-off length is reached. By plotting the $\varepsilon, N(\varepsilon)$ points on a logarithmic plane and fitting a straight line, the Minkowski–Bouligand dimension D_{MB} is obtained from the slope of that line (Foroutan-pour et al., 1999). From an analytical point of view, the D_{MB} dimension of a set S is defined in equation 5.4:

$$D_{MB}(S) = \lim_{\varepsilon \to 0} \frac{\log N(\varepsilon)}{\log\left(\frac{1}{\varepsilon}\right)} \tag{5.4}$$

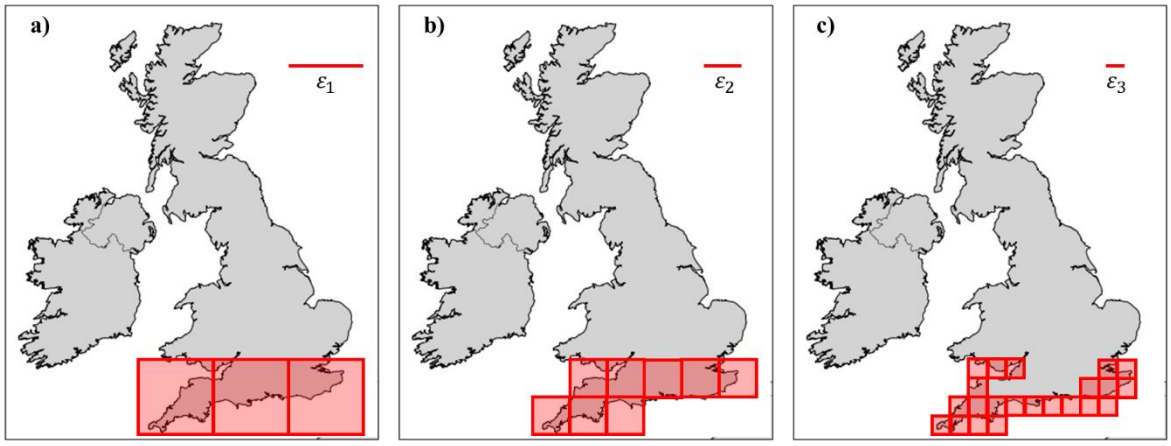

Figure 5.10. To estimate the fractal dimension of the coastline of the United Kingdom, squares of sizes $\varepsilon_3 < \varepsilon_2 < \varepsilon_1$ are used. A finer interpretation of the southern coastline is obtained with increasing numbers of squares: 3 (a), 8 (b), and 22 (c). Landlocked squares are not relevant to the BCA algorithm, and as such they were not considered.

Within the context of this Case Study, the BCA methodology was applied to the *blobs* obtained from the dataset of binarized grids introduced in paragraph 5.2.3.2. This was done to estimate the fractal dimension of each grid of daily maxima wind gusts over the study area. For

each climate horizon, the estimated fractal dimension of the time series of blobs were compared to the known fractal dimension of the synthetic surfaces to highlight the differences. The BCA methodology was not applied to the non-binarized grids as doing this would have returned the fractal dimension of the coastline of the study area. In fact, given that the grids refer to daily maxima wind gusts, very rarely do they feature $w_{10,3} = 0$ (an instance associated with gaps in the wind field texture), *de facto* returning the footprint of the study area itself.

5.3 Stage 2: modelling hierarchies and dependencies of the electricity network

5.3.1 A real-world infrastructure as a system-of-systems

5.3.1.1 An electricity distribution network

The real-world infrastructure used in Case Study 2 of this thesis was the electricity distribution network operating in Northern Lincolnshire and East Yorkshire, in England (Figure 5.11). This network comprised the overhead sections of the 132kV (high voltage, HV) and 33-66kV (medium voltage, MV) lines, and constitutes a bespoke selection of a larger system managed by a Distribution Network Operator servicing the North East of England. This network has the following characteristics:

- It serves upwards of 260,000 customers;
- It is composed of over 7,000 pylons;
- It consists of more than 1,000 km of overhead lines;
- It is connected to the National Grid by means of 6 substations, where the voltage is decreased from 400kV (extreme high voltage, EHV) to 132kV;
- It features 19 substations, defined as *bulk supply points*, where the voltage is reduced from 132kV to 33-66kV;
- It contains 95 substations, defined as *primary substations*, where the voltage is stepped down from 33-66kV to lower voltages (LV).

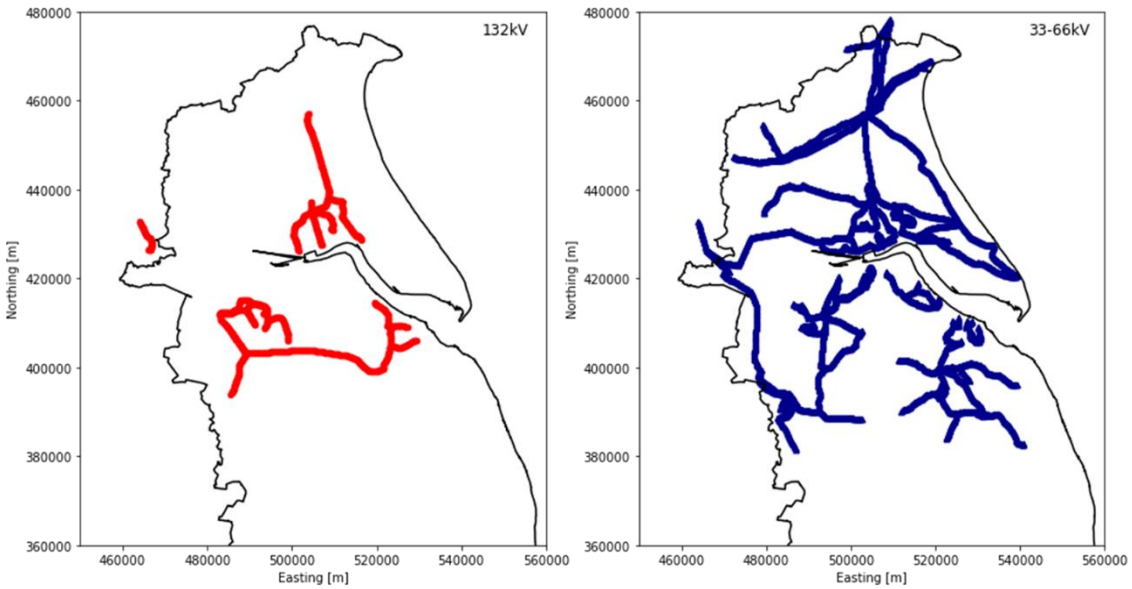

Figure 5.11. Spatial domain covered by the two-tier electricity infrastructure analyzed in Case Study 2 of this thesis. The black line represents the boundary of the study area; the red lines represent the 132kV network (left); the blue lines represent the 33-66kV network. One segment of the 132kV network is located outside the study area but was included in the case study given its proximity to the black line.

5.3.1.2 Dataset pre-processing

The spatial dataset provided for this case study consisted in an ArcGIS geodatabase populated with the shapefiles as digitized by the Asset Management Team of the Distribution Network Operator. The geodatabase consisted of the underground and overhead sections of the 230V, 11kV, 20kV, 33kV, 66kV, 132kV, and 275kV lines, and in its original form it was not appropriately structured for the purpose of Case Study 2 of this thesis. As such, a five-step pre-processing methodology was set up, with the ultimate purpose of creating a topologically valid graph:

- Step 1: selection of the appropriate networks based on their voltage and other considerations;
- Step 2: correction of digitization and drawing errors such as overshooting, undershooting, and any gaps caused by certain lines being intermittently (or inconsistently) underground and overground;
- Step 3: creation of point shapefiles representing electricity towers, which were absent from the original dataset;
- Step 4: creation of point shapefiles representing the substations, which were also absent from the original dataset;
- Step 5: creation of a topologically sound graph for impact modelling.

The first four steps were performed in ArcGIS. The 132kV and 33-66kV lines (with the 33kV and 66kV lines combined) were selected due to the need to create a well-balanced network in terms of complexity and computational costs. The study area in Figure 5.11 was selected as it offered the best possible compromise between a reasonable size and an appropriate level of representativeness. Similar considerations determined the exclusion of the 275kV network, which presence in the study area is very limited, and the 11kV network, which operates almost entirely underground and as such is not affected by high winds. The correction of the large number of digitization and drawing errors (Figure 5.12) was performed either by extending two proximal lines until a connection was created, or by trimming them to the intended connecting point. The gaps or discontinuities caused by alternating underground-overhead lines were corrected by connecting the overhead segments in which continuity was interrupted by underground segments. This task was performed in order to obtain a continuous dataset of lines, at the cost of a slight overestimation of the overall length of the network.

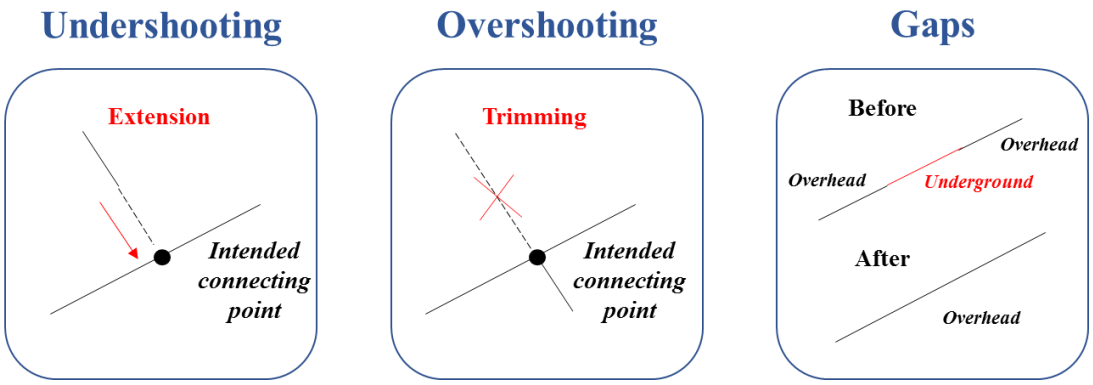

Figure 5.12. Visual representation of how undershooting, overshooting, and gaps were corrected in the pre-processing procedure.

The point shapefile representing electricity pylons was created by setting an interval distance between two adjacent pylons. For the 132kV lines, this was set at 200 m, whereas for the 33-66kV lines this was set at 150 m, following a sample measurement performed on Google Earth. The point shapefile representing the 120 substations operating over the study area was created based on the locations made available by the Distribution Network Operator. The substations were allocated in such a way as to have the 6 National Grid as entry points to the 132kV network, the 19 bulk supply points at the interface of the 132kV and the 33-66kV networks, and the 95 primary substations as the exit points of the 33-66kV network. Finally, the creation of a topologically connected network was performed by using NetworkX, the dedicated Python package for network modelling, which allowed to import the 132kV and 33-66kV shapefiles and create two topologically valid graphs. This last passage was performed by

trimming the 132kV and 33-66kV polylines at the intersection with their pylons, creating segments that only connect two adjacent pylons and providing NetworkX with the *adjacency matrix* necessary to build the graph (Figure 5.13).

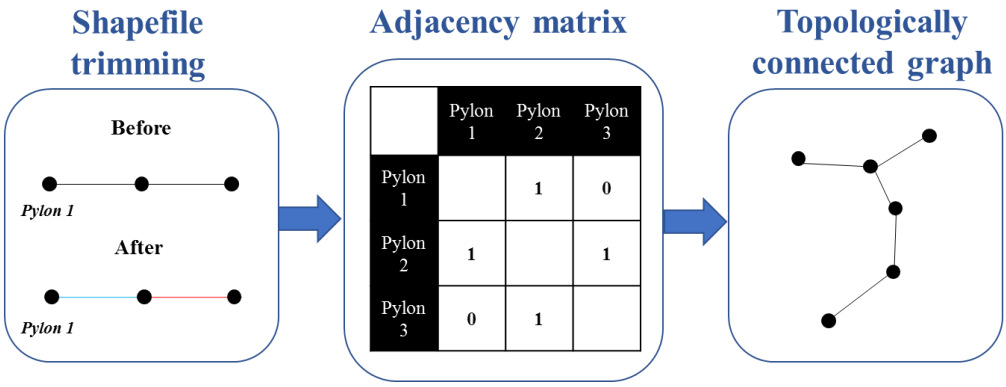

Figure 5.13. Visual representation of the creation of a topologically valid graph in NetworkX starting from a shapefile.

5.3.1.3 The modelling of intra-dependencies and the customer base

As highlighted in Figure 5.1, the electricity network used in this Case Study features a number of intra-dependencies that had to be modelled in order to create a realistic representation of the actual infrastructure. The model used to implement and define the intra-dependencies is hierarchical, as shown in Figure 2.4, and follows the flow of electricity as it enters the system at a 132kV voltage, is decreased to a 33-66kV voltage, and then exits the system at an 11kV voltage. This progressive stepdown is well in line with the idea of a hierarchical network, as discussed in paragraph 2.1.3, and it is also corroborated by fact that any substation is a node that belongs simultaneously to two networks, justifying the definition of *two-tier system*. In this context, the two networks were the 132kV system, which operates at a higher hierarchical level, and the 33-66kV network, operating at the lower level (Figure 5.14). This hierarchical model allowed to identify 26 segments composing the 132kV network, defined as *feeders*, and 19 components of the 33-66kV network, defined as *circuits*.

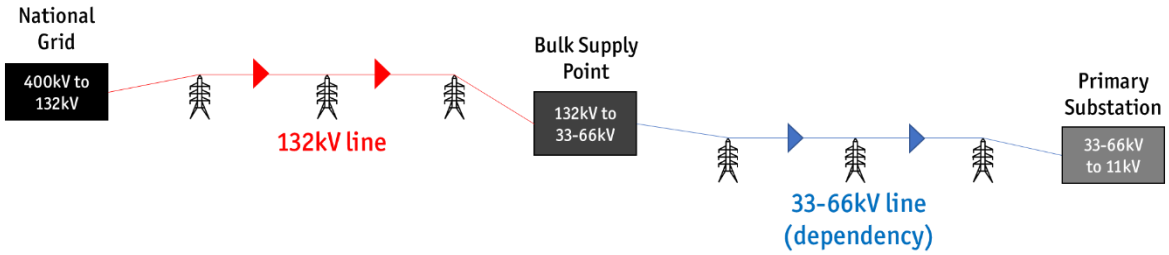

Figure 5.14. The hierarchical model adopted. The 132kV line feeds into the 33-66kV line (the dependency), and the bulk supply point is a substation belonging to both networks simultaneously.

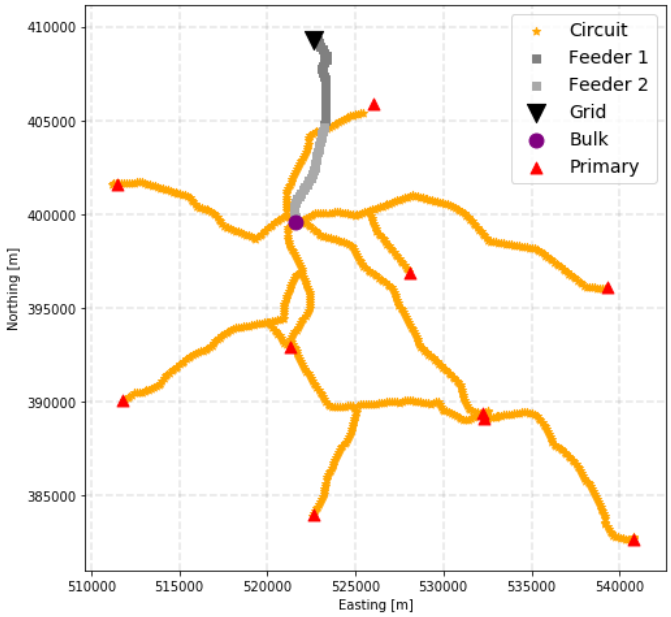

Figure 5.15. Example of two feeders serving a circuit. The substations are also visible.

The identification of feeders and circuits in the two-tier network allowed to define the distribution of dependencies across the 132kV network, and to also determine the number of feeders attached to each circuit (Figure 5.16). This task was performed based on information made available by the Distribution Network Operator. The information on the customer base of each feeder and circuit was determined in a bottom-up fashion, starting from the number of customers served by each substation provided by the Distribution Network Operator. For the feeders, the number of customers served was assumed to be the same as the substation in which they culminated. As an example, the customers served by the two feeders in Figure 5.15 was the same as the bulk supply point where they terminated. For the circuits, this number was assumed to be the sum of the customers served by each primary substation. For instance, the number of customers served by the circuit in Figure 5.15 was given by the sum of the customers served by the 10 primary substations it featured. Due to the hierarchical structure in place, the number of customers served by the 132kV components was often higher than that served by the 33-66kV segments: this was the result of the fact that the customer base of each bulk supply point was the sum of the customers served by the primary substations attached to it. A breakdown of the number of customers served by each feeder and circuit is given in Figure 3.37.

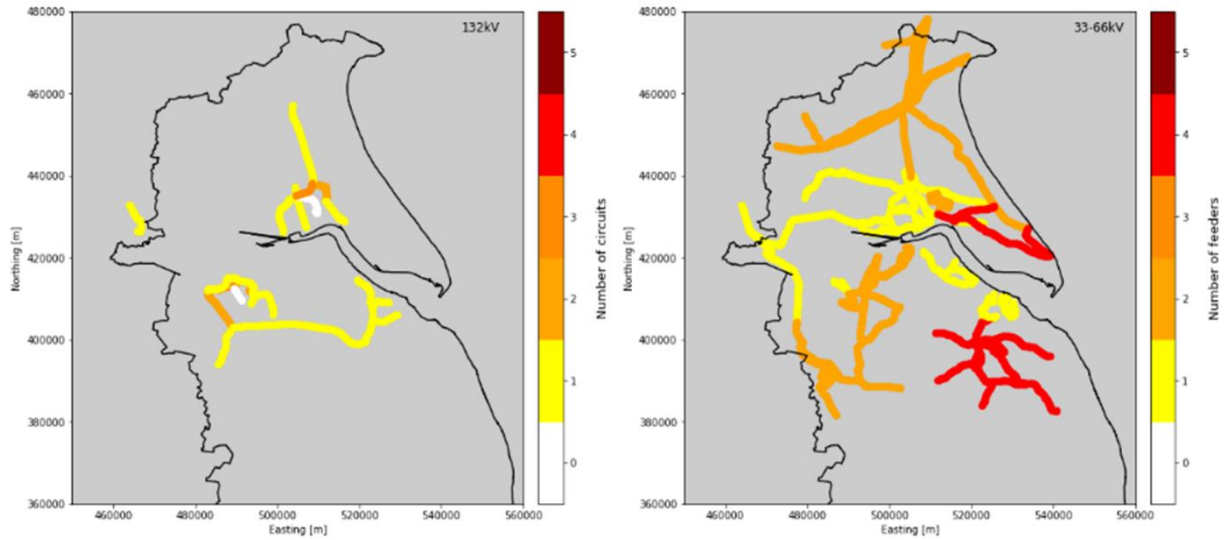

Figure 5.16. Left (132kV network): distribution of the number of circuits (dependencies) attached to each feeder. Right (33-66kV network): distribution of the number of feeders attached to each circuit. Amongst feeders, the highest number of dependencies found was 3. The highest number of feeders attached to a circuit was found to be 4.

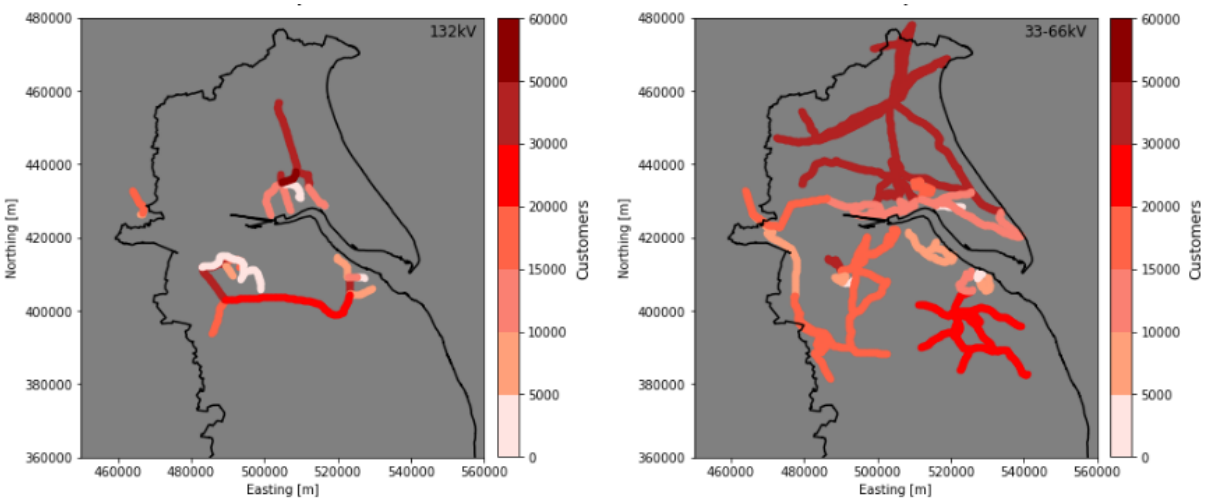

Figure 5.17. Left (132kV network): distribution of the number of customers served by each feeder. Right (33-66kV network): distribution of the number of customers served by each circuit. Amongst feeders, the largest customer base observed was 58,015, whereas the corresponding number for circuits was 30,070.

5.4 Stage 3: a network model inspired by real-world assets

At variance from Case Study 1, where the emphasis was on identifying the difference in terms of robustness between off-the-shelf topological models, Case Study 2 was entirely dedicated to analyzing an existing hierarchical infrastructure. As such, the topological layout of the network was not the result of an off-the-shelf model but was driven by the exact location of the pylons and the distance between them. As visible in Figure 5.11, this resulted in a layout

that is difficult to classify from a topological perspective. However, any topological classification aimed at identifying which theoretical model best approximates the networks in Figure 5.11 would have likely been meaningless, due to the necessary pre-processing adjustments that were applied to the asset dataset (see paragraph 5.3.1.2).

5.5 Stage 4: propagation of failures caused by wind gusts

5.5.1 Intra-systemic cascading failures

5.5.1.2 Components of the 33-66kV line exposed to intra-systemic cascading failures

The advantage of modelling the robustness of the 132kV and 33-66kV lines as the robustness of a system-of-systems was not only the ability to disentangle the behavior of each line component from that of the tier or line it belonged to, but also to model the interactions between the components. Under the assumption that switchyards, parallel lines, and loops were not present (as it was the case for the asset dataset described in paragraph 5.3.1.1), this was accomplished by determining, for each climate horizon, the number of occurrences where components of the 33-66kV line experienced interruptions to the electricity supply due to faults that had originally affected the 132kV components feeding them (Figure 5.18). The occurrence of a cascading failure was constrained by two conditions, which taken together were considered to be necessary and sufficient:

1. For the wind gust to cause the cascading failure, the necessary condition was $w_{10,3} > 17\ m/s$, as this threshold value is recognized in the literature as both the definition of gale according to the Beaufort scale (Kirchner-Bossi et al., 2019; Jönsson et al., 2007) and the value past which wind storms are observed (Dunn et al., 2018; Vajda et al., 2014). The $w_{10,3} > 17\ m/s$ condition was assumed to produce faults with a probability of 100%, e.g. $P_f = [1 \mid w_{10,3} > 17\ m/s]$;
2. For the cascading failure to occur, the 132kV component had to be affected by at least one fault and had to supply at least one 33-66kV component.

According to the conditions above, the cascading effect is to be recognized in the fact that faults occurring in one location have an effect in other locations, akin to the concept of *2nd*

order failures discussed in paragraph 2.2.4.1. This methodology allowed to produce a heatmap of the 33-66kV components, highlighting the least and most vulnerable to cascading failures. The procedure just described only identified cascading failures that are *topological* in nature, which only depend on the distribution of network edges between the 132kV and 33-66kV components, as shown in Figure 5.15. In situations where one 33-66kV component was fed by multiple 132kV components, the cascading failure was allowed only if all the relevant 132kV components had experienced faults. Following the indications provided by Hines et al. (2010), however, it must be pointed out that adopting a topological or hierarchical scheme only to describe the propagation of failures in an electricity network may return results that are not entirely accurate. As such, this procedure was developed with the aim of complementing the implementation of any algorithm describing the redistribution of flows, such as the linearized power flow equations (Soltan et al., 2017).

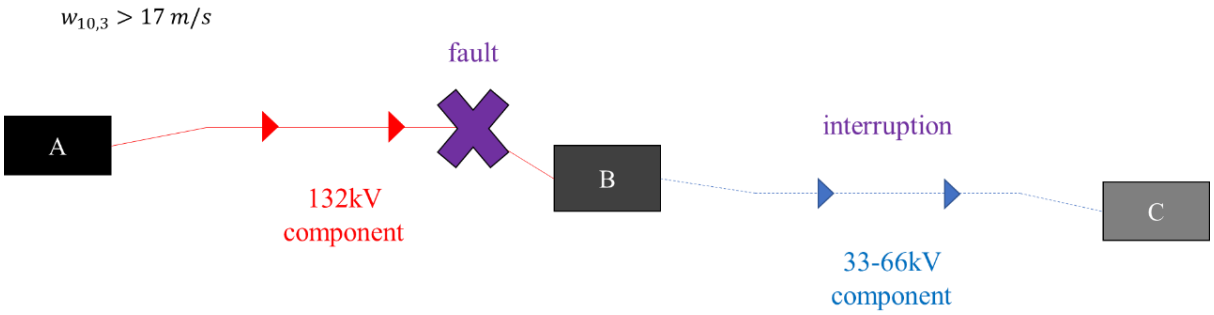

Figure 5.18. Given one 132kV component feeding one 33-66kV component, the latter experienced a cascading failure if $w_{10.3} > 17\ m/s$ and one or multiple faults had occurred at the 132kV level, resulting in the interruption to the electricity supply. The "A", "B", and "C" symbols represent substations with progressively lower voltages.

5.5.1.2 Components of the 132kV line causing intra-systemic cascading failures

In a similar fashion to paragraph 5.5.1.1, where the aim was to produce a breakdown of the 33-66kV to highlight the spread of vulnerability to topological cascading failures, it was also determined the frequency with which a given 132kV component caused cascading failures. This was accomplished by counting, for each climate horizon, the occurrences where faults affecting 132kV components resulted in service failings at the 33-66kV level. In situations where one 132kV component fed multiple 33-66kV components, this computation was performed by considering how many cascading failures the 132kV component caused among the relevant 33-66kV components. Essentially, this computation was performed by considering

the effects described in Figure 5.19 from the point of view of the 132kV component instead of the 33-66kV component. The aim of this procedure was to obtain a breakdown of 132kV components to identify those that caused the most topological cascading failures, in such a way as to provide insights regarding the vulnerability of those components and highlight the potential need for increased redundancy.

5.6 Stage 5: quantifying the fragility to wind gusts

5.6.1 Effects of the wind gusts on the electricity infrastructure

5.6.1.1 The choice of empirical fragility curves

Fragility curves are classed as a statistical method for estimating the conditional probability of the failure of a structure given the exceedance of a load threshold (Dunn et al., 2018). In the context of this thesis, the structures are electricity towers, whereas the load threshold is represented by a significant wind speed that is exceeded. For the purpose of this thesis, fragility curves can be mathematically defined as:

$$P_f = P[G(x) < 0 \mid w \geq w_{thr}] \tag{5.5}$$

In equation 5.5, P_f is the conditional probability of failure, $G(x) < 0$ represents the loss of performance of a structure that leads to the disruption, and $w \geq w_{thr}$ indicates the exceedance of a threshold wind gust (e.g., the failure condition). The quantification of failures using equation 5.5 is affected by a high degree of uncertainty and complexity, due to the number of factors involved. These include the height and geometry of the structure, its age and materials, the different degrees of exposure to the loading, and other considerations. To minimize these problems, authors in the literature have adopted different strategies that can be categorized as: *i*) *performance-based*; *ii*) *inspection-based*; and *iii*) *record-based* or *empirical*. In terms of performance-based approaches, Manis and Bloodworth (2017) focused their attention on developing a finite element model of an electricity tower subjected to extreme winds. This approach aims at detailing the physical behavior of loaded tower frames, taking into account

aspects such as the materials, the geometry of the structure, and the buckling effect as failure mechanism.

This approach was not implemented in this thesis given the computational resources required to apply a finite element procedure to a network with more than 7,000 pylons. In terms of inspection-based methodologies, the work of Ryan and Stewart (2017) provided insights regarding how the accelerated deterioration of timber poles due to climatic loading can severely affect their lifecycle. This approach relies on understanding the changes in structural stability of wooden poles, and it is speculated that its accuracy may benefit the most if larger samples of poles are surveyed, as done by Gezer et al., 2015. This method was not implemented in this thesis given the complete absence of wooden poles in the two-tier network described in paragraph 5.3.1.1. As for record-based or empirical approaches, Dunn et al. (2018) analyzed the damage due to high winds that resulted in electricity supply failings for lines at different voltage. This methodology adopted observations reported by the United Kingdom National Faults and Interruption Reporting Scheme (NaFIRS) and returned the average number of faults per 1,000 km of overhead lines as a function of the wind gust.

This thesis adopted the fragility curves devised by Dunn et al. (2018) due to the fact that they allow to estimate the number of faults directly from the wind gust values, and that they return a number of incidents that can be normalized with respect to the length of any line. The implementation revolved around considering the two curves proposed by the authors (Figure 5.19): a low-resolution curve (equation 5.6) and a high-resolution curve (equation 5.7). Analytically, the two equations are defined as:

$$F_{low} = 3 * 10^{-14} * w^{9.2676} \tag{5.6}$$

$$F_{high} = 1 * 10^{-14} * w^{10.051} \tag{5.7}$$

In equations 5.6 and 5.7, F_{low} and F_{high} refer to the average number of faults per 1000 km of overhead lines obtained with the low-resolution and high-resolution curve, respectively, and w represents the wind gust value used as predictand. The low-resolution curve was obtained by combining wind observations with wind data from a climate model in order to compensate for missing spatial coverage, whereas the high-resolution curve was derived by combining

observations, data from a climate model, and high-resolution fault data provided by a Distribution Network Operator.

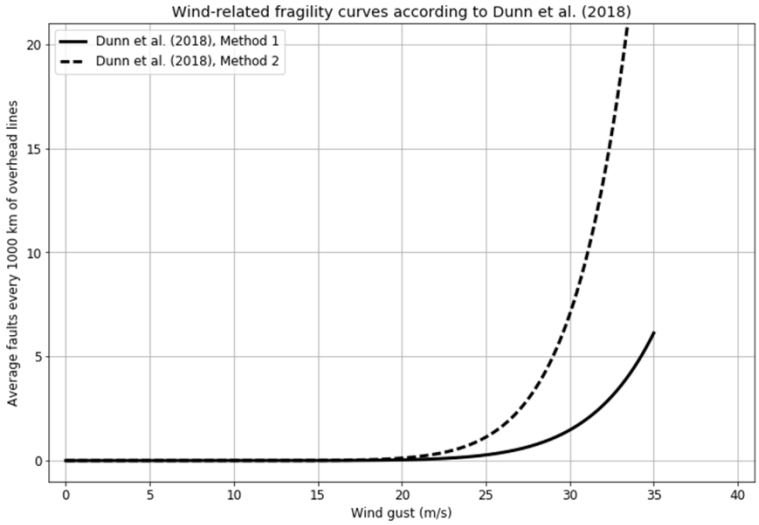

Figure 5.19. The fragility curves proposed by Dunn et al. (2018). Method 1 corresponds to the low-resolution curve (continuous line), whereas Method 2 indicates the high-resolution curve (dashed line).

In the context of this thesis, the two curves were implemented by using $w_{10,3}$ as input value in place of w. The expected number of faults for a given day was computed for each climate horizon by adding up the number of faults computed for each feeder and circuit composing the 132kV and 33-66kV lines:

$$F_{line,day} = \sum_{i=1}^{N_{comp}} F_{comp,day} = \sum_{i=1}^{N_{comp}} \frac{L_{comp}}{1000\ km} * F(\max(w_{10,3})_{comp,day}) \quad (5.8)$$

In equation 5.8, N_{comp} corresponds to the number of feeders or circuits in each 132kV or 33-66kV line, $F_{comp,day}$ is the expected number of faults for a given line component and day, F refers to either F_{low} or F_{high}, L_{comp} is the length in km of each individual component, and $\max(w_{10,3})_{comp}$ is the maximum wind gust hitting the circuit or feeder on a given day. The adoption of the maximum wind gust overlapping a feeder or a circuit was an assumption made to estimate the faults induced by the *worst-case scenario*. This choice was also driven by the ambiguity arising from the fact that, on a given day, multiple $w_{10,3}$ values could be used, as multiple CPM1.5 grid cells overlap a given feeder or circuit.

Equation 5.8 is a clear implementation of the systemic approach discussed in paragraph 2.1.3.1, as it returned the number of faults occurring at the 132kV system, for instance, as a sum of all the faults affecting the sub-systems composing that system. This approach was also implemented as, on a given day, multiple wind gust values affected the system; adopting the maximum wind gust as a reference value for the entire network would have likely resulted in an *overestimation* of the number of faults, especially if the reference value was an outlier occurring in a particularly exposed location. The overestimation in the number of faults returned by this procedure can be estimated to be in the region of +30%, owing to the fact that, on average, the maximum wind gust was found to be 30% higher than the average wind gust hitting the same sub-system.

5.6.2 Development of a bespoke fragility curve for the study area

The fragility curves mentioned in section 5.6.1.1 were developed by Dunn et al. (2018) for the South West of England, whereas the study area of Case Study 2 is located in East-Central England. Wind patterns are known to change at the regional scale (Panteli et al., 2017) due to a number of drivers, including orography, latitude, and large-scale circulation (Hueging et al., 2013; Herrmann et al., 2011). Although the UK Distribution Network Operators (DNOs) typically use assets of similar design, the wind-driven empirical approach used to generate the fragility curves in Dunn et al. (2018) means it is most accurately calibrated to a specific region.

The development of a bespoke regional fragility curve for this case study following the methodology in Dunn et al. (2018) would be sensitive to two key factors that affect the quality of the result: sample size of failure observations and spatial resolution of wind observations.

In terms of sample size of failure observations, it is worth highlighting that the study area used for Case Study 2 is a small fraction, approximately 10% of the domain covered by the Distribution Network Operator (DNO) (Figure 5.20). This entails that the sample of observed failure incidents in the case study area is very small, leading to a less reliable model. There is also only incomplete data on the type of structures, their age, maintenance logs and other aspects, which make the smaller sample size even more sensitive to recent investments or other changes.

The other important factor is the spatial resolution of the wind field. Only 5 meteorological stations maintained by the MetOffice fall within the study area (at Normanby

Hall, Leconfield, Hull East Park, Donna Nook, and Saltfleetby St. Clements), as opposed to the 31 stations used by Dunn et al. (2018).

These two aspects, combined, would produce a model of questionable statistical validity. A coarser field means the relationship between the observed windspeed and asset failure is inevitably less accurate. The availability of data in the case study site means that a low-resolution fragility curve would be coarser than the work by Dunn et al. (2018). An equivalent high-resolution curve could not be produced for Case Study 2 due to lack of knowledge regarding the sub-regions defined by the DNO.

The purpose of this research has been to focus on the effects of network structure and topology, rather than modelling the fragility of assets. The limited observations from the case study region, the assumption that the assets in the case study area are similar to those studied by Dunn et al. (2018), and the fact that the study area itself borders the domain considered by Dunn et al., 2018) (Figure 5.20), justify why specific fragility curves were not developed and those presented by Dunn et al. (2018) were used instead.

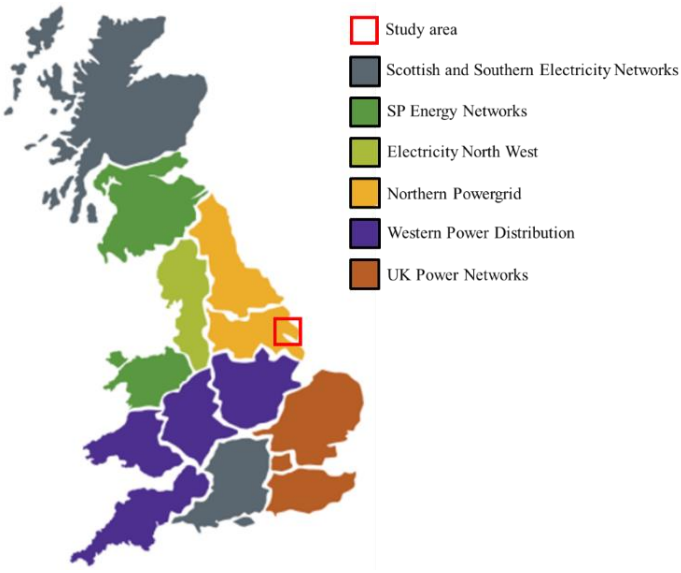

Figure 5.20. Geographical domains covered by Distribution Network Operators (DNOs) in the United Kingdom. The purple area is the one considered by Dunn et al. (2018), and it borders the study area of Case Study 2, which is shown in red. Source: ofgem.gov.uk (2019).

5.7 Stage 6: systemic indicators

5.7.1 Estimating the impact of faults on the two-tier electricity network

One of the objectives of this thesis was to also estimate the impact of the expected daily faults on the two-tier electricity network in both climate horizons. This estimation was obtained quantitatively as the product of the expected faults generated with equations 5.6 and 5.7 for each feeder and circuit by the number of customers served by each feeder and circuit as shown in Figure 5.17. For this purpose, three definitions were used: *i*) *Single Impact* (SI), referring to the impact at the daily scale on each feeder and circuit (equation 5.9); *ii*) *Tier Impact* (TI), referring to the impact at the daily scale on the 132kV or the 33-66kV tier or line (equation 5.10); and *iii*) *Time-Aggregate Impact* (TAI), referring to the impact of faults on each tier during the 13-year timeframe of each climate horizon (equation 5.11). The three definitions are rendered as follows:

$$SI_{i,day,horizon} = F_{i,day,horizon} * C_i \tag{5.9}$$

$$TI_{t,day,horizon} = \sum_{i=1}^{N_{comp}} SI_{i,day,horizon} \tag{5.10}$$

$$TAI_{t,horizon} = \sum_{day=1}^{N_{days}} TI_{t,day,horizon} \tag{5.11}$$

In equations 5.9, 5.10, and 5.11, i represents each feeder or circuit, day represents each day in the 13-year timeframe, $horizon$ corresponds to either the Control or Future climate, C_i is the number of customers served by each feeder or circuit, which was assumed to be time-invariant, t represents either the 132kV or 33-66kV tier, and N_{comp} is the number of feeders or circuits that compose each tier. Equations 5.9 to 5.11 represent a cascade of computations stemming from equation 5.9, and as such they can be combined in a unique form, the outcome being expressed in terms of faults multiplied by customers (equation 5.12):

$$TAI_{t,horizon} = \sum_{day=1}^{N_{days}} \sum_{i=1}^{N_{comp}} F_{i,day,horizon} * C_i$$

(5.12)

This approach was implemented as an alternative to the Customers-Minutes-Loss (CML) computation, which is estimated by each Distribution Network Operator (DNO) and made available via the NaFIRS database. However, although this information was accessible, the lack of a consistent geographic reference made it impossible to determine the relationship between the wind gust in a given day, the number of faults caused, and the associated CML statistic. Ideally, this would be possible if precise geographic information regarding the recorded incident was also recorded, although this is currently not performed by DNOs.

5.7.2 Risk of faults

Another objective of this Case Study was to also estimate the risk of faults to which the 132kV and 33-66kV tiers are exposed, and to investigate how such evaluation changed for the different line components in the same climate horizon, as well as from one climate horizon to another. From the canonical definition of risk adopted by the insurance industry (equation 5.13), where the risk R is generically defined as the product of the probability P of an event multiplied by its consequences C, a modified form was derived (equation 5.14):

$$R = P * C$$

(5.13)

$$AR_{comp,horizon} = \sum_{day=1}^{N_{days}} \left(\frac{F_{comp,day}}{L_{horizon}} * C_{comp} \right)$$

(5.14)

In equation 5.14, $AR_{comp,horizon}$ is the annual risk of faults associated with each component of the 132kV and 33-66kV line, $L_{horizon}$ is the length in years of the climate horizon (e.g., 13 years), N_{days} refers to the total number of days in the horizon, $F_{comp,day}$ represents the expected number of faults computed for a given day and line component by using equation 5.8, and C_{comp} designates the number of customers served by each line component. Akin to equation 5.12,

equation 5.14 returned an annual risk expressed in terms of the average number of customers lost, per year, due to wind gusts. From an analytical perspective, equation 5.14 is in essence similar to equation 5.12, except the fact that $AR_{comp,horizon}$ was an annual rate computed for each component, whereas $TAI_{t,horizon}$ is to be interpreted as an aggregate value computed for each tier or line. As with equation 5.12, $AR_{comp,horizon}$ represents an empirical estimation of the average number of customers lost per year due to wind-related faults, and it is to be considered as an alternative methodology to the use of the CML statistic, which, if geographically referenceable, would have returned more accurate results. The implementation of equation 5.14 on a partitioned two-tier system allowed to unravel potential behavioral differences between the sub-systems or components, enabling the characterization of robustness at a much finer level than allowed by equation 5.12.

5.8 Computational implications of Case Study 2

The computational architecture that was set up for Case Study 2 is conceptually the same as the one implemented for Case Study 1 (see paragraph 4.8). This entails that the algorithms created to evaluate the number of faults caused by the daily maxima high winds on the electricity infrastructure followed a 4-block, Monte Carlo-inspired, brute-force approach (Figure 5.21).

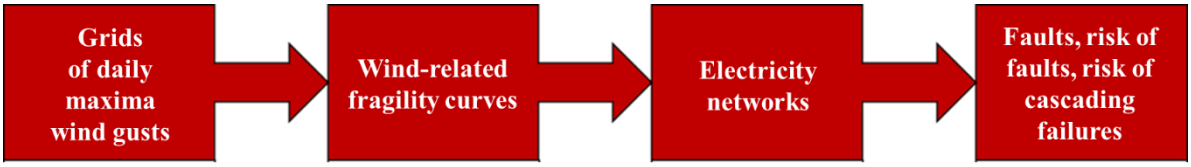

Figure 5.21. The four blocks of the Monte Carlo approach implemented in Case Study 2. This process mirrors the one described in paragraph 4.8 for Case Study 1.

The computational demand of this process was driven by only a few major factors:

1) The first factor was the temporal coverage of the two climate horizons, which corresponds to two 13-year time series of daily maxima wind gust grids. This entails that a total of approximately 4,745 grids were used for each horizon. The extent of such temporal coverage was also a factor limiting the degree of representativeness

of Case Study 2, as a brute-force approach can only generate or evaluate as many iterations or events as there are available;

2) The second factor was the spatial coverage used in this Case Study, which extent is a direct consequence of the spatial domain in which the chosen segment of the infrastructure operates. The computational demand of the spatial coverage was highly influenced by the granularity of the 1.5km resolution of the wind gust grids. In fact, although the chosen spatial domain had a footprint of only $73\ x\ 84$ cells, corresponding to $109.5km\ x\ 126km$, the computational burden on a machine was significantly higher than that of a 12km resolution grids, which would only have required processing approximately 90 cells to cover the same spatial domain;
3) The third and last factor was the computational demand associated with determining the maximum wind gust hitting any components of the 132kV and 33-66kV lines on any day (equation 5.8). This, in itself, was not a particularly demanding operation, as finding the maximum wind gust entailed iterating over the grid cells that overlapped a given 132kV or 33-66kV line and identifying the maximum value. Expressed in Big-O Notation, such operation alone has the same time complexity as finding the maximum value in an unsorted array: $O(n)$, where n is the number of elements in the array. However, this operation was repeated at the daily scale for each time horizon, resulting in an algorithm running in $d\ x\ O(n)$ time, where d is a factor representing the number of days in each horizon. Moreover, such operation was repeated for each line composing the 132kV and 33-66kV electricity networks, resulting in the algorithm running in $d\ x\ l\ x\ O(n)$ time for each electricity network and climate horizon, where l is the individual line. Given the presence of two electricity networks with two different voltages and two climate horizons, the algorithm used to find the maximum wind gust for each line, day, and time horizon ran in approximately $4\ x\ d\ x\ l\ x\ O(n)$ time, where the number 4 represents the two climate horizons and the two electricity networks.

5.9 Limitations of Case Study 2

The methodology described in Chapter 5 is affected by limitations. The first limitation that is worth mentioning revolves around the use of the maximum wind gust value hitting the overhead lines as input to the fragility curve. Whilst this led to an overestimation of the number

of faults per 1000 km of overhead lines, it represents a conservative assumption that can be made for a worst-case scenario. Alternative approaches may include using the average value or performing a sensitivity analysis on a specific segment of the infrastructure for which the number of faults is known.

The second limiting factor is the fact that, for each climate horizon, maps showing the spatial distribution of wind gust maxima were used. This corresponds to the assumption that the maximum values occurred at the same time over the study area, which led to overestimating the final number of faults. One solution to this problem is considering actual storms by using the climate output of dates associated with historical events rather than producing maps with statistical values.

Another source of limitation is the fact that the pre-processing phase described in paragraph 5.3.1.2 introduced modifications to the actual layout of the electricity network. These modifications generally resulted in lengthier overhead lines due to overhead segments, separated by underground segments, being connected. One possible solution to this could be considering the underground sections as non-existent, thus avoiding the creation of longer lines.

As with Case Study 1, the limitations discussed in this paragraph certainly constitute sources of uncertainty, although they do not diminish the significance of the final results shown in Chapter 7. Again, these limitations represent details that can be improved in future iterations of this work.

Chapter 6. Case Study 1: Results and Discussion

This chapter discusses the results and their implications with reference to the stages to which this case study offers a novel contribution. As outlined in paragraph 3.2.1, Case Study 1 contributes to Stage 1, Stage 3, and Stage 6. However, since Stage 3 refers to the generation of network models, no modelling results are available apart from the generation of the network models themselves, which is extensively discussed in paragraph 4.4.1. As such, the following results refer to Stage 1 and Stage 6.

6.1 Stage 1: fractal spatial hazards

6.1.1 Fractal spatial hazards as generic hazards

6.1.1.1 Very smooth and very fragmented surfaces were the most detrimental spatial patterns

In order to accomplish the objectives of Case Study 1 of this thesis, a total of 50,000 fractal or Brownian surfaces were generated by adopting the procedure known as the Spectral Simulation method (Priestley, 1981; Saupe, 1988). This methodology allowed to produce five arrays of 10,000 surfaces each, with the pattern of spatial autocorrelation of each array being governed by values of the Hurst exponent in the range $H = [0.6, 0.7, 0.8, 0.9, 1.0]$. Lower H values produced surfaces with a mild positive spatial correlation resulting in more fragmented objects, whereas higher H values yielded smoother objects as a result of a strong positive spatial correlation (Figure 6.1).

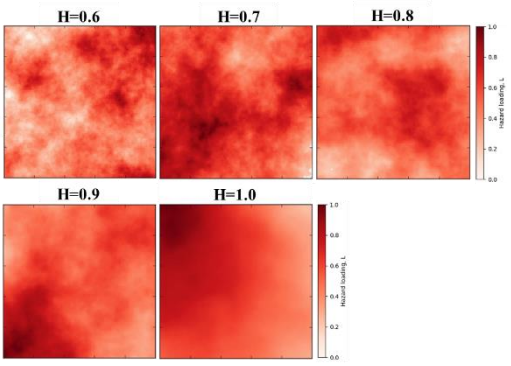

Figure 6.1. The increase with H of the spatial autocorrelation of the Brownian surfaces resulted in the appearance of progressively smoother objects.

The implementation of the flow chart described in Figure 4.26 returned a *multidimensional set of results* due to three elements: the five values used for the Hurst exponent H which resulted in five classes of spatial patterns, the five values used for the failure threshold Ft, and the four network models. With the aim of determining which spatial pattern caused the highest number of 1st and 2nd order failures altogether, the analysis of the results was preceded by the identification of the most detrimental spatial pattern for the network models. This was accomplished by first selecting two specific values of Ft, $Ft_{low} = 0.3$ and $Ft_{high} = 0.7$, which were assumed to represent a weak and a strong network, respectively. Then, the computation proceeded to determine the average number of surviving nodes left in the four networks after the failures caused by the combinations $C_{low} = (H, Ft_{low})$ and $C_{high} = (H, Ft_{high})$ of 2,000 Brownian surfaces each.

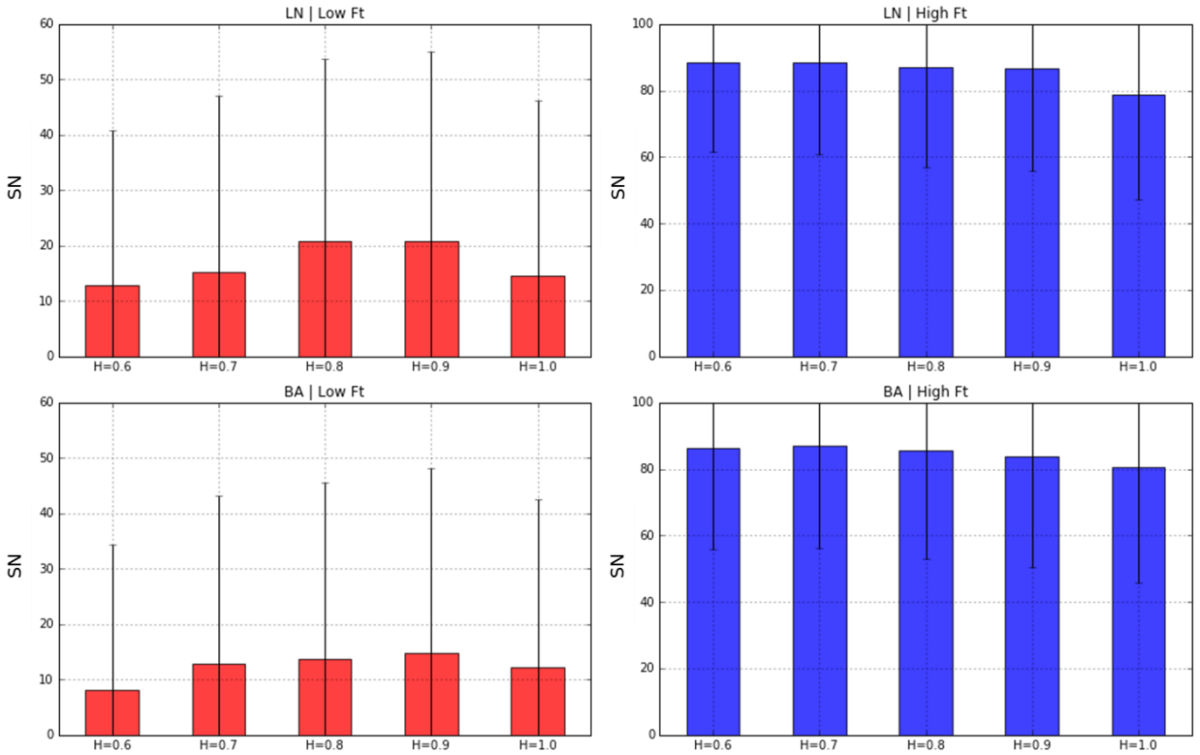

Figure 6.2. Average number (labelled as SN) of surviving nodes left in the Lattice Network (LN) and Scale-Free Network (BA) after the failures caused by the combinations C_{low} (labelled Low Ft, in red) and C_{high} (labelled High Ft, in blue). The height of each bar was computed out of 2,000 Brownian surfaces. The black line represents the standard deviation of the number of surviving nodes. On the y-axis, SN is the namesake metric described in paragraph 4.7.1.

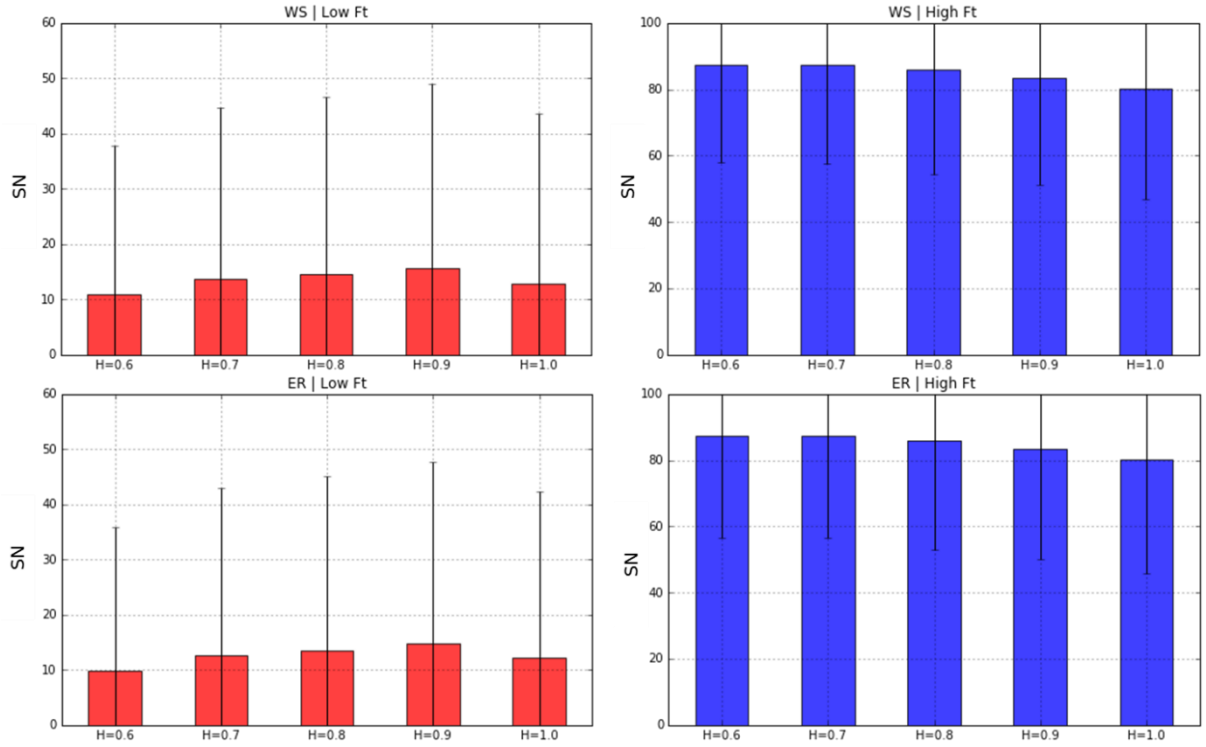

Figure 6.3. Average number (labelled as SN) of surviving nodes left in the Small-World Network (WS) and Random Network (ER) after the failures caused by the combinations C_{low} (labelled Low Ft, in red) and C_{high} (labelled High Ft, in blue). The height of each bar was computed out of 2,000 Brownian surfaces. The black line represents the standard deviation of the number of surviving nodes.

Figures 6.2 and 6.3 show that, for the combination $C_{low} = (H, Ft_{low} = 0.3)$, the lowest average number of surviving nodes $SN_{Ft=low}$ always corresponded to $H = 0.6$, which is associated with the lowest degree of spatial autocorrelation. Among all four network models, the Lattice Network (LN) showed a maximum of 12.81 surviving nodes, whereas the lowest number was found in the Scale-Free Network (BA), with 8.03 surviving nodes. In the case of the $C_{high} = (H, Ft_{high} = 0.7)$ combination, the lowest average number of surviving nodes $SN_{Ft=high}$ was consistently in correspondence of $H = 1.0$, which denotes surfaces with the highest degree of spatial autocorrelation.

The Random Network (ER) showed a maximum number of 80.96 surviving nodes, whereas the lowest number found was 78.88 surviving nodes (LN). The implication of these results is that, on average, when the networks operated with a low failure threshold, the fragmented Brownian surfaces associated with $H = 0.6$ were the ones causing the highest number of failures. On the other hand, when a high failure threshold was in place, the smoothest surfaces associated with $H = 1.0$ were on average the most detrimental. Owing to the small size of the network models adopted, which are composed of 100 nodes, the difference in height

between the lowest and the highest red bar was limited. The same was true for the difference between the lowest and the highest blue bar, and it is speculated that the adoption of larger networks may exacerbate the role of $H = 0.6$ and $H = 1.0$ as the most detrimental spatial patterns for the C_{low} and C_{high} combination, respectively.

The justification for adopting $Ft_{low} = 0.3$ and $Ft_{high} = 0.7$ instead of other values is that: *i)* $Ft_{low} = 0.1$ would have caused consistent failures, being associated with an extremely weak network, whereas on the other hand, $Ft_{high} = 0.9$ would have resulted in very limited failures; and *ii)* in both cases, an excessively low or high failure threshold would have diluted the different behaviors of the four network models. As a result of this analysis, of the 25 $C = (H, Ft)$ combinations described in Table 4.3, only the 10 combinations with $C_{low} = (H, 0.3)$ and $C_{high} = (H, 0.7)$ are reported in this chapter for analysis and discussion, as they represent a *worst-case scenario*.

6.1.1.2 Advantages, disadvantages, and limitations of the Brownian surfaces

The adoption of the synthetic Brownian surfaces as fractal spatial hazards needs adequate consideration of the limitations, advantages, and disadvantages of the SSm methodology. The list of advantages includes:

1. Limited computational demand;
2. Compatibility with Monte Carlo or other brute-force simulation algorithms where the stochasticity of the fBm process is harnessed to the fullest;
3. Isotropy and, unlike deterministic approaches, explicit control over the range of spatial patterns reproducible by means of a single parameter, the Hurst exponent H;
4. For a specific value of H, ability to reproduce the spatial distribution of natural phenomena with significant accuracy (Saupe, 1988);
5. Ability to replace the use of datasets derived from Climate Models, provided the execution of a preliminary conditioning process aimed at aligning the intrinsic isotropy of the surfaces to the study area-specific and natural hazard-specific spatial gradients.

On the other hand, the list of disadvantages includes:

1. Necessity of a preliminary conditioning process, the lack of which can cause excessive randomness in the spatial patterns, resulting in inappropriate surfaces;
2. Boundary effects (see Figure 6.4 for clarity);
3. Symmetry about the $y = x$ axis;
4. Necessity of correcting the cumulative distribution function of surface elevations with adequate techniques, such as the quantile mapping, to ensure alignment with the observed cumulative distribution function of the targeted natural hazard. This is needed as the Brownian elevations span the range $\in [0,1]$, and need to be scaled up to the range of values typical of a specific spatial natural hazard.

The adoption of the conditioning process and the correction technique mentioned above is strongly encouraged in case studies where the Brownian surfaces are used as a synthetic tool for reproducing realistic natural hazard spatial patterns. Although the additional steps may increase the computational demand associated with the Brownian surfaces, due to the importance of the aspect outlined by Saupe (1988), their advantages appear to outweigh their disadvantages. However, an important limitation has to be considered regarding periodicity. It is known from several sources in the literature (e.g., Saupe, 1988; Dieker, 2003) that the Brownian surfaces obtained with the SSm method are periodic, and this aspect may be particularly inconvenient for impact studies revolving around these surfaces. In fact, it is very unlikely, if not unrealistic, to observe spatial natural hazards featuring repeated patterns at regular intervals.

In addition to the periodicity resulting from the symmetry about the $y = x$ axis, another form of symmetry was highlighted. Mapping the distribution of frequency of peak elevations z_{max} in each $N_x * N_y = N * N = N^2 = 256x256$ surface grid revealed that increased frequencies occurred at ($x = {}^{N}/_{2} \pm k\,{}^{N}/_{2}, y = {}^{N}/_{2} \pm k\,{}^{N}/_{2}, k \in \mathbb{N}^0$) and to a lesser extent along the straight lines connecting these points (Figure 6.4), regardless of the H value used. This phenomenon is the result of a boundary effect becoming visible every $N/2$ cells, and it is here suggested that it has to be characterized for every size interval. This characterization is pivotal, allowing to identify the areas of the grid that are bereft of the boundary effect, e.g. the areas where isotropy can be observed. As a result, it is suggested that any impact study involving the use of SSm-generated Brownian surfaces should be conducted by either cutting a buffer frame out of the surface, so to minimize the boundary effect but with the disadvantage

of obtaining a smaller grid, or to consider alternative methods (see paragraph 4.2.3). In this case study, the smaller grid used as spatial hazard was sliced from the upper left corner of the grid in Figure 4.7 so to avoid the $y = x$ symmetry, and sufficiently away from the grid boundary so to avoid the other form of periodicity.

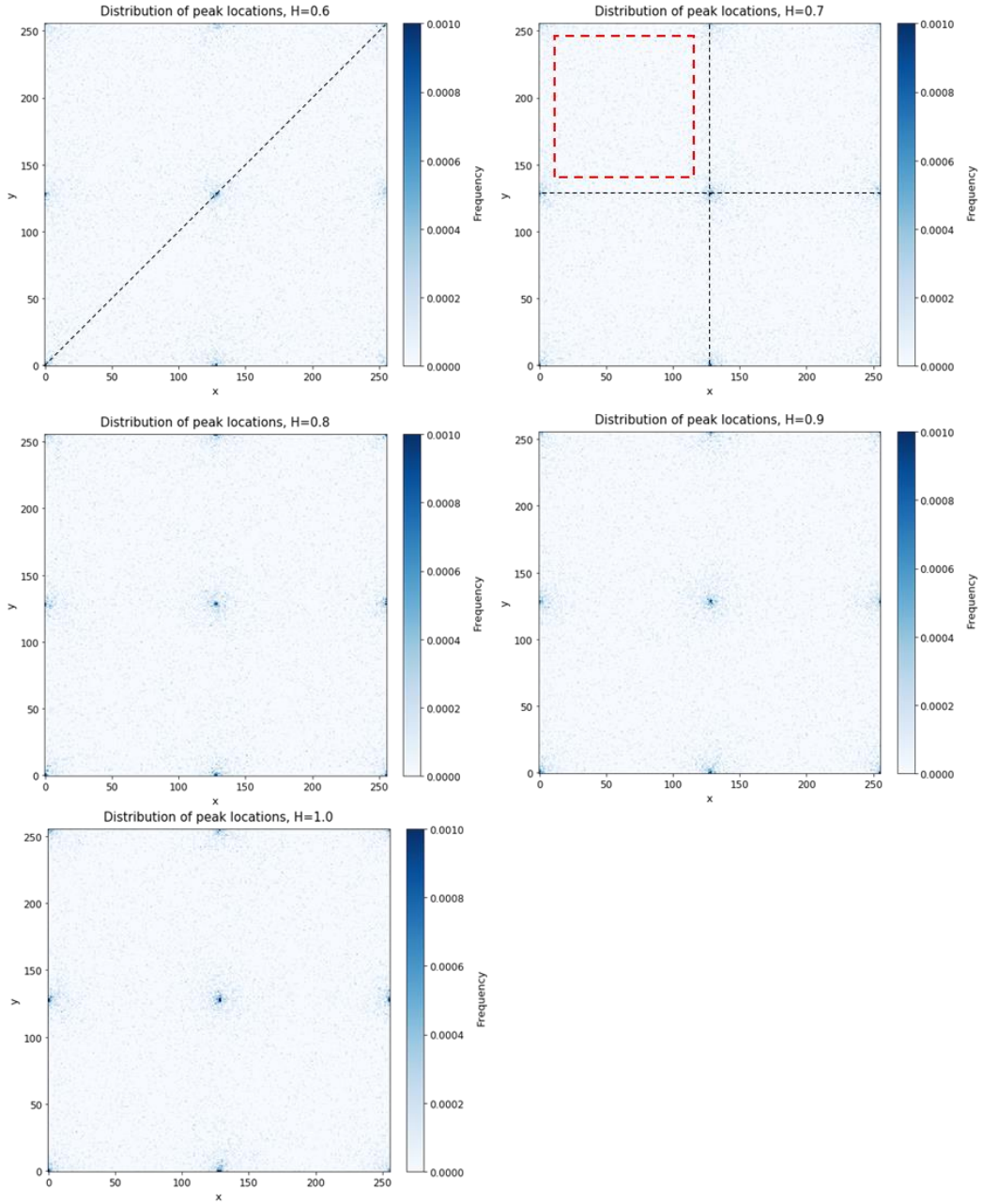

Figure 6.4. Distribution of the frequency of peak elevations z_{max} in 10,000 realizations of each class of Brownian surfaces. Regardless of the H value used, the pattern was the same, although the frequency increases with H. In the top left corner, the $y = x$ axis is shown. In the top right corner, the dashed black lines represent the periodicity found every $N/2$ cells, whereas the dashed red line indicates one suitable grid slice where periodicity and boundary effects are not present.

6.1.2 Geometrical difference between circular-shaped and fractal spatial hazards

As discussed in paragraph 4.2.8.1, one important objective of Case Study 1 of this thesis was to highlight the geometrical differences between circular-shaped spatial hazards, which are deterministic in nature, and fractal spatial hazards, which are the result of a stochastic process. Moreover, these two classes of objects differ in that the circles feature the radius as a characteristic geometric parameter, whereas fractals do not. As such, a geometrical comparison between the two classes of objects had to be performed not by using the original objects but on a level playing field. Consequently, this was done by computing the ellipses with the same 2nd central moments as the circles and fractals and analyzing them with image processing techniques. Behind the implementation of the procedure detailed in paragraph 4.2.8.1 was the hypothesis that, between a fractal and a circle of the same size, the fractal features an equivalent ellipse with a longer major axis. This hypothesis is rooted in the fact that points on a fractal surface are not evenly distributed, and they are not equally distant from the center of the surface as they are on a circle.

Figure 6.5 shows how the length of the major axis of 10,000 circles compared to that of 10,000 Brownian surfaces obtained with $C = (H = 0.8, Ft = 0.5)$. The major axis of the ellipses associated with the fractal surfaces, normalized with respect to the size of the sliced grid, appear in many cases to be longer than those of the ellipses associated with circles. This difference appears to peak when the Critical Footprint, here interpreted as the object area, nearly reaches 40%, with a maximum difference of almost 80%. It is also worth noticing that, while the determinism associated with the circles coerces the dark dots into following trends that are associable to different radiuses, the stochasticity of fractals allows the white dots to appear in many other parts of the graph.

In terms of how the points are distributed with respect to the center of the object, this highlights the fact that the SSM method generates Brownian surfaces with a significant degree of variation. As the Critical Footprint approaches 80%, entailing that the fractal surfaces and circles occupy the entire grid, the white dots are all located above the dark dots, highlighting the fact that, as the fractals increase in size, the points on their surfaces are consistently more scattered. In addition, as the Critical Footprint reaches 100%, the normalized axis length for the circles tends to 1.0, implying that circles are constrained by the size of the grid where they are generated. The same seems not to be true for fractals, as they tend to converge to a value of approximately 1.2, which entails that the separation between points on the Brownian surfaces is not constrained by the size of the grid. These results are better summarized in Figure 6.6, where the x-axis shows the binned Critical Footprint and the y-axis, for each bin, shows the

average major axis length for the fractals and circles. The results shown in Figures 6.5 and 6.6 refer to a value of the Hurst exponent $H = 1.0$, which is synonymous with smooth surfaces, whereas the failure threshold used, $Ft = 0.5$, is the central value of the range of thresholds adopted in this case study.

It is speculated that the use of a different value for the Hurst exponent has a more profound effect than a different threshold, due to the fact that the former controls the nature of the resulting spatial pattern, whereas the latter only establishes a higher or lower surface datum. Given that $H = 1.0$ is associated with fractal objects with the highest spatial autocorrelation, it is also suggested that the trend shown for fractals in Figure 6.5 is the mildest observable among fractals, and that more fragmented surfaces may show larger geometrical differences. The geometrical difference, coupled with the ability to control the degree of spatial autocorrelation featured by the fBm process and with the fact that natural hazards are unlikely to feature a deterministic footprint, constitutes a major argument in favor of the use of the Brownian surfaces in place of *any* form of deterministic hazard footprint.

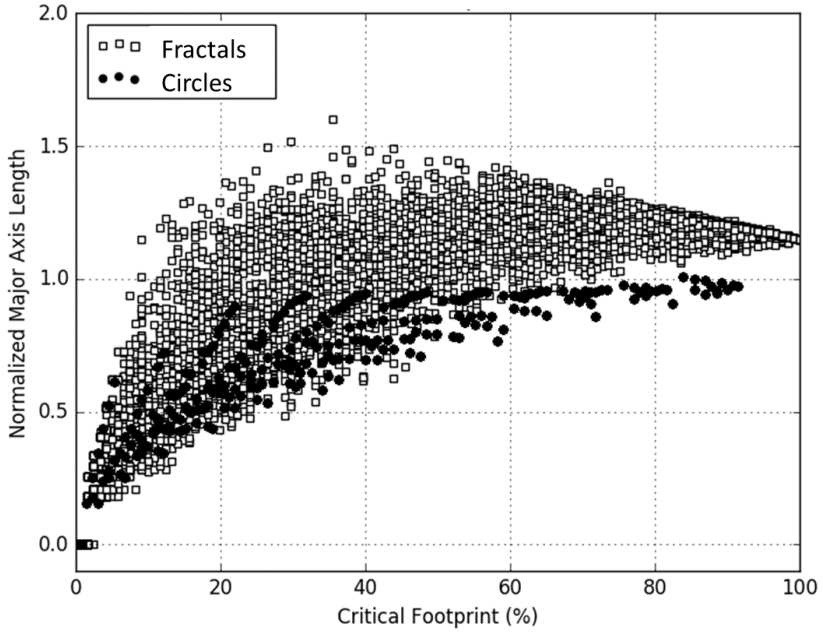

Figure 6.5. Comparison between the normalized length of the major axis of the ellipses associated with circles (here shown in black) and those associated with fractals (here shown in white). This graph was obtained by analyzing 10,000 circles and 10,000 Brownian surfaces generated with $C = (H = 1.0, Ft = 0.5)$. The Critical Footprint here represents the surface area of the circles and the surface area of the fractals where $z > Ft$ as a percentage of the grid where the circles and fractals were generated. The axis length was normalized with respect to the side of a grid composed of $256x256$ cells.

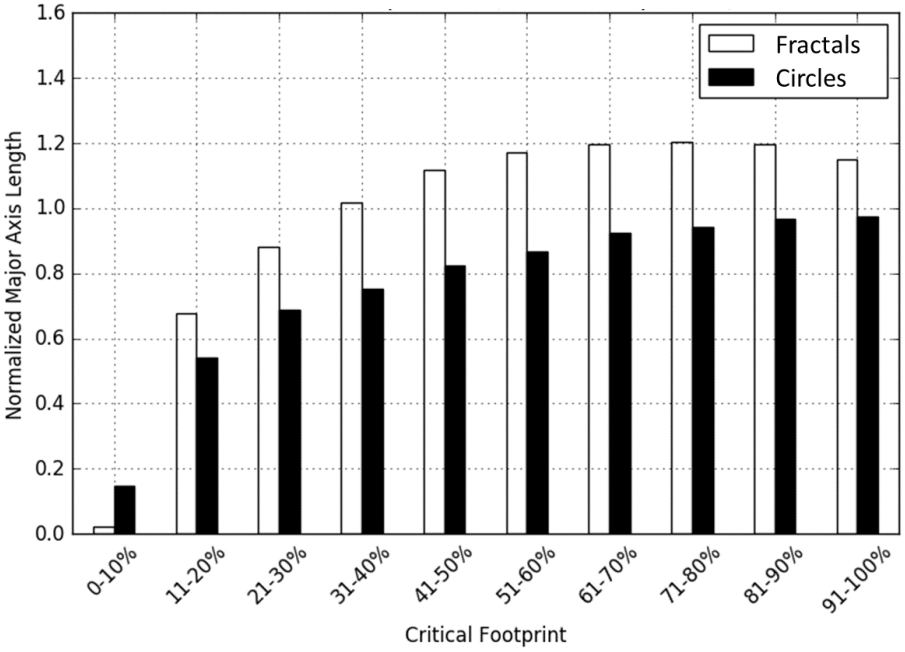

Figure 6.6. Bars showing the average major axis length for each bin of Figure 6.5. It is interesting to notice that circles only have longer axes when the fractals have very limited size. However, as the fractal size increases, the average length of the major axis of the corresponding ellipses is, on average, constantly above that of circles. The difference between the two types of bars peaks around the 41-50% bin, suggesting that fractals that occupy up to half the size of the grid where they are generated have their surface points significantly more scattered than circles.

6.2 Stage 6: impact quantification

6.2.1 Impact of the fractal spatial hazards on the infrastructure models

As a consequence of the aspects highlighted in paragraph 6.1.1.1, the results regarding the impact of fractal spatial hazards on the four network models are presented with reference to two worst-case scenarios: $S1 = (H = 0.6, Ft_{low} = 0.3)$ and $S2 = (H = 1.0, Ft_{high} = 0.7)$, each one consisting of 2,000 fractal spatial hazards. The first scenario, $S1$, refers to weak networks that show noticeable vulnerability to highly fragmented spatial hazards; the second scenario, $S2$, revolves around strong networks that are most vulnerable to continuous spatial hazards. The results are reported following the order of the *robustness metrics* as presented in paragraph 4.7.1.

6.2.1.1 Number of Surviving Nodes (SN)

The SN metric is defined in paragraph 4.7.1 as the number of nodes in the network that survive both 1st and 2nd order failures, remaining active after the superimposition of fractal spatial hazards with increasing size or Critical Footprint (CF). This also constitutes a measure of the ability of the network to preserve its functioning capacity, under the assumption that a higher number of active nodes corresponds to an actual capacity that is closer to that featured in the unperturbed condition.

From the analysis of Figures 6.7 and 6.8 it stands out that the transition from scenario S1 to scenario S2 resulted in fractals of the same size producing lower SN for all networks, which implies that the adoption of a higher failure thresholds did not prevent smoother fractal surfaces from causing more failures. In both S1 and S2, the Lattice Network (LN) had its trends almost completely above the $y = 100 - x$ line, which represents a situation where the number of failed nodes is directly proportional to the size of the fractal spatial hazard, $N'_A = \alpha * CF$, with $\alpha = 1$. This is a direct consequence of the fact that the gridlike distribution of edges in LN perfectly matches the 1-to-1 pairing between the nodes in the network and the cells in the fractal grid (Figure 4.17). This suggests that, for highly regular networks such as LN, the number of failures may not exceed the linear relationship with the size of the spatial hazard, implying that the relationship $N'_A = \alpha * CF$ constitutes an upper bound for the number of failures, with α representing the number of grid cells superimposed on each node.

A completely different behavior is observable for the Scale-Free Network (BA), where the trend was only sporadically above the $y = 100 - x$ line in scenario S1, and less frequently so in scenario S2. This means that, in both scenarios, the number of failures caused in BA was significantly larger than that caused in LN by a fractal spatial hazard of the same size. In fact, whilst fractal surfaces with $CF \cong 40\%$ corresponded to $SN \geq 60$ for LN in S1, the same surfaces would result in $SN \cong 10$ for BA. In S2, the gap would increase, as fractal surfaces with $CF > 40\%$ were able to produce $SN = 0$, entailing that the BA network had failed completely. The variability of the BA trend is noticeable in both scenarios, with the lower bound of the scatter plot resembling a non-linear behavior. This aspect may find explanation in the fact that the BA structure includes the presence of highly connected hubs, and that such hubs constitute the only connection for a significant fraction of nodes. In the worst-case scenario of a fractal surface being superimposed on one or multiple hubs, even a limited size (e.g., $CF \cong 40\%$) was enough to produce a low or null SN due to the high number of poorly connected nodes that failed.

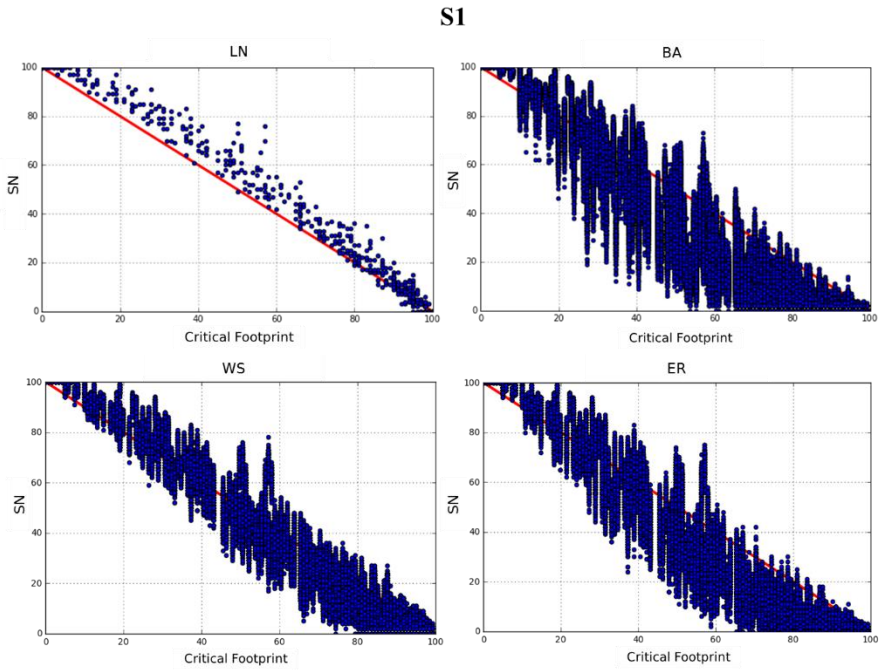

Figure 6.7. Scenario S1: graphs showing the change in SN with the increase in size of the fractal spatial hazards. Whilst the LN trend refers to only one network realization (see paragraph 4.4.1), each one of the other three panels show the aggregate trends referring to 300 network realizations. As a reference, the red line indicates the $y = 100 - x$ line, which entails that the number of failed nodes is directly proportional to the size of the fractal spatial hazard. Except for the LN trend, which is composed of 2,000 points, the BA, WS, and ER trends feature 600,000 points each.

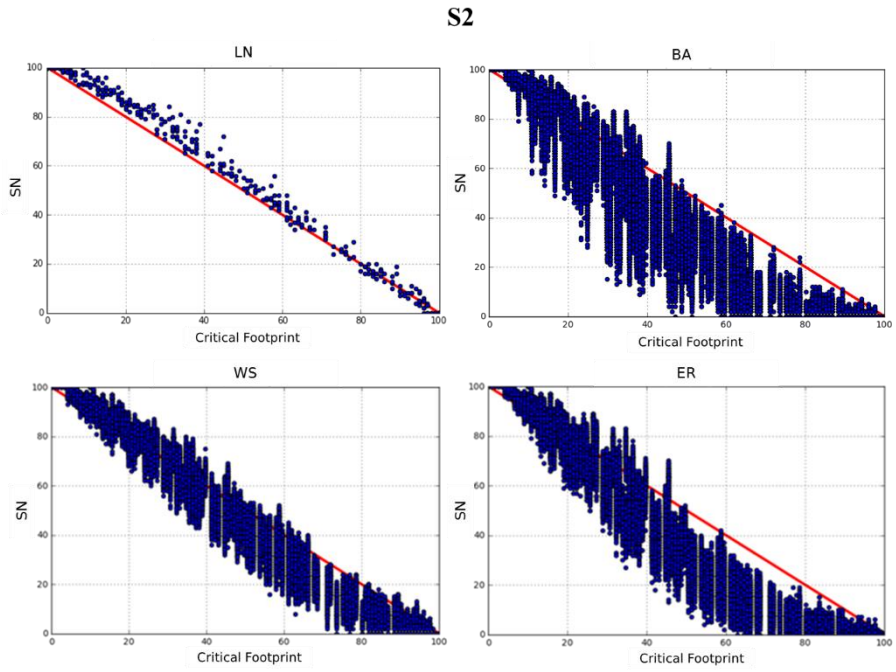

Figure 6.8. Scenario S2: graphs showing the change in SN with the increase in size of the fractal spatial hazards. Whilst the LN trend refers to only one network realization (see paragraph 4.4.1), each one of the other three panels show the aggregate trends referring to 300 network realizations. As a reference, the red line indicates the $y = 100 - x$ line, which entails that the number of failed nodes is directly proportional to the size of the fractal spatial hazard. Except for the LN trend, which is composed of 2,000 points, the BA, WS, and ER trends feature 600,000 points each.

This suggests that the relationship $N_A' = \alpha * CF$ may not be linear for the BA structure. In fact, it should be changed to account for the source of non-linearity, which is likely to correspond to the number of nodes affected by 2nd order failures. Such number is highly variable, being dictated by the network structure, the location of the fractal spatial hazard with respect to the hubs, and the seed used to generate the network. In situations where the fractal spatial hazard affected nodes with a very limited degree k, the BA trend exceeded the $y = 100 - x$ line, indicating the existence of a pseudo-linear bound, although this was more easily visible in $S1$ than in $S2$. With respect to the ER and WS networks, their behavior in both scenarios was found to be between the extremes associated with the LN and BA networks. Specifically, the variability shown by the ER trend, the shape of the lower bound of the scatter plot, and an increased vulnerability to failures in S2 seem to align the ER networks more to the BA behavior. Similarly, whilst the WS trends showed non-linearity in the lower bound of the scatter plots, their vulnerability to the fractal spatial hazards seemed mitigated with respect to both ER and BA networks.

The results shown here are in agreement with Albert et al. (2000), Buldyrev et al. (2010), and Chopra et al. (2016), who concluded that the presence of hubs remarkably increases the vulnerability of BA networks to failures caused by random or targeted attacks. Moreover, these results extend such conclusions, indicating that the peculiar vulnerability to failures shown by BA networks persists in the presence of more realistic failure patterns.

6.2.1.2 Spatial Robustness (SR)

Spatial Robustness (SR) was defined in paragraph 4.7.1 as the ability of each network to minimize the number of 2nd order failures, e.g. failures occurring outside the footprint of the fractal spatial hazard. This metric was implemented to identify the behavior of each network model under the hypothesis that the topological structure of a network may either facilitate or contrast the spreading of failures in locations that are further away from the hazard footprint. As a complement to SR, the propagation buffer p_b was also introduced, with the aim of evaluating how far from the hazard footprint the 2nd order failures occurred. As a result, a spatially robust network in the context of this thesis is not just a network with low SR, but also one with low p_b.

As a representative value for SR, table 6.1 shows its 95th percentile SR_{95}, which allows to estimate the extreme behavior of the four network models. In both scenarios, the LN networks were found to have the lowest number of 2nd order failures, with $SR_{95} = 5.05$ in $S1$

and $SR_{95} = 4.00$ in $S2$, which correspond to a very limited percentage of nodes if compared to the other models. On the other side of the spectrum were the BA networks, which reported $SR_{95} = 27.00$ in $S1$ and $SR_{95} = 23.17$ in $S2$. These numbers suggest that the 2nd order failures affected 27% of the nodes in the network in $S1$ and 23.17% in $S2$, depicting a situation where the scale-free structure was not just the most affected by 2nd order failures, but also one where failures outside the fractal footprint could affect around 25% of all nodes.

In a similar fashion to what has been described in paragraph 6.2.1.1, the ER networks showed a similar behavior to the BA networks, whereas the WS networks featured a more mitigated behavior. These results seem to confirm the structural vulnerability of the BA networks discussed earlier. In fact, values as high as $max(k) = 48$ and $k_{95} = 36$ indicate topological structures where the main hub could reach 35-50% of all nodes in the network. This entails that up to 50% of all nodes may have shared a unique connection with the main hub, potentially paving the way for the spreading of disruptions should the main hub fail. On the other hand, the ubiquitous lack of hubs and low-degree nodes found in the LN networks appears to have greatly reduced this phenomenon, as 62% of all nodes had $k = 4$ connections, and as such there was enough redundancy to avoid significant 2nd order failures.

It is worth mentioning that SR_{95} appeared to be particularly sensitive to an increase in the number of connections shared by the main hubs. In fact, the 100% increase in k_{95} observed while comparing the LN networks to the models with the closest behavior (e.g., the WS networks) produced an increase in SR_{95} of 236.6% in $S1$ and 225% in $S2$, highlighting a possible non-linear relationship between $max(k)$, or equivalently k_{95}, and SR_{95}. It is also worth noticing that the transition from $S1$ to $S2$ resulted in a decrease in SR_{95}, suggesting that the adoption of a higher failure threshold may counterbalance the increased number of failures caused by smooth hazard surfaces, as observed in paragraph 6.2.1.1.

The propagation buffer p_b was defined in paragraph 4.7.1 as the Euclidean distance, measured from the edge of the fractal footprint, between the closest and farthest 2nd order failures. The aim of this complement metric was to quantify how deep into the network structures the 2nd order failures propagated, and whether different network models exhibited different behaviors. Table 6.2 reports the 95th percentile of the propagation buffer, $p_{b,95}$, obtained from 2,000 Brownian surfaces and 1 realization for LN, and 2,000 Brownian surfaces and 300 realizations for the other network models. The values $d_{1,95}$ and $d_{2,95}$ are also reported, which represent the distance between the footprint hotspot and the closest 2nd order failures to the footprint edge and the distance between the footprint hotspot and the farthest 2nd order failures from the footprint edge, respectively (see Figure 4.21).

In both scenarios, the LN networks featured the narrowest propagation buffer, whereas the largest buffers were those of the BA and ER networks, which also showed very similar behaviors. The WS networks seemed to better limit the spatial spreading of failures when compared to the previous two. It is interesting to notice a consistent increase in $p_{b,95}$ in the transition from $S1$ to $S2$: this describes a situation where, whilst the impact of smooth fractal surfaces reduces the number of 2nd order failures for all network models, it exposes them to 2nd order failures that occur farther away from the hazard footprint. Based on a comparative analysis performed on Tables 6.1 and 6.2, it stands out that the LN networks performed as the most spatially robust in the context of this thesis, as they featured the lowest SR_{95} and $p_{b,95}$ in both scenarios, followed by the WS networks. On the other hand, the BA networks were found to possess the least spatially robust structure, with the highest SR_{95} of both scenarios and the highest $p_{b,95}$ in $S1$.

Table 6.1. The 95th percentile of Spatial Robustness (SR_{95}) for each network model and both scenarios. Also reported are the maximum degree $max(k)$ found in 300 network realizations, as well as the 95th percentile, k_{95}.

Network model	SR_{95}		$max(k)$	k_{95}
	$S1$	$S2$		
Lattice Network (LN)	5.05	4.00	4	4
Scale-Free Network (BA)	27.00	23.17	48	36
Small-World Network (WS)	17.00	13.00	10	8
Random Network (ER)	24.00	21.00	14	11

Table 6.2. The 95th percentile of the propagation buffer ($p_{b,95}$) for each network model and both scenarios. Also shown are $d_{1,95}$ and $d_{2,95}$. These values were computed for 2,000 Brownian surfaces and 1 realization for LN, and 2,000 Brownian surfaces and 300 realizations for the other network models. The values shown are normalized with respect to the width of the fractal grid.

Network model	$d_{1,95}$		$d_{2,95}$		$p_{b,95}$	
	$S1$	$S2$	$S1$	$S2$	$S1$	$S2$
Lattice Network (LN)	0.466	0.481	0.829	0.870	0.363	0.389
Scale-Free Network (BA)	0.358	0.318	0.950	1.000	0.592	0.689
Small-World Network (WS)	0.379	0.359	0.937	0.999	0.558	0.640
Random Network (ER)	0.360	0.320	0.949	1.000	0.590	0.690

6.2.1.3 Fragmentation Index (FI)

The Fragmentation Index (FI) was introduced in paragraph 4.7.1 with the aim of gauging the tendency of each network to fragment as a result of the failures induced by the fractal spatial hazards. The objective of this metric was to quantify the number of fragments, or islands, composing the perturbed networks, where each island corresponds to a cluster of active nodes or *connected component*. A high value of FI was associated with a high number of islands, entailing that the network model was particularly prone to fragmentation. On the contrary, low values of FI indicated the tendency of a network to remain intact in spite of the failures.

Figure 6.9 shows how the 95th percentile of the number of islands, labelled as FI_{95}, changed with the increase in size of the fractal spatial hazards. To obtain a neater representation of the trends, the size of the hazards (Critical Footprint, CF) was divided into 10 bins of equal width, each bin representing a percentage of the total area of the fractal grid. As a general trend, the transition from scenario $S1$ to scenario $S2$ resulted in a slight decrease in FI_{95} for certain network models. Also, the same transition produced an anticipated peak in all models except the ER networks, entailing that, in $S2$, smaller fractal spatial hazards were generally required to produce the highest FI_{95} value. This may suggest that a higher failure threshold limits the number of fragments in which the networks are divided, but it also indicates that spatially contiguous hazard surfaces do not have to be particularly large in size to result in a high number of fragments.

The LN networks showed the lowest FI_{95} values in both scenarios, reaching a maximum $FI_{95} = 3$ for $70\% \leq CF \leq 90\%$ in $S1$ and $FI_{95} = 2$ for $50\% \leq CF \leq 90\%$ in $S2$. This suggests that a network model that follows a regular grid may exhibit a remarkable robustness to fragmentation. Contrarily, the ER networks displayed the highest FI_{95} values in both scenarios, peaking at $FI_{95} = 8$ for $40\% \leq CF \leq 60\%$ in $S1$ and $FI_{95} = 7$ for $40\% \leq CF \leq 70\%$ in $S2$. The high number of islands typically displayed by the ER networks are in accordance with the results of Albert et al. (2000), who documented a remarkable proneness to fragmentation under the influence of random and targeted attacks, as well as the presence of thresholds past which the phenomenon becomes more evident. The results shown here extend the conclusions of Albert et al. (2000) to the case of realistic spatial hazards and locate the above-mentioned thresholds at $10\% \leq CF \leq 30\%$ in both $S1$ and $S2$.

Whilst the BA networks displayed the closest behavior to the ER networks, reaching $FI_{95} = 6$ for $40\% \leq CF \leq 60\%$ in $S1$ and $FI_{95} = 6$ for $30\% \leq CF \leq 60\%$ in $S2$, the WS

networks offered an interesting performance. In $S1$, the value $FI_{95} = 3$ was reached with fractals that were almost double in size than those that produced the same number for the BA networks. In $S2$, the value $FI_{95} = 6$ was reached with fractals that were nearly three times as large as those that yielded the same value for the ER networks. This suggests that, whilst the WS networks were significantly less robust than the LN networks, they offered a noticeable advantage over the BA and ER networks in both scenarios.

It is worth noticing that $FI_{95} = 1$ meant that the networks were displaying only one island, e.g. the network in its entirety. In addition, all network models displayed $FI_{95} = 0$ with $90\% \leq CF \leq 100\%$, indicating that fractals occupying the entire study area resulted in complete failures, hence the lack of islands.

The results discussed in this paragraph depict a situation where the ER and BA networks are particularly prone to fragmentation, the WS networks perform satisfactorily until the critical size $40\% \leq CF \leq 50\%$ is reached, and the LN networks are rather robust. These conclusions have implications that can be either uneventful or damaging for the infrastructure models. In fact, as pointed out by Hines et al. (2015), if an infrastructure is operated and governed centrally, as it is the case for the infrastructures of most Developed Countries, the proneness to fragmentation may play a very detrimental role, as the nodes of the network are designed to be served and not to function autonomously. On the other hand, infrastructures such as the microgrids or the water distribution systems in Developing Countries, the proneness to fragmentation may be uneventful, as the nodes composing these networks are designed to operate both on- and off-grid, as it may be the case for photovoltaic systems.

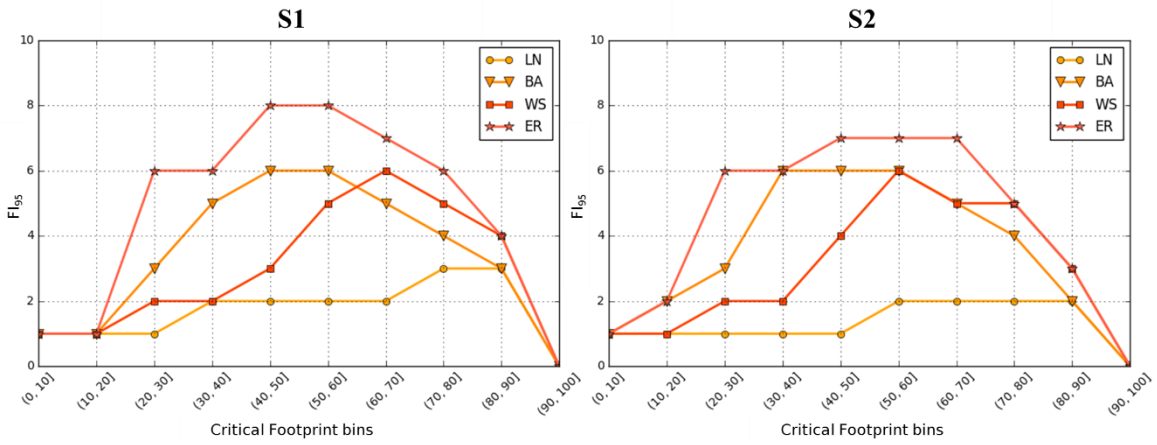

Figure 6.9. Change in the 95th percentile of the Fragmentation Index (FI_{95}) with the size of the fractal spatial hazards. The latter is binned and expressed in percentage with respect to the size of the fractal grid. The transition from scenario $S1$ to scenario $S2$ yielded slightly lower and anticipated peaks. The case $FI_{95} = 1$ indicated that the failures had not yet fragmented the networks, whereas $FI_{95} = 0$ was the result of complete failures.

6.2.1.4 Cross-Flow Index (CFI)

The Cross-Flow Index (CFI) was defined in paragraph 4.7.1 to estimate the theoretical ability of nodes to process the volumes of inward and outward flows. For each node, this metric was computed as the ratio between the ability in the perturbed state and the ability in the unperturbed state, which are based on the computation of the Stress Centrality in the relevant state, as defined by Brandes (2008). For each Brownian surface and realization, a representative value of CFI for the network was obtained by averaging the values of CFI of individual nodes.

The CFI offered a theoretical interpretation of the ability to process flows. In fact, the network models used in this thesis are generic, and as such the specifics regarding goods or services delivered were undefined on purpose. Moreover, due to the level of abstraction of the network models, which also implied the absence of the hierarchical rules that often drive how infrastructure networks are operated, it was deemed sensible to have the position of each node in the network define its ability (see Figure 4.23). As it represents a ratio, $0 \leq CFI \leq 1$, where $CFI = 0$ implied that the network had retained none of the original ability to process flows, and $CFI = 1$ meant that 100% of the original ability had been preserved despite the failures caused by the Brownian surfaces. The Stress Centrality is a key metric from which the CFI was derived, and it is a measure of node centrality based on shortest paths. This was adopted under the assumption that the undefined flow traversing the network models followed the shortest path between any pair of nodes. Other, equally valid centrality metrics based on shortest paths could have been adopted, such as the renowned Betweenness Centrality, used for instance by Pregnolato et al. (2016) to quantify the performance of a flooded road network.

However, the Stress Centrality was preferred as it returns an absolute measure of the number of connections from node i to node j that go through node v (again, see Figure 4.23), allowing to directly quantify the number of inward and outward connections of node v in both the perturbed and unperturbed state. The implementation of the count of all possible trails passing through a given node was also considered, where $N_{all\ paths} > N_{shortest\ paths}$ since the networks implemented feature $N > 2$ nodes. However, this was not pursued given the high computational cost, which was estimated to be at least $O(N^3)$, where N is the number of nodes in the network. In comparison, the computational cost of the Stress Centrality is known to have $O(N^3)$ as its upper bound.

The results are better described by looking at both Figure 6.10 and 6.11. In Figure 6.10, the 95th percentile of CFI, CFI_{95}, is shown on the y axis as a representative value, whereas the x axis shows the Critical Footprint (CF), which represents the size of the fractal surface, divided

into 10 bins of equal width. In general, it is possible to observe that the transition from scenario $S1$ to scenario $S2$ did not correspond to major changes in the trend of any network model, only yielding a marginal decrease in the ability of the networks to process flows. When $0\% \leq CF \leq 10\%$, all four network models showed $CFI_{95} \cong 1$ in both scenarios, entailing no tangible reduction in the overall ability to process flows.

On the other hand, when $90\% \leq CF \leq 100\%$, $CFI_{95} \cong 0$, indicating a complete loss of ability. The LN networks were constantly showing the lowest values of CFI_{95} of both scenarios and displayed a 20% drop in their original ability to process flows for fractals of very limited size ($10\% \leq CF \leq 20\%$). This rapid reduction was also observable for $30\% \leq CF \leq 40\%$, where $CFI_{95} \cong 0.4$ entailed a 60% reduction in the original ability to process flows. The WS networks, on the other hand, almost consistently exhibited the lowest decrease in CFI_{95}. A decrease in CFI_{95} of 20% in $S1$ and nearly 30% in $S2$ was found as a result of fractals with $30\% \leq CF \leq 40\%$. In $S2$, the range $40\% \leq CF \leq 70\%$ is associated with the largest difference in terms of CFI_{95} between the WS networks and the BA and ER networks, entailing that both networks were noticeably more sensitive to the size of the fractal hazards. The BA and ER networks were found to have comparable behaviors in $S1$, with the BA networks displaying slightly higher values of CFI_{95}.

In Figure 6.11 it is documented how CFI_{95} changed with d_{hh}, the distance between the peak or hotspot of the Brownian surface and the most highly connected hub. This analysis was performed to investigate the sensitivity of each network model to a proximal hazard surface, and to complement the results shown in Figure 6.10. Defined S_x as the width of the fractal grid, in $S1$ the LN networks featured a drop in CFI_{95} of more than 70% when $0.6 * S_x \leq d_{hh} \leq 0.75 * S_x$, entailing that a fractal spatial hazard with an hotspot located more than half grid away from the four most central hubs was highly detrimental. This drop increased as d_{hh} decreased, eventually reaching $CFI_{95} = 0$, whereas in $S2$ the LN networks performed slightly better.

Although their trend was affected by fluctuation, the WS networks showed the best performance in $S1$, retaining a residual $CFI_{95} > 0.6$ with $0 \leq d_{hh} \leq 0.15 * S_x$, indicating that the failure of the most highly connected hub did not result in a major decrease in the ability to process flows. This is likely due to the fact that, whilst a fractal hotspot resulted in the failure of the most highly connected hub, the remaining hubs were farther away, and as such continued to operate. By comparison, both the BA and ER networks, although showing fluctuating trends, featured residual values of $CFI_{95} < 0.3$. In $S2$, the transition to a higher failure threshold

seemed to create a situation where CFI_{95} remained scarcely sensitive to d_{hh}, possibly due to lower failure rates, except for the LN networks.

While interpreting these results, it is to be pointed out that the original ability to process the inward and outward flows, e.g. the Stress Centrality in the unperturbed state SC_u, was not the same for all network models. As deducible from Figure 4.23, the value of SC_u for each node is both a function of the location of the node relative to the network, as well as the topological structure of the network itself. As such, it is not advisable to interpret the CFI trends by comparing the CFI_{95} value of a network model with that of another for a specific size of the fractal hazard (e.g., CF). A normalization with respect to the maximum SC_u value found in any network was not performed due to the different topological structures. As a result, the only reasonable comparison is to map the reduction in the ability to process flows of each network with respect to the original value and discern whether a particular network is more or less sensitive to the increase in size of the fractal hazards.

The implications of these results may help drive the choice of a specific network model over another in the design phase of an infrastructure. The rapid decrease in the ability to process flows shown by the LN networks in both Figure 6.10 and 6.11 may be attributed to the fact that gridlike structures are particularly dependent on the most central nodes, under the assumption that flows are handled according to the concept expressed by the Stress Centrality. Under such hypothesis, grid-like structures operate as chain structures, where node i transfers the flow to node $i + 1$ without losses, and so forth, thus resembling a chain. Because of their position, the four most central nodes, which also happened to be adjacent to each other, were the ones with the highest SC_u, and as such, their failure was particularly detrimental to the performance of the overall network.

When spatially continuous hazards are factored in, this phenomenon is even more impactful, as it was not uncommon for the most central nodes to fail altogether, dramatically reducing CFI. The reasons leading to the scarce performance of the LN networks may be used to explain the differences with the other models. The explanation offered in this thesis is that the distance between the most important nodes may play a crucial role in the decrease of the ability to process flows. In fact, where the four hubs with the highest number of connections were very close, a high sensitivity to the proximity of the fractal hotspot was observable. For instance, the Euclidean distance between the four main hubs express in grid cells in the LN networks was always $d_{mh} = 1$.

On the contrary, the WS networks had $d_{mh} \leq 6.78$ in 95% of the realizations, depicting a situation where the four main hubs were much farther away from each other. In fact, the small-

world property featured by the WS networks tends by default not to aggregate the main hubs in one place, but to have them scattered instead. The ER networks featured $d_{mh} \leq 6.04$ in 95% of cases, explaining the closer behavior to the WS networks in Figure 6.11, although the relatively high number of connections featured by the main hub (see Table 6.1) seems to explain the mediocre response observable in Figure 6.10.

The case of the BA networks seems controversial. The algorithm generating these networks is based on *growth* and *preferential attachment*, entailing that the most highly connected hubs are the first to be created, and are also rather close to each other. In fact, the BA networks had $d_{mh} \leq 4.67$ grid cells in 95% of cases. This is reflected in Figure 6.11, where, at least in scenario $S1$, the BA networks suffer significant reductions in CFI_{95} as the fractal hotspot approaches the most highly connected hub. However, the performance of the BA networks in Figure 6.10 is not particularly negative. At any rate, this controversy only seems to affect the interpretation of how the BA networks handled the reduction in CFI given larger fractal hazards, and not how sensitive they were to their proximity. In addition, the uncertainty behind their behavior does not influence the neat trends that the other network models exhibited, and it is advised that additional studies, perhaps involving a defined flow algorithm, should be carried out to investigate this aspect further.

Overall, the results discussed here seem to highlight the negative role played by an excessive proximity of the most highly connected hubs. This in turn suggests that, when perturbed by failures, networks with more separation between their hubs are likely to offer better performances in terms of their ability to process flow.

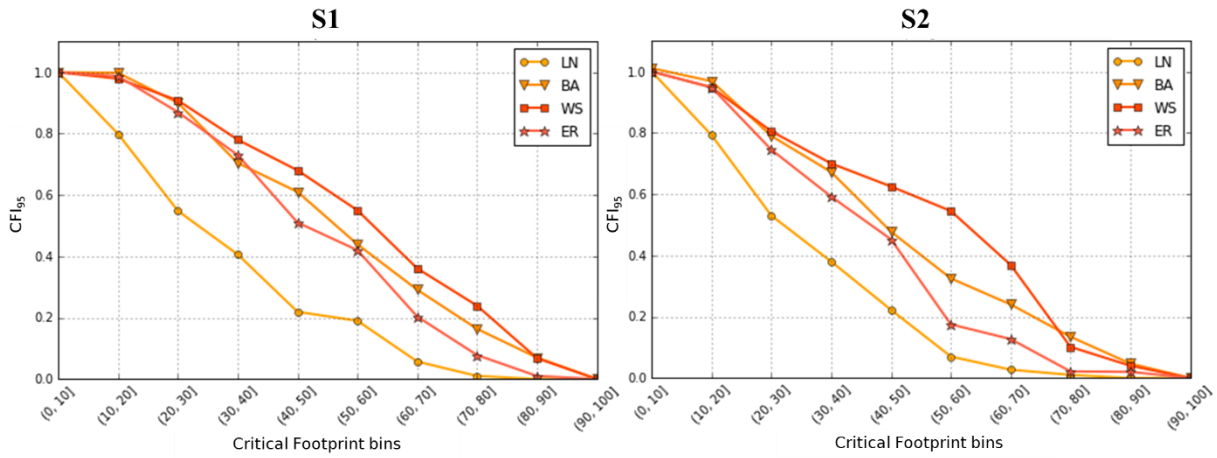

Figure 6.10. Change in the 95th percentile of the Cross-Flow Index (CFI_{95}) with the size of the fractal spatial hazards. The latter is binned and expressed in percentage with respect to the size of the fractal grid.

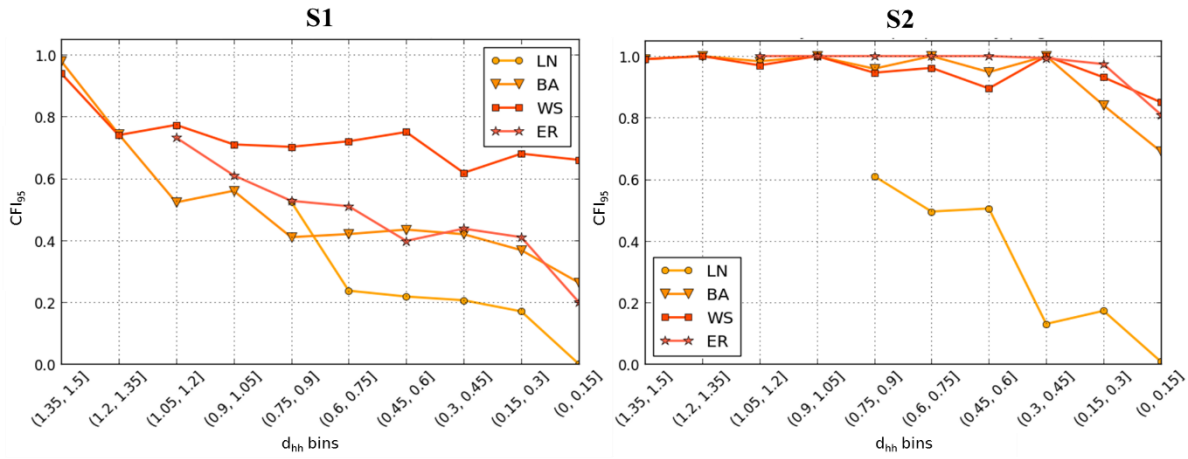

Figure 6.11. Change in the 95th percentile of the Cross-Flow Index (CFI_{95}) with the distance d_{hh} between the peak of the fractal surface and the most highly connected hub. The distance d_{hh} is binned and expressed in percentage with respect to the width of the fractal grid. The LN trends show less points than the other ones as the fractal hotspot was never located farther than $0.75 * S_x$ grid cells from the four most central nodes.

6.2.2 Difference in impact between circular-shaped and fractal spatial hazards

An important comparison was performed between the impact of fractal spatial hazards and circular-shaped hazards on the networks. This was carried out by: *i*) superimposing $N_f = 10{,}000$ fractal hazards produced with $C = (H = 0.8, Ft = 0.5)$ and $N_d = 10{,}000$ circles on the same realization A of a Barabási-Albert Scale-Free Network composed of $N_A = 2{,}500$ nodes evenly distributed on a regular grid; *ii*) applying the failure model described in paragraph 3.2.7.1 to determine the aggregate number of 1st and 2nd order failures $N'_A = N_A - SN$; *iii*) determining the aggregate number of failed nodes observed in the network as a result of the fractal hazards, $N'_{A,f}$; *iv*) determining the aggregate number of failed nodes observed in the network as a result of the circles, $N'_{A,d}$; and *v*) given a fractal hazard and a circle of the same size (e.g., $CF_f = CF_d$), comparing $N'_{A,f}$ with $N'_{A,d}$. Such comparison was performed under the hypothesis that the geometrical difference observed between fractal spatial hazards and circles (see paragraph 6.1.2) corresponded to a different impact on the same network.

This hypothesis seems to be confirmed by the trends shown in Figure 6.12. In fact, in the $10\% \leq CF \leq 100\%$ range, it can be seen that $N'_{A,f} > N'_{A,d}$ in most cases, with the failures caused by the circular-shaped hazards following a quasi-linear trend and those caused by the fractals likely following a superlinear trend. The two trends are not distinguishable when $CF < 10\%$, perhaps owing to the fact that the fractal hazards are not large enough to display their spatial properties. The largest gap between the two trends was observable for $CF \cong 40\%$, where $N'_{A,f} \cong 1.6 * N'_{A,d}$, suggesting that the use of circles may result in an overestimation of the network robustness of around 40%. When $CF = 100\%$, both trends converged at $N'_{A,f} =$

$N'_{A,d} = 2{,}500$, confirming that the failure model proposed in Chapter 4 correctly modelled the case of a spatial hazard occupying the entire grid and causing the maximum disruption. It is worth highlighting that the upper bound shown by the white dots in Figure 6.12 is likely to be the equivalent of the non-linear lower bound observed for the BA trends in Figures 6.7 and 6.8.

It is also worth mentioning that the results shown in Figure 6.12 refer to the impact of fractal hazards with the typical spatial autocorrelation shown by natural phenomena (Saupe, 1988), and to a failure threshold associated with a weak network. As such, it is possible to claim that the difference between the fractal hazards and circles refers to a typical scenario from a spatial perspective, entailing that larger gaps might be observed for $H > 0.8$, given the detrimental impact that an increased spatial autocorrelation was found to have in paragraph 6.2.1.1. The adoption of a low threshold was considered in order to characterize a typical scenario from a structural perspective, entailing that a narrower gap in the trends shown in Figure 6.12 might be observed for $Ft > 0.5$.

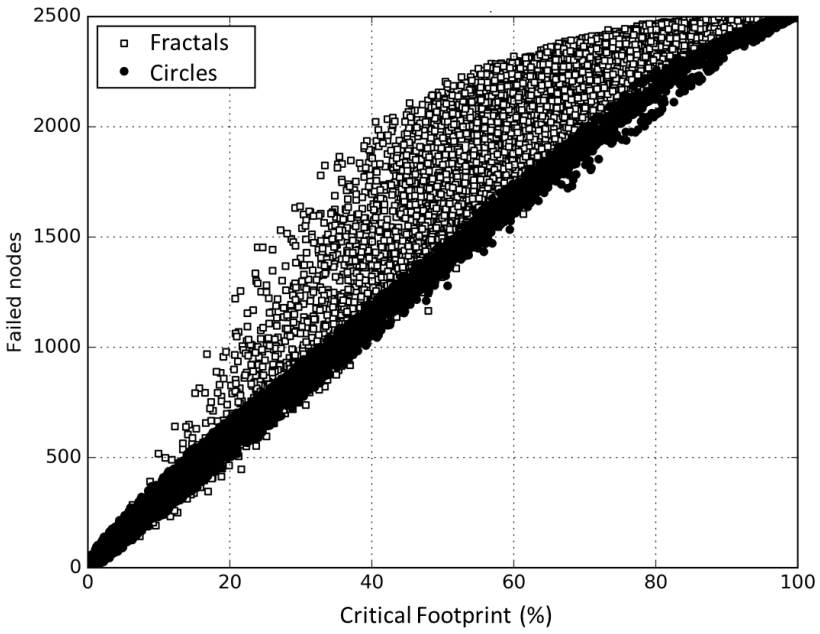

Figure 6.12. Number of failed nodes produced in the same 2,500-node BA network by fractal spatial hazards (white dots) and circular-shaped hazards (black dots) as a result of the application of the failure model presented in Part 1 of this thesis. The size of the circles had a linear effect on the number of failures, whereas a different behavior was observed for the fractal hazards. The most significant gap between the two trends occurred for $CF \cong 40\%$.

Chapter 7. Case Study 2: Results and Discussion

This chapter discusses the results and their implications with reference to the stages to which this case study offers a novel contribution. As outlined in paragraph 3.2.1, Case Study 2 contributes to Stage 1, Stage 2, and Stage 6. However, since Stage 2 refers to the implementation of the hierarchies found in the electricity infrastructure, no modelling results are available apart from the hierarchies themselves, which are presented in paragraph 5.3.1. Together with Stage 1 and Stage 6, the following results also refer to Stage 5, where the impact of the wind gusts on the electricity infrastructure is quantified.

7.1 Stage 1: infrastructure robustness at the system-of-systems level

7.1.1 A realistic, non-isotropic dataset of wind gust grids

The grids of daily maxima wind gusts described in paragraph 5.2.2 constitute a highly representative dataset. Evidence of this can be found in Figure 7.1, where the annual frequency of exceedance of events with wind gust $w_{10,3} > 17\ m/s$ over the study area is depicted for both the Control and Future climate horizon. The above-mentioned threshold was adopted as it is mentioned in the literature as a wind speed value past which wind storms are typically observed (Dunn et al., 2018; Vajda et al., 2014). As such, $w_{10,3} > 17\ m/s$ was assumed to be a critical value to take into account.

Several aspects can be observed by analyzing Figure 7.1. Firstly, the spatial distribution of the above-threshold events is in accordance with the exposure to high winds that characterizes the North York Moors and the Humber Estuary: parts of these areas were exposed to as many as 140 above-threshold events per year in the Control climate horizon. It is also evident how frequently the coastal areas are impacted, as it is the case for Spurn Head. Secondly, as pointed out by Kirchner-Bossi et al. (2019) and Tobin et al. (2016), a widespread decrease in the frequency of above-threshold events is observable in the transition to the Future climate horizon, with the North York Moors and the Humber Estuary experiencing up to 130 above-threshold events per year. Finally, Figure 7.1 highlights the non-isotropic nature of realistic spatial natural hazards, which are intuitively characterized by spatial gradients driven

by a number of different factors. Such factors include the type of natural hazard, the location of the study area, the length of the timeframe (e.g., timeframes might not be long enough to adequately reveal a consistent or realistic spatial gradient), the resolution with which the spatial data are sampled, the topographic influence, and so forth.

The non-isotropic nature of the wind gust grids is relevant to the aspects discussed in paragraph 6.1.1.2, where the Brownian surfaces are described as an instrument that in certain circumstances can be used to reproduce realistic spatial natural hazards. In fact, Figure 7.1 highlights the importance of properly investigating the hazard-specific spatial gradients. This also corroborates the recommendation that any Brownian surface used in impact studies should be overlapped with a grid depicting the spatial gradient of the study area, akin to Figure 7.1.

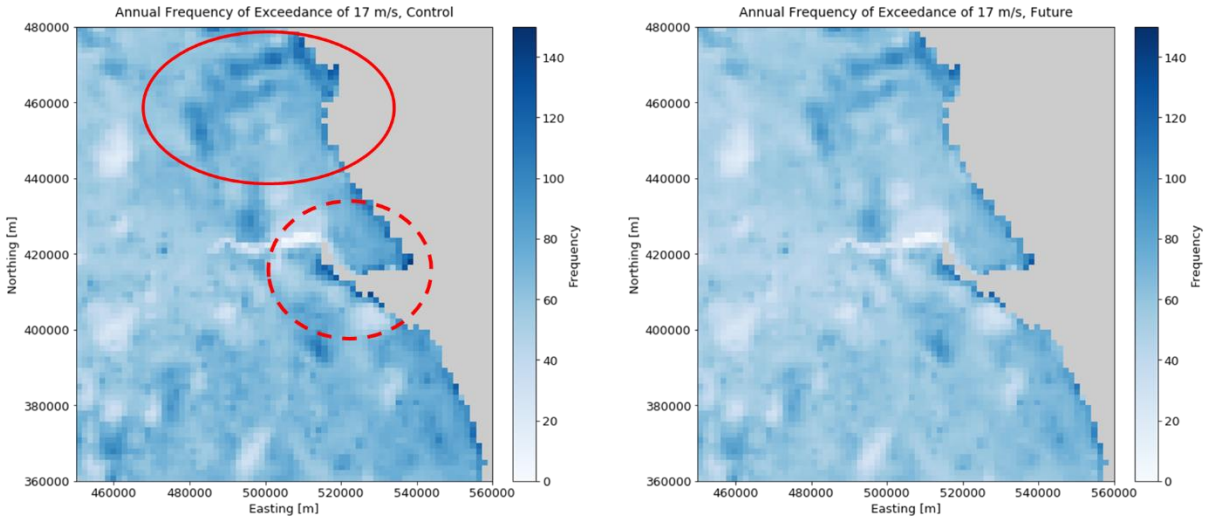

Figure 7.1. Annual frequency of exceedance of $w_{10,3} > 17\ m/s$ critical events for the Control (left) and Future (right) climate horizons. Highlighted are two of the sectors with the highest annual frequency of critical events: the North York Moors (continuous line) and the Humber Estuary (dashed line). The grey area represents the land-sea mask.

7.1.2 Fractal properties of the wind gust grids

The investigation of the fractal properties of wind gusts was implemented with two purposes: *i*) determining whether fractal properties emerged from the spatial distribution of daily maxima wind gusts, in conjunction with the temporal fractal properties observed in literature, and *ii*) exploring a research topic that is at the interface between fractal spatial hazards and wind gusts and allows a smooth transition between them. As described in paragraph 5.2.3, the study of the fractal properties of wind gusts in the spatial domain was carried out by plotting

the Area-Frequency curve in order to highlight possible scale-free behaviors, and then by adopting the Box-Counting algorithm to estimate the Hausdorff or fractal dimension D associated with each grid of daily maxima wind gusts.

These two methods were adopted to investigate both the Control and Future climate horizons, with the aim of characterizing possible changes. Moreover, these two methods were adopted in conjunction as a way to test two necessary and sufficient conditions regarding the possible presence of spatial fractal properties: *i*) the emergence of scale-free behaviors in the distribution of blobs, as described in paragraph 5.2.3.2, and *ii*) the estimation of the Hausdorff or fractal dimension D as a *non-integer* number.

7.1.2.1 Area-Frequency curves

Central to the idea of Area-Frequency curves is the identification of objects of different size found in the wind gust grids, which were defined as *blobs*. If plotted on a three-dimensional space, the grids would constitute continuous surfaces that closely follow the coastline due to the applied sea-land mask, which is visible in grey in Figure 7.1. Also, the surface elevations would represent daily maxima wind gusts, and very rarely did they feature values such as $w_{10,3} = 0$. Consequently, the grids were *binarized* by selecting a range of thresholds that were proportional to those implemented for the Brownian surfaces. These thresholds are listed in Table 5.2. The binarization implied that all values exceeding the threshold were assigned a unitary value, whereas the other values were nullified. This allowed to identify the *blobs*, e.g. islands of cells in the wind gust grids which size could be determined by simply counting the number of cells composing their footprints (see Figure 5.9). The same reasoning was applied to find the blobs in the Brownian surfaces.

Figure 7.2 shows the Area-Frequency distributions for the Control climate horizon in a double logarithmic scale, whereas Figure 7.3 displays the same for the Future climate horizon. In each panel, the x-axis displays the size of the blobs found in the wind gust grids, measured in grid cells, where one grid cell equals $1.5\ km * 1.5\ km = 2.25\ km^2$. On the y-axis is the frequency with which each size was found in the grids. To avoid visualization problems due to linear binning techniques, the log-log plots feature the Complementary Cumulative Distribution Function (CCDF) of the frequency of the size of the blobs (Barabási, 2016). The CCDF, which is also known in literature as *exceedance* or *reliability function*, is computed as the frequency with which the value of a given size i was exceeded by the rest of the values. Each panel shows a red series, referring to the wind gust grids, and five blue series, one for fractal combination

$C = (H, Ft^*)$, where H represented the five values of the Hurst exponent ∈ [0.6,1.0] and Ft^* was one of the failure thresholds in Table 5.2. As a reference, panel a) in Figure 7.2 depicts the Area-Frequency curve of the wind gust grids binarized by using the value 4.98, which corresponds to the value $Ft = 0.1$ used for the Brownian surfaces (see Table 5.2). The blue trends are the Area-Frequency curves for the five classes of Brownian surfaces binarized by adopting $Ft = 0.1$. The use of proportional failure thresholds was adopted in order to perform meaningful evaluations. In each panel, the visual comparison between the Area-Frequency curve of the wind gust grids and those referring to the Brownian surfaces allows to identify for which range of size, along the x-axis, the wind gust grids followed a linear trend, which is associated in the literature with the presence of scale-free phenomena.

In Figure 7.2, panel a) shows that the wind gust Area-Frequency distribution followed a linear trend in the log-log plot. Defined s_b as the blob size measured in grid cells, with a single grid cells measuring 2.25 km^2, such linear trend was observed for $0 \leq Log(s_b) \leq 60$, which corresponds to $0 \leq Area \leq 60 * 2.25\ km^2 = 135\ km^2$. This was the longest size interval in the Control climate horizon where the wind gusts exhibited a scale-free phenomenon. For $Area > 135\ km^2$, $Log(s_b)$ was associated with lower frequencies with respect to the blue trends, indicating that the frequency of larger blobs was visibly reduced with respect to the Brownian surfaces.

In panel b), the scale-free phenomenon was observed for the narrower interval $0 \leq Log(s_b) \leq 40$, corresponding to $0 \leq Area \leq 40 * 2.25\ km^2 = 90\ km^2$. In panel c), such interval narrowed down even further to $0 \leq Area \leq 10 * 2.25\ km^2 = 22.5\ km^2$. These values suggest that the wind gust grids displayed scale-free properties in the spatial domain until a critical size s_c was reached. The comparison with the Area-Frequency curves of the associated Brownian surfaces reveals that blobs with $Area > s_c$ were present less frequently in the wind gust grids, suggesting that the blobs found were not large enough to sustain a scale-free phenomenon and, consequently, a possible fractal behavior.

Panels d) and e) describe behaviors for which the scale-free phenomenon may be ruled out. It is here suggested that this might be a consequence of the thresholds with which the relevant blobs were obtained, namely $w_f = 34.85$ for panel d) and $w_f = 44.81$ for panel e). In fact, thresholds so high aimed at isolating only the peaks of the wind gust grids and evaluating their scale-free properties while neglecting the vast majority of the study area. The use of very high thresholds also had an influence on the scale-free behavior of the Brownian surfaces, which are fractals by definition, causing their behavior to depart from a purely fractal pattern. In fact, as observable in panels a) to e), a critical size $s_{c,f}$ was observed for the Brownian

surfaces as well. With the increase of the failure threshold Ft, a progressively smaller $s_{c,f}$ was observed, which caused the Area-Frequency curves of the Brownian surfaces to depart from the linear trend that is clearly visible in panel a), and to display a curved trend that in literature is associated with distributions that do not describe scale-free phenomena (e.g., exponential distributions, double exponential distributions, log-normal distributions, and so forth) (Clauset et al., 2009).

Almost identical behaviors were found in Figure 7.3 for the Future climate horizon: the same critical values s_c were found for the size of the wind gust blobs, and the same progressive departure from the fractal pattern was observed for the Brownian surfaces. This indicates that, from a scale-free perspective, there are likely to be no projected changes from the Control to the Future climate horizon.

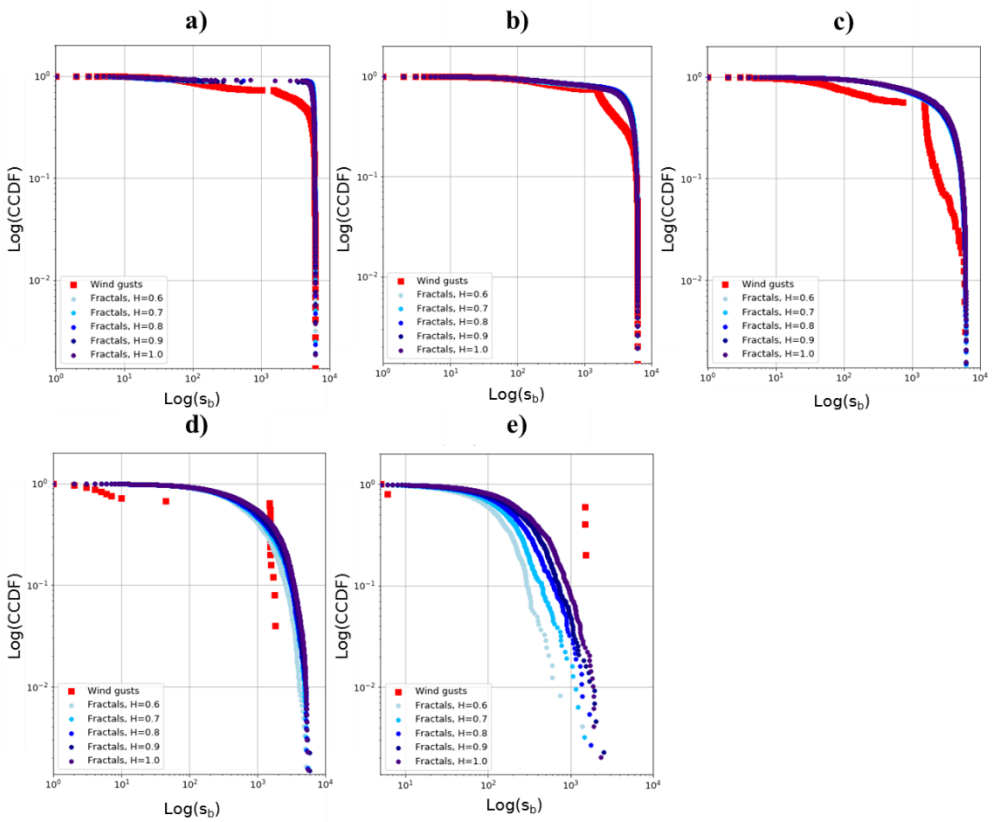

Figure 7.2. Area-Frequency distribution of the wind gust grids for the Control climate horizon in log-log plots. On the x-axis is the size in grid cells of the blobs found in the wind gust grids after the binarization described in paragraph 5.2.3.2. On the y-axis is the Complementary Cumulative Distribution Function (CCDF) of the frequency of each dot. The red dots represent the frequency with which each size was found in the wind gust grids, whereas the blue dots represent the frequency with which each size was found in the Brownian surfaces. The panels a) to e) refer to the five thresholds listed in Table 5.2.

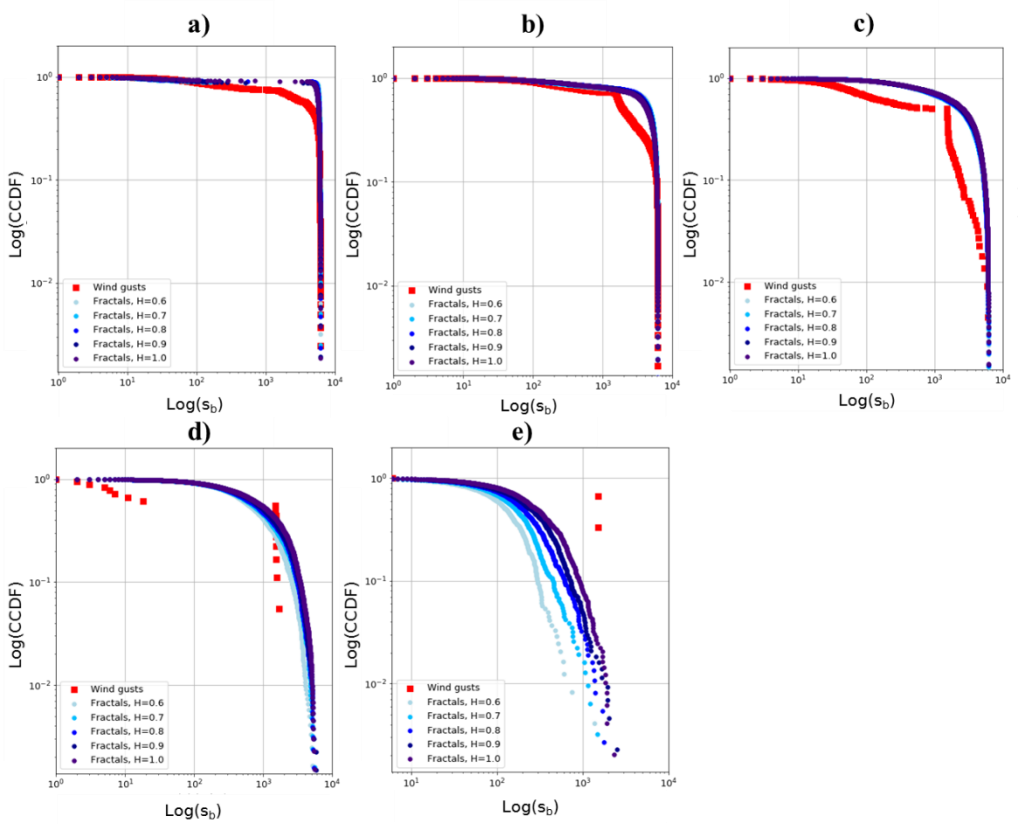

Figure 7.3. Area-Frequency distribution of the wind gust grids for the Future climate horizon in log-log plots. On the x-axis is the size in grid cells of the blobs found in the wind gust grids after the binarization described in paragraph 5.2.3.2. On the y-axis is the Complementary Cumulative Distribution Function (CCDF) of the frequency of each dot. The red dots represent the frequency with which each size was found in the wind gust grids, whereas the blue dots represent the frequency with which each size was found in the Brownian surfaces. The blue dots are the same dots as in Figure 7.2. The panels a) to e) refer to the five thresholds listed in Table 5.2.

While the use of progressively increasing filters (e.g., Ft and w_f) resulted in a departure from a scale-free pattern for both the Brownian surfaces and the wind gust grids and in both climate horizons, their implementation was performed in order to: *i*) properly identify the blobs in both the Brownian surfaces and the wind gust grids; *ii*) avoid the trivial case of computing the Area-Frequency curve of the footprint of the study area; and *iii*) ensure that the wind gust grids were actually comparable with the Brownian surfaces, which had a filter applied.

However, while there is a clear indication that panels b) to e) in both Figure 7.2 and 7.3 are heavily influenced by the adoption of high filters and as such cannot be taken into consideration, panels a) evidently show the presence of scale-free properties for the range $0 \leq Area \leq 135\ km^2$. This suggests that the wind gust grids are likely to possess, to a limited extent, one of the two necessary and sufficient conditions to be considered as fractals. It is possible to hypothesize that the limitation imposed on the fractal spatial behavior of the wind gust blobs is attributable to physical constraints, such as the presence of the coast, and to

climatic constraints, which are driven by the different climatic patterns observed at different latitudes and longitudes. On the contrary, the Brownian surfaces were not limited by any physical or climatic constraints, save for the adoption of the failure threshold. Overall, the constraints mentioned previously are likely to *de facto* limit the growth of the blobs, highlighting the fact that meaningful results may only be obtained if the large domain of a civil engineering infrastructure is divided into smaller, regional domains to be analyzed.

7.1.2.2 The Box-Counting algorithm

The Box-Counting algorithm was implemented with the aim of estimating the Hausdorff or fractal dimension D for each one of the panels in Figures 7.2 and 7.3. The time series shown in Figure 7.4 are associated with the Area-Frequency curves in Figure 7.2, whereas those in Figure 7.5 are associated with the Area-Frequency curves in Figure 7.3. For purposes of comparison, the known fractal dimension D of the Brownian surfaces is also shown. In Figure 7.4, panel a) shows that the blobs found in the wind gust grids were almost consistently displaying a fractal dimension $D = 2.1$, entailing that they were occupying a three-dimensional space in a similar way as any bi-dimensional plane. This also suggests an alignment with the Brownian surfaces generated with $H = 0.9$, the fractal class with the second highest degree of spatial autocorrelation, entailing that the wind gust grids exhibited a spatial pattern close to that of smooth surfaces.

The same can be observed in Figure 7.5 for the Future climate horizon. The increase in the filter value w_f caused an increase in the D range of the time series, as well as an increase in the number of grids for which the estimation was either not possible or returned $D = 0$, which is representative of the non-dimensionality of a single point. These results seem to support the points made in the previous paragraph, suggesting that, overall, the wind gust grids behave as fractals in the spatial domain. However, such behavior is limited by a critical size past which the phenomenon is no longer discernible, and by a fractal dimension $D = 2.1$, which can be associated with relatively smooth surfaces.

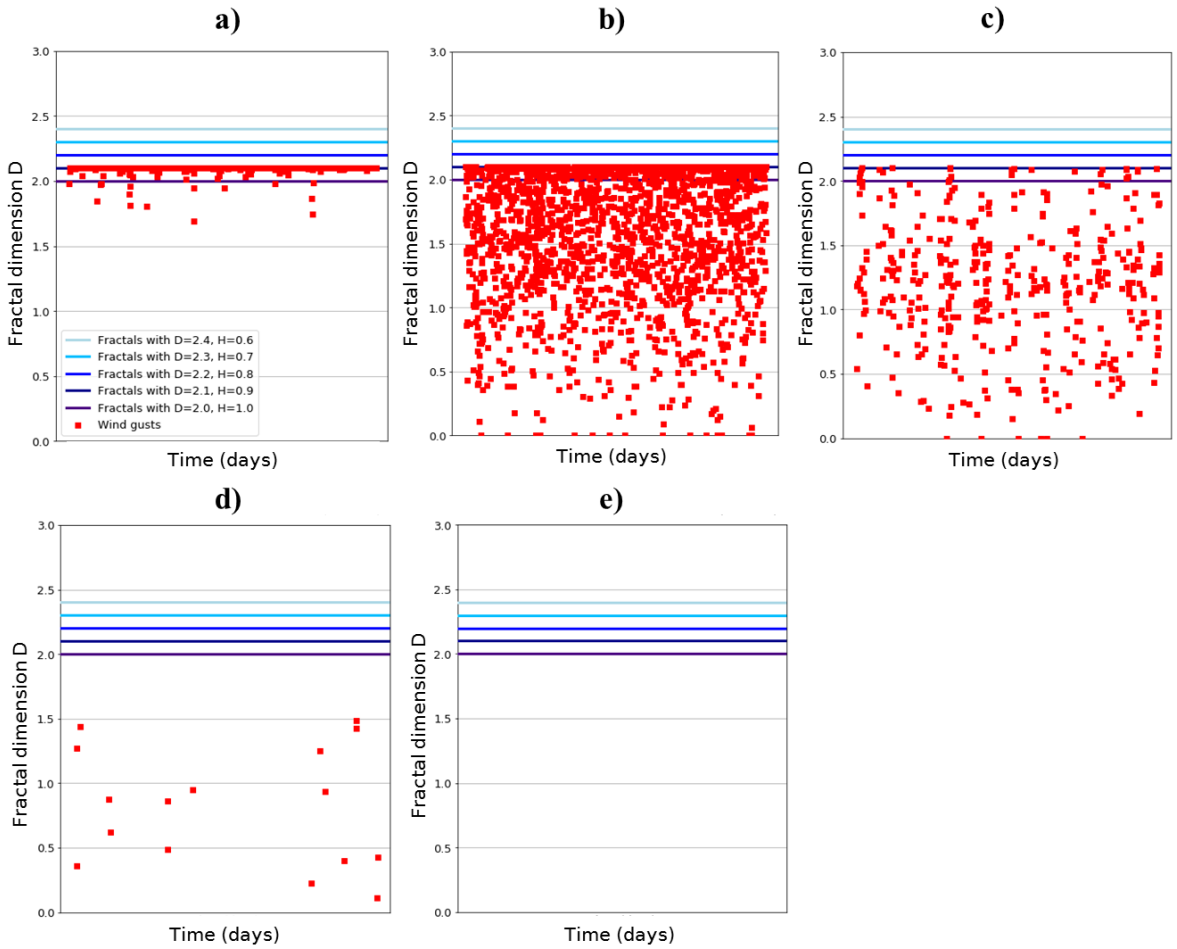

Figure 7.4. Time series of the fractal dimension D computed for the Control climate horizon. Panels a) to e) refer to the same panels in Figure 7.2. The progressive increase in the filter values Ft and w_f observed from panel a) to panel e) caused a general downward shift, as well as an increasing number of instances where the fractal dimension could not be determined. The five colored lines refer to the known fractal dimensions of the five classes of fractals generated with $H = [0.6, 0.7, 0.8, 0.9, 1.0]$.

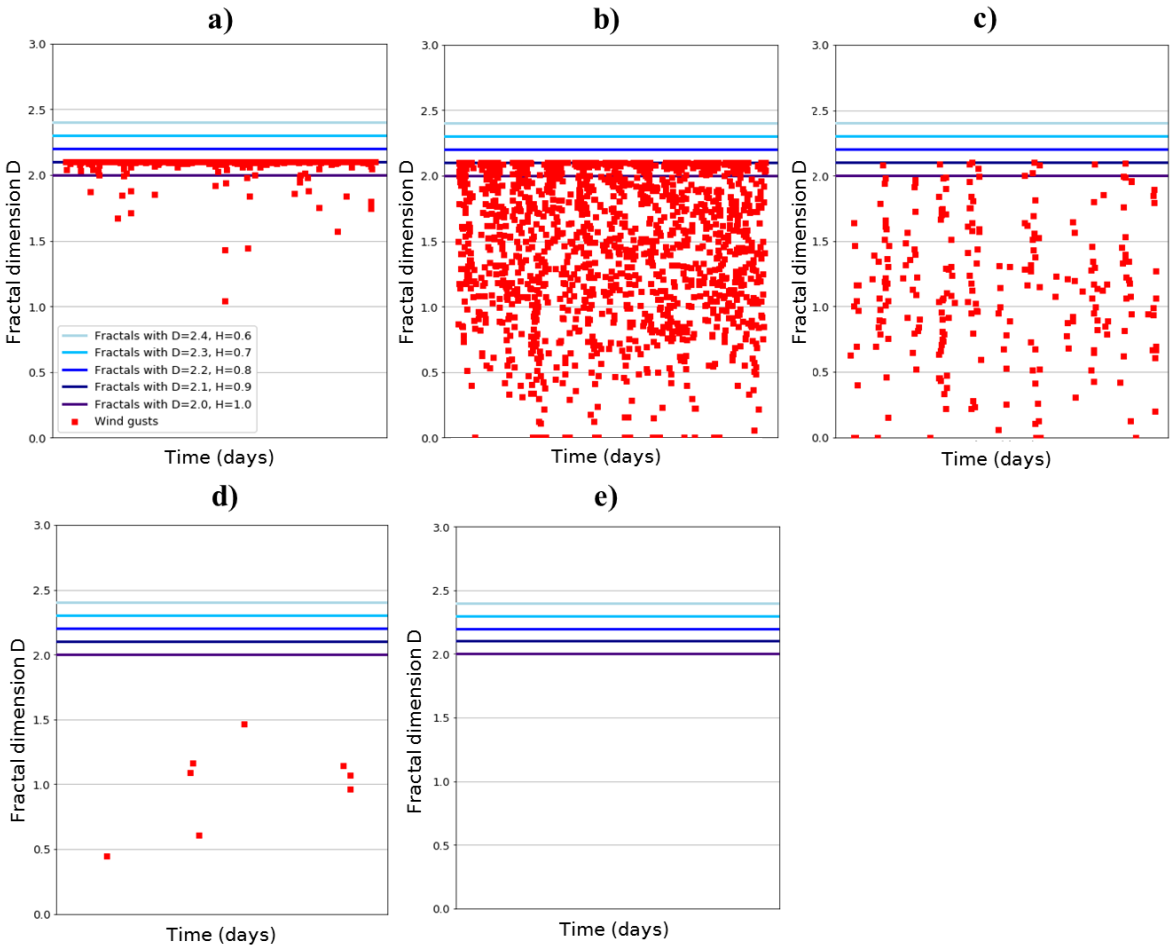

Figure 7.5. Time series of the fractal dimension D computed for the Future climate horizon. Panels a) to e) refer to the same panels in Figure 7.3. The progressive increase in the filter values Ft and w_f observed from panel a) to panel e) caused a general downward shift, as well as an increasing number of instances where the fractal dimension could not be determined. The five colored lines refer to the known fractal dimensions of the five classes of fractals generated with $H = [0.6, 0.7, 0.8, 0.9, 1.0]$.

7.2 Stage 5: impact of the daily maxima wind gusts on the electricity infrastructure

7.2.1 Faults obtained with the low-resolution fragility curve

The low-resolution fragility curve developed by Dunn et al. (2018) provided an empiric tool for estimating the average number of faults occurring every 1,000 km of overhead lines as a result of wind gusts. The low-resolution fragility curve was obtained by combining observations with spatial data from a 12-km Climate Model. Given the system-of-systems approach followed in this case study, the faults were computed with respect to partitions, or components, of the two tiers composing the electricity network. The expected number of faults was then multiplied by the ratio between the length of the relevant component and 1,000 km. Then, for each day in each climate horizon, the expected number of faults per tier was obtained by adding the quantities relative to each component.

Figure 7.6 shows the time series of the expected number of faults for each tier (e.g., the 132kV tier and the 33-66kV tier) composing the electricity network in the Control climate horizon. The first aspect that stands out is the possibility to identify a seasonal component in the time series by noticing the frequency with which the peaks occur. This is a direct consequence of the fact that wind storms tend to occur during specific periods of the year, such as the winter. According to the low-resolution curve, the 132kV tier recorded a maximum of 0.42 expected faults and a total of 11.52 expected faults during the 13-year horizon, corresponding to an average of 0.89 faults per year. On the other hand, the 33-66kV tier recorded a peak of 13.43 expected faults and a total of 166.71 expected faults over the 13-year horizon, corresponding to 12.82 faults per year.

The striking difference between these numbers may be explained by two important aspects that involve *structural* and *spatial properties* of the electricity network. In terms of *structural properties*, the overall length of the 33-66kV tier, $L_{33-66kV} \cong 882\ km$, was significantly greater than the overall length of the 132kV tier, $L_{132kV} \cong 205\ km$, with $L_{33-66kV} > 4 * L_{132kV}$. In terms of *spatial properties*, the territorial coverage offered by the two tiers was not the same, as the 33-66kV network, being at a lower hierarchical level, operated in areas where the 132kV was not present. The structural properties had a significant impact on the results, as the actual length of each tier influenced the final expected number of faults, which was originally computed for 1,000 km of overhead lines. As such, it is possible to categorize the low-fragility curve as an empirical tool that is significantly sensitive to the actual length L.

The spatial properties had an equally important influence on the final number of expected faults. An example of this is the fact that the 33-66kV tier operates in areas where the 132kV tier is absent, and in the same areas there is more exposure to high winds, such as the North York Moors or the coast. Overall, the structural properties may explain the difference of two orders of magnitude between the total number of expected faults of the two time series, whereas the spatial properties may be the reason why the peaks in the 33-66kV time series do not always correspond to the peaks in the 132kV time series. This aspect suggests the emergence and importance of a complex factor, namely the location of the peak wind gust in a study area relative to where the infrastructures operate. The distance between the location of the peak and the infrastructure might be a key factor in the non-linear relationship between severity and impact of wind gusts, given that extreme events would result in limited consequences should they occur in areas with lack of infrastructures.

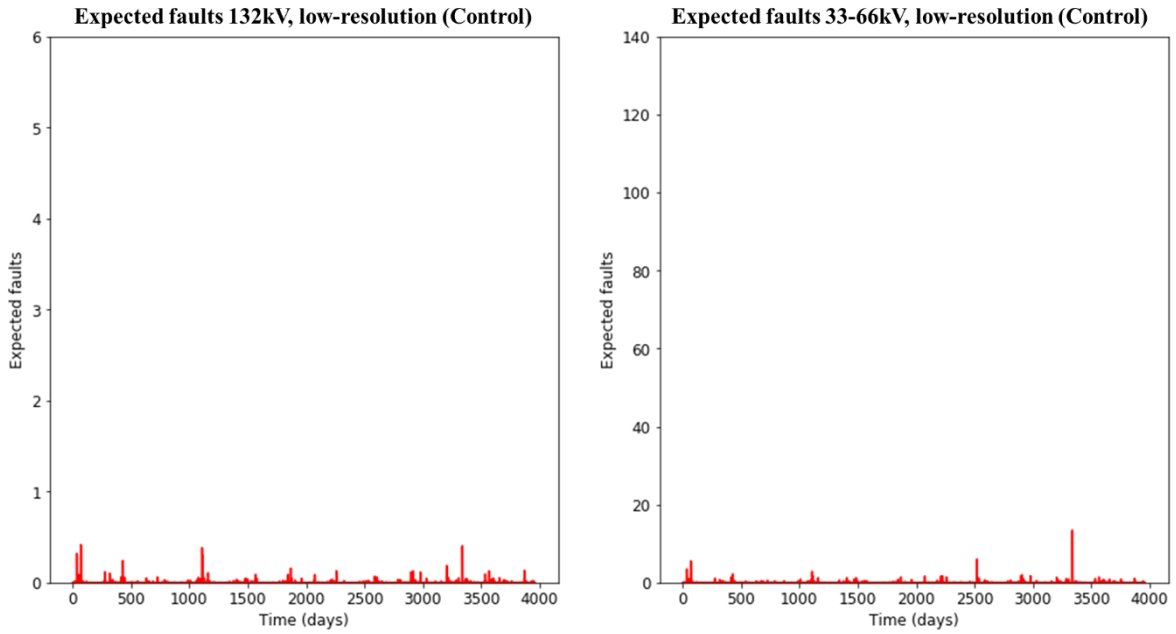

Figure 7.6. Time series of the number of expected faults in the 132kV tier (left) and 33-66kV tier (right) of the electricity network. These trends refer to the Control climate horizon and the low-resolution fragility curve. The y-axis scales are set in such a way as to correspond to those used in the following sections.

Figure 7.7 shows the time series of the expected number of faults for the 132kV and 33-66kV tier in the Future climate horizon. The 132kV tier recorded a daily maximum of 0.95 expected faults and a total of 13.11 expected faults during the 13-year horizon, corresponding to an average of slightly over 1 fault per year. On the other hand, the 33-66kV tier recorded a daily peak of 20.44 expected faults and a total of 161.14 expected faults in 13 years and an average of 12.40 faults per year. The differences between the two time series may be explained using the same reasoning outlined for the Control climate horizon, as the differences in the structural and spatial properties of the two tiers did not change in the Future climate horizon.

What stands out in the comparison between Figure 7.6 and Figure 7.7 is that both the maximum number of expected faults and the total number of expected faults for the 132kV tier are projected to increase by 126.2% and 13.8%, respectively. The first number is exaggerated by the fact that the maximum number of expected faults in a day for the Control climate horizon is rather small and as such very sensitive to any increase. The second number, instead, is likely to be a more reliable indicator. For the 33-66kV tier, the transition to the Future climate horizon entailed an increase in the maximum number of expected faults in a day of 52.2%, and a decrease in the total number of expected faults of 3.3%. Overall, these numbers seem to indicate a slightly increased exposure of the 132kV tier to wind-related faults, and less faults over the same timespan but more extreme daily maxima for the 33-66kV tier.

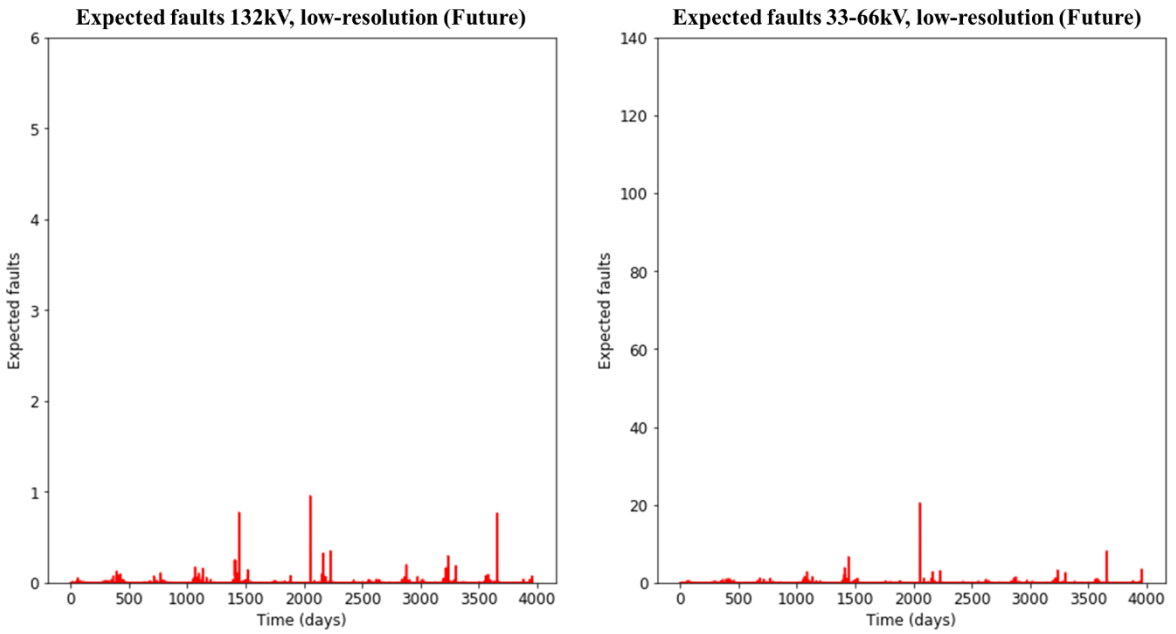

Figure 7.7. Time series of the number of expected faults in the 132kV tier (left) and 33-66kV tier (right) of the electricity network. These trends refer to the Future climate horizon and the low-resolution fragility curve. The y-axis scales are set in such a way as to correspond to those used in the following sections.

7.2.2 Faults obtained with the high-resolution fragility curve

As with the low-resolution case, the high-resolution fragility curve developed by Dunn et al. (2018) provided an empiric tool for estimating the average number of faults occurring every 1,000 km of overhead lines as a result of wind gusts. The high-resolution fragility curve was obtained by combining observations, spatial data from a 12-km Climate Model, and high-detail spatial information regarding faults provided by a Distribution Network Operator. Owing to the system-of-systems approach described in paragraph 5.3.1.3, the faults were computed with respect to each component of the 132kV and 33-66 tiers of the electricity network. The expected number of faults was then multiplied by the ratio between the length of the relevant component and 1,000 km. Then, for each day in each climate horizon, the expected number of faults per tier was obtained by adding the quantities of each component.

Figure 7.8 shows the time series of the expected number of faults for the 132kV and the 33-66kV tier in the Control climate horizon. As with the low-resolution case, it is possible to identify the seasonal trend of the time series by evaluating the frequency with which the peaks occur. On the whole, the 132kV tier recorded a daily maximum of 2.08 expected faults and a total of 48.11 expected faults during the 13-year horizon, coinciding with an average of 3.70 faults per year. In contrast, the 33-66kV tier featured a daily peak of 82.49 expected faults and a total of 790.94 expected faults in the 13-year horizon, namely 60.84 faults per year.

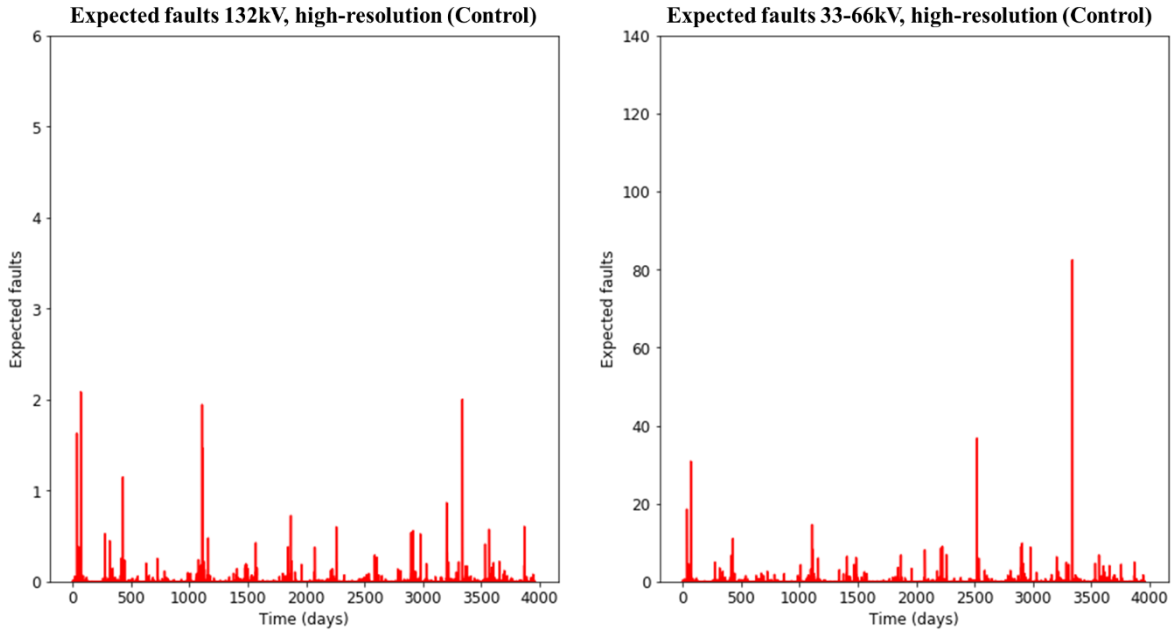

Figure 7.8. Time series of the number of expected faults in the 132kV tier (left) and 33-66kV tier (right) of the electricity network. These trends refer to the Control climate horizon and the high-resolution fragility curve. The y-axis scales match those used in the previous sections.

Finally, Figure 7.9 shows the time series of the expected number of faults for the 132kV and the 33-66kV tier in the Future climate horizon. According to the high-resolution curve, the 132kV tier showed a daily maximum of 5.30 expected faults and a total of 57.59 expected faults in the 13-year horizon, resulting in an average of 4.43 faults per year. Alternatively, the 33-66kV tier displayed a daily peak of 130.64 expected faults and a total of 786.53 expected faults during the same 13-year horizon, entailing that an average of 60.50 faults had occurred on a yearly basis. As with the low-resolution approach, the discrepancies between the 132kV and 33-66kV time series may be explained by using the differences in the structural and spatial properties of the two tiers, which remained unaltered during the Future climate horizon.

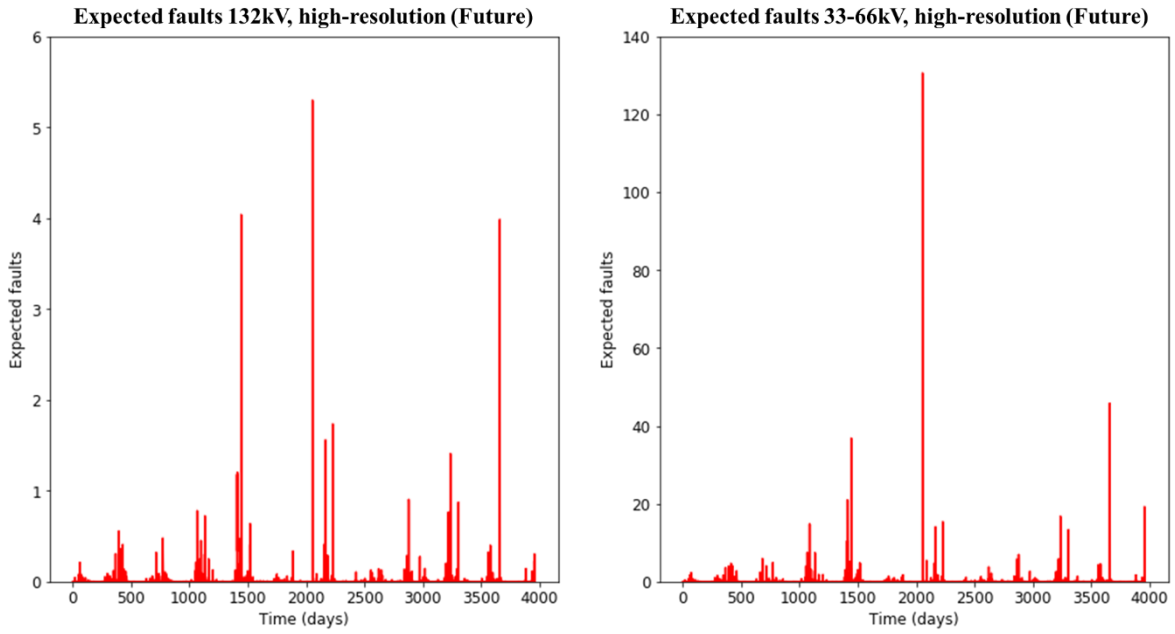

Figure 7.9. Time series of the number of expected faults in the 132kV tier (left) and 33-66kV tier (right) of the electricity network. These trends refer to the Future climate horizon and the high-resolution fragility curve. The y-axis scales match those used in the previous sections.

7.2.3 Comparison between theoretical and observed faults

Remarkable differences exist between the 132kV and the 33-66kV tiers, which are due to the electricity network itself, and between the Control and Future climate horizons, which arise from the CPM1.5 model. However, these are accompanied by noteworthy discrepancies in both climate horizons between the expected faults of the low-resolution approach, f_{low}, and those of high-resolution approach, f_{high}. As a general trend, the expected number of faults determined by using the high-resolution curve were found to exceed those determined with the low-resolution approach, for both tiers.

As observable from the comparison between Table 7.1 and Table 7.2, the 132kV tier was found to be exposed to a total number of expected faults in the Control climate horizon that increased significantly from the low-resolution to the high-resolution approach, namely $f_{high,132,Control} = 4.18 * f_{low,132,Control}$. In the Future climate horizon, such increase was comparable, namely $f_{high,132,Future} = 4.39 * f_{low,132,Future}$. The 33-66kV tier was found to be subjected to slightly larger increases, such as $f_{high,33-66,Control} = 4.74 * f_{low,33-66,Control}$ in the Control climate horizon and $f_{high,33-66,Future} = 4.88 * f_{low,33-66,Future}$ in the Future climate horizon. This difference is ascribable to the dissimilarities between the two fragility curves, identified by Dunn et al. (2018) to be an underestimation of the number of faults obtained with the low-resolution fragility curve due to the coarser resolution of the input spatial information.

Table 7.1. The maximum number of expected faults, together with the total number of expected faults in the two 13-year climate horizons, for the two tiers of the electricity network. Values obtained with the low-resolution fragility curve.

Daily maximum expected faults, low-resolution fragility curve		
	132kV	33-66kV
Daily maximum expected faults, Control	0.42	13.43
Daily maximum expected faults, Future	0.95	20.44
Total expected faults, Control	11.52	166.71
Total expected faults, Future	13.11	161.14

Table 7.2. The maximum number of expected faults, together with the total number of expected faults in the two 13-year climate horizons, for the two tiers of the electricity network. Values obtained with the high-resolution fragility curve.

Daily maximum expected faults, high-resolution fragility curve		
	132kV	33-66kV
Daily maximum expected faults, Control	2.08	82.49
Daily maximum expected faults, Future	5.30	130.64
Total expected faults, Control	48.11	790.94
Total expected faults, Future	57.59	786.53

An interesting discussion arises from the analysis of Table 7.3, which documents the comparison between the average number of faults per year yielded by the low-resolution and high-resolution fragility curves and the same number of observed faults. These are reported by the United Kingdom National Faults Incident Reporting Scheme (NaFIRS) in the period January 2004 to March 2017. The figures in Table 7.3 reveal that both the low-resolution and the high-resolution fragility curves overestimated the number of expected faults per year in the two-tier electricity network, where the overestimation factor for faults $o_{f,faults}$ is obtained as the ratio between the theoretical number of faults and the observed number of faults.

In the Control climate horizon, the low-resolution fragility curve featured a lower overestimation factor, e.g. $o_f = 1.05$ for the 132kV tier and $o_f = 4.77$ for the 33-66kV tier. In the case of the high-resolution fragility curve, the overestimation factors increased to $o_f = 4.35$ for the 132kV tier and $o_f = 22.62$ for the 33-66kV tier. In the Future climate horizon, the low-resolution curve returned an overestimation factor of $o_f = 1.18$ for the 132kV tier and $o_f = 22.49$ for the 33-66kV tier. It is also possible to observe that, although Kirchner-Bossi et al. (2019) and Tobin et al. (2016) mentioned a general decrease in the wind gusts going from the Control to the Future climate horizon, the numbers in Table 7.2 reveal that the 132kV tier is projected to face a higher number of faults, with the 33-66kV tier being slightly less exposed. It can be suggested that this is due to an increased *local severity* of the wind gusts, which in the Future climate horizons may have taken place in close proximity to the spatial domain covered by the 132kV tier. This has an important influence on a hierarchical system, as an increased number of faults at a higher level imply more faults at a lower level due to the domino effect.

It is here hypothesized that the observed increase in o_f is due to two aspects. The first aspect is the sensitivity to the actual length of the overhead line of the output of the fragility curve. In fact, the less extended of the two tiers, the 132kV tier, always featured the lowest o_f compared to the 33-66kV tier, e.g. $1.05 \leq o_{f,faults,132} \leq 4.35$ for the former as opposed to $4.77 \leq o_{f,faults,33-66} \leq 22.62$ for the latter in the Control climate horizon.

The second aspect is the nature of the dataset that was used to obtain both the low-resolution and the high-resolution fragility curves. In fact, Dunn et al. (2018) adopted both wind data and fault data for the South West of England, which is likely to be affected by more severe wind gusts given its location and the prevalence of westerly winds in comparison to the study area targeted by this case study. As much as these fragility curves represent the state-of-the-art in terms of empirical tools for the estimation of wind-related faults, the adoption of regional wind values is likely to regionalize the fragility curve, rendering its application in a different location less reliable. The climate pattern of a targeted location may in fact be significantly different from that of the area for which the fragility curve was originally developed, resulting in remarkable positive or negative differences. As a consequence of this, it is important to highlight that the next step in the development of wind-related fragility curves is to probably identify a set of regional parameters, so that the estimation of the expected number of faults is less affected by either overestimation or underestimation.

Table 7.3. Expected number of faults per year as a comparison between the low-resolution, high-resolution, and NaFIRS observations.

	Expected number of faults per year				
Tier	Control, low-resolution	Control, high-resolution	Future, low-resolution	Future, high-resolution	Observed, NaFIRS
132kV	0.89	3.70	1.01	4.43	0.85
33-66kV	12.82	60.84	12.40	60.50	2.69

7.2.4 Impacts determined with the low-resolution fragility curve

The impacts were determined by adopting a quantitative metric that computed, for each day in the climate horizons and each tier component i (e.g., the feeder or circuit), the value of the Single Impact $SI_{i,day,horizon}$, expressed in number of expected faults multiplied by the

number of customers affected. This was done to characterize a *worst-case scenario*, under the assumption that a fault occurring anywhere along the overhead line of a component resulted in a service failing affecting the entire component and the entirety of its customer base. For each day in the climate horizons and component, the $SI_{i,day,horizon}$ values were then added to produce the Tier Impact $TI_{t,day,horizon}$. The latter constitutes a time series of impact at the daily scale for both the 132kV tier and the 33-66kV tier.

Figure 7.10 shows the time series of the Tier Impact corresponding to the low-resolution fragility curve and the Control climate horizon. It can be observed that $\max(TI_{132,day,Control}) \cong 1.8 * 10^5$ faults-customers, whereas $\max(TI_{33-66,day,Control}) \cong 3.5 * 10^6$ faults-customers, revealing a difference between the two of 1 order of magnitude. It is apparent how the trends in Figure 7.10 retrace those of Figure 7.6, with peaks in the number of expected faults corresponding to peaks in Tier Impact. The only difference between the two is that the individual Tier Impact time series were shifted upwards due to their being magnified by the relevant number of customers served.

However, although the impact of the wind-related faults on the 33-66kV tier was greater than that on the 132kV tier, the difference between the two time series was narrower than observed for the expected faults. In fact, while the 33-66kV tier experienced more faults in the Control climate horizon, its customer base was significantly smaller than that of the 132kV tier, e.g. $customers_{132} = 1.68 * customers_{33-66}$. This is a direct consequence of the fact that, while the 33-66kV tier operated almost entirely within the boundaries of the study area, a fraction of the customers served by the 132kV tier was located outside of it, as the latter operated at a higher hierarchical level.

For the purpose of this case study, such fraction was included for two reasons: *i*) in terms of impact, it was deemed unrealistic not to consider it, as this would have downplayed the importance of the 132kV tier; and *ii*) objective difficulties, mostly owing to lack of detailed information, prevented the isolation of the customers located inside the study area. This aspect sheds light on the difficulty to identify a self-contained study area, as the two main components of this case study, e.g. the electricity network and the wind gusts, follow very different geographical patterns. As a consequence, it is here proposed that the regionalism needed to perform an accurate impact study (see paragraph 7.2.3) has to be mediated by realistic considerations about the geographical shape of the infrastructure.

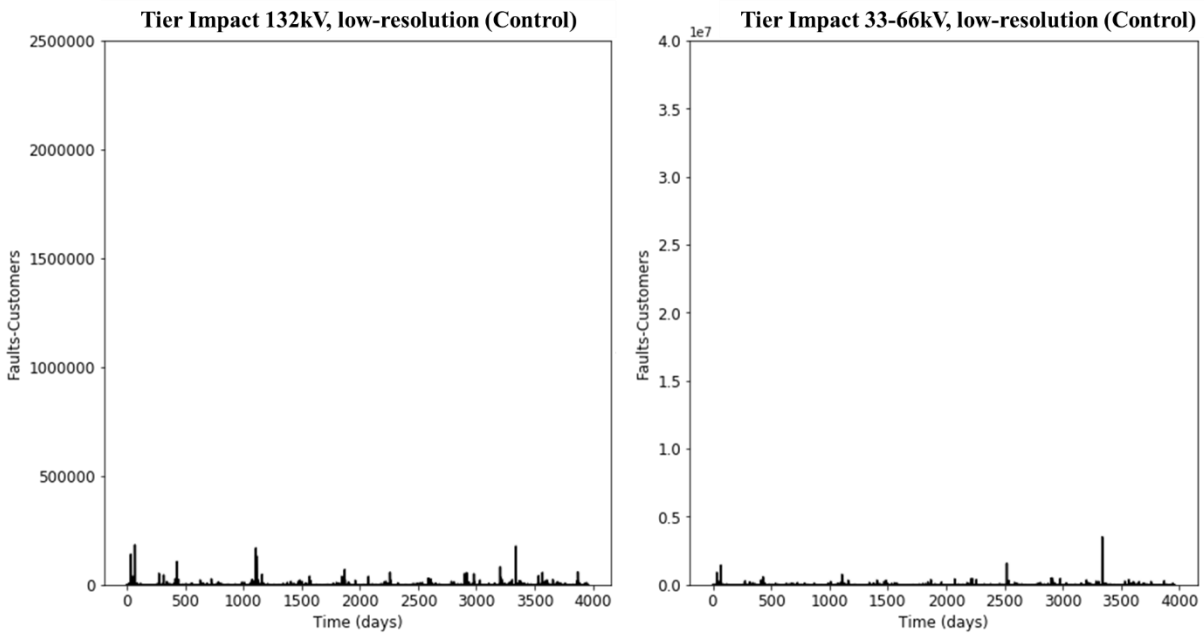

Figure 7.10. Time series of the Tier Impact for the 132kV tier (left) and 33-66kV tier (right) of the electricity network. These trends refer to the Control climate horizon and the low-resolution fragility curve.

Figure 7.11 shows the time series of the Tier Impact corresponding to the low-resolution fragility curve and the Future climate horizon. Owing to the upwards shift caused by the number of customers served, the difference in the number of expected faults observed in the transition from the Control to the Future climate horizon was maintained, signaling a projected increase in impact. In fact, the Future climate horizon was found to have a significantly increased peak for the 132kV tier, $\max(TI_{132,day,Future}) \cong 2.29 * \max(TI_{132,day,Control})$. In addition, whilst the threshold of $4 * 10^5$ faults-customers was never exceeded in the Control climate horizon, the same threshold was surpassed three times in the Future climate horizon. The situation observed for the 33-66kV tier was slightly different, with one instance where $TI_{33-66,day,Future} \geq 5 * 10^6$ faults-customers was surpassed compared to none in the Control climate horizon. These results seem to confirm the points made earlier in this paragraph, which can be extended to include an increased impact of the wind-related faults on the 132kV tier and a decreased impact on the 33-66kV tier.

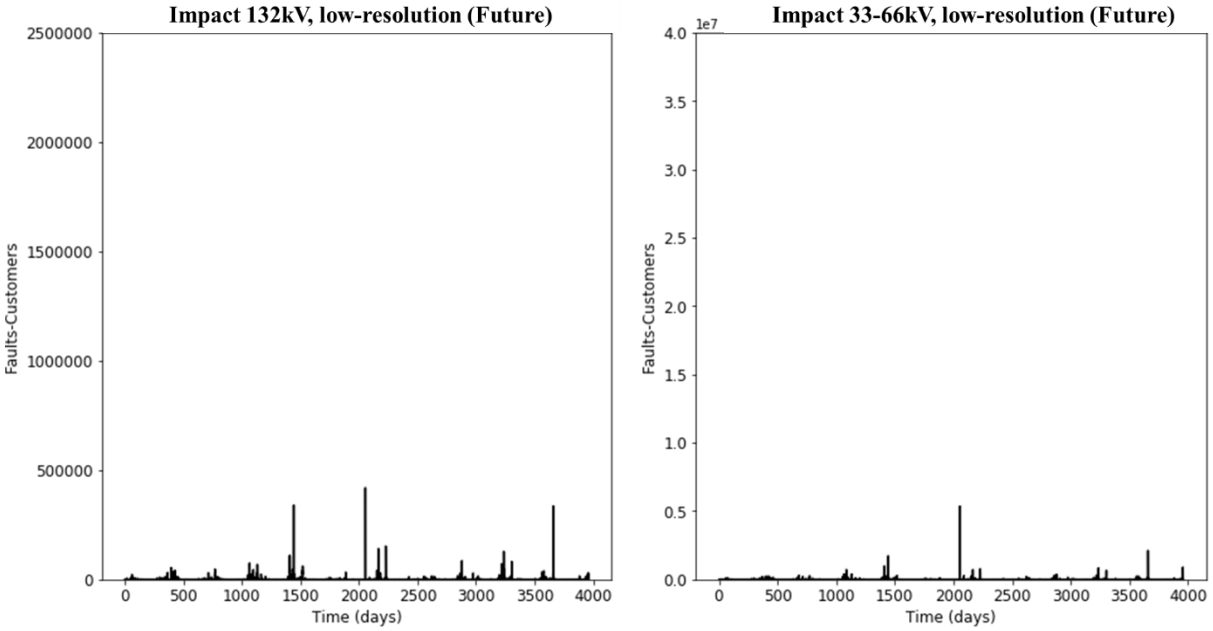

Figure 7.11. Time series of the Tier Impact for the 132kV tier (left) and 33-66kV tier (right) of the electricity network. These trends refer to the Future climate horizon and the low-resolution fragility curve.

7.2.5 Impacts determined with the high-resolution fragility curve

As with the number of expected faults, the transition from the low-resolution to the high-resolution fragility curve was accompanied by a remarkable increase in Tier Impact. Figure 7.12 depicts the time series of Tier Impact for both the 132kV and the 33-66kV tier in the Control climate horizon. Compared to the low-resolution case, the 132kV tier in the Control climate horizon featured five instances where $TI_{132,day,Control} \geq 4 * 10^5$ faults-customers, and a peak of $\max(TI_{132,day,Control}) \cong 9.1 * 10^5$ faults-customers which was more than fivefold the low-resolution peak for the Control climate horizon.

With respect to the 33-66kV tier, not only there were four instances where $TI_{33-66,day,Future} \geq 5 * 10^6$ faults-customers, but it was also found that $\max(TI_{33-66,day,Control}) \cong 2.1 * 10^7$ faults-customers, a sixfold increase with respect to the low-resolution Control climate horizon. It is apparent that the discrepancy between the low-resolution and the high-resolution Tier Impact for the Control climate horizon is not negligible, and that justification for this may be in the effect of the more detailed spatial information used to construct the fragility curves, as pointed out in paragraph 7.2.3. Finally, Figure 7.13 shows the time series of high-resolution Tier Impact for the 132kV and the 33-66kV tier in the Future climate horizon. The 132kV tier was found to exceed the $4 * 10^5$ faults-customers threshold

eight times, with a maximum value of $\max(TI_{132,day,Future}) = 2.3 * 10^6$ faults-customers. The latter corresponds to an increase of nearly six times with respect to the low-resolution Future climate horizon. In the case of the 33-66kV tier, it was found that the threshold of $5 * 10^6$ faults-customers was surpassed five times, with a peak value of $\max(TI_{33-66,day,Future}) = 3.4 * 10^7$ faults-customers.

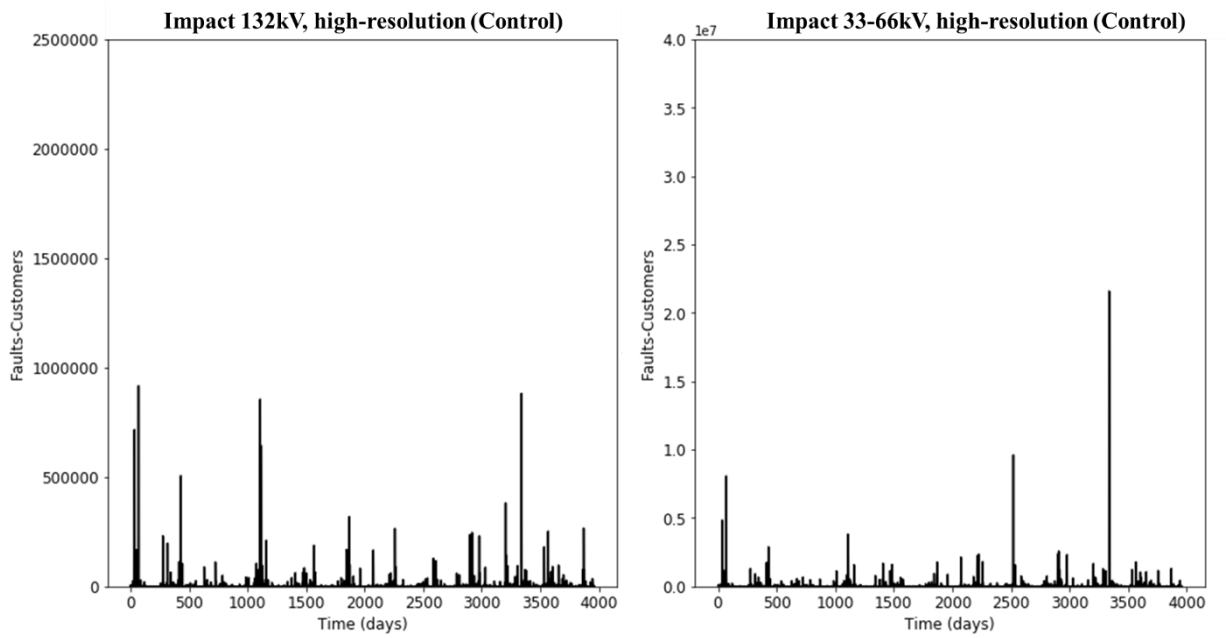

Figure 7.12. Time series of the Tier Impact for the 132kV tier (left) and 33-66kV tier (right) of the electricity network. These trends refer to the Control climate horizon and the high-resolution fragility curve.

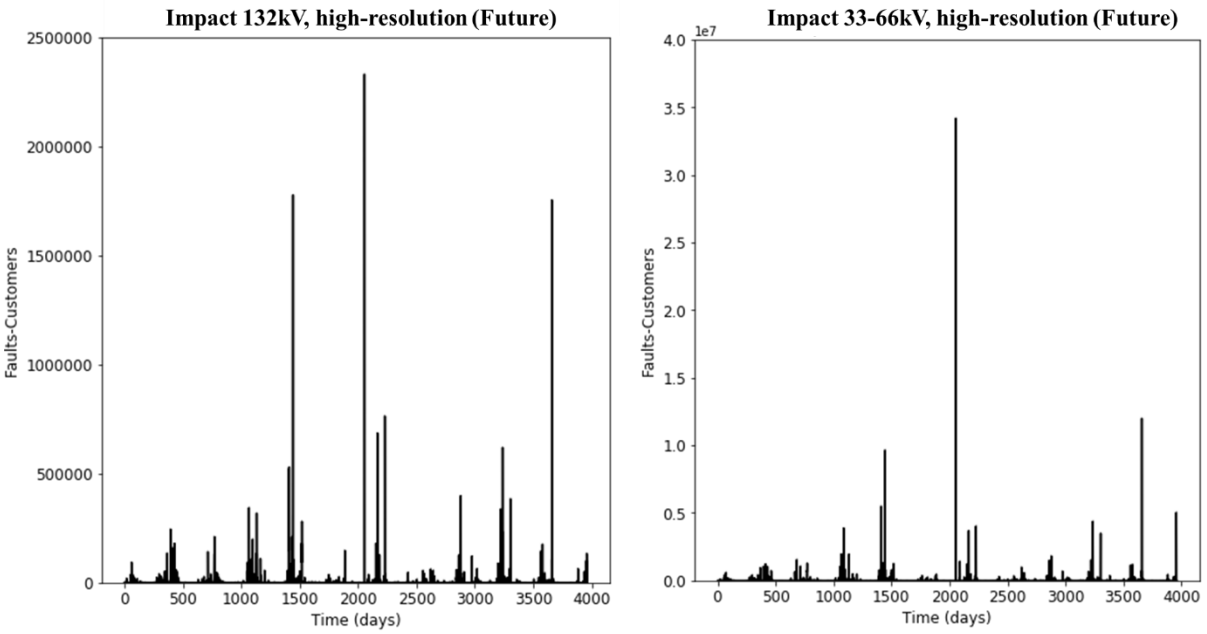

Figure 7.13. Time series of the Tier Impact for the 132kV tier (left) and 33-66kV tier (right) of the electricity network. These trends refer to the Future climate horizon and the high-resolution fragility curve.

7.2.6 Comparison between low-resolution and high-resolution impacts

Remarkable differences were found to exist between the 132kV and the 33-66kV tiers. Table 7.4 highlights these differences by reporting the values of the Time-Aggregate Impact $TAI_{t,horizon}$, which was obtained by integrating over time the Tier Impact to produce an aggregate, 13-year estimation of the impact of wind-related faults in terms of faults-customers. The discrepancies between the low-resolution and high-resolution Time-Aggregate Impact are a direct consequence of the differences between the two fragility curves. In the Control climate horizon, $TAI_{132,Control,high} = 4.12 * TAI_{132,Control,low}$, with an overestimation factor for the impact $o_{f,impact} = 4.12$. For the 33-66kV tier, $TAI_{33-66,Control,high} = 5.11 * TAI_{33-66,Control,low}$, with $o_{f,impact} = 5.11$. In the Future climate horizon, $TAI_{132,Future,high} = 4.31 * TAI_{132,Future,low}$, with $o_{f,impact} = 4.31$. For the 33-66Kv tier, it was found that $TAI_{33-66,Future,high} = 5.00 * TAI_{33-66,Future,low}$, with $o_{f,impact} = 5.00$.

What is interesting to observe, as with the faults, is the comparison between the Time-Aggregate Impact of each tier and climate horizon and the Faults-Customers reported in the NaFIRS database. This specific statistic is not directly present in the latter, but it was derived by computing the number of faults for each tier in the 13-year timespan of recorded data and the total number of customers affected. Surprisingly, the 132kV tier apparently recorded zero faults-customers in the January 2004-March 2017 period, despite 13 faults with damage were reported. This is due to the fact that the Distribution Network Operators are used to report the impact of each fault with respect to lower voltages.

As such, the only meaningful comparison that can be made is with the 33-66kV tier, where the Time-Aggregate Impact overestimated the number of faults-customers by as much as 3 orders of magnitude. This remarkable difference may be the result of the lack of regionalization in the fragility curves, but also of an intrinsic inaccuracy in the computation, which may be affected by the assumption that one fault was enough for the individual circuit or feeder to stop supplying electricity.

Due to this reason, it is here proposed that a more accurate metric for the estimation of the impact is needed. This metric could take advantage of the Customers-Minutes-Loss (CML) statistic that in the NaFIRS database is associated with each fault. This quantity is a more precise estimation of the impact, as it is recorded directly by the Distribution Network Operators, and it could be used to generate a *loss curve* describing the relationship between the wind gusts and the CML statistic. However, difficulties may arise in trying to accurately locate each fault in

the study area, as rarely does the NaFIRS database include geographical indications. The latter is also the justification for the fact that a loss curve was not developed in this case study.

Table 7.4. Time-Aggregate Impact in faults-customers for the 13-year climate horizons as a comparison between the low-resolution, high-resolution, and Faults-Customers NaFIRS observations.

	Low-resolution fragility curve		High-resolution fragility curve		Faults-Customers, NaFIRS
Tier	Control	Future	Control	Future	
132kV	$5.1 * 10^6$	$5.8 * 10^6$	$2.1 * 10^7$	$2.5 * 10^7$	0
33-66kV	$4.3 * 10^7$	$4.2 * 10^7$	$2.2 * 10^8$	$2.1 * 10^8$	$3.9 * 10^5$

7.3 Stage 6: systemic indicators of robustness

7.3.1 Risk of faults

The risk of faults was computed as the Annual Risk of faults $AR_{comp,horizon}$ to which the individual components of the 132kV and 33-66kV tiers were exposed in both climate horizons. This metric, expressed in customers lost per year, is equivalent to the Time-Aggregate Impact divided by the length of the climate horizons (e.g., 13 years), and it was aimed at estimating how many faults-customers were associated, on an annual basis and with both fragility curves, with each tier component.

Figure 7.14 shows the breakdown by component of the associated Annual Risk computed by using the low-resolution fragility curve, superimposed on the annual frequency of exceedance of events with wind gust $w_{10,3} > 17\ m/s$. The superimposition is provided as a reference for associating the spatial gradient of the severity of the natural spatial hazard to the risk to which each component was exposed. Overall, both as a result of the higher number of faults and the presence in highly exposed locations, the 33-66kV tier was found to be the most exposed of the two tiers, with the average component Annual Risk exceeding that of the 132kV tier by a factor of 22.40 in the Control climate horizon and 19.09 in the Future climate horizon.

More specifically, a very interesting spatial gradient can be observed, with certain components being exposed to a risk significantly higher than others. Among the 33-66kV components, the line served by the Driffield Bulk Supply Point, identified by the label ”1”,

showed the highest exposure, facing an Annual Risk $AR_{Driffield,Control,low} = 128{,}679$, entailing that 128,679 customers were lost every year due to wind-related faults in the Control horizon. This number was found to be almost 3.40 times higher than that associated with the second most exposed 33-66kV component, identified by the label "2".

In the Future climate horizon, the Annual Risk of the line served by the Driffield Bulk Supply Point was found to decrease to $AR_{Driffield,Future,low} = 116{,}373$, signaling a 9.5% drop. In the case of the 132kV tier, the most highly exposed component was found to be the line served by the Keadby National Grid substation, labelled as "3". In the Control climate horizon, such line was found to be exposed to an Annual Risk $AR_{Keadby,Control,low} = 5{,}686$, corresponding to a total of 5,686 customers lost each year due to wind-related faults. Compared to the second most exposed 132kV line, this number was 2.70 times higher. In the Future climate horizon, $AR_{Keadby,Future,low} = 6{,}359$, corresponding to a 11.8% increase. Two important aspects are to be highlighted with respect to the 132kV tier: *i*) the Annual Risk of faults for the 132kV components is computed based on the total number of customers that are served by the component, including those served by the 33-66kV components that are fed by each individual 132kV component (see Figure 5.17), and *ii*) the 132kV component served by the Keadby National Grid substation appears to be rather influential in the structure of the two-tier system in that, although it was exposed to a relatively limited risk, it serves as a bridge between the Keadby Power Plant (the black triangle in Figure 7.14) and the city of Grimsby and supplies three 33-66kV components.

Figure 7.15 displays the distribution of the Annual Risk computed by using the high-resolution fragility curve, again superimposed on the annual frequency of exceedance of events with wind gust $w_{10,3} > 17\ m/s$. The spatial gradient observed for the low-resolution fragility curve was confirmed, although, as a consequence of the higher number of faults produced by the high-resolution fragility curve, higher risks were highlighted. For instance, the average component Annual Risk of the 33-66kV tier exceeded that of the 132kV tier by a factor of 25.33 in the Control climate horizon and 21.08 in the Future climate horizon. In the Control climate horizon, the line served by the Driffield Bulk Supply Point showed the highest exposure, facing an Annual Risk $AR_{Driffield,Control,high} = 612{,}127$, an increase of 476% with respect to the same quantity computed with the low-resolution curve.

The second most exposed 33-66kV component was found to change, being the line served by the Hull East Bulk Supply Point, although the difference with respect to the line labelled as "2" in Figure 4.26 is less than 3%. Such difference is likely to be ascribable to the accumulation of round-off errors. In the Future climate horizon, the line served by the Driffield

Bulk Supply Point was found to be exposed to an Annual Risk $AR_{Driffield,Future,high} = 556{,}301$, a 9.1% drop that almost mirrors the decrease observed between the Control and Future climate horizons with the low-fragility curve. With respect to the 132kV component served by the Keadby National Grid substation, the Annual Risk went up from $AR_{Keadby,Control,high} = 24{,}311$ to $AR_{Keadby,Future,high} = 28{,}673$, an increase of 428% and 451%, respectively. With respect to the second most exposed 132kV component, the line labelled as "3" was found to face between 2.75 times and 3.61 times the Annual Risk.

Overall, these results indicate that, whilst the frequency of more extreme events in the study area is not reflected in the risks, possibly due to the differences in spatial structure between the wind gusts and the electricity network, a non-linear causal relationship between the two can certainly be observed. Identifying the risk by component, which is a direct consequence of the system-of-systems approach adopted in this case study, was pivotal in allowing to pinpoint the most exposed segments of the electricity network.

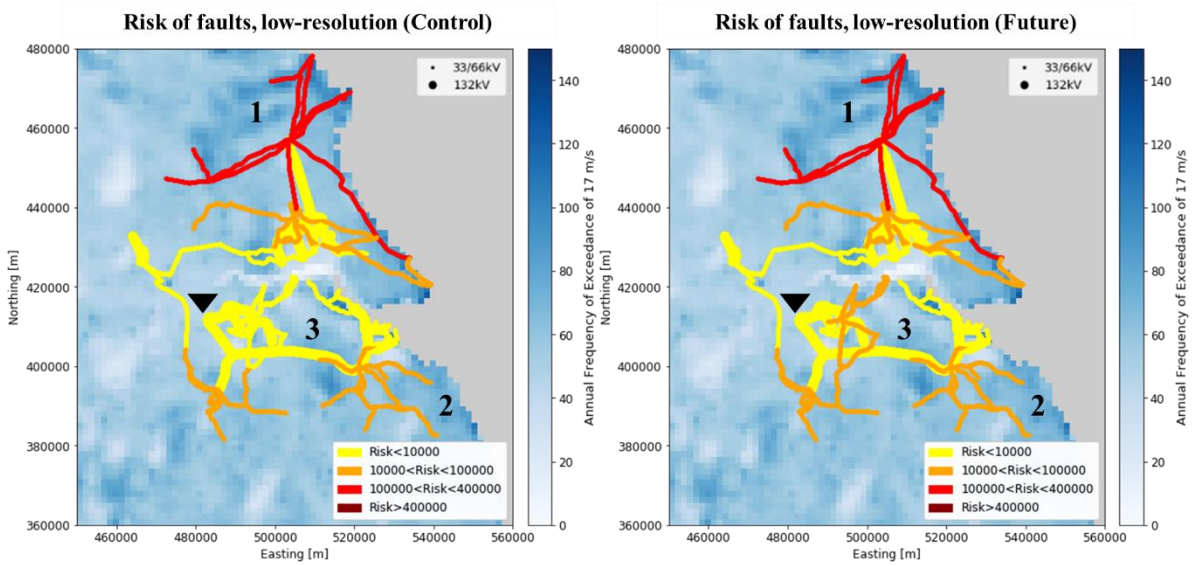

Figure 7.14. Annual Risk of faults according to the low-resolution fragility curves for the 132kV tier (thick lines) and 33-66kV tier (thin lines) in the Control (left) and Future (right) climate horizons. The risk is expressed in customers lost per year. The labels refer to: (1) 33-66kV component served by the Driffield Bulk Supply Point, (2) 33-66kV component served by the Wold Newton Bulk Supply Point, (3) 132kV component served by the Keadby National Grid substation. The location of the latter is identified by the black triangle.

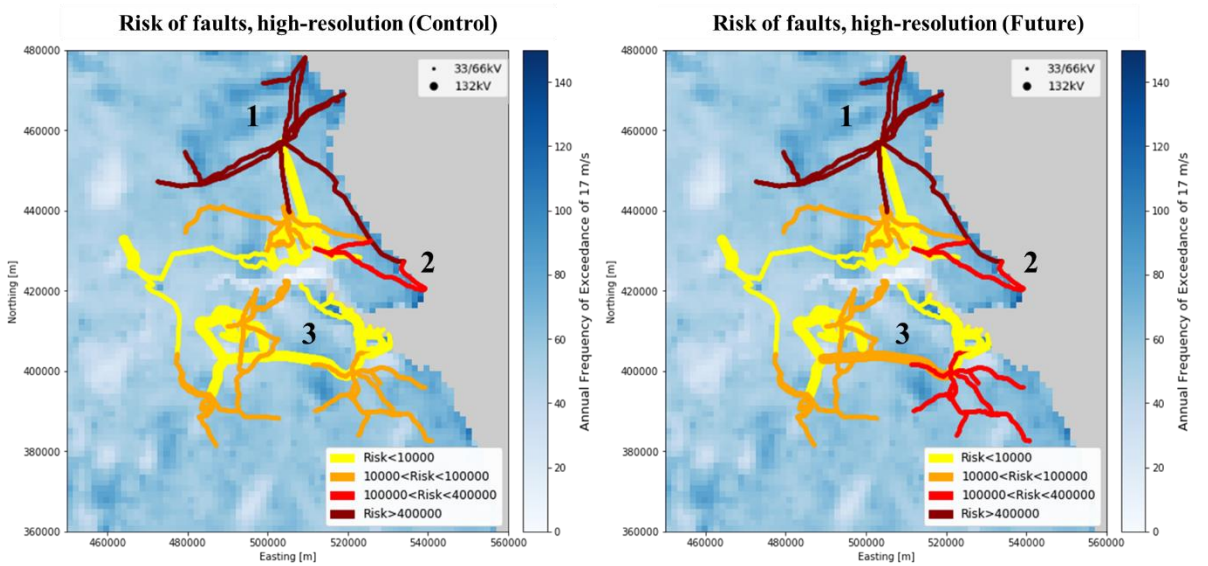

Figure 7.15. Annual Risk of faults according to the high-resolution fragility curves for the 132kV tier (thick lines) and 33-66kV tier (thin lines) in the Control (left) and Future (right) climate horizons. The risk is expressed in customers lost per year. The labels refer to: (1) 33-66kV component served by the Driffield Bulk Supply Point, (2) 33-66kV component served by the Hull East Bulk Supply Point, (3) 132kV component served by the Keadby National Grid substation.

7.3.2 Intra-systemic cascading failures

7.3.2.1 Breakdown of frequency of cascading failures and risk of cascading failures

The robustness of the two-tier electricity network to cascading failures was evaluated by analyzing intra-systemic failures, e.g. wind-driven faults which effects propagated from components of the 132kV line down to the supplied 33-66kV components by virtue of the hierarchical connections. This is a bottom-up approach implemented to highlight the 33-66kV components that, in the two 13-year climate horizons, were impacted the most by failures that only originated at the 132kV level. Also implemented was a top-down approach aimed at evaluating the frequency with which the 132kV components caused the cascading failures, with the purpose of highlighting the most influential components of the 132kV line. The bottom-up and top-down approaches were both relying on the number of 132kV components supplying each 33-66kV component (see Figure 5.16).

Another important element of such computation was the assumption that the faults occurred at the 132kV level were the result of a wind gust $w_{10,3} > 17\,m/s$, which was interpreted as a critical wind speed threshold. The lack of information regarding the actual presence of switchyards forced this analysis to assume that one wind-driven fault originating at the 132kV level was enough to cause service failings to the entire line of the supplied 33-66kV component (see Figure 5.18). However, when a 33-66kV component was supplied by multiple

132kV components, all of the latter had to fail for the cascading failure to propagate down to the 33-66kV component.

Figure 7.16 depicts the breakdown, in the form of a heatmap, of the daily frequency of cascading failures that affected the 33-66kV components in the Control climate horizon. The most heavily hit component, labelled as "1", was the one supplied by the Wold Newton Bulk Supply Point, which recorded a frequency of cascading failures $f_{casc,Control,1} = 0.367$. This value implies that, approximately every 3 days, the component labelled as "1" experienced one cascading failure due to the simultaneous failure of all the 132kV components supplying it. The second most impacted 33-66kV component, labelled as "2", was found to have been affected with a frequency of $f_{casc,Control,2} = 0.319$.

In the Future climate horizon, said components were subjected to cascading failures with a frequency of cascading failures that decreased by 4% and 11.9%, respectively. The most significant decrease in frequency was found in the 33-66kV component supplied by the Immingham Bulk Supply Point, which is labelled as "4". In this case, the decrease peaked at 22.4%.

Whilst the majority of the components experienced a decrease in the frequency of cascading failures, which is attributable to the decrease in the wind gust severity observed for the Future climate horizon, two exceptions were found. The first one is the 33-66kV component labelled as "3", which experienced a negligible increase of 0.5%, essentially maintaining its level of exposure unchanged, and the component labelled as "5", which recorded an increase in frequency of 15%. Whilst the component labelled as "3" constitutes an interesting and possibly alarming case, the component labelled as "5" had a rather low frequency value in the Control climate horizon which was very sensitive to any increase.

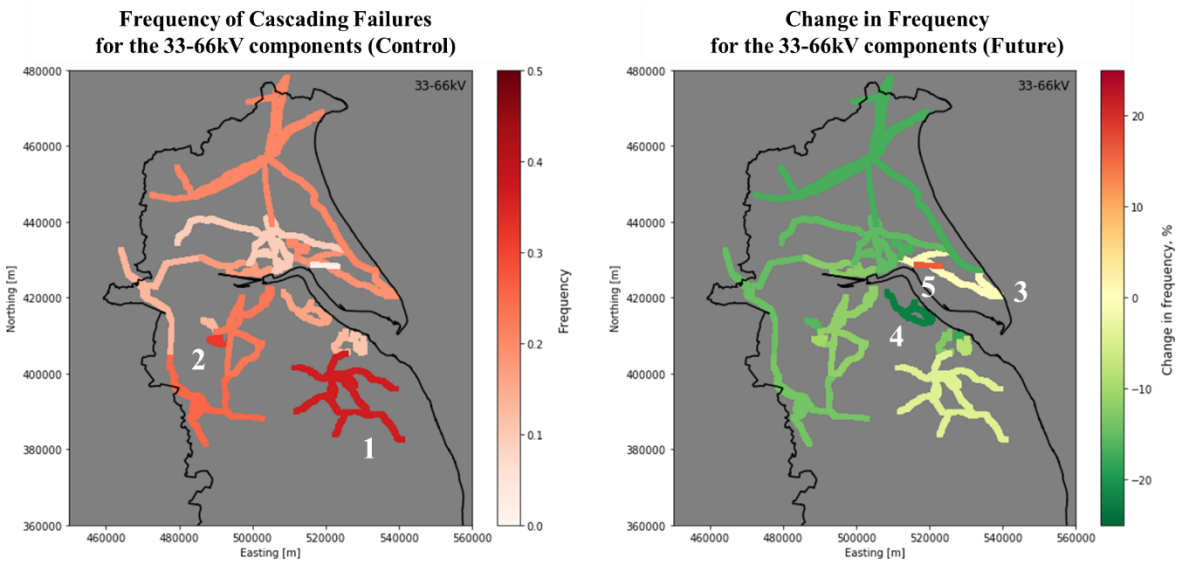

Figure 7.16. Left: breakdown of the frequency of cascading failures that hit the 33-66kV components in the Control climate horizon. Right: change in frequency in the transition from the Control to the Future climate horizon. The label refers to: the component supplied by the Wold Newton Bulk Supply Point ("1"), the component supplied by the Scunthorpe South Bulk Supply Point ("2"), the component supplied by the Hull East bulk Supply Point ("3"), the component supplied by the Immingham Bulk Supply Point ("4"), and the component supplied by the Saltend Bulk Supply Point ("5").

Figure 7.17 shows the breakdown of risk of cascading failures associated with each 33-66kV component. The heatmap was obtained by multiplying the frequency of cascading failures of each component by the number of customers served. This produced a metric indicating the potential impact, in terms of customers lost per day, of the cascading failures. Owing to the fact that a different number of customers was served by each component, the risk heatmap does not exactly mirror that of the frequency of cascading failures. In fact, whilst the component labelled as "1" is subjected to both the highest frequency and the highest risk, with $r_{casc,Control,1} = 7966$ customers per day, the second most exposed component, labelled as "2", was not the one supplied by the Scunthorpe South Bulk Supply Point but the one supplied by the Driffield Bulk Supply Point, with $r_{casc,Control,2} = 5787$ customers per day. In terms of changes with respect to the Future climate horizon, the 33-66kV component supplied by the Hull East Bulk Supply Point confirmed a steady risk, whereas the component with the highest decrease in risk, labelled as "4", was also the one with the highest decrease in frequency of cascading failures.

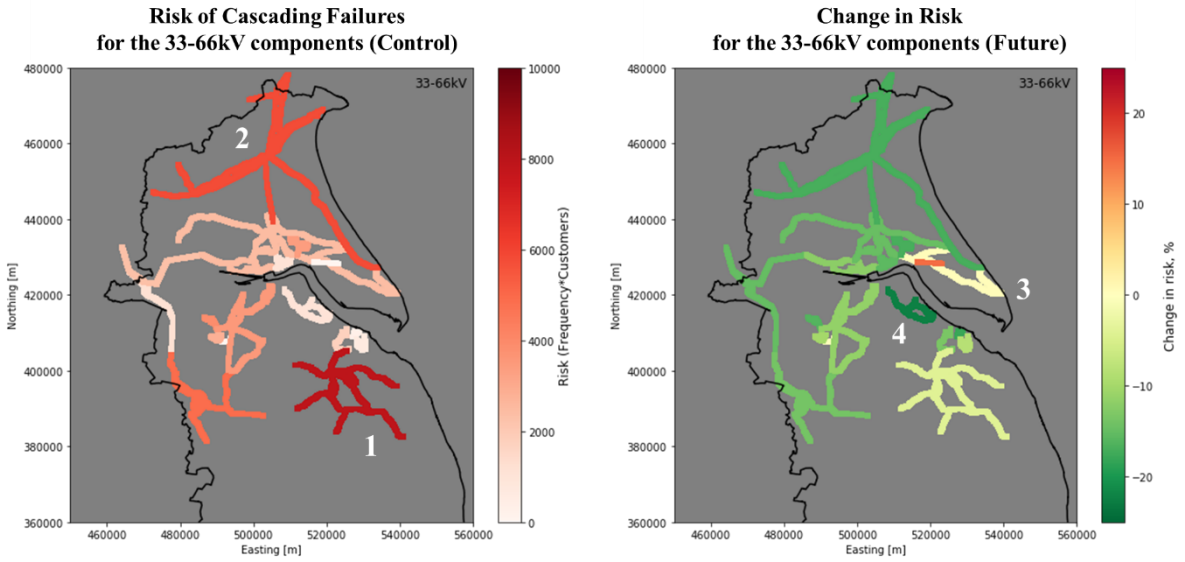

Figure 7.17. Left: breakdown of the risk of cascading failures that hit the 33-66kV components in the Control climate horizon. Right: change in risk in the transition from the Control to the Future climate horizon. The label refers to: the Driffield Bulk Supply Point ("2"), the component supplied by the Hull East bulk Supply Point ("3"), and the component supplied by the Immingham Bulk Supply Point ("4").

Objective of this case study was to also investigate the frequency with which the 132kV components caused the cascading failures. Figure 7.18 shows the heatmap of the frequency with which the 132kV components caused cascading failures. Two areas could be identified with significant frequencies. The first includes the component labelled as "1", which was found to produce cascading failures with a frequency of $f_{caused,Control,1} = 0.623$, as well as other clustered components with $f_{caused,Control} > 0.6$. The other area includes the component labelled as "2", which caused cascading failures with a frequency of $f_{caused,Control,2} = 0.608$. The transition to the Future climate horizon showed, in alignment with the previous paragraphs, a general decrease in the frequency of caused cascading failures, although the component labelled as "3" stood out as it experienced an increase of 2.4%.

As with the 33-66kV components, the risk of causing cascading failures r_{caused} was computed for each 132kV component. This was determined by multiplying the frequency of caused cascading failures per day by the number of customers served by the 33-66kV components served by each 132kV component. Figure 7.19 shows that, once again, the risk heatmap does not perfectly mirror the frequency heatmap, due to the uneven distribution of customers served among the 33-66kV components.

The component that was found to be most exposed to the risk of cause cascading failures, labelled as "1", did not correspond with the one that featured the highest frequency of caused cascading failures. The former was exposed to a risk of $r_{caused,Control,1} = 3967$ customers per day, entailing that, on a daily basis, an average of 3967 customers were at risk of

service failings due to cascading failures originating in that component. By contrast, the component labelled as "2", which matched the one causing the second highest frequency of cascading failures, was exposed to a risk of $r_{caused,Control,2} = 3432$ customers. As a direct consequence of the frequency heatmap in Figure 7.18, the Future climate horizon produced a general decrease in the risk, although the component labelled as "3" was found to exposed to a projected increase in risk of 2.3%.

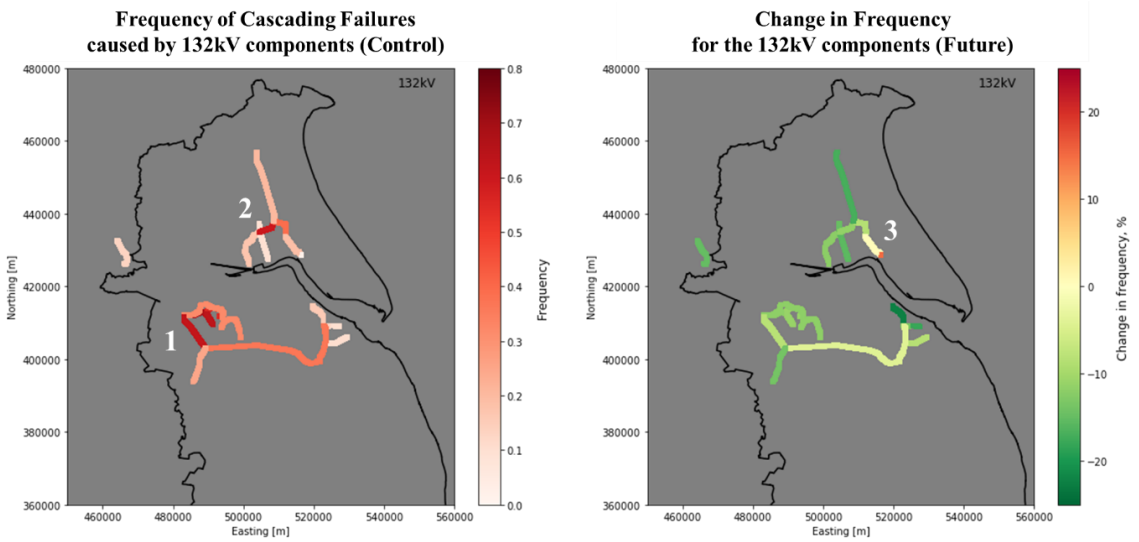

Figure 7.18. Left: breakdown of the frequency of cascading failures caused by the 132kV components in the Control climate horizon. Right: change in frequency in the transition from the Control to the Future climate horizon. The labels refer to: the component with the highest frequency in the Control climate horizon ("1"), the component with the second highest frequency in the Control climate horizon ("2"), and the component with the highest positive change in the Future climate horizon ("3").

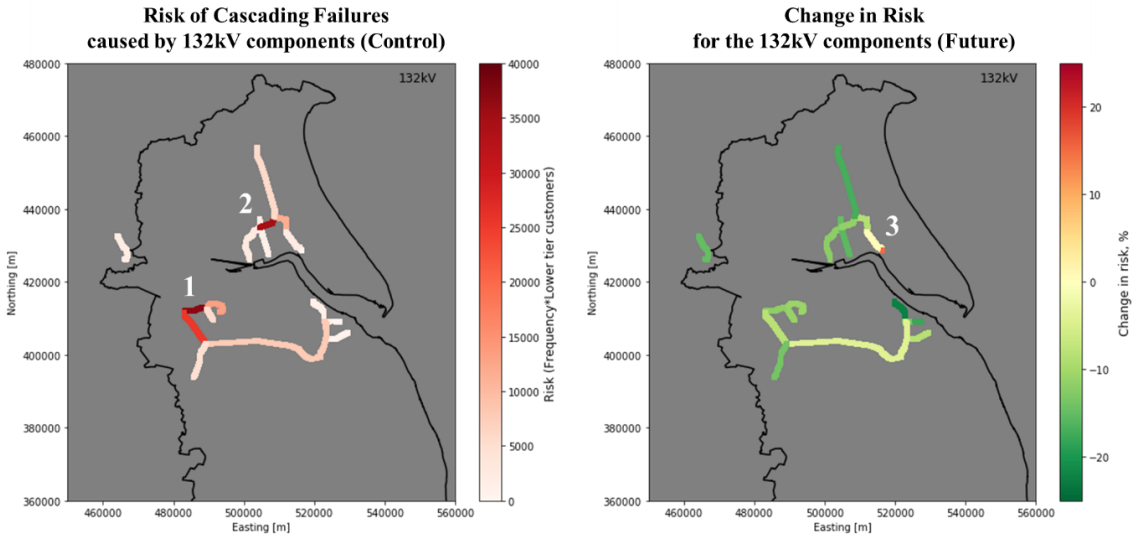

Figure 7.19. Left: breakdown of the risk of cascading failures caused by the 132kV components in the Control climate horizon. Right: change in risk in the transition from the Control to the Future climate horizon. The labels refer to: the component with the highest risk in the Control climate horizon ("1"), the component with the second highest risk in the Control climate horizon ("2"), and the component with the highest positive change in the Future climate horizon ("3").

Overall, this procedure highlights components of the 33-66kV tier that are associated with high frequency of cascading failures and risk, offering a strategic investment plan several important indications regarding where an increased redundancy may be most effective. At the same time, the identification of the 132kV components that cause the highest number of cascading failures offers investors and infrastructure operators important information regarding the locations where an increased robustness may be necessary. However, as much as the projections for the Future climate horizon indicate a general and appreciable decrease in both the frequency and risk of cascading failures and for both tiers, the results for the Control climate horizon are likely to offer an overestimation of the actual frequency and risk.

The lack of cascading failure records in the NaFIRS database or anywhere else did not allow to validate the above-mentioned results, and as such, a benchmark is missing. From a critical perspective, the justification for categorizing these results as an overestimation is in the fact that a specific 33-66kV component was found to experience one cascading failure approximately every 3 days, as a result of the simultaneous failure of all the 132kV components supplying it. Notwithstanding the lack of a benchmark, such frequency appears to be rather high, depicting an infrastructure that is far less reliable than the official numbers reveal.

A number of factors are likely to contribute to this hypothesized overestimation: *i*) it is possible to categorize the cascading failures so far analyzed as *topological cascading failures*, entailing that they were the result of the topological-hierarchical structure of the network rather than actual cascading failures; *ii*) the adoption of a topological scheme to describe the propagation of failures is likely to have introduced an assumption of causal linearity, whereby one fault occurring at the 132kV level automatically meant the interruption of electricity supply at the lower level; *iii*) the fact that the propagation of failures was triggered by the exceedance of a wind speed threshold is likely to have introduced an additional assumption of causal linearity, whereby faults occurred with a probability of 100% every time the threshold was exceeded; and *iv*) additional uncertainty was introduced by the fact that information regarding the presence and functionality of switchyards was lacking, together with the implementation of a flow algorithm describing the power flow equations.

However, notwithstanding the assumptions and uncertainties previously highlighted, this procedure is deemed worthy of consideration, as it offered a methodology that highlights the most vulnerable components of the electricity network. However, adequate information regarding how the failures spread in a system should not neglect the flow algorithm nor the topology of the system but should include both.

Chapter 8. Conclusions

8.1 Introduction

This chapter reports the most important findings and distills the key messages from the work carried out. This thesis comprised two case studies that were used to characterize the robustness of infrastructure networks to spatial hazards. The two case studies share a common research framework that provided insights into the relationship between infrastructure network design and robustness to spatial hazards.

1. ***Case Study 1: Response of synthetic infrastructure networks to synthetic, although realistic, spatial hazards***

   Case Study 1 developed a new fractal model to generate fields that correspond to spatial hazards. The response of a range of infrastructure network types to different spatial hazard structures was analyzed. By loading the networks with generic spatial hazards, important principles applicable to the design phase were derived. These suggest that different network layouts, or topologies, offer different robustness performances, and that specific layouts seem to be fitter than others;

2. ***Case Study 2: Impacts of windstorms on electrical distribution infrastructure networks***

   Case Study 2 showed that spatial wind gust data have fractal properties, creating continuity with Case Study 1. These data were superimposed to a two-tier electricity network in which robustness to faults was evaluated under a current and future climatic scenario. The hierarchical structure of the network was reasonably preserved, leading to the identification of segments that appeared more vulnerable to both direct and knock-on effects. This seems to provide a clear list of priorities that can feed into strategic investment plans.

8.2 Main findings and implications

8.2.1 Overview

Both case studies assessed the robustness of infrastructure networks and considered how they could be made more robust to spatial natural hazards. The insights gained from Case Study 1 highlight how robustness can be embedded into networks from the outset at the design and planning stage. Case Study 2 identifies strategies to improve the robustness of existing networks by ascertaining priorities for strengthening components, increasing redundancy, or a combination of both. The key findings are now considered in the context of the objectives set out in the Introduction.

Case Study 1 showed how infrastructure layout and robustness to spatial hazards could improve the design phase, whilst Case Study 2 demonstrated how interactions between components of the same operating infrastructure could make the latter a more robust system.

In the context of a decision-making process that facilitates network recovery, the outcome of Case Study 1 is an example of ex-ante decisions (e.g., planning in advance for extreme events, learning from past experiences, etc.), whilst the outcome of Case Study 2 is aligned with ex-post decisions (e.g., implementing back-up systems or effective communication, removing restrictions, etc.).

8.2.2 Objective 1: reviewing existing methods for modelling spatial hazards and proposing a new approach

A careful evaluation of the techniques used in the literature to reproduce spatial hazards revealed that these are generally attractive due to the relative ease of implementation, although they may require extensive data or computational resources to be reliable. However, it was also highlighted how these techniques fail to thoroughly consider the spatial attributes of spatial hazards, such as variation in the spatial structure and intensity over their domain.

A new approach has been presented in Case Study 1, based on the use of fractal surfaces known as Brownian surfaces. These are non-deterministic, isotropic, three-dimensional fields originating from a stochastic process that mimics the erratic behavior of Brownian motion. The elevation of each surface was adopted as the severity or intensity index $\in [0,1]$ of a generic spatial hazard.

The Brownian surfaces were found to reproduce the spatial variability of spatial hazards more accurately than deterministic approaches. Only one tuning parameter, the Hurst exponent H, is needed to control the spatial autocorrelation of the fractal surfaces. By adopting a range of values for $H \in [0.6, 0.7, 0.8, 0.9, 1.0]$, it was possible to produce an array of hazard fields with increasing degrees of spatial correlation, ranging from highly fragmented ($H = 0.6$) to smooth surfaces ($H = 1.0$).

The implications for impact studies are manifold. Firstly, Brownian surfaces allow the generation of hazard fields at different spatial scales and with different degrees of spatial autocorrelation. This significantly improves upon other methods where spatial autocorrelation is largely uncontrolled, and extents are defined by regular shapes, such as circles or ellipses, in which the intensity varies deterministically, if at all. Secondly, it was demonstrated that fractal surfaces induced up to 100% more failures in the same network compared to circular-shaped hazard fields, suggesting that deterministic fields may underestimate the impact of spatial hazards by 100%. Thirdly, this methodology requires limited computational resources, and it can be implemented using open-source programming languages such as Python, with no license fees. Overall, computational efficiency and generation of varied hazard structures make fractal surfaces a viable option for uncertainty and sensitivity analysis. However, because Brownian surfaces exhibit periodicity and boundary effects, before usage the surfaces need to be cropped to approximately 25% the size of the original surface.

8.2.3 Objective 2: comparing the spatial properties of non-deterministic and real spatial hazards

In Case Study 1, the Hurst exponent *H* was varied between 0.6 and 1.0 to test the impact of different spatial hazards on infrastructure networks. In Case Study 2, H was not known a priori. By comparison of the Area-Frequency curves, the wind gust fields are shown to exhibit fractal properties both in the Control and Future climate model outputs, corresponding to $H = 0.9$. However, this relationship seems weaker for $w > 28\, m/s$. This is possibly because the atmospheric processes driving high winds typically manifest at a regional scale, with climatic conditions changing from region to region. Although there is absolute freedom to generate Brownian surfaces with any degree of spatial autocorrelation, typically most natural hazards fall between $H = 0.8$ and $H = 1.0$, which corresponds to a fractal dimension $2.0 < D < 2.2$. As the windstorms were found to be largely associated with $H = 0.9$, they can be seen as the real-world equivalent of the most severe hazard structures considered in Case Study 1.

The binarization, performed to identify which areas of the spatial domain exhibited severity exceeding a certain threshold, offered limited value, being only meaningful in the case of the lowest threshold. In fact, whilst the binarization allowed to generate several H, Ft combinations in Case Study 1, not all of these combinations found a real incarnation in Case Study 2, where the goal was to verify the presence of fractal properties and estimate the fractal dimension of wind gusts.

Whilst the spatial properties of the Brownian surfaces are fractal by nature, the comparison with the wind gust hazard fields revealed that the latter also exhibit fractal properties comparable with Brownian surfaces with $H = 0.9$.

8.2.4 Objective 3: interaction between spatial hazards and synthetic infrastructures

The interaction between spatial hazards and synthetic network models has been investigated with a binary failure propagation mechanism. Network nodes were either active or, if their failure threshold F_t had been exceeded, failed. If nodes became isolated because the other nodes they were connected to had failed, then 2nd order failures occurred, affecting between 5% (for Lattice Networks) and 27% (for Scale-Free Networks) of the active nodes left in the network.

In Case Study 1, highly fragmented surfaces ($H = 0.6$) caused the highest number of failures in weak networks (up to 30% more failures than other surfaces), whereas highly smooth surfaces ($H = 1.0$) were most detrimental to strong networks (up to 42% more failures than other surfaces). This is because scattered severity peaks can cause multiple disruptions in weak networks that subsequently propagate through the network, whereas strong networks require hazards with more spatial continuity to be taken down.

The implications are that evaluating the potential impact of natural spatial hazards on infrastructures is most valuable if it is possible to determine the failure threshold of infrastructure components. In practical terms, this entails defining the levels of service that the infrastructure can guarantee under the constraints posed by failures and disruptions. In conclusion, the aspects highlighted above are derived from simulations involving small networks. As such, these should be validated against larger networks and using a different range of H.

8.2.5 Objective 4: assessing infrastructure robustness using topology-based metrics

The response of synthetic infrastructure models to fractal hazards has been evaluated using four topology-based metrics. Given the complex interactions between synthetic models and hazards, adopting multiple metrics instead of one enabled to capture the many facets of these interactions. These metrics assessed the extent of the network surviving the impact (SN), how far from the hazard hotspot the failures propagated (SR), the tendency of to generate partitions (FI), and the ability to distribute flow in the face of disruptions (CFI).

Two extreme behaviors where identified. The regular structure of LN enabled it to withstand the impact of spatial hazards better than other networks, resulting in an average 31% less failures. Such regularity also limited the occurrence of 2nd order failures, which were located closest to the hazard hotspot. The LN recorded the lowest number of partitions, 2, given the infrequent occurrence of failures due to isolation. The absence of shortcuts from one node to another, however, strongly limited the ability to process flows in the presence of failures, resulting in a 20% performance decrease for hazards affecting 10-20% of the network.

The WS model behaved rather differently, recording the second lowest number of failures (19% less than the ER and BA models on average), the second lowest number of partitions, 3, and 5% more robust to the spread of failures across its structure than the WS and BA models. Most importantly, however, the WS networks exhibited the least reduction in the ability to process flows, dropping their performance by only 4% for hazards affecting 10-20%

of the network. The BA and ER models were between these two extremes, with the former slightly closer to WS and the latter more aligned with LN.

These results show that there may be advantages in adopting a grid model (LN), however it proved most vulnerable to disruptions when flow of resource is an important aspect of the infrastructure service. Networks with a small number of critical hubs – often the case for many infrastructure types – were more vulnerable to fragmentation whenever the hub itself was impacted by the disruption. This shows that there is an intrinsic risk of fragmentation in scale-free infrastructure networks. These properties were shown to be consistent over the range of H and F_t. Although eloquent, these results are affected by the number of iterations adopted for each network model and the failure propagation algorithm.

8.2.6 Objective 5: interaction between real natural hazards and real infrastructures

The average number of faults per 1000 km and the impact in terms of customers served reflected the seasonality of wind gusts, which were more frequent and 57% stronger in the winter on average. Differences between the Control and Future horizons were also observed: coastal areas experienced slower wind gusts (up to -10%) from Control to Future, whilst inner areas faced an increase of up to 12%. However, there is significant uncertainty in the prediction of future wind.

Any climate-related natural hazards, if considered over the large spatial domains in which infrastructures often operate, should be considered over smaller, regional domains for impact studies to yield a more realistic outcome. This entails that the size of the infrastructure analyzed should be constrained by the footprint of the hazard. This requires regional domains that are both meaningful for the infrastructure and the hazard. If this aspect is not considered, there is a clear risk of underestimating or overestimating the impact of failures with respect to the recorded events.

Different number of faults were obtained with different fragility curves. The high-resolution fragility curve returned a number of faults which was almost 5 times as large as that returned by the low-resolution curve for both tiers.

This may be because the high-resolution fragility curve, with a spatial scale 64 times smaller than the low-resolution curve, was able to capture the impact of wind gusts much more locally.

It is also worth noting that a remarkable difference in the average number of faults was observed between the 132kV and the 33-66kV systems. The number of faults in the 33-66kV

network exceeded those observed at the 132kV level by a factor of 12 in Control and by a factor of 15 in Future. This is in part due to the different spatial footprint of the two networks, with the 33-66kV system being approximately 4 times more extended as the 132kV system. However, the spatial variability of the hazard influences the impact depending on the location of the highest windspeeds. In Case Study 2, there were more 33-66kV lines in areas more exposed to greater windspeeds. This can be the case in more remote areas, for instance the North York Moors, where the topographic and orographic conditions make it inconvenient for the higher voltage lines to operate.

8.2.7 Objective 6: highlighting the most critical segments of the infrastructure and their potential to trigger cascading failures

For each segment (or component) of the 132kV network, the potential to trigger cascading failures was determined by computing the frequency of 2nd order failures occurring in the 33-66kV components being fed by the 132kV component.

Given the hierarchical nature of the electricity network, both the risk of faults and the potential to trigger or be impacted by cascading failures returned different results depending on the voltage. Across the domain, the variation in risk resulted from the combination of two factors: a severe wind hazard, and a high number of customers served.

The 132kV components were more likely to be in areas with lower windspeeds, but they fed up to 14 33-66kV segments, meaning that failure of a 132kV segment would disrupt many more customers. At the 33-66kV level, the situation was inverted: although exposure to more severe wind gusts resulted in 12-15 times more faults, this did not guarantee a higher risk than for the 132kV network as there were an average 70% less customers served. For both systems and in both Control and Future, consistent segments of infrastructure with higher risk were identifiable.

In terms of cascading failures, specific 33-66kV segments experienced a cascading failure with a frequency of 40%, due to the simultaneous failure of the 132kV segments feeding them. In the transition from Control to Future, the 33-66kV segments experienced an average decrease in frequency of 17%. This is the consequence of the projected general decrease in wind hazard discussed in paragraph 7.3.2, although the presence of isolated spikes demonstrates that the spatial variability of the hazard field is such that it is necessary to zoom in on the behavior of the individual components rather than considering the network as a whole.

It emerged that individual 132kV segments triggered cascading failures in the lower 33-66kV network which impacted as many as 45,000 customers (more than 15% of the customer base considered in Case Study 2). Unlike the 33-66kV network, an average decrease in frequency of 9% was observed. Overall, this seems to indicate that, as shown in Case Study 1 for 2nd order failures, the risk of cascading failures is influenced by the spatial properties of the hazard and those of the network.

Using data on only the number of faults to determine the impact of high winds is likely to be misleading without proper spatial context. Knowing where faults are more likely to occur is crucial for devising an investment plan. A trivial asset protection strategy might only tackle the vulnerability observed at the highest hierarchical levels, seeking to increase the robustness of the lines at highest voltage (e.g., the 132kV lines, the 275kV lines, or even the National Grid's 400kV lines). However, this strategy could have dramatic impacts on the customer base itself, leaving it unshielded from faults occurring at lower voltages which, as shown in this thesis, could also be the most exposed to the hazard.

Finally, two aspects are worthy of consideration. First, these results refer to an asset dataset without loops or switches, which are used to increase the redundancy of the system and offer an alternative supply route in the event of faults. By not incorporating this type of information, it is easier to overestimate the faults, risks, and impacts. Second, the underlying assumption behind the origin of cascading failures was that it is a necessary and sufficient condition to have a single fault along a component for the electricity supply to be interrupted downstream.

8.2.8 Objective 7: key recommendations for engineers, policy makers, and other stakeholders

In both Case Studies, a systemic approach was applied to understand the behavior of infrastructure networks subjected to spatial hazards. The results show the importance of two crucial aspects: *redundancy*, which can be simplistically associated with the availability of alternative supply routes, and *robustness*, entailing increased ability to withstand disruptions.

Analysis of network response using several performance metrics showed how different network types are impacted by different types of hazards and how the impacts can be mitigated. This work has identified three important design principles that should be considered in the design and management of civil engineering infrastructure systems:

1. To minimize the impacts of disruptions from spatial hazards, networks should minimize the number of hubs and have a constant number of network connections. This increases the *redundancy* of the network, enabling nodes to be reached from multiple alternative supply routes, sustaining network operations in the face of failures;
2. The number of connections should be more evenly spread across the network to limit the diffusion of failures, by virtue of having less nodes with a single connection to hubs. This entails that less 2nd order failures;
3. Infrastructure networks should avoid spatial clusters of hubs, as increased spacing between them was found to reduce the vulnerability to spatially contiguous hazards.

Analyzing the robustness of an existing electrical infrastructure to a real natural hazard revealed the importance of the hierarchical model regulating the interaction between infrastructure assets. This work has highlighted the importance of the following aspects:

1. In an existing infrastructure with different assets interacting with each other, a system-of-systems perspective is needed to identify partitions (or subsystems) and their boundaries. This can lead to a better understanding of the overall behavior of the network, as ignoring the presence of partitions may lead to misrepresentation of individual behaviors;
2. Partitioning the infrastructure into a set of meaningful subsystems and capturing their interactions is a crucial step in defining the number of customers potentially affected, which may be harder to define otherwise;
3. Impact studies can leverage on an accurate representation of subsystems as this may highlight which ones would benefit from increased robustness, and which ones would benefit from increased redundancy. This level of detail is very informative for asset managers, as it adds value and effectiveness to prioritized investment plans addressing the most crucial assets.

In conclusion, it is recommended that the design principles derived from Case Study 1 be integrated in the design process of civil engineering infrastructures, together with aspects such as demand, efficiency, and costs. It is also recommended that the partitioning methodology presented in Case Study 2 be adopted by studies assessing the impacts of natural hazards, so that more realistic and representative outcomes are produced. If adopted, these

recommendations may potentially result in important monetary savings, including a reduction of fines imposed by regulators, improved levels of service, and improved customer satisfaction.

8.3 Future work

8.3.1 Improvements to the case studies implementation

The systems framework coupled a number of different components. Opportunities for future research and development are now considered, with a view to provide researchers with a list of possible next steps to develop the content of this thesis further.

The analysis presented in Case Study 1 could benefit from a set of possible improvements that are summarized as follows in a step-by-step fashion:

1. The investigation regarding different network behaviors should be extended to larger networks, in which there are more than 10x10 nodes. This would also enable to gauge the effect of larger fractal spatial hazards, which may result in a wider difference in terms of network response. This poses significant requirements in terms of computational resources, but technological solutions such as parallel computing and multi-threading may reduce the burden;
2. The range of networks adopted in this thesis is limited. It is recommended that the investigation be extended to models such as exponential networks, complete graphs, or even scale-free networks mirroring existing infrastructures. This would result in a stretched array of topologies which would contribute to a deeper understanding of the robustness to realistic spatial hazards;
3. The adoption of different failure models may help reproduce a more realistic behavior, especially if the relationships between nodes are modelled after an existing infrastructure;
4. Finally, an improved representation of the capacity of a network to process flows (eg, goods, passengers, or services) may be achieved adopting flow algorithms that resemble those of existing infrastructures.

The analysis performed in Case Study 2 would also benefit from steps that could increase the value of this research. These steps include, but are not only limited to:

1. This Case Study focuses on a distribution electricity network, and as such, an obvious extension of this work is to transfer it to electricity networks at lower voltages, as well as to other infrastructure sectors;
2. Wind fields are shown to exhibit fractal structure. Future research could explore how different hazards natural hazards such as rain fields, wildfires etc. correspond to different fractal structures. The use of process models to simulate hazards allows for aspects such as timing to be considered (for example, how floodwaters rise and fall with river flow). A further extension of the fractal model would therefore be to include a temporal component;
3. Future work could provide improved functional description of power flows in the electricity networks (or equivalent processes in other networks) to allow for feedbacks and responses to be considered;
4. Additional improvements could result from the use of network models that capture aspects such as accurate asset location, absence of connectivity gaps, material, age, and capacity of components, and so forth. This would make the results of impact studies produced in both Academia and Industry more grounded in reality;
5. Ongoing research at the UK Met Office and elsewhere is improving the resolution and availability of hazard modelling projections which will improve infrastructure risk analysis in the future by resolving convective phenomena.

8.3.2 Vision for the future

Case Study 2 of this thesis implemented a digital representation of an electricity infrastructure to evaluate its response to high winds. In the process, this thesis also proposed the idea of a digital twin to determine the level of resilience of an infrastructure exposed to a spatial natural hazard. The underlining idea behind this is the vision for a digital twin for resilience. The latter can be thought of as a digital object that includes the infrastructure assets, as well as appropriate modelling attributes that include the following elements (Figure 8.1):

- A topological model, where the infrastructure components are modelled as nodes, their connections are modelled as edges, and all node-node relationships are identifiable;

- A hierarchical model, where the infrastructure components are clearly identifiable, and their relationships are explicit;
- A real-time functional model, where relevant mathematical models are implemented to reproduce the processes that occur across the infrastructure;
- A real-time failure model, which specifies how the infrastructure responds to natural spatial hazards or events currently impacting on the network;
- A real-time supply and demand model that allows to determine how the flow of goods or services takes place across the infrastructure.

As with any model, the utility of a digital twin is modulated by how processes are modelled, as well as on the availability of the relevant datasets, which should feed back into the model. Given the extensive limitations involved in developing a self-contained digital twin, this thesis went as far as illustrating the steps needed to implement only the topological, hierarchical, and failure models. The implementation of the additional components would be a major research endeavor.

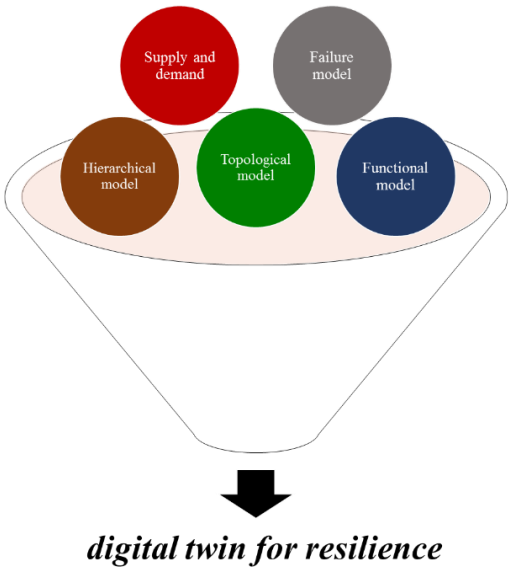

Figure 8.1. Vision for a *digital twin for resilience*. This thesis implemented a topological model, a hierarchical model, and a failure model only.

The idea of a digital twin for resilience may leverage on the increased availability of datasets. In fact, recent technological advancements in project design, sensing, and measurements, have paved the way for a widespread use of models of digital representation.

These models couple the three-dimensional representation of objects, such as bridges or other structural elements, with layers of information regarding materials, dimensions, physical properties, functionality, and data regarding other aspects. These elements can be grouped together to characterize what is known in Civil Engineering as Building Information Modelling (BIM), that is, a strategy to blend Information Technology into Civil Engineering practices.

More specifically, a BIM object operates on digitally-stored databases as opposed to paper-based sources, it allows to share design solutions and real-time changes, and it collects data that can be used multiple times and at any stage of the lifecycle of the designed physical element. Although the use of BIM in civil engineering is becoming more and more widespread, its applications are predominantly limited to the design phase, with recent developments addressing aspects such as energy consumption and safety performance. However, other authors have shown that BIM can be used to detect the occurrence of faults of energy systems serving buildings, suggesting that, among all performance indicators, *resilience* can also be investigated. In light of this, additional directions for future research should include the investigation of how to integrate digital twins for resilience into design best practices.

Appendix

Python scripts used in this thesis

Case Study 1

This thesis used a number of bespoke scripts written in Python to carry out the research tasks. The scripts used in Case Study 1 are allowed to be released in their entirety. The following paragraphs contain the scripts used to generate:

1. The function generating the fractal surfaces (see paragraphs 4.2.4, 4.2.5);
2. The Critical Footprints given the fractal surfaces (see paragraph 4.2.5);
3. The circles representing the localized attacks (see paragraph 4.2.8);
4. The geometrical comparison between the fractal surfaces and the circles (see paragraph 4.2.8);
5. The four synthetic models of infrastructure networks (see paragraph 4.4.1);
6. The superimposition of the Hazard Loading on the synthetic infrastructure network models (see paragraph 4.5.1).

1 Fractal Surfaces

Reference: paragraphs 4.2.4 and 4.2.5

```
"""
Title: fractional Brownian motion (fBm) with Spectral Synthesis on a 2D, square lattice
OPEN SOURCE CODE
Source
Ref: Peitgen, O.H., Saupe, D. 1988. The Science of Fractal Images, Springer-
Vorlag. Chapter 2, Page 108.
"""

from __future__ import division
import numpy
import random
import math
import pylab

def SpectralSynthesisFM2D(max_level, sigma, H, seed=100, normalise=True, bounds=[0,1]):
  """
  ____________________________________________________________________________
  Args:
      max_level : Maximum number of recursions (N = 2^max_level)
      sigma     : Initial standard deviation
      H         : Roughness constant (Hurst exponent), varies form 0.0 to 1.0
      H=0.8 is a good representation of many natural phenomena (Voss, 1985)
      seed      : seed value for random number generator
      normalise : normalizes the data using bound
      bounds    : used for normalization of the grid data
  Result:
      Output is given in the form of an array (grid) which holds surface
      values for a square region.
```

```
    _____________________________________________________________________
    """

    N = int(2**max_level)
    A = numpy.zeros((N,N), dtype = complex)
    random.seed() #Seeds the random number generator
    PI = 3.141592
    for i in range(0,int((N-1)/2)):
      for j in range(0,int((N-1)/2)):
        phase = 2*PI*random.random() #/random.randrange(1,Arand)
        if i != 0 or j != 0:
          rad = pow((i*i + j*j),(-(H+1)/2) )*random.gauss(0.0, sigma)
        else:
          rad = 0.0

        A[i][j] = rad*math.cos(phase) + rad*math.sin(phase)*j

        if i ==0:
          i0 = 0
        else:
          i0 = N - i

        if j==0:
          j0 = 0
        else:
          j0 = N - j

        A[i0][j0] = rad * math.cos(phase) - rad*math.sin(phase)*j

    for i in range(1,int((N-1)/2)):
      for j in range(1,int((N-1)/2)):
        phase = 2*PI*random.random() #/random.randrange(1,Arand)
        rad = pow((i*i + j*j),(-(H+1)/2) )*random.gauss(0.0, sigma)
        A[i][N-j] = rad * math.cos(phase) + rad* math.sin(phase)*j
        A[N-i][j] = rad * math.cos(phase) - rad* math.sin(phase)*j

    Grid = numpy.real(pylab.ifft2(( A ))) #Implements the Discrete Inverse FFT on a 2D lattice
    if(normalise):
          Grid += numpy.amin(Grid)*-1 + bounds[0]
          Grid = (Grid/numpy.amax(Grid)) * bounds[1]
    return Grid
```

2 Critical Footprints

Reference: paragraph 4.2.5

```
"""
GENERATING FRACTAL FOOTPRINTS

Created on Thu Apr 06 16:06:29 2017

Author: Francesco Castellani, Newcastle University - f.castellani2@ncl.ac.uk
"""

from __future__ import division
import numpy as np
import matplotlib.pyplot as plt
import matplotlib.colors as mc
import SSFM2D
import random
import os

num_events=[10]
Hurst_values=[0.6,0.7,0.8,0.9] #Hurst exponent (0.8 is a recommended value for natural phenomena, but it can be brought to the limits [-1,1])
#1) Defining the number of events & the thresholds
ft=[0.1,0.3,0.5,0.7,0.9] #The threshold past which a given node fails. Ranges 0.0 to 1.0.
#All cell values >fail_thre contribute to determining the critical footprint. Ranges 0.0 to 1.0.
for H in Hurst_values:
    for fail_thre in ft:
        for v in num_events:
            directoryPath=r'C:\Users\mydir' #Creates a new folder
            os.chdir(directoryPath)

            #3) Parameter assignments
            max_level=8               #This is the exponent controlling the grid size. In this case N=2^8=256. Use only integers.
            N=2**max_level            #The size of the matrix. N as size is not used in this script. It is used by SSFM2D.
            sigma=1                   #Variation for random Gauss generation (standardised normal distribution)
            seed = random.random()    #Setting the seed for random Gauss generation

            #4) Defining dicts for statistics & initializing the for loop. Change as needed.
            event=0 #Initializing the event counter to 0
            from collections import OrderedDict
            event_max=OrderedDict() #An empty dict to store the max value for each fBm image produced. It is calculated after the zeroset has been raised to the failure threshold value.
            event_avg=OrderedDict() #An empty dict to store the avg value for each fBm image produced. It is calculated after the zeroset has been raised to the failure threshold value.
            event_sampdev=OrderedDict() #An empty dict to store the sample variation value for each fBm image produced. It is calculated after the zeroset has been raised to the failure threshold value.
            event_min=OrderedDict() #An empty dict to store the min value for each fBm image produced. It is calculated after the zeroset has been raised to the failure threshold value.
            critical_cells=OrderedDict() #An empty dict to store the fraction of cells exceeding the node failure threshold
            event_index=[''] #Empty list for indexing events to be associated with footprint values
            for event in range(0,v):

                #5) Lattice initialization
                Lattice=np.zeros((256,256))

                #6) Calling Spectral fBm function
                Lattice=SSFM2D.SpectralSynthesisFM2D(max_level, sigma, H, seed, normalise=True, bounds=[0,1])
```

```
50.
51.                 #7) Creating the original 256x256 lattice
52.                 M=np.zeros((257,257))
53.                 for i in range(0,256):
54.                     for j in range(0,256):
55.                         M[i][j]=Lattice[i][j]
56.
57.                 #8) Normalizing the output matrix
58.                 M = M/M[-257:, -257:].max() #Matrix normalization with respect to max
59.
60.                 #9) Producing the images
61.                 N=np.zeros((257,257))
62.                 plt.figure()
63.                 north=int(0) #Allows to slice the main image
64.                 east=int(0)  #Allows to slice the main image
65.                 for i in range(257):
66.                     for j in range(257):
67.                         if M[east+i][north+j]<fail_thre:
68.                             N[i][j]=0
69.                         else:
70.                             N[i][j]=M[east+i][north+j] #The sliced image. Periodicity is avoid
    ed.
71.
72.                 #Plotting the images
73.                 plt.imshow(N[-257:,-
    257:].T, origin='lower',interpolation='nearest',cmap='Reds', norm=mc.Normalize(vmin=0,vmax=M.m
    ax()))
74.                 title_string=('Fractal footprint')
75.                 subtitle_string=('fBm-SSm | Array size: 256x256')
76.                 plt.suptitle(title_string, y=0.99, fontsize=17)
77.                 plt.title(subtitle_string, fontsize=8)
78.                 #Making a custom list of tick mark intervals for color bar (assumes minimum is
     always zero)
79.                 numberOfTicks = 5
80.                 ticksListIncrement = M.max()/(numberOfTicks)
81.                 ticksList = []
82.                 for i in range((numberOfTicks+1)):
83.                     ticksList.append(ticksListIncrement * i)
84.                 plt.tick_params(axis='x', labelsize=8)
85.                 plt.tick_params(axis='y', labelsize=8)
86.                 plt.show()
87.                 plt.xlim(0, 256)
88.                 plt.xlabel('X',fontsize=12)
89.                 plt.ylim(256, 0)
90.                 plt.ylabel('Y',fontsize=12)
91.
92.                 plt.savefig(directoryPath+'\\H_'+str(H)+'_ft_'+str(fail_thre)+'_'+str(event)+'
    .jpg', bbox_inches='tight',dpi=300)
93.                 plt.close()
```

3 Circles representing Localized Attacks

Reference: paragraph 4.2.8

```
"""
GENERATING LOCALIZED ATTACKS
Modified Bresenham's circle algorithm.
Variation of the Midpoint Circle Algorithm.
Plots the circular load of a generic hazard on a 2D map.
Output values are either 0.0 or 1.0.

Created on Tue Apr 11 10:51:28 2017

@author: Francesco Castellani, Newcastle University - f.castellani2@ncl.ac.uk
"""

from __future__ import division
import numpy
import random
import os
from collections import *
import glob
import math
import pickle

#1) Directory where to dump the pickle
directoryPath=r'C:\Users\mydir'
os.chdir(directoryPath)

#2) Set number of events
num_slots=25
events_per_slots=2000
events={}

for e in range(1,num_slots+1): #Index for each 2000-event slot. Ranges 1 to 25.

    index=str(e)
    if len(index)==1:
        front='000'+str(index)
    if len(index)==2:
        front='00'+str(index)

    for k in range(1,events_per_slots+1):

        if len(str(k))==1: #Events 1-9
            back='000'+str(k)
        if len(str(k))==2: #Events 10-99
            back='00'+str(k)
        if len(str(k))==3: #Events 100-999
            back='0'+str(k)
        if len(str(k))==4: #Events 1000-2000
            back=str(k)

        event_name=str(front)+str(back) #Dictiona key
'00010001' to '00252000' (50000 events)

        n=21 #Grid size, 4 times my visualized output in order to be able to truncate circles
        empty_lattice=numpy.zeros((n,n)) #The empty 2D grid
        radius=int(numpy.random.uniform(1,10)) #Radius | Sampling from uniform distribution [1
, 10]
        xc=int(numpy.random.uniform(0,n-radius)) #X center
        yc=int(numpy.random.uniform(0,n-radius)) #Y center
        r2 = radius ** 2

        #Bresenham's Algorithm
        for dx in range(0, radius):
```

```
            x = xc + dx
            dx2 = dx ** 2
            for dy in range(0, dx + 1):
                y = yc + dy
                dy2 = dy ** 2
                if (dx2 + dy2 <= r2):
                    if (xc + dx <= n and yc + dy <= n):
                        empty_lattice[xc+dx][yc+dy]=1 #1st octant
                    if (xc - dx >= 0 and yc + dy <= n):
                        empty_lattice[xc-dx][yc+dy]=1 #2nd octant
                    if (xc + dx <= n and yc - dy >= 0):
                        empty_lattice[xc+dx][yc-dy]=1 #3rd octant
                    if (xc - dx >= 0 and yc - dy >= 0):
                        empty_lattice[xc-dx][yc-dy]=1 #4th octant
                    if (xc + dy <= n and yc + dx <= n):
                        empty_lattice[xc+dy][yc+dx]=1 #5th octant
                    if (xc - dy >= 0 and yc + dx <= n):
                        empty_lattice[xc-dy][yc+dx]=1 #6th octant
                    if (xc + dy <= n and yc - dx >= 0):
                        empty_lattice[xc+dy][yc-dx]=1 #7th octant
                    if (xc - dy >= 0 and yc - dx >= 0):
                        empty_lattice[xc-dy][yc-dx]=1 #8th octant

        loaded_cells=0
        visualized=numpy.zeros(shape=(int(n/2)+1,int(n/2)+1))

        #Flood-fill Algorithm
        for i in range(0,int(n/2)+1):
            for j in range(0,int(n/2)+1):
                visualized[i][j]=empty_lattice[int(n/4)+i][int(n/4)+j]
                if empty_lattice[int(n/4)+i][int(n/4)+j]==1:
                    loaded_cells+=1
        CF=round(100*loaded_cells/(((n/2)+1)*((n/2)+1)),2) #Critical Footprint of the disks

        events[event_name]=visualized,CF #"visualized" is an auxiliary 2D array that allows di
    sk centers to occur outside the fixed study area

        print ('event: '+str(event_name))

#3) Dumping everything to a pickle dictionary
pickle.dump(events,open('local_events_50k.p','w'))
```

4 Geometrical comparison between fractal surfaces and circles

Reference: paragraph 4.2.8

```
'''''
Geometrical comparison between fractals and circles:
Maximum separation of fractal surfaces
vs
Maximum separation of circles (Localized Attacks)
'''
from __future__ import division
import numpy as np
from scipy import ndimage
import os
import glob
import csv
from matplotlib import pyplot as plt
from collections import OrderedDict
from numpy import genfromtxt
import pickle
import skimage as sk
from skimage import measure
from skimage.measure import label
import pandas as pd

#Load fractals first
dirfr=r'C:\Users\mydir\fractals'

subdir=[x[0] for x in os.walk(dirfr)]
subdir.pop(0)

N=121 #Number of cells in each image
fractals=OrderedDict() #Key: event; Value: (major axis, CF)

for i in subdir:
    temp_dir=r''+i
    os.chdir(temp_dir)
    for file in glob.glob("*.csv"):
        event=file[0:8]
        path = os.path.join(i, file)
        raw_data=np.genfromtxt(path,delimiter=',')[:,2]
        image=np.delete(raw_data, 0, 0)
        Ft=float(file[2]+'.'+file[3])
        blobs=image>Ft
        temp=0
        for j in range(blobs.shape[0]):
            if blobs[j]==True:
                temp=temp+1
        CF=round(temp/N,2)
        labels,nlabels = ndimage.label(blobs)
        labelled=label(blobs)
        resh_labelled=labelled.reshape((11,11))
        props=sk.measure.regionprops(resh_labelled)
        if CF==0:
            max_sep=0.0
        else:
            diams=[]
            for p in props:
                diams.append(p.major_axis_length)
            max_sep=round(max(diams),3)
            #max_sep=round(sum(diams)/len(diams),3)
        fractals[event]=(CF,max_sep,nlabels)
    break
cf_maj_ax_fra=[]
for key, value in fractals.items():
    cf_maj_ax_fra.append(value[0:2])
```

```
fra=zip(*cf_maj_ax_fra)


#Load circles (Localized Attacks)
dirloc=r'C:\Users\mydir\circles'

subdir=[x[0] for x in os.walk(dirloc)]
subdir.pop(0)

N=100 #Number of cells in each image
localized=OrderedDict() #Key: event; Value: (major axis, CF)

for i in subdir:
    temp_dir=r''+i
    os.chdir(temp_dir)
    for file in glob.glob("*.csv"):
        event=file[0:8]
        path = os.path.join(i, file)
        raw_data=np.genfromtxt(path,delimiter=',')[:,2]
        image=np.delete(raw_data, 0, 0)
        Ft=0.99
        blobs=image>Ft
        temp=0
        for j in range(blobs.shape[0]):
            if blobs[j]==True:
                temp=temp+1
        CF=round(temp/N,2)
        labels,nlabels = ndimage.label(blobs)
        labelled=label(blobs)
        resh_labelled=labelled.reshape((10,10))
        props=sk.measure.regionprops(resh_labelled)
        if CF==0:
            eq_diam=0.0
        else:
            diams=[]
            for p in props:
                diams.append(p.major_axis_length)
            max_sep=round(sum(diams)/len(diams),3)
        localized[event]=(CF,max_sep,nlabels)
    break
cf_maj_ax_loc=[]
for key, value in localized.items():
    cf_maj_ax_loc.append(value[0:2])
loc=zip(*cf_maj_ax_loc)

#Binning
cf_maj_ax_fra.sort(key = lambda x: x[0])
cf_maj_ax_loc.sort(key = lambda x: x[0])
bins = [0.1, 0.2, 0.3, 0.4, 0.5, 0.6, 0.7, 0.8, 0.9, 1.0]
binned_fra = {key: [] for key in bins}
binned_loc = {key: [] for key in bins}
for item in cf_maj_ax_fra: #Islands
    for bin in bins:
        if item[0] <= bin:
            binned_fra[bin].append(item[1])
            break
for item in cf_maj_ax_loc: #Islands
    for bin in bins:
        if item[0] <= bin:
            binned_loc[bin].append(item[1])
            break

average_fra={}
for key, value in binned_fra.iteritems():
    numerator={k:sum(v) for k,v in binned_fra.items()}
    denominator={k:len(v) for k,v in binned_fra.items()}
for key, value in denominator.iteritems():
```

```
    if denominator[key]==0:
        average_fra[key]=0
    else:
        average_fra[key]=round((numerator[key]/denominator[key]),3)

average_loc={}
for key, value in binned_loc.iteritems():
    numerator={k:sum(v) for k,v in binned_loc.items()}
    denominator={k:len(v) for k,v in binned_loc.items()}
for key, value in denominator.iteritems():
    if denominator[key]==0:
        average_loc[key]=0
    else:
        average_loc[key]=round((numerator[key]/denominator[key]),3)

fig1 = plt.figure()
ax1 = fig1.add_subplot(111)
ax1.scatter(*fra, s=20, c='r', marker="o", label='fractals (H=0.8, Ft=0.5)',edgecolors=None)
ax1.scatter(*loc, s=20, c='k', marker="o", label='circles',edgecolors=None)
plt.legend(loc='upper left')
plt.xlim(-0.001,1)
plt.ylim(-0.1,50)
plt.xlabel("Critical Footprint (*100)") #Measured in % cells
plt.ylabel("Perimeter") #Measured in pixels
plt.title('Perimeter Comparison')
plt.grid('on')
plt.show()

#Bar chart with bins
labels = ['0-10%','11-20%','21-30%','31-40%','41-50%','51-60%','61-70%','71-80%','81-90%','91-100%']
x = [0, 1, 2, 3, 4, 5, 6, 7, 8, 9]
df=pd.DataFrame([average_fra,average_loc])
df.columns=['0-10%','11-20%','21-30%','31-40%','41-50%','51-60%','61-70%','71-80%','81-90%','91-100%']
df.index=['Fractal','Localized']
df.T.plot(kind='bar', title='Binned comparison (perimeter vs perimeter)',grid=True, color=['red','black'])
plt.xlabel("Critical Footprint")
plt.ylabel("Average Perimeter")
plt.xticks(rotation=45)
plt.ylim(0, 50)
plt.tight_layout()
plt.legend(["Fractals (H=0.8, Ft=0.5)", "Circles"],fontsize=9);
plt.show()
```

5 Synthetic models of infrastructure networks

Reference: paragraph 4.4.1

```
"""
GENERATING INFRASTRUCTURE NETWORK MODELS

Created on Tue Apr 11 10:27:16 2017

@author: Francesco Castellani, Newcastle University - f.castellani2@ncl.ac.uk
"""

import pickle
import os
import networkx as nx
from pylab import *
import matplotlib.pyplot as plt


#Lattice Network (LN) | No seeds are required
N=10 #Nodes per side
G=nx.grid_2d_graph(N,N)
labels = dict( ((i,j), i + (N-1-j) * N ) for i, j in G.nodes() )
nx.relabel_nodes(G,labels,False)
inds=labels.keys()
vals=labels.values()
inds=[(N-j-1,N-i-1) for i,j in inds]
pos2=dict(zip(vals,inds))
#Saving object as pickle
pickle_dir=r'C:\Users\mydir'
with open(pickle_dir+'\\LN.pickle', 'wb') as handle:
  pickle.dump(G, handle)


#Seeding for BA, WS, and ER
from __future__ import division
from collections import Counter
seeds=range(300) #Same seeds for all networks


#Barabasi-Albert Scale-Free Network (BA) | Seeds: 1 through 300
BA={}
for j in seeds:
    m=2  #Number of initial links
    n=100 #Number of nodes
    ncols=10 #Number of columns in a 10x10 grid of positions
    G=nx.barabasi_albert_graph(n, m, seed=j)
    pos = {i : (i // ncols, (n-i-1) % ncols) for i in G.nodes()}
    BA[j]=G
with open(pickle_dir+'\\BA.pickle', 'wb') as handle:
  pickle.dump(BA, handle)


#Watts-Strogatz Small-World Network (WS) | Seeds: 1 through 300
WS={}
for j in seeds:
    n=100 #Number of nodes
    ncols=10 #Number of columns in a 10x10 grid of positions
    p=0.3 #Probability of rewiring
    G=nx.watts_strogatz_graph(n,4,p, seed=j) #4=number of nearest neighbours
    pos = {i : (i // ncols, (n-i-1) % ncols) for i in G.nodes()}
    WS[j]=G
with open(pickle_dir+'\\WS.pickle', 'wb') as handle:
  pickle.dump(WS, handle)


```

```
#Erdos-Renyi Random Network (ER) | Seeds: 1 through 300
ER={}
for j in seeds:
    n=100 #Number of nodes
    ncols=10 #Number of columns in a 10x10 grid of positions
    p=0.0385 #Probability of connecting to an existing node
    G=nx.erdos_renyi_graph(n,p,seed=j)
    pos = {i : (i // ncols, (n-i-1) % ncols) for i in G.nodes()}
    ER[j]=G
with open(pickle_dir+'\\ER.pickle', 'wb') as handle:
  pickle.dump(ER, handle)
```

6 Superimposition of the Hazard Loading on the synthetic infrastructure network models

Reference: paragraph 4.5.1

```
"""
APPLYING THE FRACTAL HAZARD LOADING TO A BARABASI-ALBERT SCALE-FREE NETWORK (BA)
The BA model is used as an example. To simulate the loading of other models,
just change the network object according to the script at point 5.

Created on Tue Apr 11 11:00:01 2017

@author: Francesco Castellani, Newcastle University - f.castellani2@ncl.ac.uk
NB: Low Ft = Scenario S1, High Ft = Scenario S2

"""

from __future__ import division
import networkx as nx
import math
from pylab import *
import matplotlib.pyplot as plt
import pandas as pd
import random
import pickle
import numpy
from collections import OrderedDict
import itertools
import os

#Final container (dict of pandas DataFrames)
BA_ensemble={}
BA_ens_gra_post_attack={} #Dict with all post-attack graphs later dumped to a pickle

#Seeds
seeds=sorted(random.sample(range(300), 300)) #300 seeds=300 networks (0-299)

#Load dict of events & select relevant events
pickle_dir_1=r'C:\Users\mydir'
events=pickle.load(open(pickle_dir_1+'\\fractal_events_50k.p',"r"))
#There needs to be a pickle containing all the fractal footprints generated with the script at point 2. This pickle is a dictionary containing numpy 2D arrays of the fractal objects.
sel_events={}
for i,event in enumerate(sorted(events.keys())):
    if i>=2000 and i<4000: #Low Ft | Scenario S1
        sel_events[event]=events[event]
    if i>=46000 and i<48000: #High Ft | Scenario S2
        sel_events[event]=events[event]

#Load excel file with hotspot locations
xls = pd.ExcelFile('C:\Users\Hotspots_Coordinates.xlsx') #There needs to be a file containing the hotspot coordinates for each fractal footprint
lowft=xls.parse(sheetname='Low_Ft',converters={'event':str,'x (column)':int,'y (row)':int}) #(x,y) Low Ft
highft=xls.parse(sheetname='High_Ft',converters={'event':str,'x (column)':int,'y (row)':int}) #(x,y) High Ft

#Ensemble of networks and spatial hazard loading
#The network classes are generated in this code right away, but could be loaded from a pickle

for s in seeds:

    m=2  #Number of initial links
    n=100 #number of nodes
    N=ncols=10 #Number of columns in a 10x10 grid of positions
    G=nx.barabasi_albert_graph(100, m, seed=s)
    pos = {i : (i // ncols, (n-i-1) % ncols) for i in G.nodes()}
```

```
58.
59.     #Connected neighbors
60.     connected_neigh={}
61.     all_nodes=G.nodes()
62.     for j, e in enumerate(all_nodes):
63.     connected_neigh[e]=G.neighbors(e)
64.
65.     #The 4 main hubs and their cumulative degree (pre-attack)
66.     main_hubs=[]
67.     sort_deg = sorted(G.degree().items(), key=lambda value: value[1]) #Sorting nodes by their
    egree (highest to lowest)
68.     main_hubs.append(sort_deg[-1])
69.     main_hubs.append(sort_deg[-2])
70.     main_hubs.append(sort_deg[-3])
71.     main_hubs.append(sort_deg[-4])
72.     cum_pre=0
73.     hubs_ID=[]
74.     for i,j in enumerate(main_hubs):
75.         cum_pre=cum_pre+main_hubs[i][1]
76.         hubs_ID.append(main_hubs[i][0])
77.
78.     #Stress Centrality for each node (pre-attack)
79.     max_stress_centrality=OrderedDict()
80.     for n in G.nodes(): max_stress_centrality[n]=0
81.     for n in G.nodes():
82.         for j in G.nodes():
83.             if (n!=j):
84.                 try:
85.                     gener=nx.all_shortest_paths(G,source=n,target=j)
86.                     for p in gener:
87.                         for v in p: max_stress_centrality[v]+=1
88.                 except nx.NetworkXNoPath: #If nodes n and j are not connected
89.                     continue
90.
91.     #The empty dicts for storing the four metrics
92.     size_n=OrderedDict()           #Size(N) (active nodes after 2nd order failures)
93.     rhc=OrderedDict()              #RHC=Retained Hub Connectivity
94.     fragmentation=OrderedDict()    #Fragmentation
95.     cfi=OrderedDict()              #Cross-Flow Index
96.
97.     #The rest
98.     fail_1=OrderedDict() #Failed 1st Phase (1st order)
99.     act_1=OrderedDict() #Active 1st Phase (1st order)
100.    fail_2=OrderedDict() #Failed 2nd Phase (2nd order)
101.    fail_tot=OrderedDict() #Tot failed nodes (1+2)
102.    act_tot=OrderedDict() #Final active nodes (after 2nd order failures)
103.    event_order=[]
104.    crit_foot=[]
105.    iterator=[]
106.    filename=[]
107.
108.    #Read in the fBm events from the dict of events
109.    order=sorted(sel_events.keys())
110.    for i, event in enumerate(order):
111.
112.        print ('BA'),
113.        print ('| seed: '+str(s+1)+' of 300'),
114.        print ('| event: '+str(event))
115.
116.        post_attack_graphs={} #Stores the post-attack graphs
117.
118.        iterator.append(i)
119.        Hurst=float(order[i][0:2])/10
120.        fail_thre=float(order[i][2:4])/10
121.        event_no=int(order[i][4:8])
122.        event_order.append(event_no)
123.        filename.append(event)
```

```
124.        crit_foot.append(round(sel_events[event][1],2)) #Critical Footprint (spatial extent of
     events)
125.        fractal=sel_events[event][0] #ndarray
126.        fractal_to_list=fractal.tolist() #to list of lists
127.        merged_fra=list(itertools.chain(*fractal_to_list)) #to flat list
128.        loading=[merged_fra[i:i+(N+1)] for i in range(0, len(merged_fra), (N+1))] #row-
    wise ordered list of loading values
129.        H=G.copy() #Copy of the graph
130.
131.        #Create a dictionary which has the cell ID as key and the fBm value as value (Indexing
     the 2D mesh grid)
132.        cellid=numpy.arange(0,((N+1)*(N+1)),1) #When populating the dictionary, read the celli
    d from this array
133.        cellid_list=cellid.tolist() #Convert the numpy array into a list to allow dictionary o
    perations later on
134.        proper_cellid_list = [cellid_list[i:i+(N+1)] for i in range(0, len(cellid_list), (N+1)
    )] #This is the list later used in dictionarize1
135.        fra_dict={} #The dictionary containing the cell ID and the fBm value
136.        for index, n in enumerate(cellid_list): #For loop to populate the dictionary
137.            fra_dict[n]=merged_fra[index] #Dictionary with the pair: cell ID, loading value
138.        nodeid=numpy.arange(0,(N*N),1) #Do not delete. It is used later
139.
140.        #Create a dictionary in which each key is a node ID, and which value is a tuple (x1,x2
    ,x3,etc.) containing the neighboring cells
141.        #The Assignation List
142.        def dictionarize1(array):
143.            dict1 = {}
144.            count = 0
145.            for x in range(len(array[0]) - 1):
146.                for y in range(len(array[0]) - 1):
147.                    dict1[count] = [array[x][y], array[x][y+1], array[x+1][y], array[x + 1][y+
    1]]
148.                    count = count + 1
149.            return dict1
150.        neighborhood=dictionarize1(proper_cellid_list) #This dictionary has the node ID as key
     and the cell IDs of the neighboring cells
151.
152.        #Create a dictionary in which each key is a node ID, and its input value is the avg va
    lue of the 4 neighboring cells (defined as per the neighborhood dictionary)
153.        def dictionarize2(array):
154.            dict2 = {}
155.            counter = 0
156.            for a in range(len(array[0]) - 1):
157.                for b in range(len(array[0]) - 1):
158.                    dict2[counter] = (array[a][b] + array[a][b+1] + array[a+1][b] + array[a+1]
    [b+1])/4
159.                    counter = counter + 1
160.            return dict2
161.        neigh_mean=dictionarize2(loading) #This dictionary has the node ID as key and the avg
    neighborhood value from fBm as value
162.
163.        #1st order failures
164.        nodeid_list=nodeid.tolist()
165.        status_haz={} #Store the node ID (labels) and the status after the event (1=active, 0=
    failed).
166.        for index, n in enumerate(nodeid_list): #for loop to populate the dictionary
167.            status_haz[n]=1 #The status_haz dictionary is initiated with all nodes active (sta
    tus=1)
168.        for key in status_haz.keys(): #This will evaluate if the threshold is surpassed or not
     for each node (ID)
169.            if (neigh_mean[key]>fail_thre):
170.                status_haz[key]=0
171.            else:
172.                status_haz[key]=1
173.        node_status=numpy.array(status_haz.items(),dtype=int) #A 2D array to store the pairs (
    Node ID, status) failed at Stage 1
174.        act_nodes_haz=sum(1 for x in status_haz.values() if x==1)
```

```
175.         failed_nodes_haz=(N*N)-act_nodes_haz
176.
177.         #Remove 1st order failed nodes from graph
178.         G1=dict((k, v) for k, v in status_haz.items() if v < 1) #All nodes that have failed du
    ring Phase 1
179.         H.remove_nodes_from(G1)
180.
181.         if len(H)==0 or len(H)==100: #If graph is all failed or 100% active
182.             failed_nodes_model=0 #No 2nd order failures
183.
184.         else:
185.             #2nd order failures
186.             still_active_haz=dict((k, v) for k, v in status_haz.items() if v == 1) #A dictiona
    ry with all nodes that have not failed at Stage 1 (a filtered version of status_haz where all
    nodes have status=1)
187.             nodeids=sorted(still_active_haz.keys()) #The IDs of the nodes that are still activ
    e, sorted smallest to largest
188.             neigh_still_active={} #For each active node, this carries its connections
189.             for k in nodeids:
190.                 neigh_still_active[k]=connected_neigh[k] #This will hold the connected nodes o
    f all nodes that are still active (status=1) - a filtered version of connected_neigh (Node ID,
     [connected IDs])
191.             status_nodes_model={} #The dict containing information of possibly failed nodes (N
    ode ID, status=0 or 1) after modeling
192.             for k in neigh_still_active.keys():
193.                 temporary_neigh=neigh_still_active.get(k) #Picks up the list of connected node
    s associated with each node
194.                 temporary_status=[0 for x in range(len(temporary_neigh))] #This list will stor
    e the status of the connections of node k
195.                 for index, val in enumerate(temporary_neigh):
196.                     if status_haz[val]==0: #If the connection i of node k has failed
197.                         temporary_status[index]=0 #It is assigned 0
198.                     else:
199.                         temporary_status[index]=1 #Else, it is assigned 1
200.                 temp_status=0 #This is a boolean. After the for loop it will give 0 if all con
    nections have failed and 1 if at least 1 connection is active
201.                 for i, val in enumerate(temporary_status):
202.                     if temporary_status[i]==0: #If a connection has failed
203.                         temp_status=0 #Temp_status takes on "0" and the loop goes on to check
    the next connection
204.                     else: #If a connection has not failed
205.                         temp_status=1 #Temp_status takes on "1" and the loop goes on to check
    the next connection
206.                 status_nodes_model[k]=temp_status #To fill this dictionary with the format (No
    de ID, status=0 or 1) to see who has failed due to connections and who has not
207.             act_nodes_model=sum(1 for x in status_nodes_model.values() if x==1)
208.             failed_nodes_model=act_nodes_haz-
    act_nodes_model #Number of failed nodes due to modeled interactions
209.
210.         #Remove 2nd order failed nodes from graph
211.         if len(H)>0 and len(H)<100:
212.             G2=dict((k, v) for k, v in status_nodes_model.items() if v < 1) #All nodes that ha
    ve failed during Phase 2
213.             H.remove_nodes_from(G2)
214.
215.         #Removing isolated nodes
216.         rem = [node for node,degree in H.degree().items() if degree <1] #len(remove) is an add
    itional share of failed nodes
217.         H.remove_nodes_from(rem) #To get rid of nodes with degree=0 that otherwise are plotted
     and counted as active
218.
219.         #Save event statistics
220.         if sel_events[event][1]==100: #Critical Footprint=100%
221.             size_n[event]=0
222.             fail_1[event]=100
223.             fail_2[event]=0
224.             act_tot[event]=0
```

```
            fragmentation[event]=0
        if sel_events[event][1]==0: #Critical Footprint=0%
            size_n[event]=100
            fail_1[event]=0
            fail_2[event]=0
            act_tot[event]=100
            fragmentation[event]=1
        else:
            fail_1[event]=failed_nodes_haz

            act_1[event]=(N*N)-
    fail_1[event]
            fail_2[event]=failed_nodes_model+len(rem)

            fail_tot[event]=fail_1[event]+fail_2[event]
            size_n[event]=len(H)  #Size(N)

            act_tot[event]=(N*N)-fail_tot[event]
            fragmentation[event]=nx.number_connected_components(H) #Islands

        #Stress Centrality for post-attack networks
        if len(H)<=2:
            cfi[event]=0
        if len(H)>=98:
            cfi[event]=1
        else:
            counts=OrderedDict()
            for n in H.nodes(): counts[n]=0
            for n in H.nodes():
                for j in H.nodes():
                    if (n!=j):
                        try:
                            nx.bidirectional_dijkstra(H, n, j)
                            gener=nx.all_shortest_paths(H,source=n,target=j)
                            for p in gener:
                                for v in p: counts[v]+=1
                        except nx.NetworkXNoPath:
                            continue

            altered_shortest_paths = counts.values() #List with values
            post_attack_cfi={k: float(counts[k])/max_stress_centrality[k] for k in counts.view
    keys() & max_stress_centrality.viewkeys()} #Dict with final values
            post_attack_cfi_values=post_attack_cfi.values()
            denom=len(post_attack_cfi_values)
            numer=sum(post_attack_cfi_values)
            cfi[event]=round(numer/denom,2)

        #Post-attack cumulative degree of the main hubs
        #Not used in the paper
        cum_post=0
        for i,j in enumerate(hubs_ID):
            if hubs_ID[i] not in H.nodes():
                continue
            else:
                cum_post=cum_post+H.degree(j)
        rhc[event]=round(cum_post/cum_pre,3)

        #Distance main hub-hotspot (format is column, row)
        hubs_loc=[] #List with all (x,y) coordinates of the main hub
        mainhub=str(main_hubs[0][0]) #Select the most highly connected hub
        column=int(mainhub[0]) #Column is always first digit in "mainhub"
        if len(mainhub)==1: #If node is 0-9, row is 0
            row=0
        else:
            row=int(mainhub[1]) #Else, row is second digit in "mainhub"
        coord=(column,row)
        hubs_loc.append(coord)
```

```
287.
288.         post_attack_graphs[event]=H #Dumps the graph into a dictionary
289.
290.     BA_ens_gra_post_attack[s]=post_attack_graphs #Dict of dicts; 1 seed=4000 graphs
291.
292.     #Building the lists composing each pandas DataFrame
293.     #1)
294.     dataframe_events=order #The event name, e.g. '06030001' to '10072000' | First two digits:
    H value; Next two digits: failure threshold value; Last four digits: progressive event number
    1-2000
295.     #2)
296.     spa_ext=crit_foot #The spatial extent of the fractal events
297.     #3)
298.     sizen=size_n.values() #Size (N)
299.     #4)
300.     first_order=fail_1.values() #1st order failures
301.     #5)
302.     second_order=fail_2.values() #The list of 2nd order failures for the 4000 events of the cu
    rrent seed
303.     #6)
304.     ret=rhc.values() #Retained Hub Connectivity
305.     retained=[1 if x>1 else x for x in ret] #Bringing all outliers down to rhc=1
306.     #7)
307.     frag=fragmentation.values() #Number of islands or connected components
308.     #8)
309.     cr=cfi.values() #Cross-Flow Index
310.     cro=[0 if math.isnan(x) else x for x in cr] #To convert all "nan" values to zero
311.     cross=[1 if x>1 else x for x in cro] #Bringing all outliers down to cfi=1
312.     #9)
313.     distances=[] #List with distances hotspot-main hub
314.     dist_df=pd.concat([lowft,highft], axis=0,ignore_index=True) #Putting all hotspot locations
     together
315.     for i in range(0,4000):
316.         if dist_df.ix[i,1]==-9999 or dist_df.ix[i,2]==-9999:
317.             dist=-9999
318.         else:
319.             dist=round(math.sqrt((dist_df.ix[i,1]-hubs_loc[0][0])**2+(dist_df.ix[i,2]-
    hubs_loc[0][1])**2),3) #Euclidean distance
320.         distances.append(dist)
321.     hotsp_dist=[v/10 if v >0 else v for v in distances] #List of normalized distances to be lo
    aded into the DataFrame
322.
323.     #Creating the Dataframe
324.     df=pd.DataFrame({'event':dataframe_events,'Footprint (%)':spa_ext,'Size (N)':sizen,
325.                      '1st order failures':first_order,'2nd order failures':second_order,'RHC':
    retained,
326.                      'Fragm':frag,'CFI':cross,'Distances':hotsp_dist})
327.     #Re-ordering
328.     df=df[['event','Footprint (%)','Size (N)','1st order failures','2nd order failures','RHC',
    'Fragm','CFI','Distances']] #Re-order
329.
330.     #Loading the DataFrame into the final dictionary
331.     BA_ensemble[s]=df
332.
333.#Dumping the dict into the final pickle
334.folder=r'C:\Users\mydir\BA_ensemble'
335.os.chdir(folder)
336.pickle.dump(BA_ensemble,open('BA_ens_300seeds.p','w')) #The final data
337.pickle.dump(BA_ens_gra_post_attack,open('BA_ens_post_attack.p','w'))  #Final networkx objects
```

Case Study 2

Owing to confidentiality agreements signed before Case Study 2 was undertaken, the scripts used in that section of this thesis cannot be released to the general public. Such limitation covers both the asset dataset and the wind gust datasets, which are considered as sources of sensitive information. As a consequence, only very short lists of instructions are allowed to be released. Whilst these scripts do not document the exact steps undertaken to achieve the results, they can be used as a reference to build similar studies regardless of the programming language used. The following pages contain the instructions used to:

1. **Extract grids from the wind gust dataset and convert their coordinates from geographic to projected** (see paragraph 5.2.2);
2. **Pre-process asset dataset** (see paragraph 5.3.1);
3. **Identify network partitions** (see paragraph 5.5.1);
4. **Apply fragility models** (see paragraph 5.6);
5. **Compute systemic indicators** (see paragraph 5.7).

List 1: Extract grids from climate dataset and convert their coordinates from geographic to projected

1.1 Load files from Climate Model, typically NetCDF;
1.2 Identify where the actual grid containing the values is located;
1.3 Extract the grid and determine spatial and temporal resolution;
1.4 Extract information on the original geographic coordinate system, as well as the rotation, encoded in the NetCDF file;
1.5 Convert geographic coordinates to projected systems, such as the British National Grid, and plot;
1.6 Repeat procedure for all files in a loop, if a time series is available.

List 2: Pre-process asset dataset

2.1 Load files with asset dataset, typically a shapefile;
2.2 Ensure the coordinate system is the same as that in List 1, to enable the grids with climate data and the asst dataset to be plotted in the same map;
2.3 Ensure there are no gaps, undershootings, or overshootings in the asset dataset, as these will create an invalid topological object;
2.4 Convert pre-processed shapefile into topological object (e.g., graph) using the available tools (e.g., Python's NetworkX).

List 3: Identify network partitions

3.1 Identify substations of different voltages in the asset dataset;
3.2 Identify substations of voltage v_1 that are directly fed by substations of voltage $v_2 > v_1$;
3.3 One possible partition is composed of the overhead lines connecting substations of voltage v_1 with substations of voltage $v_2 > v_1$;
3.4 If available, incorporate information regarding switches and loops, which are typically visible in the shapefile mentioned in List 2.

List 4: Apply fragility models

4.1 Identify the correct fragility models for the climate loading considered;
4.2 Evaluate length of the partitions, as the models might return the likelihood of failure normalized with respect to a reference length (in Cast Study 2, for instance, this was 1000 km);
4.3 Identify which cell grid is proximal to which node or edge in the network by overlaying them in a plot (use ArcGIS or QGIS);
4.4 Use the climatic loading of that cell as input value for the fragility model in the proximity of that cell, where the closest nodes or edges are;
4.5 Compute the likelihood of failure as a result of points 4.3 and 4.4.

List 5: Compute systemic indicators

5.1 Identify suitable systemic indicators;
5.2 Identify temporal scale for the systemic indicators (e.g., daily, monthly, yearly);
5.3 Identify relationship between systemic indicators and climatic loading (e.g., $failures = f(wind\ speed)$);
5.4 Compute systemic indicators for each partition;
5.5 Consider plotting the values for each partition to identify the most vulnerable ones;
5.6 Consider computing occurrence of cascading failures given the identified partitions and dependencies;
5.7 Consider plotting the risk of cascading failures and the customer base exposed to that.

References

A

Aberson, S. D. (2001) 'The Ensemble of Tropical Cyclone Track Forecasting Models in the North Atlantic Basin (1976–2000)', Bulletin of the American Meteorological Society, 82(9), pp. 1895-1904. Doi: 10.1175/1520-0477(2001)082<0000:TEOTCT>2.3.CO;2.

Abry, P., Gonçalvés, P. and Flandrin, P. (1995) 'Wavelets, spectrum analysis and 1/f processes', in: Antoniadis, A. and Oppenheim, G. (eds.) Wavelets and statistics, vol. 103 of Lecture Notes in Statistics. New York: Springer-Verlag, pp. 15–30. ISBN-13: 978-1-4612-2544-7.

Abundo, C., Monterola, C. and Legara, E. F. (2014) 'Criticality of forcing directions on the fragmentation and resilience of grid networks', Scientific Reports, 4, 6195. Doi: 10.1038/srep06195.

Agarwal, P. K., Efrat, A., Ganjugunte, S. K., Hay, D., Sankararaman, S. and Zussman, G. (2010) 'Network vulnerability to single, multiple, and probabilistic physical attacks', proceedings of the 2010 IEEE Military Communications Conference MILCOM, San Jose, California. Doi: 10.1109/MILCOM.2010.5679556.

Agarwal, P. K., Efrat, A., Ganjugunte, S. K., Hay, D., Sankararaman, S. and Zussman, G. (2013) 'The resilience of WDM networks to probabilistic geographical failures', IEEE/ACM Transactions on Networking, 21(5), pp. 1525-1538. Doi: 10.1109/TNET.2012.2232111.

Albalate, D., Bel, G. and Fageda, X. (2015) 'When supply travels far beyond demand: Causes of oversupply in Spain's transport infrastructure', Transport Policy, 41, pp. 80-89. Doi: 10.1016/j.tranpol.2015.03.004.

Albert, R., Jeong, H. and Barabási, A.-L. (2000) 'Error and attack tolerance of complex networks', Nature, 406(6794): pp. 378-382. Doi: 10.1038/35019019.

Albert, R. and Barabási, A.-L. (2002) 'Statistical mechanics of complex networks', Reviews of Modern Physics, 74(47). Doi: 10.1103/RevModPhys.74.47.

Albert, R., Albert, I. and Nakarado, G. L. (2004) 'Structural vulnerability of the North American power grid', Physical Review E, 69, 025103(R). Doi: 10.1103/PhysRevE.69.025103.

Amin, M. (2000) 'National Infrastructures as Complex Interactive Networks', in: T. Samad and J. Weyrauch (eds.), Automation, Control, and Complexity: An Integrated Approach. Chapter 14, pp. 263-286. ISBN-13: 978-0-471-81654-6.

Angelou, N, Elizondo, A. G., Banerjee, S. G., Bhatia, M., Bushueva, I., Inon, J. G., Jaques Goldenberg, I., Portale, E. and Sarkar, A. (2013) 'Global tracking framework: Executive summary (English). Sustainable energy for all', The World Bank, Washington DC. Available at: http://documents.worldbank.org/curated/en/250491468182351466/Executive-summary (Accessed 23 December 2018).

Apostolakis, G. E. and Lemon, D. M. (2005) 'A Screening Methodology for the Identification and Ranking of Infrastructure Vulnerabilities Due to Terrorism', Risk Analysis, 25(2), pp. 361-376. Doi: 10.1111/j.1539-6924.2005.00595.x.

Arayici, Y., Fernando, T., Munoz, V. and Bassanino, M. (2018) 'Interoperability specification development for integrated BIM use in performance based design', Automation in Construction, 85, pp. 167-181. Doi: 10.1016/j.autcon.2017.10.018.

Asmussen, S. (1999) 'Stochastic simulation with a view towards stochastic processes', notes of a Concentrated Advanced Course at MaPhySto. Aarhus, Denmark, February 1999. Available at: http://www.maphysto.dk/oldpages/events/SAcourse99/ (Accessed 11 February 2016).

Autodesk (2002) 'Building Information Modeling', white paper. Available at: http://www.laiserin.com/features/bim/autodesk_bim.pdf (Accessed 1 December 2017).

B

Baas, A. C. W. (2002) 'Chaos, fractals and self-organization in coastal geomorphology: simulating dune landscapes in vegetated environments', Geomorphology, 48, pp. 309–328. Doi: 10.1016/S0169-555X(02)00187-3.

Baccarini, D. (1996) 'The concept of project complexity – a review', International Journal of Project Management, 14(4), pp. 201-204. Doi: 10.1016/0263-7863(95)00093-3.

Bagler, G. (2009) 'Complex Network view of performance and risks on Airport Networks', in: P.B. Larauge, M.E. Castille (eds.) Airports: Performance, Risks, and Problems. Hauppage, New York: Nova Science. ISBN-13: 978-1-60692-393-1.

Balog, I., Ruti, P. M., Tobin, I., Armenio, V. and Vautard, R. (2016) 'A numerical approach for planning offshore wind farms from regional to local scales over the Mediterranean', Renewable Energy, 85, pp. 395-405. Doi: 10.1016/j.renene.2015.06.038.

Barabási, A.-L. (2016) 'Network Science', 1st edition, Cambridge, UK: Cambridge University Press. ISBN-13: 978-1-1070-7626-6.

Barthélemy, M. (2011) 'Spatial Networks', Physics Reports, 499(1), pp. 1-101. Doi: 10.1016/j.physrep.2010.11.002.

Barton, D. C., Eidson, E. D., Schoenwald, D. A., Stamber, K. L. and Reinert, R. K. (2000) 'Aspen-EE: An Agent-Based Model of Infrastructure Interdependency', Report of the Sandia National Laboratories, SAND2000-2925. Available at: http://prod.sandia.gov/techlib/access-control.cgi/2000/002925.pdf (Accessed 6 November 2017).

Barzel, B. and Barabási, A.-L. (2013) 'Universality in network dynamics', Nature Physics, 9, pp. 673–681. Doi: 10.1038/nphys2741.

Barzel, B., Liu, Y.-Y. and Barabasi, A.-L. (2015) 'Constructing minimal models for complex system dynamics', Nature Communications, 6, 7186. Doi: 10.1038/ncomms8186.

Batista e Silva, F., Forzieri, G., Marin Herrera M. A., Bianchi, A., Lavalle, C. and Feyen, L. (2019) 'HARCI-EU, a harmonized gridded dataset of critical infrastructures in Europe for large-scale risk assessments', Sci Data, 6(1), 126. Doi: 10.1038/s41597-019-0135-1.

Beamond, E. J., Owczarek, A. L. and Cardy, J. (2003) 'Quantum and classical localization and the Manhattan lattice', Journal of Physics A: General Physics, 36(41), pp. 10251-10268. Doi: 10.1088/0305-4470/36/41/001.

Begg, C., Walker, G. and Kuhlicke, C. (2015) 'Localism and flood risk management in England: the creation of new inequalities?', Environment and Planning C: Politics and Space, 33(4), pp. 685-702. Doi: 10.1068/c12216.

Beljaars, A. C. M. (1987) 'The Influence of Sampling and Filtering on Measured Wind Gusts', Journal of Atmospheric and Oceanic Technology, 4, pp. 613-626. Doi: 10.1175/1520-0426(1987)004<0613:TIOSAF>2.0.CO;2.

Berezin, Y., Bashan, A., Danziger, M. M., Li, D. and Havlin, S. (2015) 'Localized attacks on spatially embedded networks with dependencies', Scientific Reports, 5, 8934. Doi: 10.1038/srep08934.

Bhatia, U., Kumar, D., Kodra, E. and Ganguly, A. R. (2015) 'Network Science Based Quantification of Resilience Demonstrated on the Indian Railways Network', PLoS ONE10(11), e0141890. Doi: 10.1371/journal.pone.0141890.

Blockley, D. I. and Godfrey, P. S. (2017) 'Systems for rethinking infrastructure', 2nd edition. London: ICE publishing. ISBN-13: 978-0-7277-6082-1.

Bocchini, P., Frangopol, D. M., Ummenhofer, T. and Zinke, T. (2014) 'Resilience and sustainability of civil infrastructure: toward a unified approach', Journal of Infrastructure Systems, 20(2), 04014004. Doi: 10.1061/(ASCE)IS.1943-555X.0000177.

Boin, A. and McConnell, A. (2007) 'Preparing for Critical Infrastructure Breakdowns: The Limits of Crisis Management and the Need for Resilience', Journal of Contingencies and Crisis Management, 15(1), pp. 50-59. Doi: 10.1111/j.1468-5973.2007.00504.x.

Borgatti, S. P. (2005) 'Centrality and network flow', Social Networks, 27(1), pp. 55-71. Doi: 10.1016/j.socnet.2004.11.008.

Borrough, P. A. (1981) 'Fractal dimensions of landscapes and other environmental data', Nature, 294, pp. 240–242. Doi: 10.1038/294240a0.

Bošković, B. and Bugarinović, M. (2015) 'Why and how to manage the process of liberalization of a regional railway market: South-Eastern European case study', Transport Policy, 41, pp. 50-59. Doi: 10.1016/j.tranpol.2015.03.009.

Brady, T. and Davies, A. (2014) 'Managing Structural and Dynamic Complexity: A Tale of Two Projects', Project Management Journal, 45(4), pp. 21-38. Doi: 10.1002/pmj.21434.

Brandes, U. (2008) 'On variants of shortest-path betweenness centrality and their generic computation', Social Networks, 30(2), pp. 136-145. Doi: 10.1016/j.socnet.2007.11.001.

Bresenham, J. (1977) ‘A Linear Algorithm for Incremental Digital Display of Circular Arcs’, Communications of the Association for Computing Machinery, 20(2), pp. 100-106. Doi: 10.1145/359423.359432.

Brown, R. (1828) ‘A brief account of microscopical observations made in the months of June, July and August 1827, on the particles contained in the pollen of plants; and on the general existence of active molecules in organic and inorganic bodies’, Philosophical Magazine, 4, pp. 161–173.

Browning, K. A. (2004) ‘The sting at the end of the tail: damaging winds associated with extratropical cyclones’, Quarterly Journal of the Royal Meteorological Society, 130(597), pp. 375-399. Doi: 10.1256/qj.02.143.

Bruneau, M., Chang, S. E., Eguchi, R. T., Lee, G. C., O’Rourke, T. D., Reinhorn, A. M., Shinouzuka, M., Tierney, K. and Wallace, W. A. (2003) ‘A framework to quantitatively assess and enhance the seismic resilience of communities’, Earthquake Spectra, 19(4), pp. 733-752. Doi: 10.1193/1.1623497.

Buldyrev, S. V., Parshani, R., Paul, G., Stanley, H. E. and Havlin, S. (2010) ‘Catastrophic cascade of failures in interdependent networks’, Nature, 464(7291), pp. 1025-1028. Doi: 10.1038/nature08932.

Burton, A., Kilsby, C. G., Fowler, H. J., Cowpertwait, P. S. P. and O'Connell, P. E. (2008) ‘RainSim: A spatial-temporal stochastic rainfall modelling system’, Environmental Modelling & Software 23(12), pp. 1356-1369. Doi: 10.1016/j.envsoft.2008.04.003.

Buxton, R. and Pringle, R. J. (2014) ‘The development of a proof-of-concept, agent-based interdependencies model’, GNS Science Report 2013/60. Lower Hutt, New Zealand: GNS Science Report. ISBN-13: 978-1-927278-11-6. Available at: https://www.gns.cri.nz/static/pubs/2013/SR%202013-060.pdf (Accessed 23 October 2017).

C

Cabinet Office of the UK Government (2011) ‘Keeping the Country Running: Natural Hazards & Infrastructure’. Available at: https://assets.publishing.service.gov.uk/government/uploads/system/uploads/attachment_data/file/61342/natural-hazards-infrastructure.pdf (Accessed 11 November 2017).

Callaghan, S. and Vilar, E. (2007) ‘Fractal generation of rain fields: synthetic realization for radio communications systems’, Iet Microwaves Antennas & Propagation 1(6), pp. 1204-1211. Doi: 10.1049/iet-map:20060126.

Callaway, D. S., Newman, M. E. J., Strogatz, S. H. and Watts, D. J. (2000) ‘Network robustness and fragility: percolation on random graphs’, Physical Review Letters, 85, pp. 5468-5471. Doi: 10.1103/PhysRevLett.85.5468.

Carvalho, R., Buzna, L., Bono, F., Gutierrez, E, Just, W. and Arrowsmith, D. (2009) 'Robustness of trans-European gas networks', Physical Review E, 80, 016106. Doi: 10.1103/PhysRevE.80.016106.

Castellani, F., Kirchner-Bossi, N., Ford, A., Kilsby, C., Wilkinson, S., Kendon, E., Fowler, H. and Dawson, R. (2017) 'Analysis of Electricity Network Risks from Daily Maxima Wind Gusts using a high-resolution Climate Model', proceedings of the 2017 International Symposium for Next Generation Infrastructures, pp. 73-79. Institution of Civil Engineers, London. Available at: http://isngi.org/wp-content/uploads/2017/10/ISNGI-Conference-Proceedings-v2.pdf (Accessed 17 November 2017).

Cavalieri, F., Franchin, P., Gehl, P. and D'Ayala, D. (2017) 'Bayesian Networks and Infrastructure Systems: Computational and Methodological Challenges', in P. Gardoni (ed.), Risk and Reliability Analysis: Theory and Applications, pp. 385-415. Berlin: Springer. Doi: 10.1007/978-3-319-52425-2_17.

Cello, G. and Malamud, B. D. (2006) 'Fractal Analysis for Natural Hazards', special publication 261 of the Geological Society of London. ISBN-13: 978-1-86239-201-4.

Chan, S. C., Kendon, E. J., Fowler, H. J., Blenkinsop, S. and Roberts, N. M. (2014) 'Projected increases in summer and winter UK sub-daily precipitation extremes from high-resolution regional climate models', Environmental Research Letters, 9(8), 084019. Doi: 10.1088/1748-9326/9/8/084019.

Chang, T.-P., Ko, H.-H., Liu, F.-J., Chen, P.-H., Chang, Y.-P., Liang, Y.-H., Jang, H.-Y., Lin, T.-C. and Chen, Y.-H. (2012) 'Fractal dimension of wind speed time series', Applied Energy, 93, pp. 742-749. Doi: 10.1016/j.apenergy.2011.08.014.

Chatterton, J., Viavattene, C., Morris, J., Penning-Roswell, E. and Tapsell, S. (2010) 'The costs of the summer 2007 floods in England'. Available at: https://assets.publishing.service.gov.uk/government/uploads/system/uploads/attachment_data/file/291190/scho1109brja-e-e.pdf (Accessed 23 December 2018).

Chopra, S.S., Dillon, T., Bilec, M.M. and Khanna, V. (2016) 'A network-based framework for assessing infrastructure resilience: a case study of the London metro system', Journal of the Royal Society Interface, 13(118), pii: 20160113. Doi: 10.1098/rsif.2016.0113.

Clauset, A., Shalizi, C.R. and Newman, M.E.J. (2009) 'Power-Law Distributions in Empirical Data', SIAM Review, 51(4), pp. 661-703. Doi: 10.1137/070710111.

Comegna, A., Coppola, A., Comegna, V., Sommella, A. and Vitale, C.D. (2013) 'Use of a fractional Brownian motion model to mimic spatial horizontal variation of soil physical and hydraulic properties displaying a power-law variogram', Procedia Environmental Sciences, 19, pp. 416-425. Doi: 10.1016/j.proenv.2013.06.048.

Cotilla-Sanchez, E., Hines, P. D. H., Barrows, C. and Blumsack, S. (2011) 'Comparing the Topological and Electrical Structure of the North American Electric Power Infrastructure', IEEE Systems Journal, 6(4), pp. 616-626. Doi: 10.1109/JSYST.2012.2183033.

Cova, T. J, Theobald, D. M., Norman III, J. B. and Siebeneck, L. K. (2011) 'Mapping wildfire evacuation vulnerability in the western US: the limits of infrastructure', GeoJournal, 78(2), pp. 273-285. Doi: 10.1007/s10708-011-9419-5.

Cowpertwait, P. S. P. (1991) 'Further developments of the Neyman-Scott clustered point process for modelling rainfall', Water Resources Research, 27(7), pp. 1944-7973. Doi: 10.1029/91WR00479.

Cowpertwait, P. S. P. (1995) 'A Generalized Spatial-Temporal Model of Rainfall Based on a Clustered Point Process', Proceedings of Mathematical and Physical Sciences, 450(1938), pp. 163-175. Doi: 10.1098/rspa.1995.0077.

Crucitti, P., Latora, V. and Marchiori, M. (2004) 'Model for cascading failures in complex networks', Physical Review E, 69(4), 045104R. Doi: 10.1103/PhysRevE.69.045104.

Cullen, M. J. P. (1993) 'The unified forecast/climate model', Meteorological Magazine, 122(1449), pp. 81-94.
Available at: https://www.ecmwf.int/sites/default/files/elibrary/1991/8836-unified-forecastclimate-model.pdf (Accessed 17 January 2018).

D

D'Amato Avanzi, G., Galanti, Y., Giannecchini, R. and Puccinelli, A. (2013) 'Fragility of Territory and Infrastructures Resulting from Rainstorms in Northern Tuscany (Italy)', In: Margottini C., Canuti P., Sassa K. (eds) Landslide Science and Practice. Springer, Berlin, Heidelberg, pp. 239-246. Doi: 10.1007/978-3-642-31319-6_33.

D'Lima, M. and Medda, F. (2015) 'A new measure of resilience: An application to the London Underground', Transportation Research Part A: Policy and Practice, 81, pp. 35-46. Doi: 10.1016/j.tra.2015.05.017.

Darabi, H. R. and Mansouri, M. (2015) 'Governing Competition and Collaboration in Network Industries Using Agent-Based Modeling: A Case-Study of US Air Transportation Network', IEEE Systems Journal, PP(99). Doi: 10.1109/JSYST.2015.2448635.

Davies, R. B. and Harte, D. S. (1987) 'Tests for Hurst effect', Biometrika, 74, pp. 95-102. Doi: 10.1093/biomet/74.1.95.

Davies, T., Cullen, M. P. J., Malcolm, A. J., Mawson, M. H., Staniforth, A., White, A. A. and Wood, N. (2005) 'A new dynamical core for the Met Office's global and regional modelling of the atmosphere', Quarterly Journal of the Royal Meteorological Society, 131(608), pp. 1759-1782. Doi: 10.1256/qj.04.101.

Dawson, R. J. and Hall, J. W. (2006) 'Adaptive importance sampling for risk analysis of complex infrastructure systems', Proceedings of the Royal Society A, 462(2075), pp. 3343-3362. Doi: 10.1098/rspa.2006.1720.

Dawson, R. J. (2007) 'Re-engineering cities: a framework for adaptation to global change', Philosophical Transactions of the Royal Society A, 365(1861), pp. 3085-3098. Doi: 10.1098/rsta.2007.0008.

Dawson, R. J. (2015) 'Handling Interdependencies in Climate Change Risk Assessment', Climate, 3, pp. 1079-1096. Doi: 10.3390/cli3041079.

Dawson, R. J., Thompson, D., Johns, D., Wood, R., Darch, G., Chapman, L., Hughes, P. N., Watson, G. V. R., Paulson, K., Bell, S., Gosling, S. N., Powrie, W. and Hall, J. W. (2018) 'A systems framework for national assessment of climate risks to infrastructure', Phylosophical Transactions of the Royal Society A, 376(2121), 20170298. Doi: 10.1098/rsta.2017.0298.

De Durana, J.-M. G., Barambones, O., Kremers, E. and Varga, L. (2015) 'Agent based modelling of local energy networks as instances of complex infrastructure systems', Emergence: Complexity and Organization, 17(2), pp. 1-11. Doi: 10.emerg/10.17357.6bbf8c719fe8297768ce3f8be212957c.

Derrible, S. and Kennedy, C. (2010) 'The complexity and robustness of metro networks', Physica A: Statistical Mechanics and its Applications, 389(17), pp. 3678-3691. Doi: 10.1016/j.physa.2010.04.008.

Derrible, S. (2017) 'Complexity in future cities: the rise of networked infrastructure', International Journal of Urban Sciences, 21(sup1), pp. 68-86. Doi: 10.1080/12265934.2016.1233075.

Diao, K., Guidolin, M., Fu, G., Farmani, R. and Butler, D. (2014) 'Hierarchical Decomposition of Water Distribution Systems for Background Leakage Assessment', Procedia Engineering, 89, pp. 53-58. Doi: 10.1016/j.proeng.2014.11.159.

Dieker, A. B. (2002) 'Simulation of fractional Brownian motion'. M.Sc. Thesis: Vrije Universiteit Amsterdam, Amsterdam, The Netherlands. Available at: http://www.columbia.edu/~ad3217/fbm/thesis.pdf (Accessed 17 February 2016).

Dieker, A. B. (2003) 'On the Spectral Simulation of fractional Brownian motion', Probability in the Engineering and Informational Sciences, 17(3), pp. 417–434, 2003. Doi: 10.1017/S0269964803173081.

Dong, B., O'Neill, Z. and Li, Z. (2014) 'A BIM-enabled information infrastructure for building energy fault detection and diagnostics', Automation in Construction, 44, pp. 197-211. Doi: 10.1016/j.autcon.2014.04.007.

Dong, S., Li, H. and Yin, Q. (2018) 'Building information modeling in combination with real time location systems and sensors for safety performance enhancement', Safety Science, 102, pp. 226-237. Doi: 10.1016/j.ssci.2017.10.011.

Dudenhoeffer, D. D., Permann, M. R., Woolsey, S., Timpany, R., Miller, C., McDermott, A. and Manic, M. (2007) 'Interdependency Modeling and Emergency Response', proceedings of the 2007 Summer Computer Simulation Conference, San Diego, California, USA, pp. 1230-1237. Doi: 10.1145/1357910.1358101.

Dueñas-Osorio, L. and Vemuru, S. M. (2009) 'Cascading failures in complex infrastructure systems', Structural Safety, 31(2), pp. 157-167. Doi: 10.1016/j.strusafe.2008.06.007.

Dunović, I. B., Radujković, M. and Škreb, K. A. (2014) 'Towards a New Model of Complexity – The Case of Large Infrastructure Projects', Procedia - Social and Behavioral Sciences, 119, pp. 730-738. Doi: 10.1016/j.sbspro.2014.03.082.

Dunn, S., Fu, G., Wilkinson, S. M. and Dawson, R. J. (2013) 'Network theory for infrastructure systems modelling', Proceedings of the Institution of Civil Engineers: Engineering Sustainability, 166(5), pp. 281-292. Doi: 10.1680/ensu.12.00039.

Dunn, S., Wilkinson, S. M. and Ford, A. (2016a) 'Spatial structure and evolution of infrastructure networks', Journal of Sustainable Cities and Society, 27, pp. 23-31. Doi: 10.1016/j.scs.2016.08.011.

Dunn, S. and Wilkinson, S. M. (2016b) 'Increasing the resilience of air traffic networks using a network graph theory approach', Transportation Research Part E: Logistics and Transportation Review, 90, pp. 39-50. Doi: 10.1016/j.tre.2015.09.011.

Dunn, S., and Wilkinson, S. M. (2017) 'Hazard tolerance of spatially distributed complex networks', Reliability Engineering & System Safety, 157, pp. 1-12. Doi: 10.1016/j.ress.2016.08.010.

Dunn, S., Wilkinson, S. M., Alderson, D., Fowler, H. and Galasso, C. (2018) 'Characterizing the Resilience of Electricity Infrastructure using an Extensive Fault Database and Empirical Fragility Curves', ASCE Natural Hazards Review, 19(1). Doi: 10.1061/(ASCE)NH.1527-6996.0000267.

Dunn, S. and Holmes, M. (2019) 'Development of a hierarchical approach to analyse interdependent infrastructure system failures', Reliability Engineering & System Safety, 191, 106530. Doi: 10.1016/j.ress.2019.106530.

E

El Morjani, Z. E. A., Ebener, S., Boos, J., Ghaffar, E. A. and Musani, A. (2007) 'Modelling the spatial distribution of five natural hazards in the context of the WHO/EMRO Atlas of Disaster Risk as a step towards the reduction of the health impact related to disasters', International Journal of Health Geographics, 6(8). Doi: 10.1186/1476-072X-6-8.

Edmondson, V., Cerny, M., Lim, M., Gledson, B., Lockley, S. and Woodward, J. (2018) 'A smart sewer asset information model to enable an 'Internet of Things' for operational wastewater management', Automation in Construction, 91, pp. 193-205. Doi: j.autcon.2018.03.003.

Eleutério, J., Hattemer, C. and Rozan, A. (2013) 'A systemic method for evaluating the potential impacts of floods on network infrastructures', Natural Hazards and Earth System Sciences, 13(4), pp. 983-998. Doi: 10.5194/nhess-13-983-2013.

Erdős, P. and Rényi, A. (1959) 'On Random Graphs I', Publicationes Mathematicae (Debrecen, Hungary), 6, pp. 290-297. Available at: https://gnunet.org/node/1644 (Accessed 6 July 2016).

Esposito, S., Iervolino, I., d'Onofrion, A., Santo, A., Cavalieri, F. and Franchin, P. (2015) 'Simulation-Based Seismic Risk Assessment of Gas Distribution Networks', Computer-Aided Civil and Infrastructure Engineering, 30, pp. 508-523. Doi: 10.1111/mice.12105.

Estrada, E. (2006) 'Network robustness to targeted attacks. The interplay of expansibility and degree distribution', European Physics Journal B, (52), pp. 563-574. Doi: 10.1140/epjb/e2006-00330-7.

Estrada, E. and Knight, P. (2015) 'A First Course in Network Theory'. 1st Edition. Oxford: Oxford University Press. ISBN-13: 978-0198726463.

ETI (2018) 'Enabling Resilient UK Energy Infrastructure: Natural Hazard Characterization: Technical Volumes and Case Studies'. Available at: http://www.imeche.org/policy-and-press/energy-theme/enabling-resilient-uk-energy-infrastructure (Accessed 5 January 2019).

Eusgeld, I., Nan, C and Dietz, S. (2011) '"System-of-systems" approach for interdependent critical infrastructures', Reliability Engineering & System Safety, 96(6), pp. 679-686. Doi: 10.1016/j.ress.2010.12.010.

F

Faber, M. H. and Stewart, M. G. (2003) 'Risk assessment for civil engineering facilities: critical overview and discussion', Reliability Engineering and System Safety, 80(2), pp. 173-184. Doi: 10.1016/S0951-8320(03)00027-9.

Fares, H. and Zayad, T. (2010) 'Hierarchical Fuzzy Expert System for Risk of Failure of Water Mains', ASCE Journal of Pipeline Systems Engineering and Practice, 1(1), pp. 53-62. Doi: 10.1061/(ASCE)PS.1949-1204.0000037.

Ferranti, E., Chapman, L. and Whyatt, D. (2017) 'A Perfect Storm? The collapse of Lancaster's critical infrastructure networks following intense rainfall on 4/5 December 2015', Weather, 72(1), pp. 3-7. Doi: 10.1002/wea.2907.

Ferreira, A., Leitão, P. and Vrba, P. (2015) 'Simulating smart grid using a two-layer multiagent framework', Proceedings of the IEEE International Conference on Industrial Technology, Seville, Spain. Doi: 10.1109/ICIT.2015.7125538.

Flint, A. R. (1981) 'Risks and Their Control in Civil Engineering', Proceedings of the Royal Society of London. Series A, Mathematical and Physical Sciences, 376(1764), pp. 167-179. Available at: http://www.jstor.org/stable/2397125 (Accessed 18 October 2017).

FLO-2D Software, Inc. (2009) 'FLO-2D User's manual', Version 2009.01, Arizona, USA. Available at: https://www.flo-2d.com/download/ (Accessed 11 October 2017).

Flyvbjerg, B., Bruzelius, N. and van Wee, B. (2008) 'Comparison of Capital Costs per Route-Kilometre in Urban Rail', European Journal of Transport and Infrastructure Research, 8(1), pp. 17-30. ISSN: 15677141.

Fontanazza, C. M., Freni, G. and La Loggia, G. (2007) 'Analysis of intermittent supply systems in water scarcity conditions and evaluation of the resource distribution equity indices', WIT Transactions on Ecology and the Environment, 103, pp. 635-644. Doi: 10.2495/WRM070591.

Ford, A., Barr, S., Dawson, R. J., Virgo, J., Batty, M. and Hall, J. W. (2019) 'A multi-scale urban integrated assessment framework for climate change studies: A flooding application', Computers, Environment and Urban Systems, 75, pp. 229-243. Doi: 10.1016/j.compenvurbsys.2019.02.005.

Foroutan-pour, K., Dutilleul, P. and Smith, D. L. (1999) 'Advances in the implementation of the box-counting method of fractal dimension estimation', Journal of Applied Mathematics and Computation, 102(2-3), pp. 195-210. Doi: 10.1016/S0096-3003(98)10096-6.

Fortuna, L., Nunnari, S. and Guariso, G. (2014) 'Fractal order evidences in wind speed time series', proceedings of the International Conference on Fractional Differentiation and its Applications, Catania, Italy. Doi: 10.1109/ICFDA.2014.6967450.

Fournier, A., Fussell, D. and Carpenter, L. (1982) 'Computer rendering of stochastic models', Communications of the Association for Computing Machinery, 25(6), pp. 371–384. Doi: 10.1145/358523.358553.

Fowler, H. J., Kilsby, C. G. and O'Connell, P. E. (2000) 'A stochastic rainfall model for the assessment of regional water resource systems under changed climatic conditions', Hydrology and Earth System Sciences, 4, pp. 261-280. Doi: 10.5194/hess-4-263-2000.

Fowler, H. J., Kilsby, C. G., O'Connell, P. E. and Burton, A. (2004) 'A weather-type conditioned multi-site stochastic rainfall model for the generation of scenarios of climatic variability and change', Journal of Hydrology, 308(1-4), pp. 50-66. Doi: 10.1016/j.jhydrol.2004.10.021.

Frangopol, D. and Tsompanakis, Y. (2014) 'Maintenance and Safety of Aging Infrastructure', Boca Raton, Florida: CRC Press. ISBN-13: 978-0-20338-628-6.

Fu, G. Dawson, R., Khoury, M. and Bullock, S. (2014) 'Interdependent networks: Vulnerability analysis and strategies to limit cascading failure', European Physical Journal B, 87(7), 148. Doi: 10.1140/epjb/e2014-40876-y.

Fu, G., Wilkinson, S. M. and Dawson, R. J. (2016) 'A Spatial Network Model for Civil Infrastructure System Development', Computer-Aided Civil and Infrastructure Engineering, 31(9), pp. 661-680. Doi: 10.1111/mice.12204.

Fu, G., Wilkinson, S., Dawson, R., Fowler, H., Kilsby, C., Panteli, M. and Mancarella, P. (2017) 'Integrated Approach to assess the Electricity Infrastructure Networks to Climate Hazards', IEEE Systems Journal, PP(99), pp. 1-12. Doi: 10.1109/JSYST.2017.2700791.

G

Gao, J., Li, D. and Havlin, S. (2014) 'From a single network to a network of networks', National Science Review, 1(3), pp. 346-356. Doi: 10.1093/nsr/nwu020.

Gao, J., Liu, X., Li, D. and Havlin, S. (2015) 'Recent progress on the resilience of complex networks', Energies, 8(10), pp. 12187-12210. Doi: 10.3390/en81012187.

Gao, J., Barzel, B. and Barabási, A.-L. (2016) 'Universal resilience patterns in complex networks', Nature, 530(7590), pp. 307–312. Doi: 10.1038/nature16948.

Gastner, M. T. and Newman, M. E. J. (2006a) 'The spatial structure of networks', The European Physical Journal B, 49(2), pp. 247-252. Doi: 10.1140/epjb/e2006-00046-8.

Gastner, M. T. and Newman, M. E. J. (2006b) 'Optimal design of spatial distribution networks', Physical Review E, 74, 016117. Doi: 10.1103/PhysRevE.74.016117.

Gebbeken, N., Videkhina, I. Pfeiffer, E., Garsch, M. and Rüdiger, L. (2016) 'Risk assessment and protection of the built infrastructure for flood events', Bautechnik, 93(4), pp. 199-213 (in German). Doi: 10.1002/bate.201600003.

Geraldi, J. G. (2008) 'The balance between order and chaos in multi-project firms: A conceptual model', International Journal of Project Management, 26(4), pp. 348-356. Doi: 10.1016/j.ijproman.2007.08.013.

Gezer, E. D., Temiz, A. and Yüksek, T. (2015) 'Inspection of Wooden Poles in Electrical Power Distribution Networks in Artvin, Turkey', Advances in Materials Science and Engineering, 2015, 11 pages. Doi: 10.1155/2015/659818.

Ghosn, M., Dueñas-Osorio, L., Frangopol, D. M., McAllister, T. P., Bocchini, P., Manuel, L., Ellingwood, B. R., Arangio, S., Bontempi, F., Shah, M., Akiyama, M., Biondini, F., Hernandez, S. and Tsiatas, G. (2016) 'Performance Indicators for Structural Systems and Infrastructure Networks', Journal of Structural Engineering, 142(9), F4016003. Doi: 10.1061/(ASCE)ST.1943-541X.0001542.

Gibson, A. D., Forster, A., Culshaw, M. G., Cooper, A. H. and Farrant, A. (2005) 'Rapid geohazard assessment system for the UK Natural Gas Pipeline Network', International Symposium on Geology and Linear Developments, Lyon, France, 23-25 May 2005. Available at http://nora.nerc.ac.uk/id/eprint/7355/. Retrieved August 5, 2019.

Gill, J. C. and Malamud, B. (2014) 'Reviewing and visualizing the interactions of natural hazards', Reviews of Geophysics, 52(4), pp. 680-722. Doi: 10.1002/2013RG000445.

Giustolisi, O., Simone, A. and Ridolfi, L. (2017) 'Network structure classification and features of water distribution systems', Water Resources Research, 53(4), pp. 3407-3423. Doi: 10.1002/2016WR020071.

Glenis, V., McGough, A. S., Kutija, V., Kilsby, C. and Woodman, S. (2013) 'Flood modelling for cities using Cloud computing', Journal of Cloud Computing: Advances, Systems and Applications, 2(7). Doi: 10.1186/2192-113X-2-7.

Grimsey, D and Lewis, M. K. (2002) 'Evaluating the risks of public-private partnerships for infrastructure projects', International Journal of Project Management, 20(2), pp. 107-118. Doi: 10.1016/S0263-7863(00)00040-5.

Gross, W. F., Hayden, C. and Butz, C. (2012) 'About the impact of rising oil price on logistics networks and transportation greenhouse gas emission', Logistic Research, 4(3-4), pp. 147-156. Doi: 10.1007/s12159-012-0072-2.

Grossi, P. and Kunreuther, H. (2005). 'Catastrophe modeling: A new approach to managing risk'. New York: Springer. ISBN-13: 978-0387241050.

Guha-Sapir, D., Rodriguez-Llanes, J. M. and Jakubicka, T. (2011) 'Using disaster footprints, population databases and GIS to overcome persistent problems for human impact assessment in flood events', Natural Hazards, 58(3), pp. 845-852. Doi: 10.1007/s11069-011-9775-y.

Guidolin, M., Chen, A. S., Ghimire, B., Keedwell, E.C., Djordjević, S. and Savić, D. A. (2016) 'A weighted cellular automata 2D inundation model for rapid flood analysis', Environmental Modelling and Software, 84, pp. 378-394. Doi: 10.1016/j.envsoft.2016.07.008.

Guimerà, R. and Amaral, L. A. N. (2004) 'Modeling the world-wide airport network', The European Physical Journal B, 38, pp. 381-385. Doi: 10.1140/epjb/e2004-00131-0.

Guimerà, R., Mossa, S., Turtschi, T. and Amaral, L. A. N. (2005) 'The worldwide air transportation network: Anomalous centrality, community structure, and cities' global roles', Proceedings of the National Academy of Sciences of the United States of America, 102(22), pp. 7794-7799. Doi: 10.1073/pnas.0407994102.

Guo, H., Zheng, C., Iu, H. H.-C. and Fernando, T. (2017) 'A critical review of cascading failure analysis and modeling of power system', Renewable and Sustainable Energy Reviews, 80, pp. 9-22. Doi: 10.1016/j.rser.2017.05.206.

H

Hagberg, A. A., Schult D. A. and Swart, P. J. (2008) 'Exploring network structure, dynamics, and function using NetworkX', in: Varoquaux, G., Vaught, T. and Millman, J. (eds) Proceedings of the 7th Python in Science Conference, pp. 11-15, Pasadena, California. Available at: http://conference.scipy.org/proceedings/SciPy2008/paper_2/ (Accessed 24 July 2015).

Hall, J. W., Henriques, J. J., Hickford, A. J. and Nicholls, R. J. (2015) 'Systems-of-systems analysis of national infrastructure', Proceedings of the Institution of Civil Engineers - Engineering Sustainability, 166(5), pp. 249-257. Doi: 10.1680/ensu.12.00028.

Hall, J. W., Thacker, S., Ives, M. C., Cao, Y., Chaudry, M., Blainey, S P. and Oughton, E. J. (2017) 'Strategic analysis of the future of national infrastructure', Proceedings of the Institution of Civil Engineers - Civil Engineering, 170(CE1), pp. 39-47. Doi: 10.1680/jcien.16.00018.

Harper, B. A., Kepert, J. D. and Ginger, J. D. (2010) 'Guidelines for converting between various wind averaging periods in tropical cyclone conditions'. World Meteorological Organization, WMO/TD, 1555.
Available at: https://www.wmo.int/pages/prog/www/tcp/documents/WMO_TD_1555_en.pdf (Accessed 17 January 2018).

Havlin, S., Stanley, H. E., Bashan, A., Gao, J. and Kenett, D. Y. (2015) 'Percolation of interdependent network of networks', Chaos, Solicitons & Fractals, 72, pp. 4-19. Doi: 10.1016/j.chaos.2014.09.006.

Hawick, K. A. (2011) 'Water Distribution Network Robustness and Fragmentation using Graph Metrics', proceedings of the 2012 International Conference on Water Resource Management, pp. 304-310, Gaborone, Botswana. Doi: 10.2316/P.2012.762-037.

Hawick, K. A. (2012) 'Node-Failure and Islanding in National Grid Scale Electricity Distribution Networks', proceedings of the 2012 International Conference on Power and Energy Systems and Applications, pp. 52-58, Las Vegas, Nevada. Doi: 10.2316/P.2012.788-089.

Herrera, M., Abraham, E. and Stoianov, I. (2016) 'A Graph-Theoretic Framework for Assessing the Resilience of Sectorised Water Distribution Networks', Water Resources Management, 30(5), pp. 1685–1699. Doi: 10.1007/s11269-016-1245-6.

Herrmann, M., Somot, S., Calmanti, S., Dubois, C. and Sevault, F. (2011) 'Representation of spatial and temporal variability of daily wind speed and of intense wind events over the Mediterranean Sea using dynamical downscaling: impact of the regional climate model configuration', Natural Hazards and Earth System Sciences, 11, pp. 1983-2001. Doi: 10.5194/nhess-11-1983-2011.

Hickford, A. J., Blainey, S. P., Hortelano, A. O. and Pant, R. (2018) 'Resilience engineering: theory and practice in interdependent infrastructure systems', Environment Systems and Decisions, 38(3), pp. 278-291. Doi: 10.1007/s10669-018-9707-4.

Hines, P. D. H., Cotilla-Sanchez, E. and Blumsack, S. (2010) 'Do topological models provide good information about electricity infrastructure vulnerability?', Chaos: An Interdisciplinary Journal of Nonlinear Science, 20(3), 033122. Doi: 10.1063/1.3489887.

Hines, P. D. H., Blumsack, S. and Schläpfer, M. (2015) 'When are Decentralized Infrastructure Networks Preferable to Centralized Ones?', proceedings of the 50th Hawaii International Conference on System Sciences, pp. 3241-3250, Honolulu, Hawaii. Doi: 10.24251/HICSS.2017.392.

Holden, R., Val, D. V., Burkhard, R. and Nodwell, S. (2013) 'A network flow model for interdependent infrastructures at the local scale', Safety Science, 53, pp. 51-60. Doi: 10.1016/j.ssci.2012.08.013.

Hong, L., Ouyang, M., Peeta, S., He, X. and Yan, Y. (2015) 'Vulnerability assessment and mitigation for the Chinese railway system under floods', Journal of Reliability Engineering & System Safety, 137, pp. 58-68. Doi: 10.1016/j.ress.2014.12.013.

Horne III, J. F. and Orr, J. E. (1998) 'Assessing behaviors that create resilient organizations', Employment Relations Today, 24(4), pp. 29–39. Doi: 10.1002/ert.3910240405.

Hosking, J. R. M. (1984) 'Modeling persistence in hydrological time series using fractional differencing', Water Resources Research, 20(12), pp. 1898-1908. Doi: 10.1029/WR020i012p01898.

Hu, F., Yeung, C.H., Yang, S., Wang, W. and Zeng, A. (2016) 'Recovery of infrastructure networks after localized attacks', Scientific Reports, 6, 24522. Doi: 10.1038/srep24522.

Hunter, J. D. (2007) 'Matplotlib: A 2D graphics environment', Computing in Science & Engineering, 9(3), pp. 90-95. Doi: 10.1109/MCSE.2007.55.

Hurst, H. E. (1951) 'Long-term storage capacity of reservoirs', Transactions of the American Society of Civil Engineers (ASCE), 116(1), pp.770-799. Available at: http://cedb.asce.org/CEDBsearch/record.jsp?dockey=0292165 (Accessed 1 September 2015).

Inanloo, B., Tansel, B., Shams, K., Jin, X. and Gan, A. (2016) 'A decision aid GIS-based risk assessment and vulnerability analysis approach for transportation and pipeline networks', Safety Science, 84, pp. 57-66. Doi: 10.1016/j.ssci.2015.11.018.

I

ICE (Institution of Civil Engineers). (2017) 'State of The Nation 2017: Digital Transformation'. Available at: https://www.ice.org.uk/getattachment/news-and-insight/policy/state-of-the-nation-2017-digital-transformation/ICE-SoN-Report-Web-Updated.pdf.aspx (Accessed 13 October 2017).

J

Jing-Zhou, L. and Yi-Fa, T. (2005) 'An exponential distribution network', Chinese Physics, 14(4), pp. 643-645. Doi: 10.1088/1009-1963/14/4/001.

Jönsson, M. T., Fraver, S., Jonsson, B. G., Dynesius, M., Rydgård, M. and Esseen, P. A. (2007) 'Eighteen years of tree mortality and structural change in an experimentally fragmented Norway spruce forest', Journal of Forest Ecology and Management, 242(2), pp. 306-313. Doi: 10.1016/j.foreco.2007.01.048.

K

Kajewski, P. (2016) 'Infrastructure Procurement in a Resource Constrained Market'. ARCADIS report. Available at: https://www.arcadis.com/media/7/D/0/%7B7D0D10A0-BA7B-4775-9F51-E058B4503D15%7DINFRASTRUCTURE%20PROCUREMENT%20IN%20A%20RESOURCE%20CONSTRAINED%20MARKET.pdf (Accessed 1 November 2017).

Kalapala, V., Sanwalani, V., Causet, A. and Moore, C. (2006) 'Scale invariance in road networks', Physical Review E, 73(2), 062130. Doi: 10.1103/PhysRevE.73.026130.

Karakostas, C., Lekidis, V., Makarios, T., Salonikos, T., Sous, I. and Demosthenous, M. (2005) 'Seismic response of structures and infrastructure facilities during the Lefkada, Greece earthquake of 14/8/2003', Engineering Structures, 27(2), pp. 213-227. Doi: 10.1016/j.engstruct.2004.09.009.

Kang, X., Jiang, L., Bai, Y. and Caprani, C. C. (2017) 'Seismic damage evaluation of high-speed railway bridge components under different intensities of earthquake excitations', Engineering Structures, 152, pp. 116-128. Doi: 10.1016/j.engstruct.2017.08.057.

Kaplan, S., Perla, H. F. and Bley, D. C. (1983) 'A Methodology for Seismic Risk Analysis of Nuclear Power Plants', Risk Analysis, 3(3), pp. 169-180. Doi: 10.1111/j.1539-6924.1983.tb00118.x.

Karim, K. R. and Yamazaki, F. (2003) 'A simplified method of constructing fragility curves for highway bridges', Earthquake Engineering & Structural Dynamics, 32(10), pp. 1603–1626. Doi: 10.1002/eqe.291.

Kaufman, S., Qing, C., Levenson, N. and Hanson, M. (2012) 'Transportation During and After Hurricane Sandy'. Available at: https://wagner.nyu.edu/files/rudincenter/sandytransportation.pdf (Accessed 4 December 2017).

Kellermann, P., Schöbel, A., Kundela, G. and Thieken, A. H. (2015) 'Estimating flood damage to railway infrastructure – the case study of the March River flood in 2006 on the Austrian Northern Railway', Natural Hazards and Earth System Sciences, 15, pp. 2485-2496. Doi: 10.5194/nhess-15-2485-2015.

Kendon, E. J., Roberts, N. M., Fowler, H. J., Roberts, M. J., Chan, S. C. and Senior, C. A. (2014) 'Heavier summer downpours with climate change revealed by weather forecast resolution model', Nature Climate Change, 4, pp. 570-576. Doi: 10.1038/nclimate2258.

Khoury, M., Bullock, S., Fu, G. and Dawson, R. J. (2014) 'Improving measures of topological robustness in networks of networks and suggestion of a novel way to counter both failure propagation and isolation', Infrastructure Complexity, 2(1). Doi: 10.1186/s40551-015-0004-9.

Kirchner-Bossi, N., Kendon, E. J., Fowler, H. J., Dawson, R. J. and Wilkinson, S. M. (2019) 'Present and Future Wind Gust Climatology using a Convection-Permitting Climate Model over the Southern UK', Climate Dynamics, in revision.

Klinkenberg, B. (1992) 'Fractals and morphometric measures: is there a relationship?', Geomorphology, 5(1), pp. 5–20. Doi: 10.1016/0169-555X(92)90055-S.

Klinkenberg, B. (2004) 'Fractal', in: Goudie, A. (ed.) Encyclopedia of Geomorphology, Volume 1. London & New York: Routledge Limited. ISBN-10: 0-415-32737-7.

Koks, E. E., Rozenberg, J., Zorn, C., Tariverdi, M., Vousdoukas, M., Fraser, S. A., Hall, J. W. and Hallegatte, S. (2019) 'A global multi-hazard risk analysis of road and railway infrastructure assets', Nature Communications, 10, 2677. Doi: 10.1038/s41467-019-10442-3.

Kong, R., Han, C., Guo, T. and Pei, W. (2013) 'An Energy-Based Centrality for Electrical Networks', Energy and Power Engineering, 5, pp. 597-602. Doi: 10.4236/epe.2013.54B115.

Korkali, M., Veneman, J. G., Tivnan, B. F., Bagrow, J. P. and Hines, P. D. H. (2017) 'Reducing Cascading Failure Risk by Increasing Infrastructure Network Interdependence', Scientific Reports, 7, 44499. Doi: 10.1038/srep44499.

Kluyver, T., Ragan-Kelley, B., Perez, F., Granger, B., Bussonnier, M., Frederic, J., Kelley, K., Hamrick, J., Grout, J., Corlay, S., Ivanov, P., Avila, D., Abdalla, S., Willing, C. and Jupyter Development Team (2016) 'Jupyter Notebooks—a publishing format for reproducible computational workflows', in F. Loizides and B. Schmidt (eds.), Positioning and Power in Academic Publishing: Players, Agents and Agendas, Proceedings of the 20th International Conference on Electronic Publishing, Göttingen, Germany, pp. 87-90. Doi: 10.3233/978-1-61499-649-1-87.

Kroese, D. P. and Botev, Z. I. (2013) 'Spatial Process Generation. Lectures on Stochastic Geometry', in: V. Schmidt (ed.) Spatial Statistics and Random Fields, Volume II: Analysis, Modeling and Simulation of Complex Structures. Berlin: Springer-Verlag. Available at: http://arxiv.org/abs/1308.0399 (Accessed 17 July 2015).

Kröger, W. (2019) 'Achieving Resilience of Large-Scale Engineered Infrastructure Systems', Resilient Structures and Infrastructures. In: Noroozinejad Farsangi E., Takewaki I., Yang T., Astaneh-Asl A., Gardoni P. (eds) Resilient Structures and Infrastructure. Springer, Singapore, Chapter 10, pp. 289-313. ISBN-13: 978-981-13-7445-6. Doi: 10.1007/978-981-13-7446-3_12.

Kundur, D., Feng, X., Mashayekh, S., Liu, S., Zourntos, T. and Butler-Purry, K. L. (2011) 'Towards modelling the impact of cyber-attacks on a smart grid', International Journal of Security and Networks, 6(1), pp. 2-13. Doi: 10.1504/IJSN.2011.039629.

L

Lämmer, S., Gehlsen, B. and Helbing, D. (2006) 'Scaling Laws in the Spatial Structure of Urban Road Networks', Physica A: Statistical Mechanics and its Applications, 363(1), pp. 89-95. Doi: 10.1016/j.physa.2006.01.051.

Lamond, J., Wilkinson, S., Rose, C. and Proverbs, D. (2014) 'Sustainable urban drainage: retrofitting for improved flood mitigation in city centers', Project Report, Royal Institution of Chartered Surveyors, London. Available at: http://eprints.uwe.ac.uk/25017 (Accessed 4 December 2017).

Langford, G. O. (2013) 'Toward A General Theory of Systems Integration: Research in the Context of Systems Engineering', PhD Thesis: University of South Australia.

Latora, V. and Marchiori, M. (2001) 'Efficient Behavior of Small-World Networks', Physical Review Letters, 87(19), 198701. Doi: 10.1103/PhysRevLett.87.198701.

Latora, V. and Marchiori, M. (2005) 'Vulnerability and Protection of Critical Infrastructure Networks', Physical Review E, 71, 015103(R). Doi: 10.1103/PhysRevE.71.015103.

Lean, H. W., Clark, P. A., Dixon, M., Roberts, N. M., Fitch, A., Forbes, R. and Halliwell, C. (2008) 'Characteristics of High-Resolution Versions of the Met Office Unified Model for

Forecasting Convection over the United Kingdom', Monthly Weather Review, 136(9), pp. 3408-3424. Doi: 10.1175/2008MWR2332.1.

Leavitt, W. M. and Kiefer, J. J. (2006) 'Infrastructure Interdependency and the Creation of a Normal Disaster: the Case of Hurricane Katrina and the City of New Orleans', Public Works Management & Policy, 10(4), pp. 306-314. Doi: 10.1177/1087724X06289055.

Leclercq, L. (2007) 'Hybrid approaches to the solutions of the "Lighthill–Whitham–Richards" model', Transportation Research Part B: Methodological, 41(7), pp. 701-709. Doi: 10.1016/j.trb.2006.11.004.

Lewis, T. G. (2006) 'Critical Infrastructure Protection in Homeland Security: Defending a Networked Nation'. Hoboken, New Jersey: John Wiley & Sons. ISBN-13: 978-0471786283.

Lévy, P. (1953) 'Random functions: general theory with special references to Laplacian random functions', University of California Publications in Statistics 1, pp. 331–390.

Li, J., Du, Q. and Sun, C. (2009) 'An improved box-counting method for image fractal dimension estimation', Journal of Pattern Recognition, 42(11), pp. 2460-2469. Doi: 10.1016/j.patcog.2009.03.001.

Li, Y., Zhang, L., Huang, C. and Shen, B. (2016) 'The structural robustness of geographical networks against regional failure and their pre-optimization', Physica A: Statistical Mechanics and its Applications, 451(1), pp. 420-428. Doi: 10.1016/j.physa.2016.01.071.

Little, R. G. (2003) 'Controlling cascading failure: understanding the vulnerabilities of interconnected infrastructures', Journal of Urban Technology, 9(1), pp. 109-123. Doi: 10.1080/106307302317379855.

Llasat, M. C. (2007) 'Book review of "Fractal Analysis for Natural Hazards"', Natural Hazards Earth System Sciences, 7, 343–344. Doi: 10.5194/nhess-7-343-2007.

Long, X., Tipper, D. and Gomes, T. (2014) 'Measuring the survivability of networks to geographic correlated failures', Optical Switching and Networking, 14(2), pp. 117-133. Doi: 10.1016/j.osn.2014.05.004.

Lu, L., Wang, X., Ouyang, Y., Roningen, J., Myers, N. and Calfas, G. (2018) 'Vulnerability of Interdependent Urban Infrastructure Networks: Equilibrium after Failure Propagation and Cascading Impacts', Computer-Aided Civil and Infrastructure Engineering, 33(4), pp. 300-315. Doi: 10.1111/mice.12347.

M

Madni, A. and Jackson, S. (2009) 'Towards a conceptual framework for resilience engineering', IEEE Systems Journal, 3(2), pp. 181-191. Doi: 10.1109/JSYST.2009.2017397.

Malamud, B. D., Turcotte, D. L., Guzzetti, F. and Reichenbach, P. (2004) 'Landslide inventories and their statistical properties', Earth Surface Processes and Landforms, 29(6), pp. 687-711. Doi: 10.1002/esp.1064.

Malamud, B. D. and Turcotte, D. (2006) 'An inverse cascade explanation for the power-law frequency-area statistics of earthquakes, landslides, and wildfires'. in: Cello, G. and Malamud, B. D. (eds.) Fractal Analysis for Natural Hazards, special publication 261 of the Geological Society of London, pp. 1-9. ISBN-13: 978-1862392014.

Mandelbrot, B. B. (1967) 'How long is the coast of Britain? Statistical Self-Similarity and Fractional Dimension', Science, New Series, 156(3775), pp. 636-638. Available at: https://classes.soe.ucsc.edu/ams214/Winter09/foundingpapers/Mandelbrot1967.pdf (Accessed 17 July 2015).

Mandelbrot, B. B. and Van Ness, J. W. (1968) 'Fractional Brownian Motions, Fractional Noises, and Applications', SIAM Review, 10(4), pp. 422-437. Doi: 10.1137/1010093.

Manis, P. and Bloodworth, A. G. (2017) 'Climate change and extreme wind effects on transmission towers', Proceedings of the Institution of Civil Engineers Structures and Buildings, 170(SB2), Paper 1600013, pp. 81-97. Doi: 10.1680/jstbu.16.00013.

Marzo, J. L., Cosgaya, S. G., Skorin-Kapov, N., Scoglio, C. and Shakeri, H. (2019) 'A study of the robustness of optical networks under massive failures', Optical Switching and Networking, 31, pp. 1-7. Doi: 10.1016/j.osn.2018.07.002.

Marzouk, M. and Aty, A. A. (2012) 'Maintaining Subway Infrastructure Using BIM', proceedings of the 2012 Construction Research Congress, Lafayette, Indiana. Doi: 10.1061/9780784412329.233.

Massie, A. and Watson, N. R. (2011) 'Impact of the Christchurch Earthquakes on the Electrical Power System Infrastructure', Bulletin of the New Zealand Society for Earthquake Engineering, 44(4), pp. 425-430. Available at: http://www.nzsee.org.nz/db/Bulletin/Archive/44(4)0425.pdf (Accessed 15 February 2018).

Met Office (2012) 'The UKV model'. Available at: https://www.metoffice.gov.uk/research/news/2012/ukv (Accessed 17 January 2018).

McConnell, S. (2004) 'Code Complete 2'. Redmond, Washington: Microsoft Press. ISBN-13: 9780735619678.

McDaniels, T., Chang, S., Cole, D., Mikawoz, J. and Longstaff, H. (2008) 'Fostering resilience to extreme events within infrastructure systems: Characterizing decision contexts for mitigation and adaptation', Global Environmental Change, 18(2), pp. 310-318. Doi: 10.1016/j.gloenvcha.2008.03.001.

Mikovits, C., Rauch, W. and Kleidorfer, M. (2017) 'Importance of scenario analysis in urban development for urban water infrastructure planning and management', Computers, Environment and Urban Systems, 68, pp. 9-16. Doi: 10.1016/j.compenvurbsys.2017.09.006.

Mostafavi, A. (2017) 'A System-of-Systems Approach for Integrated Resilience Assessment in Highway Transportation Infrastructure Investment', Infrastructures, 2(22). Doi: 10.3390/infrastructures2040022.

Myint, S. W., Yuan, M., Cerveny, R. S. and Giri, C. (2008) 'Categorizing natural disaster damage assessment using satellite-based geospatial techniques', Natural Hazards Earth System Sciences, 8(4), pp. 707–719. Doi: 10.5194/nhess-8-707-2008.

Musa, I.J., Shehu, A. and Lukman, S. (2009) 'The Distribution Methods and Supply Problems of Tap Water in Urban Zaria Area, Kaduna State', Electronic Journal of Environmental, Agricultural and Food Chemistry, 8(4), pp. 294-300. Available at: https://www.researchgate.net/publication/255716508_The_Distribution_Methods_and_Supply_Problems_of_Tap_Water_in_Urban_Zaria_Area_Kaduna_State (Accessed 1 July 2016).

N

National Hurricane Center (2017) 'Harvey Graphics Archive: 5-day Probability of Hurricane-Force Winds'. Available at: http://www.nhc.noaa.gov/archive/2017/Harvey_graphics.php?product=wind_probs_64_F120 (Accessed 10 October 2017).

National Infrastructure Commission (2016) 'Congestion, Capacity, Carbon: priorities for national infrastructure'. Available at: https://www.nic.org.uk/wp-content/uploads/Congestion-Capacity-Carbon_-Priorities-for-national-infrastructure.pdf (Accessed 23 December 2018).

National Statistics (2017) 'UK Energy in Brief 2017'. Available at: https://assets.publishing.service.gov.uk/government/uploads/system/uploads/attachment_data/file/631146/UK_Energy_in_Brief_2017.pdf (Accessed 23 December 2018).

Neumayer, S., Zussman, G., Cohen, R. and Modiano, E. (2011) 'Assessing the vulnerability of the fiber infrastructure to disasters', IEEE/ACM Transactions on Networking, 19(6), pp. 1610–1623. Doi: 10.1109/TNET.2011.2128879.

Neumayer, S. and Modiano, E. (2016) 'Network reliability under geographically correlated line and disk failure models', Computer Networks, 94, pp. 14-28. Doi: 10.1016/j.comnet.2015.11.025.

Newman, M. E. J. (2003) 'The Structure and Function of Complex Networks', SIAM Review, 45(2), pp. 167-256. Doi: 10.1137/S003614450342480.

Niazi, M. and Hussain, A. (2009) 'Agent based Tools for Modeling and Simulation of Self-Organization in Peer-to-Peer, Ad-Hoc and other Complex Networks', IEEE Communications Magazine, 47(3), pp. 163–173. Doi: 10.1109/MCOM.2009.4804403.

Nikulin, G., Kjellström, E., Hansson, U., Strandberg, G. and Ullerstig, A. (2011) 'Evaluation and future projections of temperature, precipitation and wind extremes over Europe in an ensemble of regional climate simulations', Tellus A: Dynamic Meteorology and Oceanography, 63(1), pp. 41-55. Doi: 10.1111/j.1600-0870.2010.00466.x.

Norrbin, P., Lin, J. and Parida, A. (2016) 'Infrastructure Robustness for Railway Systems', International Journal of Performability Engineering, 12(3), pp. 249-264. ISSN: 09731318.

O

O'Donnell, J., Nosenzo, G., Preston, J. and Sturman, T. (2014) 'Installation of optical fibre based sensors within sprayed concrete lined tunnels to measure strain and temperature', London: ICE Publishing. Available at: https://learninglegacy.crossrail.co.uk/documents/installation-of-optical-fibre-based-sensors-within-sprayed-concrete-lined-tunnels-to-measure-strain-and-temperature/ (Accessed 13 October 2017).

OFGEM, Office of Gas and Electricity Markets (2017) 'RIIO-ED1 regulatory instructions and guidance: Annex F – Interruptions', page 5. Available at: https://www.ofgem.gov.uk/ofgem-publications/95354/annexfinterruptions-pdf (Accessed 17 January 2018).

Ouyang, M. (2014) 'Review on modeling and simulation of interdependent critical infrastructure systems', Reliability Engineering and System Safety, 121, pp. 23-40. Doi: 10.1016/j.ress.2013.06.040.

Ouyang, M. (2016) 'Critical location identification and vulnerability analysis of interdependent infrastructure systems under spatially localized attacks', Reliability Engineering and System Safety, 154, pp. 106-116. Doi: 10.1016/j.ress.2016.05.007.

P

Padgett, J., DesRoches, R., Nielson, B., Yashinsky, M., Kwon, O.-S., Burdette, N. and Tavera, E. (2008) 'Bridge Damage and Repair Costs from Hurricane Katrina', ASCE Journal of Bridge Engineering, 13(1), pp. 6-14. Doi: 10.1061/(ASCE)1084-0702(2008)13:1(6).

Palermo, A., Liu, R., Rais, A., McHaffie, B., Andisheh, K., Pampanin, S., Granerio, M., Loporcaro, G., McGann, C. and Wotherspoon, L. (2017) 'Performance of road bridges during the 14 November 2016 Kaikōura earthquake', Bulletin of the New Zealand Society for Earthquake Engineering, 50(2), pp. 253-270. ISSN: 11749857.

Panofsky, H. A., Tennekes, H., Lenschow, D. H. and Wyngaard, J. C. (1977) 'The characteristics of turbulent velocity components in the surface layer under convective conditions', Boundary-Layer Meteorology, 11(3), pp. 355-361. Doi: 10.1007/BF02186086.

Pant, R., Thacker, S., Hall, J. W., Alderson, D. and Barr, S. (2016) 'Critical infrastructure impact assessment due to flood exposure', Journal of Flood Risk Management, 11(1), pp. 22-33. Doi: 10.1111/jfr3.12288.

Panteli, M., Mancarella, P., Wilkinson, S. M., Dawson, R. J. and Pickering, C. (2015) 'Assessment of the resilience of transmission networks to extreme wind events', IEEE Eindhoven PowerTech 2015, Eindhoven, The Netherlands. Doi: 10.1109/PTC.2015.7232484.

Panteli, M., Trakas, D. N., Mancarella, P. and Hatziargyriou, N. D. (2016) 'Boosting the Power Grid Resilience to Extreme Weather Events Using Defensive Islanding', IEEE Transactions on Smart Grid, 7(6), pp. 2913-2922. Doi: 10.1109/TSG.2016.2535228.

Panteli, M., Pickering, C., Wilkinson, S. M., Dawson, R. J. and Mancarella, P. (2017) 'Power System Resilience to Extreme Weather: Fragility Modelling, Probabilistic Impact Assessment, and Adaptation Measures', IEEE Transactions on Power Systems, PP(96). Doi: 10.1109/TPWRS.2016.2641463.

Panzieri, S. and Setola, R. (2008) 'Failures propagation in critical interdependent infrastructures', International Journal of Modelling, Identification and Control, 3(1), pp. 69-78. Doi: 10.1504/IJMIC.2008.018186.

Pavlidis, T. (1979) 'Filling algorithms for raster graphics', Computer Graphics and Image Processing, 10(2), pp. 126–141. Doi: 10.1016/0146-664X(79)90046-7.

Pearson, J., Punzo, G., Mayfield, M., Brighty, G., Parsons, A., Collins, P., Jeavons, S. and Tagg, A. (2018) 'Flood resilience: consolidating knowledge between and within critical infrastructure sectors', Environment Systems and Decisions, 38(3), pp. 318-329. Doi: 10.1007/s10669-018-9709-2.

Peerenboom, J. P., Fisher, R. E. and Whitfield, R. (2001) 'Recovering from Disruptions of Interdependent Critical Infrastructures', presented at the CRIS/DRM/IT/NSF Workshop, Alexandria, VA.

Peitgen, H.-O., Jürgens, H. and Saupe, D. (2004) 'Chaos and Fractals: New Frontiers of Science', 2nd edition, Berlin: Springer. ISBN-13: 978-0-387-21823-6.

Peleg, S., Naor, J., Hartley, R. and Avnir, D. (1984) 'Multiple Resolution Texture Analysis and Classification', IEEE Transactions on Pattern Analysis and Machine Intelligence, 6(4), pp. 518-523. Doi: 10.1109/TPAMI.1984.4767557.

Petrenj, B. and Trucco, P. (2014) 'Simulation-based characterization of critical infrastructure system resilience', International Journal of Critical Infrastructures, 10(3-4). Doi: 10.1504/IJCIS.2014.066366.

Pinelli, J.-P., Pita, G., Gurley, K., Torkian, B., Hamid, S. and Subramanian, C. (2009) 'Damage Characterization: Application to Florida Public Hurricane Loss Model', ASCE Natural Hazard Review, 12(4), pp. 190-195. Doi: 10.1061/(ASCE)NH.1527-6996.0000051.

Pitilakis, K., Argyroudis, S., Kakderi, K. and Selva, J. (2016) 'Systemic vulnerability and risk assessment of transportation systems under natural hazards towards more resilient and robust infrastructures', Transportation Research Procedia, 14, pp. 1335-1344. Doi: 10.1016/j.trpro.2016.05.206.

Polemio, M. and Lollino, P. (2011) 'Failure of infrastructure embankments induced by flooding and seepage', Natural Hazards and Earth Systems Science, 11(12), pp. 3383-3396. Doi: 10.5194/nhess-11-3383-2011.

Poljanšek, K., Bono, F. and Gutiérrez, E. (2012) 'Seismic risk assessment of interdependent critical infrastructure systems: the case of European gas and electricity networks', Earthquake Engineering Structural Dynamics, 41(1), pp. 61-79. Doi: 10.1002/eqe.1118.

Postance, B., Hillier, J., Dijkstra, T. and Dixon, N. (2017) 'Extending natural hazard impacts: an assessment of landslide disruptions on a national road transportation network', Environmental Research Letters, 12(1), 014010. Doi: 10.1088/1748-9326/aa5555.

Pradhan, B. (2018) 'Artificial Intelligence and Spatial Modelling in Natural Hazards and Environmental Applications', In: El-Askary H., Lee S., Heggy E., Pradhan B. (eds) Advances in Remote Sensing and Geo Informatics Applications. Advances in Science, Technology & Innovation (IEREK Interdisciplinary Series for Sustainable Development). Springer, Cham. Doi: 10.1007/978-3-030-01440-7_3.

Pregnolato, M., Ford, A., Robson, C., Glenis, V., Barr, S. and Dawson, R. J. (2016) 'Assessing urban strategies for reducing the impacts of extreme weather on infrastructure networks', Royal Society Open Science, 3(5), 160023. Doi: 10.1098/rsos.160023.

Pregnolato, M., Ford, A., Wilkinson, S. M. and Dawson, R. J. (2017) 'The impact of flooding on road transport: A depth-disruption function', Transportation Research Part D: Transport and Environment, 55, pp. 67-81. Doi: 10.1016/j.trd.2017.06.020.

Priestley, M. B. (1981) 'Spectral analysis and time series', Volume 1. London: Academic Press. Doi: 10.1002/for.3980010411.

Proske, D., Krawtschuk, A., Zeman, O., Scheidl, C. and Chiari, M. (2018) 'No Access Debris flow impacts on masonry arch bridges', Proceedings of the Institution of Civil Engineers - Bridge Engineering, 171(1), pp. 25-26. Doi: 10.1680/jbren.16.00005.

Q

Qin, J. and Faber, M. H. (2019) 'Resilience Informed Performance Assessment of Infrastructure Systems', 13th International Conference on Applications of Statistics and Probability in Civil Engineering (ICASP13), Seoul, South Korea, May 26-30, 2019. Doi: 10.22725/ICASP13.393.

R

Rachunok, B. and Nateghi, R. (2019) 'The Sensitivity of Electric Power Infrastructure Resilience to the Spatial Distribution of Disaster Impacts', preprint, available at: arXiv:1902.02879. Retrieved August 18, 2019.

Radicchi, F. (2015) 'Percolation in real interdependent networks', Nature Physics, 11, pp. 597-602. Doi: 10.1038/NPHYS3374.

Rahnamay-Naeini, M. and Hayat, M. M. (2016) 'Cascading Failures in Interdependent Infrastructures: An Interdependent Markov-Chain Approach', IEEE Transactions on Smart Grid, 7(4). Doi: 10.1109/TSG.2016.2539823.

Regan, M., Smith, J. and Love, P. (2011) 'Infrastructure Procurement: Learning from Private–Public Partnership Experiences 'Down Under', Environment and Planning C: Politics and Space, 29(2), pp. 363-378. Doi: 10.1068/c10122b.

Remington, K. and Pollack, J. (2007) 'Tools for Complex Projects'. Hampshire: Gower Publishing Ltd. ISBN-13: 978-0566087417.

Ren, H.-P., Song, J., Yang, R., Baptista, M. S. and Grebogi, C. (2016) 'Cascade failure analysis of power grid using new load distribution law and node removal rule', Physica A: Statistical Mechanics and its Applications, 442, pp. 239-251. Doi: 10.1016/j.physa.2015.08.039.

Riahi, K., Rao, S., Krey, V., Cho, C., Chirkov, V., Fischer, G., Kindermann, G., Nakicenovic, N. and Rafaj, P. (2011) 'RCP 8.5—A scenario of comparatively high greenhouse gas emissions', Climatic Change, 109(33). Doi: 10.1007/s10584-011-0149-y.

Rinaldi, S., Peerenboom, J. P. and Kelly, T. (2001) 'Identifying, understanding, and analyzing critical infrastructure interdependencies', IEEE Control Systems Magazine 21(6), pp. 11–25. Doi: 10.1109/37.969131.

Robson, C., Barr. S., James, P. and Ford, A. (2014) 'Resilience of Hierarchical Critical Infrastructure Networks', proceedings of the 2014 International Symposium for Next Generation Infrastructures, Vienna, Austria. Available at: https://pdfs.semanticscholar.org/b0c4/d781e5fae1055caacdbb3e69a8703e93a4ca.pdf (Accessed 6 November 2017).

Robson, C. (2016) 'Robustness of hierarchical spatial critical infrastructure networks'. PhD Thesis: Newcastle University.

Roelich, K., Knoeri, C., Steinberger, J. K., Varga, L., Blythe, P. T., Butler, D., Gupta, R., Harrison, G. P., Martin, C. and Purnell, P. (2015) 'Towards resource-efficient and service-oriented integrated infrastructure operation', Technological Forecasting and Social Change, 92, pp. 40-52. Doi: 10.1016/j.techfore.2014.11.008.

Rosato, V., Issacharoff, L., Tiriticco, F., Meloni, S., De Porcellinis, S. and Setola, R. (2008) 'Modelling interdependent infrastructures using interacting dynamical models', International Journal of Critical Infrastructures, 4(1/2), pp. 63-79. Doi: 10.1504/IJCIS.2008.016092.

Royal Academy of Engineering (2012) 'Smart infrastructure: the future'. Available at: http://www.raeng.org.uk/publications/reports/smart-infrastructure-the-future (Accessed 18 October 2017).

Russ, J. C. (1994) 'Fractal Surfaces, Volume 1'. Berlin, Germany: Springer Science and Business Media. ISBN-13: 978-0-3064-4702-0.

Ryan, P. C. and Stewart, M. G. (2017) ‘Cost-benefit analysis of climate change adaptation for power pole networks’, Climatic Change, 143(3-4), pp. 519-533. Doi: 10.1007/s10584-017-2000-6.

S

Saito, H. (2015) ‘Spatial design of physical network robust against earthquakes’, Journal of Lightwave Technology, 33(2), pp. 443-458. Doi: 10.1109/JLT.2014.2385100.

Saupe, D. (1988) ‘Algorithms for random fractals’, in: H.-O. Peitgen and D. Saupe (eds.) The Science of Fractal Images, pp. 71-136. Berlin, Germany: Springer-Verlag. ISBN-13: SBN 978-1-4612-3784-6.

Sánchez, L., Elicegui, I., Cuesta, J., Muñoz, L. and Lanza, J. (2013) ‘Integration of Utilities Infrastructures in a Future Internet Enabled Smart City Framework’, Sensors, 13(11), pp. 14438-14465. Doi: 10.3390/s131114438.

Sanchez-Silva, M. and Gómez, C. (2013) ‘Risk assessment and management of civil infrastructure networks: A systems approach’, in: S. Tesfamariam and K. Goda (eds.), Handbook of Seismic Risk Analysis and Management of Civil Infrastructure Systems, Chapter 17, pp. 437-464. Doi: 10.1533/9780857098986.4.437.

Sarker, P. and Lester, H. D. (2019) ‘Post-Disaster Recovery Associations of Power Systems Dependent Critical Infrastructures’, Infrastructures, 4(2), 30. Doi: 10.3390/infrastructures4020030.

Sathaye, J., Dale, L., Larsen, P., Fitts, G., Koy, K., Lewis, S. and Lucena, A. (2011) ‘Estimating risk to California energy infrastructure from projected climate change’, California Energy Commission. Publication number: CEC-500-2011-XXX. Available at: http://escholarship.org/content/qt14r3v942/qt14r3v942.pdf (Accessed 20 October 2017).

Saupe, D. (1988) ‘Algorithms for random fractals’, in: H.-O. Peitgen and D. Saupe (eds.) The Science of Fractal Images, pp. 71-136. Berlin: Springer-Verlag. ISBN-13: SBN 978-1-4612-3784-6.

Sayers, P., Walsh, C. and Dawson, R. J. (2015) ‘Climate impacts on flood and coastal erosion infrastructure’, Infrastructure Asset Management, 1400040. Doi: 10.1680/iasma.14.00040.

Schäfer, B., Witthaut, D., Timme, M. and Latora, V. (2017) ‘Dynamically induced cascading failures in supply networks’. Arxiv [preprint]. Available from: https://arxiv.org/abs/1707.08018 (Accessed 16 February 2018).

Scheidegger, A. E. (1997) ‘Complexity theory of natural disasters; boundaries of self-structured domains’, Natural Hazards, 16(2-3), pp. 103-112. Doi: 10.1023/A:1007930411053.

Schweikert, A., Chinowsky, P., Espinet, X. and Tarbert, M. (2014) ‘Climate change and infrastructure impacts: comparing the impact on roads in ten countries through 2100’, Procedia Engineering, 78, pp. 306-316. Doi: 10.1016/j.proeng.2014.07.072.

Schwierz, C., Köllner-Heck, P., Zenklusen Mutter, E., Bresch, D. N., Vidale, P.-L., Wild, M. and Schär, C. (2010) 'Modelling European winter wind storms losses in current and future climate', Climatic Change, 101(3-4), pp. 485-514. Doi: 10.1007/s10584-009-9712-1.

Setola, R., Luiijf, E. and Theocharidou, M. (2016) 'Critical Infrastructures, Protection, and Resilience', in: R. Setola, V. Rosato, E. Kyriakides, E. Rome (eds.), Managing the Complexity of Critical Infrastructures, Chapter 1, pp. 1-18. Doi: 10.1007/978-3-319-51043-9.

Setola, R. and Theocharidou, M. (2016) 'Modelling Dependencies Between Critical Infrastructures', in: R. Setola, V. Rosato, E. Kyriakides, E. Rome (eds.), Managing the Complexity of Critical Infrastructures, Chapter 2, pp. 19-41. Doi: 10.1007/978-3-319-51043-9_2.

Shao, S., Huang, X., Stanley, H. E. and Havlin, S. (2015) 'Percolation of localized attacks on complex networks', New Journal of Physics, 17, 023049. Doi: 10.1088/1367-2630/17/2/023049.

Shuang, Q., Liu, Y., Tang, Y., Liu, J. and Shuang, K. (2017) 'System Reliability Evaluation in Water Distribution Networks with the Impact of Valves Experiencing Cascading Failures', Water, 9(6), pp. 413-430. Doi: 10.3390/w9060413.

Sipser, M. (2012) 'Introduction to the Theory of Computation'. 3rd edition. Boston: Cengage Learning/Course Technology. ISBN-13: 978-1133187790.

Smith, A. P. (2009) 'A national scale rainfall analysis and event-based model of extremes for the UK'. PhD Thesis: Newcastle University.

Soille, P. and Rivest, J.-F. (1996) 'On the Validity of Fractal Dimension Measurements in Image Analysis', Journal of Visual Communication and Image Representation, 7(3), pp. 217-229. Doi: 10.1006/jvci.1996.0020.

Soltan, S., Mazauric, D. and Zussman, G. (2017) 'Analysis of Failures in Power Grids', IEEE Transactions on Control of Network Systems, 4(2), pp. 288-300. Doi: 10.1109/TCNS.2015.2498464.

Stauffer, D. and Aharony, A. (1991) 'Introduction to percolation theory'. 1st edition. London: Taylor and Francis. ISBN-13: 978-0748402533.

Stein, M. L. (2002) 'Fast and exact simulation of fractional Brownian motion', Journal of Computational and Graphical Statistics, 11 (3), pp. 587–599. Doi: 10.1198/106186002466.

Sterbenz, J. P. G., Çetinkaya, E. K., Hameed, M. A., Jabbar, A. and Rohrer, J. P. (2011) 'Modelling and analysis of network resilience', proceedings of the Third International Conference on Communication Systems and Networks COMSNETS, Bangalore, India, pp. 1-10. Doi: 10.1109/COMSNETS.2011.5716502.

Stevenson, J. (2013) 'Difference between object-oriented programming and procedural programming languages'. Available at: https://neonbrand.com/website-design/procedural-programming-vs-object-oriented-programming-a-review/ (Accessed 6 December 2017).

Sultana, S. and Chen, Z. (2009) 'Modeling flood induced interdependencies among hydroelectricity generating infrastructures', Journal of Environmental Management, 90(11), pp. 3272-3282. Doi: 10.1016/j.jenvman.2009.05.019.

Svendsen, N. K. and Wolthusen, S. D. (2007) 'An Analysis of Cyclical Interdependencies in Critical Infrastructures', in: Lopez J., Hämmerli B.M. (eds), Critical Information Infrastructures Security, CRITIS 2007, Lecture Notes in Computer Science, 5141, pp. 24-36. Berlin, Heidelberg: Springer. Doi: 10.1007/978-3-540-89173-4_3.

T

Tanizawa, T., Paul, G., Cohen, R., Havlin, S. and Stanley, H. E. (2005) 'Optimization of network robustness to waves of targeted and random attacks', Physical Review E, 71, 047101. Doi: 10.1103/PhysRevE.71.047101.

Terranova, O. G., Gariano, S. L., Bruno, C., Greco, R., Pellegrino, A. D. and Iovine, G. G. R. (2016) 'Landslide-risk scenario of the Costa Viola mountain ridge (Calabria, Southern Italy)', Journal of Maps, 12(sup1), pp. 261-270. Doi: 10.1080/17445647.2016.1195300.

Thacker, S., Barr, S., Pant, R., Hall, J. W. and Alderson, D. (2017a) 'Geographic Hotspots of Critical National Infrastructure', Risk Analysis, 37(12), pp. 2490-2505. Doi: 10.1111/risa.12840.

Thacker, S., Pant, R. and Hall, J. W. (2017b) 'System-of-systems formulation and disruption analysis for multi-scale critical national infrastructures', Reliability Engineering and System Safety, 167, pp. 30-41. Doi: 10.1016/j.ress.2017.04.023.

Thacker, S., Hall, J. W. and Pant, R. (2018) 'Preserving Key Topological and Structural Features in the Synthesis of Multilevel Electricity Networks for Modeling of Resilience and Risk', ASCE Journal of Infrastructure Systems, 24(1), 04017043. Doi: 10.1061/(ASCE)IS.1943-555X.0000404.

Tijera, M., Maqueda, G., Yagüe, C. and Cano, J. L. (2012) 'Analysis of Fractal Dimension of the Wind Speed and Its Relationships with Turbulent and Stability Parameters', in Ouadfeul, S.-A. (ed.), Fractal Analysis and Chaos in Geosciences, Chapter 2, pp. 29-46. Doi: 10.5772/51876.

Tobin, I., Jerez, S., Vautard, R., Thais, F., Van Meijgaard, E., Prein, A. and Noël, T. (2016) 'Climate change impacts on the power generation potential of a European mid-century wind farms scenario', Environmental Research Letters, 11(3), 034013. Doi: 10.1088/1748-9326/11/3/034013.

U

UNFCCC (2014) 'Glossary of climate change acronyms and terms'. Available at: http://unfccc.int/essential_background/glossary/items/3666.php (Accessed 4 December 2017).

V

Vajda, A., Tuomenvirta, H., Juga, I., Nurmi, P., Jokinen, P. and Rauhala, J. (2014) 'Severe weather affecting European transport systems: the identification, classification and frequencies of events', Natural Hazards, 72, pp. 169-188. Doi: 10.1007/s11069-013-0895-4.

van der Meer, J. W., ter Horst, W. L. A. and van Velzen, E. H. (2009) 'Calculation of fragility curves for flood defence assets', in P. Samuels, S. Huntington, W. Allsop and J. Harrop (eds.), Flood Risk Management – Research and Practice, Chapter 65, pp. 567-573. ISBN-13: 978-0-203-88302-0. Doi: 10.1201/9780203883020.

van der Walt, S., Schönberger, J. L., Nunez-Iglesias, J., Boulogne, F., Warner, J. D., Yager, N., Gouillart, E., Yu, T. and the Scikit-image contributors. (2014) 'scikit-image: Image processing in Python', PeerJ, 2(e453). Doi: 10.7717/peerj.453.

van Rossum, G. (1995) 'Python tutorial', Technical Report CS-R9526, Centrum voor Wiskunde en Informatica (CWI), Amsterdam, The Netherlands. Available at: https://ir.cwi.nl/pub/5007/05007D.pdf (Accessed 6 December 2015).

Voss, R. F. (1985) 'Random fractal forgeries', in: R. A. Earnshaw (ed.) Fundamental Algorithms for Computer Graphics, pp. 805-835. Berlin: Springer-Verlag. ISBN-13: 978-3-540-54397-8.

W

Walker, J. (1991) 'ppmforge', Netpbm. Available at: http://netpbm.sourceforge.net/doc/ppmforge.html (Accessed 10 February 2016).

Walsh, C. L., Roberts, D. and Dawson, R. J. (2013) 'Experiences of integrated assessment of climate impacts, adaptation and mitigation modelling in London and Durban', Environment and Urbanization, 25(2), pp. 361-380. Doi: 10.1177/0956247813501121.

Ward, D. M. (2013) 'The effect of weather on grid systems and the reliability of electricity supply', Climatic Change, 121(1), pp. 103-113. Doi: 10.1007/s10584-013-0916-z.

Wang, J.W. and Rong, L.-L. (2011) 'Robustness of the western United States power grid under edge attack strategies due to cascading failures', Safety Science, 49(6), pp. 807-812. Doi: 10.1016/j.ssci.2010.10.003.

Wang, S., Hong, L., Chen, X., Zhang, J. and Yan, Y. (2011) 'Review of interdependent infrastructure systems vulnerability analysis', proceedings of the 2nd International Conference on Intelligent Control and Information Processing, Harbin, China. Doi: 10.1109/ICICIP.2011.6008284.

Wang, S., Hong, L. and Chen, X. (2012) 'Vulnerability analysis of interdependent infrastructure systems: A methodological framework', Physica A, 391(11), pp. 3323-3335. Doi: 10.1016/j.physa.2011.12.043.

Watts, D. J. and Strogatz, S. H. (1998) 'Collective dynamics of small-world networks', Nature, 393(6684), pp. 440-442. Doi: 10.1038/30918.

Weisstein, E. W. (2008) 'Fast Fourier Transform', MathWorld, A Wolfram Web Resource. Available at: http://mathworld.wolfram.com/FastFourierTransform.html (Accessed 5 February 2016).

Wildavsky, A. (1991) 'Searching for Safety', Studies in Social Philosophy and Policy, No 10. New Brunswick, New Jersey: Transaction Publishers. ISBN-13: 978-0-912-05117-8.

Willets, R., Burdon, J., Glass, J. and Frost, M. (2010) 'Fostering sustainability in infrastructure development schemes', Proceedings of the ICE: Engineering Sustainability, 163(3), pp. 159 – 166. Doi: 10.1680/ensu.2010.163.3.159.

Williams, T. (2002) 'Modelling Complex Projects'. West Sussex: John Wiley & Sons. ISBN-13: 978-0-471-89945-7.

Willinger, W., Taqqu, M. S., Sherman, R. and Wilson, D. V. (1997) 'Self-similarity through high variability: statistical analysis of Ethernet LAN traffic at the source level', IEEE/ACM Transactions on Networking, 5(1), pp. 71–86. Doi: 10.1109/90.554723.

Wilkinson, S., Dunn, S. and Ma, M. (2012) 'The vulnerability of the European air traffic network to spatial hazards', Natural Hazards, 60(3), pp. 1027-1036. Doi: 10.1007/s11069-011-9885-6.

Whyte, J. (2016) 'The future of systems integration within civil infrastructure: A review and directions for research', proceedings of the 2016 INCOSE International Symposium, 26(1): pp. 1541–1555. Doi: 10.1002/j.2334-5837.2016.00244.x.

World Economic Forum (WEF) (2013) 'Global Risks 2013', 8th edition. Available at: http://www3.weforum.org/docs/WEF_GlobalRisks_Report_2013.pdf (Accessed 19 October 2017).

Y

Yerra, B. and Levinson, D. (2005) 'The emergence of hierarchy in transportation networks', The Annals of Regional Science, 39, pp. 541-553. Doi: 10.1007/s00168-005-0230-4.

Yu, L., Zhong, S., Bian, X. and Heilman, W. (2015) 'Temporal and Spatial Variability of Wind Resources in the United States as Derived from the Climate Forecast System Reanalysis', Journal of Climate, 28, pp. 1166–1183. Doi: 10.1175/JCLI-D-14-00322.1.

Yuan, X., Shao, S., Stanley, H. E. and Havlin, S. (2015) 'How breadth of degree distribution influences network robustness: comparing localized and random attacks', Physical Review E - Statistical, Nonlinear, and Soft Matter Physics, 92(3), 032122. Doi: 10.1103/PhysRevE.92.032122.

Z

Zavrl, M. S. and Zeren, M. T. (2010) ‘Sustainability of Urban Infrastructures’, Sustainability, 2(9), pp. 2950-2964. Doi: 10.3390/su2092950.

Zhao, S., Liu, X. and Zhuo, Y. (2017) ‘Hybrid Hidden Markov Models for resilience metrics in a dynamic infrastructure system’, Reliability Engineering & System Safety, 164, pp. 84-97. Doi: 10.1016/j.ress.2017.02.009.

Zhu, L., Ng, W.K. and Han, S. (2011) ‘Classifying Graphs Using Theoretical Metrics: A Study of Feasibility’ in: Xu, J., Yu, G., Zhou, S. and Unland, R. (eds) Database Systems for Advanced Applications. Lecture Notes in Computer Science, vol. 6637. Berlin, Heidelberg: Springer. Doi: 10.1007/978-3-642-20244-5_6.